UNIVERSITÀ DEGLI STUDI DI BOLOGNA

Research Doctorate in Geophysics – GEO/10

XIX Cycle

Glacial isostasy and sea level change in the Mediterranean: near and far–field effects on a millennium to century time–scale

Candidate:

Dr. Paolo Stocchi

Tutor:

Prof. Giorgio Spada

to my parents and my best friends

This work has been funded by Ministero dell'Universitá, dell' Istruzione, e della Ricerca (MIUR) by the PRIN2004 grant *"Variazioni globali di livello marino e riaggiustamento isostatico postglaciale: effetti delle proprietà reologiche del mantello terrestre sul tasso di incremento del livello marino"*.

Contents

Part I

Preface

Chapter 1

Ice ages and sea level change

Introduction

The long–term sea level variations represent one of the most important consequences of climate change. The present–day concern about the on–going global warming has recently pointed out the necessity to investigate the causes of the globally observed secular sea level rise. Despite of its role as indicator of the global temperature trend, sea level is strongly affected by different physical processes acting on a wide spectrum of time–scales ranging from seconds to millennia (Pirazzoli, 1991). To identify the presence of significant anthropogenic effects on present–day sea level rise it is necessary to decompose and evaluate the long term mechanisms unrelated to present–day climate change.

The *mean sea level* in the proximity of a coast is defined as the height of sea surface referred to a local terrestrial benchmark and averaged over a period of time long enough to remove high–frequency oscillations. However, given the high space– and time–variability of the physical processes perturbing sea surface, the definition of *true mean sea level* becomes extremely difficult, or even impossible, and puts on the characteristics of an elusive concept (Daly, 2002).

The employment of instruments and techniques able to averaging out high fre-

quency periodic signals, thus removing the effects of noise, does not allow the determination of the true mean sea level because of the presence of wide–ranging processes acting on medium to long time scales. Since both the present–day measurements from the tide–gauges and the paleo–sea level indicators are referred to the solid surface of the Earth, and also considering that both the sea and the solid surfaces undergo vertical movements with respect to the center of mass of the earth, the sea level variations are defined as *relative sea level changes*.

The long–term vertical movements of the sea surface which are ascribed to the volume change of the oceanic masses represent the climatic signal and are caused by two factors:

1. the water mass exchange between the ocean basins and the land based glaciers (i. e. the cryosphere),

2. the volume increase of the water as a consequence of warming of the oceanic shallow layers (i. e. *steric change*).

This global climate related alteration of the water volume contained in the ocean basins was termed by Suess (1906) as *eustatic* sea level change.

The history of the Earth has been cyclically marked by periodic phases of significant water exchange between the oceans and the land glaciers. Geology revealed the traces left during relative warm periods by the melting of huge ice sheets which had formed and expanded over northern and southern latitudes during previous and longer cold stages. The first contribution to the study of the glacial ages came during the XIX century from the field observations of the swiss geologist Louis Agassiz who, in the course of his expeditions in Northern Europe and North America identified different erosional and depositional glacial features. The wide extent of the areas covered by moraine deposits and erratic boulders could only be explained by assuming the presence of huge continental ice caps. In 1837 Agassiz announced the new theory that a vast *"ocean of ice"* had once extended from the polar to the present–day temperate regions. The subsequent geological, paleoclimatological

and stratigraphic investigations revealed the existence of different layers of glacial deposits characterized by an age increment with depth and corresponding to older *ice ages*. The presence between the glacial layers of well developed soils rich in fossils of plants which are characteristic of warm climates, demonstrated that the ice sheets had retired as a consequence of a global warming. Thus the ice ages had been succeeded by warmer *interglacials* during which the continental ice caps retired or even completely disappeared.

Though stratigrafic and sedimentologial data from the Antarctica and the oceans indicate the occurrence of glacial periods since the Miocene epoch, when the present–day polar ice caps started to form, the most studied and well known glaciations pertain to the recent Pleistocene epoch (1,600,000 – 10,000 yrs before present, BP). Since earlier investigation it became evident that the unconsolidated nature of the moraines sediments indicated a recent deposition, which later could be proved to be of Pleistocene epoch by means of radiocarbon dating methods. The geological evidences collected until the first half of XX century indicated a succession of at least five great continental glaciations which had been generated by global oceanic and atmospheric temperature changes and which in turn resulted in global sea level oscillations.

A fundamental contribution to the comprehension of the alternating global climate changes came from the studies of Cesare Emiliani (1955–1958) who developed a method based on the analysis of the isotopic ratio between the *"heavy"* oxygen (^{18}O) isotope and the ordinary *"light"* oxygen isotope (^{16}O) recorded in the sea bottom carbonate sediments. Foraminefera are unicellular ocean–wide diffused organisms characterized by en external calcareous shell ($CaCO_3$) which deposits on the sea bottom after the death. The ratio between ^{18}O and ^{16}O isotopes in the calcite shells of living organisms is the same as the ratio in the surrounding sea water which, in turn, is a direct function of the temperature of water. ^{18}O is two neutrons heavier than ^{16}O and causes the water molecule in which it is present to be heavier by that amount. The addition of more energy is therefore required to vaporize it than for

^{16}O, and the molecule must lose less energy to condense. As a consequence cooler water releases vapor that contains more ^{16}O while cooler air precipitates more ^{18}O than warmer air. In conclusion cooler water collects more ^{18}O relative to ^{16}O than does warmer water. On the basis of their temperature dependence the two oxygen isotopes behave differently in relation to the global hydrological cycle. During the glaciations, when the sea water temperature is $10 - 15\ ^{\circ}C$ lower than present, the water vapor characterized by a high content of ^{16}O moves towards higher latitudes and releases ^{18}O through condensation as approaches lower atmospheric temperatures. Afterwards, the precipitation of the vapor in form of snow and its subsequent accumulation as ice in the continental ice sheets store large amounts of ^{16}O while, at the same time, the ocean water gets richer in ^{18}O and the sea level drops. Conversely, during the *interglacials* the sea water is up to $5\ ^{\circ}C$ warmer than present and the ^{18}O content is lower.

The ^{18}O to ^{16}O ratio is commonly defined as

$$\delta^{18}O = ([(^{18}O/^{16}O)_{sample}/(^{18}O/^{16}O)_{standard}] - 1) \times 10^3, \tag{1.1}$$

where $\delta^{18}O$ indicates the deviation in part per thousand of the isotopic ratio measured by means of mass spectrometry in a benthic core sample and referred to a standard value, that is the mean isotopic ratio of ocean water. It is estimated that each 1 part per thousand change in $\delta^{18}O$ represents roughly a 1.5 - 2.0 $^{\circ}C$ change in tropical sea surface temperatures (Veizer et al., 2000). It turns out that high values of $\delta^{18}O$ indicate an increase in the global volume of continental glaciers. The analysis of the oxygen isotope data from the deep sea bottom core samples reveals the existence of cyclical variations in the $\delta^{18}O$ called Oxygen Isotope Ratio Cycles, which are correlated to alternating warm and cool periods in the paleoclimate of the Earth, called Marine Isotopic Stages (MIS).

Recently the the long–term evolution of the oxygen isotope ratio has been extended to 550 Myrs BP (Figure 1.1), thus covering the entire Phanerozoic Eon (Veizer et al., 1999). The new data have allowed for a better resolution of the paleoclimatic change during the last 65 Myrs (Zachos et al., 2001) and have permitted

the identification of the *stadials* and *interstadials* (see Figure 1.2). A stadial is a period of colder temperatures during an interglacial, characterized by an insufficient duration or intensity to be considered a glaciation, or a glacial period. Conversely, an interstadial is a warmer period during a glaciation of insufficient duration or intensity to be considered an interglacial.

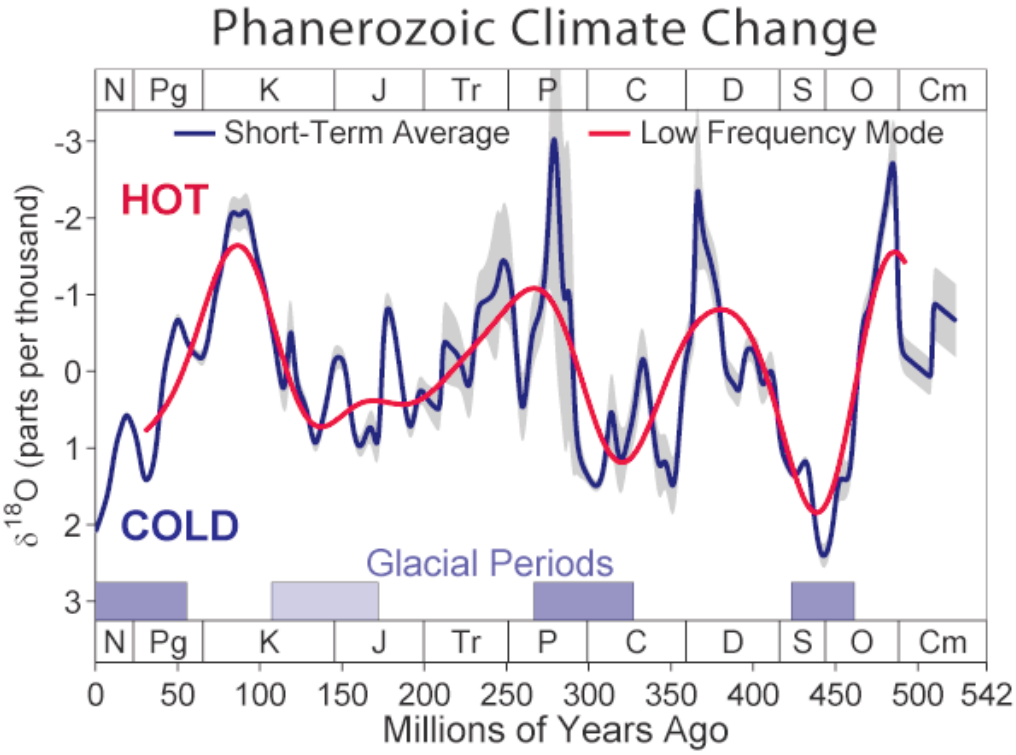

Figure 1.1: Phanerozoic Eon (from Veizer et al., 2000).

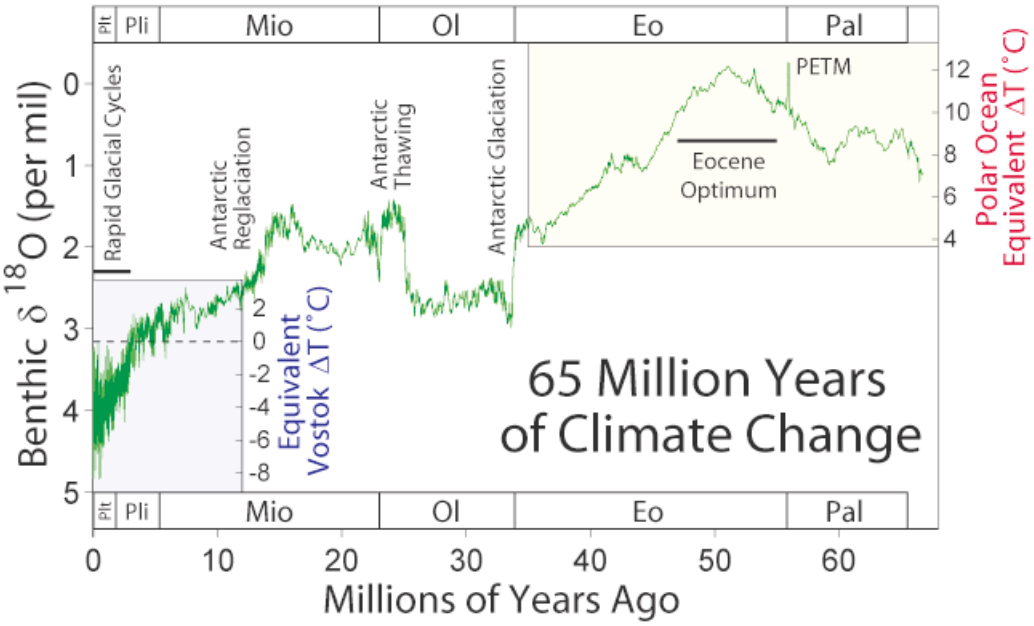

Figure 1.2: Cenozoic Era (from Zachos et al., 2001).

The early results of Cesare Emiliani were in good agreement with the climatic theory of Milutin Milankovitch (1930) based on the cyclical fluctuations of the astronomical parameters of the Earth. Milankovitch proposed that variations of orbital parameters could affect the amount of radiating solar energy received by the Earth, thus contributing to significant changes in the global climate and producing cyclical glaciations. The astronomical parameters affected by periodical variations are the eccentricity of the terrestrial orbit, and the inclination of the earth rotation axis in space. Since the XVII century Kepler evidenced that the terrestrial orbit was nearly elliptic and therefore that the distance between the Earth and the Sun was not constant during the year. Since the eccentricity of the elliptic orbit of the Earth varies from a minimum to a maximum with a period of 100000 years, the amount of solar energy received at the aphelion and perihelion varies with the same periodicity and produces more intense seasons in one hemisphere while cushions them in the opposite one. Furthermore, the timing of the passage of the Earth at the perihelion

is not constant because of the movement of precession which implies a cyclical variation of the position of the rotation axis with a period of 21000 - 26000 years. In conjunction with the variations of the eccentricity of the orbit and the movement of precession, Milankovitch considered also the inclination of the axis of rotation, which oscillates between 21.5° and 24.5° with respect to the ecliptic in a period of 41000 years. A decrease in the inclination produces an increase of the yearly solar radiation over the equatorial band and a reduction of radiating heat over the polar regions.

Milankovitch showed that the combined effect of the three astronomical parameters may induce significant oscillations of the intensity of the solar radiation at global scale or, at least, along the latitudinal bands of the Earth. However, also other factors such as the albedo, the heat accumulated into the oceans and the dynamics of the ice sheets have to be considered. In particular, the existence of short period climatic fluctuations does not rule out the effects of different factors such as the variations of the solar activity, the passage of the Earth through cosmic powder, the impact of meteorites and the volcanic eruptions. From both the astronomical theory of Milankovitch and the geochemical investigations based on the analysis of the oxygen isotopic ratio, a detailed description of the glacial events and an explanation of their periodicity during the Pleistocene clearly come out. It is nowadays accepted that the climate is subject to regular global changes with a long term glaciation every 100,000 years and shorter term glaciations every 40,000 and 20,000 years (see Figure 1.3, from Lisiecki and Raymo, 2005). When the long term periods are multiples of the shorter term periods, the changes are significantly greater. The data suggest, as a first approximation, a simple scheme for the evolution of the glaciations. The phase of ice accumulation at a constant rate over the continents is characterized by a length of 90,000 years and is subsequently followed by a 10,000 years of rapid disintegration of the ice caps. During the middle Pleistocene, from 700,000 to 125,000 years BP, 5 - 7 glaciations alternated with a periodicity of 100,000 years (see Figure 1.4).

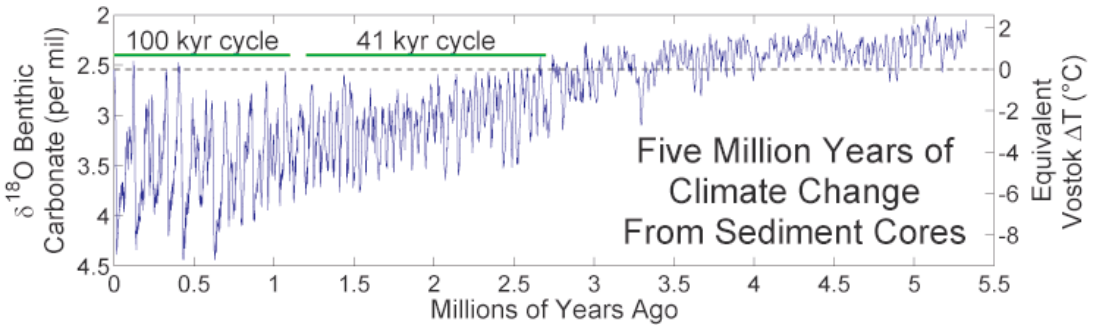

Figure 1.3: $\delta^{18}O$ anomaly over the last 5.0×10^3 years (from Lisiecki and Raymo, 2005).

During the last interglacial (125,000 years BP), the climate and the vegetation were similar to those pertaining to the Holocene (from 10,000 years BP to present) and the sea level was globally 5 - 6 m higher than present. Later the global climate became colder and at about 80,000 years BP the *Last Great Ice Age* began with the growth of isolated centers of ice expansion. In the course of time both the northern and southern Hemisphere glaciers coalesced to form composite ice sheets which reached their maximum extension between 30,000 and 18,000 years BP.

During the *Last Glacial Maximum* (LGM, 21000 - 18000 years BP) huge and thick ice caps covered not only Greenland and Antarctica but also North America and Eurasia, while the global sea level was 120 - 130 m lower than present (Denton and Hughes, 1981). The limit of the perennial snow was generally 1000 m below the present level and smaller mountain and alpine glaciers developed at lower latitudes (Smiraglia, 1992). Furthermore many regions which nowadays experience a temperate climate were characterized by periglacial to cold-desert environmental conditions while the tropical to subtropical deserts reached wider extensions. Conversely, the African and South American pluvial forests were significantly reduced. It is estimated that during the LGM the global volume of the ice stored over the continents was about 78×10^6 km^3 and that the regions covered by the ice were about the 30% of the emerged land, while nowadays their extent is reduced by about one third.

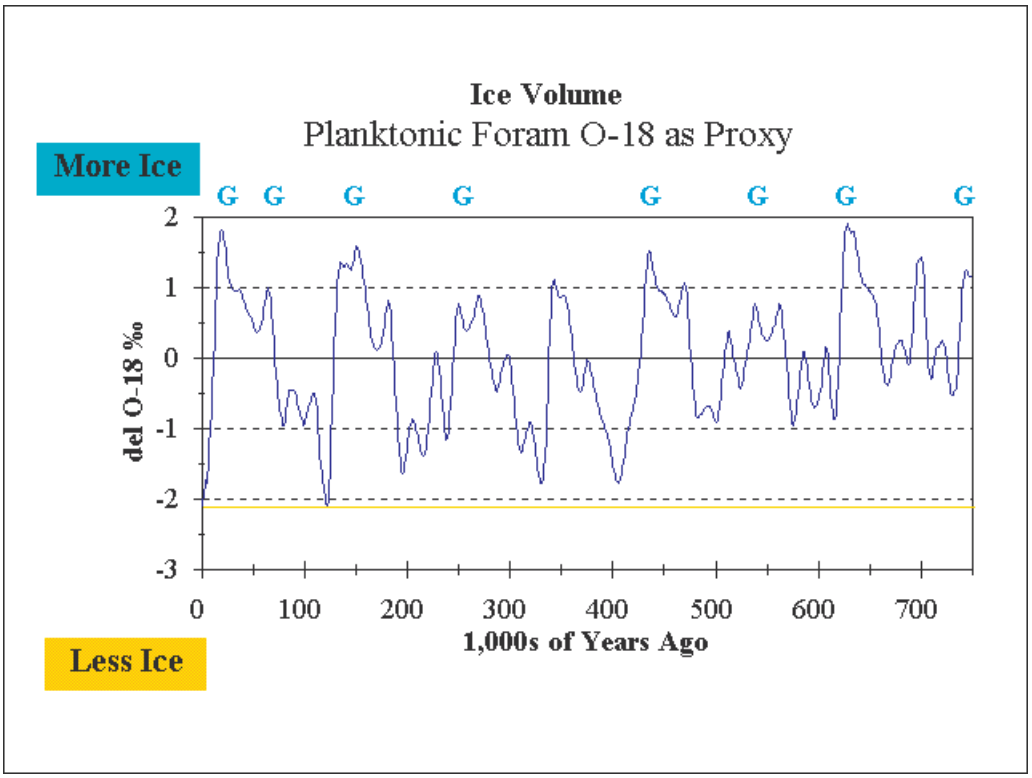

Figure 1.4: Pleistocene glacial to interglacial phases.

The Eurasian ice sheet reached a maximum extent of about 9×10^3 km^2 and was composed by three centers of ice expansion whereof the scandinavian region was the most important. During the LGM the fennoscandian ice cap was connected with the british glacier and to the siberian and Ural ice sheets. The main dome was characterized by a maximum thickness of 2500 - 3000 m and, with an extent of about 5×10^3 km^2, it covered the Baltic sea region, the Poland, a part of Russia and extended to the plains of central Europe which was delimitated in the south by the small alpine ice cap.

During the LGM the North American ice sheet reached a maximum thickness of 4000 - 5000 m and an extension of about 16×10^6 km^2 (Peltier, 1989), thus covering the whole Canada, part of Alaska and of the USA (up till the confluence of Ohio and Missisippi rivers) and making contact with the Greenland ice cap.

The main components of this huge *inlandsis* were the Cordilleran ice sheet on the west, the Ellesmere–Baffin ice sheet on the east and the most important central dome named Laurentide. The North American inlandsis formed following the coalescence of small northeastern ice caps (Baffin Island, Labrador) which generated the Laurentide ice sheet. The latter expanded further on until reached the Cordilleran Ice sheet. The huge North American inlandsis, given its dimensions, could affect the climate above its surface and on the surrounding areas (Fairbanks, 1989).

During the last Pleistocene glaciation, also defined as Wisconsinian, Vistola or Würm glaciation respectively from the North American, the Eurasian and the European Alpine ice sheets, the face of the planet appeared different with respect to the present configuration. In addition to the northern Hemisphere continental ice sheets, variations in the form of the emerged lands ascribed to the global sea level low stand were noticeable. The Strait of Bering was closed and Papua New Guinea was connected to Australia, while Japan was linked to the asiatic continent and the Black sea was disconnected from the Mediterranean Sea (Ryan and Pitman, 1997). Subsequently a global climate change caused the passage from glacial to interglacial conditions. As a consequence of global warming the Pleistocene continental ice sheets underwent a relatively rapid melting which occurred between 16,000 and 6,000 years BP. Besides the global climate and temperature modifications also other factors such as the ice sheets dynamics, the oceanographic and atmospheric regimes contributed to the rapid melting episodes which punctuated the retire of the North American and eurasian continental ice sheets. The present Holocene epoch, which began 10,000 years BP following a phase of rapid sea level rise was characterized by a general climatic amelioration and reached a *climatic optimum* at about 7,000 years BP, when the global glaciers extent was reduced with respect to the present–day configuration. During the last 6,000 years the glaciers experienced different short period phases of ice re–advance and retreat and the global climate reached a temperature minimum represented by an ice expansion between the XVI and XIX centuries called *Little Ice Age*. Later, a global increase in temperature triggered

the retire of the glaciers that had formed during the Little Ice Age and led to the present–day situation.

As stated above, during the last 125,000 years the global sea level experienced at first a drop of about 130 m and then a subsequent rise to the present level as a consequence of continental ice accumulation and melting. Despite the first historical observations of Celsius and Linneus, who both ascribed the observed sea level lowering in Sweden to a global evaporation or diminishing water supply (Saarman, 1948), the first authority considering the idea of world–wide sea level changes as a general working theory was Eduard Suess (1906). Starting from the ideas of Strabo who ruled out the existence of slopes on the ocean surface, Suess introduced the concept of *"eustatic"* changes in sea level, that is, since the oceans are interconnected, the vertical displacements of the ocean surface would follow a uniform pattern throughout the world. Despite the strong influence of this concept over the sea level research, the observed evidences of the Holocene relative sea level (RSL) variations collected around the world during the XX century indicated a strong influence of local to regional scale factors. The post–glacial global sea level variation could not be explained by a single sea level curve as stated by Suess. During the first decades of the XX century Daly (1920, 1940, and 1943) stressed the importance of the glacio–isostatic effects accompanying the lasts deglaciation phase, with uplift movements in areas of ice melting and subsidence movements in a wide peripheral belt (Figure 1.5). It soon became clear that during the last glaciation the huge ice sheets isostatically deformed the surface of the Earth as a consequence of their load. While the regions covered by the ice caps were depressed below the level prior to the glaciation, the surrounding peripheral regions were raised up above. Following the subsequent melting phase, the depressed regions started uplifting, thus locally reducing the entity of the sea level rise, while, at the same time, the peripheral forebulges started subsiding and therefore accelerating the rate of sea level rise.

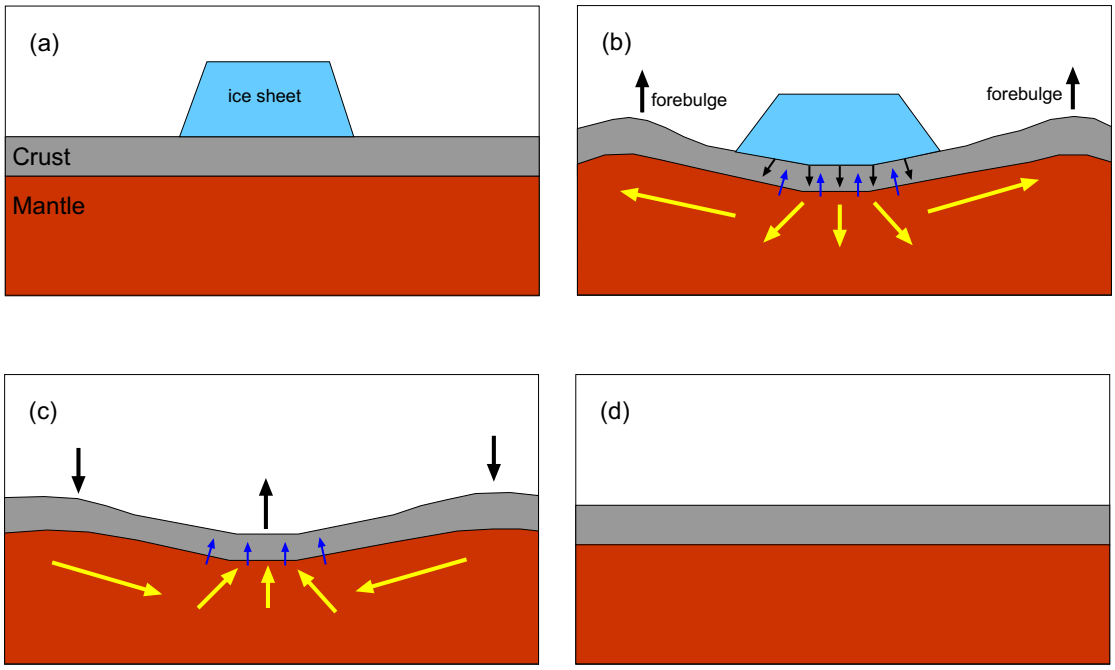

Figure 1.5: Glacial isostatic adjustment. The presence of an ice load (a) causes a depression of the surface of the Earth and a contemporaneous migration of the mantle material to peripheral region (b). Following ice melting, the depressed region undergoes a strong uplift while the forebulge collapses (c) to restore the original isostatic equilibrium (d).

The early insights into the glacio–isostatic effects on the sea level change solved the problem of the sea level lowering observed in Sweden by Celsius and Linneus (Saarman, 1948). During the LGM the Baltic sea region underwent a depression of about 500 m (Cathles, 1975) and later the melting of the fennoscandian ice cap caused a slow uplift of the solid surface which is still nowadays operating and constantly under measurement. This geophysical phenomenon, which also affects the North America, and especially the Hudson Bay (Canada), is called Post–Glacial Rebound (PGR) or even Glacio Isostatic Adjustment (GIA) and its study has provided significant results concerning the rheology, the structure and the composition of the mantle and of the lithosphere. Vertical movements of the solid surface are driven by the isostatic adjustment which results from the slow viscoelastic response of the Earth to the melting of the ice loads and to the contemporaneous addition of meltwater into the ocean. As a result, PGR contributes to vertical movements of the solid surface on a global scale. Furthermore, variations in the distribution of the surface loads, both in the cryosphere and in the hydrosphere, induce an interior redistribution of mass which in turn affects the equipotential surface of the terrestrial gravity field (*geoid*), and therefore modifies sea level.

The main task of the analysis of the past and present–day sea level data lies in the effort of separating the two main contributions to the sea level change, that is the eustatic and the glacio– hydro–isostatic forcing. While the eustatic signal provides information about global climate change, isostatic contribution yields insights in the nature of the solid Earth. Since different physical observables such as crustal deformations, sea level changes and free–air gravity anomalies are directly influenced by GIA, their measurement represents the fundamental set of informations against which the results of forward modeling can be tested. Vertical crustal velocities measured in the regions formerly covered by ice sheets are a function of the mantle viscosity. Therefore, from the analysis of the sea level variations in general it is possible to retrieve the mean value of the mantle viscosity which, in turn, allows for a better understanding of mantle rheology.

1.1 GIA modeling

The physical and mathematical approach to the study of the post–glacial rebound is based upon the analysis of the deformations which are induced in a continuum by forces associated to the presence of ice loads acting on its external surface. In a geophysical context, the first original modeling of the glacio–isostatic adjustment acting in northern Europe was performed by Haskell (1935, 1936) by means of a relatively simple earth model based on a viscous half–space characterized by a newtonian rheology and affected by an external ice load.

The main characteristics of the viscous model of Haskell can be summarized as follows:

- density and viscosity do not vary with depth (the continuum is homogeneous and isotropic),
- the continuum constitutive relation is linear,
- the geometry is bidimensional (the sphericity of the planet is not considered).

The fundamental governing equation for the flow of a highly viscous incompressible fluid with Newtonian rheology and constant viscosity is the Navier–Stokes equation

$$-\overrightarrow{\nabla p} + \rho_0 \, \vec{g} + \nu \Delta^2 \, \vec{v} = 0, \tag{1.2}$$

where p is the pressure, ρ_0 and ν are respectively the density and the viscosity of the fluid, $\vec{v}$ is the velocity field associated with the interior flux of matter and $\vec{g}$ is the gravity acceleration. By assuming that the quantities contained in Eq (1.2), with the exception of viscosity, are all functions of coordinates (x, y), where x is parallel to the external surface and y is positive downward, the problem describes the case of plane deformation.

The continuity equation for an incompressible fluid

$$\nabla\cdot \vec{v} = 0, \tag{1.3}$$

is satisfied for a vector field (v_x, v_y) such as

$$v_x = -\frac{\partial\psi}{\partial y} \qquad ; \qquad v_y = +\frac{\partial\psi}{\partial x}, \tag{1.4}$$

where the *stream function* $\psi = \psi(x, y)$ satisfies the biarmonic equation

$$\left(\frac{\partial^4}{\partial x^4} + 2\frac{\partial^4}{\partial x^2\partial y^2} + \frac{\partial^4}{\partial y^4}\right)\psi = \nabla^4\psi = 0, \tag{1.5}$$

by the introduction of ψ, the vector equation (1.2) reduces to a simple differential equation involving one unknown. Let suppose that at time $t = 0$ the external surface of the half space is subject to a displacement

$$h(x, t = 0) = h_0 \cos\frac{2x\pi}{\lambda}, \tag{1.6}$$

where λ is the characteristic wavelength of initial displacement, and $h_0 << \lambda$ is maximum vertical displacement. By assuming as a boundary condition that the horizontal velocity at the surface becomes void and by imposing the regularity of the solutions for $y \to \infty$, the temporal evolution of the displacement becomes

$$h(x, t) = h_0 \cos\frac{2x\pi}{\lambda} e^{-t/\tau_H}, \tag{1.7}$$

(Turcotte and Shubert, 1982) where τ_H is the *Haskell's characteristic relaxation time*,

$$\tau_H = \frac{4\pi\nu}{\lambda\rho_0 g_0}, \tag{1.8}$$

where g_0 is the modulus of the gravity acceleration at the free surface of the half space.

Together, the RSL data from the regions affected by the PGR, the time elapsed from melting of the Pleistocene ice sheets and the amount of the residual uplift represent the necessary information to retrieve an estimate of τ_0. From the available information it is possible to deduce a relaxation time of about 3000 years relatively

to the uplifting processes which affect the region once covered by the pleistocene fennoscandian ice sheet. By assuming for this glacier a lateral extent (wavelength) $\lambda \approx 3 \times 10^3$ km, and for $\rho_0 \approx 2.5 \times 10^3$ kg/m^3 and $g_0 = 9.8$ m/s^2, it is possible obtain, by inverting for the viscosity

$$\nu \approx 10^{21} Pa \cdot s, \tag{1.9}$$

which is the order of magnitude of the mean mantle viscosity.

Previously with respect to the study of Haskell, Darwin (1879) investigated the deformations at the free surface of a sphere by means of a spherical symmetry model consisting in a homogeneous viscous fluid characterized by a linear rheology. Unlike the half space model of Haskell, the spherical model incorporates selfgravitation and thus reproduces the geopotential variations induced by surface loads. Besides this fundamental difference, which nowadays characterizes the most recent PGR models, the relaxation of the surface of the sphere follows the same course of the Haskell's half space. The relaxation time of Darwin, τ_D, is

$$\tau_D = \frac{(2l^2 + 4l + 3)}{l} \frac{\nu}{\rho_0 g_0 a}, \tag{1.10}$$

where a is the radius of the sphere, and l is the harmonic degree of the Legendre polynomial expansion of the velocity field. The relaxation time τ_D depends only on the geometrical and mechanical parameters of the model.

Since the Earth exhibits an elastic behavior on short geological time scales, while, for longer time scales, it acts as a high–viscosity fluid, the simple viscous models are not enough adequate to the study of the GIA. On the contrary, a viscoelastic body perturbed by surface loads exhibits both an instantaneous elastic and a delayed viscous relaxation. The governing equations for a linear viscoelastic continuum are described in details in Appendix A.

The study of post–glacial rebound which followed the original work of Haskell replaced the early constant–viscosity half–space Earth model by taking into account the spherical symmetry of the Earth, the presence of a high–viscosity lithosphere, the depth–dependency of the mantle viscosity, and the perturbations of the geoid caused by the melting of the ice sheets (see e. g., Ranalli, 1987).

From the second half of the XX century to the present day, the modeling approach to the GIA has generally adopted a *(i)* spherically symmetric, *(ii)* incompressible, *(iii)* non–rotating, *(iv)* stratified, and *(v)* Maxwell viscoelastic Earth model (see Appendix A) where, for each layer, density, rigidity and Maxwell viscosity are constant. Furthermore, the inner core is assumed to be homogeneous and inviscid and the lithosphere is perfectly elastic. For this model the readjustment of the deformed surface is governed by a spectrum of relaxation times. The results obtained for different ice chronologies and viscosity profiles have proved to satisfactorily account for the GIA–related phenomena without the need to consider different rheologies and lateral heterogeneities of rheological parameters. However, during the last decade, attempts have been made to implement non–Newtonian rheologies and lateral variations of the rheological parameters such as lithospheric thickness and mantle viscosity (e. g., Spada et al., 2006; Gasperini et al, 2004).

1.2 Sea level variations and GIA

The exhaustive studies which followed the work of Daly (1920) stressed the inadequacy of a global eustatic sea level curve and, on the basis of different geological sea level indicators and studies on the rheology of the Earth, recognized the existence of regional differences in sea level response to deglaciation.

Farrell and Clark (1976) proposed a numerical model for the PGR–driven sea level change based on a spherical layered viscoelastic Earth and on different assumptions of the extent of the Pleistocene glaciers and of post–glacial melting rates. This mathematical description of the relation between the ice loads and the sea level change was called Sea Level Equation (SLE, see Chapters 2–6 for further details). According to a spatio–temporal discretization in which the ice sheets distributions vary by steps and the basic unknowns are decomposed in series of spherical harmonics, Clark et al. (1978) solved the SLE and found global complex patterns for the post–glacial relative sea level curves. The main limitations of the model were the little knowledge about both the viscoelastic response of the Earth and the rates of ice melting in a regional context and finally the lack of the Antarctic ice contribution to the global post–glacial melting. Despite the limitations and the in–built drawbacks which this circular reasoning involved, at least three significant consequences came out: *(i)* no part of the Earth's crust can be considered stable, *(ii)* the relationship between eustatic change and isostatic adjustment is not obvious and *(iii)* the concept of a global eustatic sea level change must be rejected.

The apparent differences between RSL predictions and observations pointed out the need to refine the assumptions on the ice sheets extent and melting and on the Earth's rheology, and, following the words of Kidson (1982):

"...suggested that as much is to be learned of glacial history and the earth's rheology from observations on sea level change as of the history of sea level change from studies of the earth's rheology".

Clark et al. (1978) confirmed the existence of significant regional differences in the post–glacial sea level rise and demonstrated the importance of the different glacio– and hydro–isostatic effects of the ice melting on the global sea level. The geophysical phenomena which operate simultaneously during the formation and the melting of the continental glaciers can be summarized as follows:

1. **Glacio–eustasy**. As previously stated, the post–glacial eustatic sea level variation is referred to the modification of the oceanic water volume which follows the mass exchange between the cryosphere and the hydrosphere in the absence of any deformational and gravitational effect (Figure 1.6).

2. **Glacio–isostasy**. A previously depressed region tends to restore its original surface of isostatic equilibrium (solid black line in Figure 1.7) through a significant uplift movement, which results in a regional sea level lowering. On the contrary, the surrounding circular forebulge zone is subject to subsidence that enhances the rate of post–glacial sea level rise.

3. **Hydro–isostasy**. The eustatic sea level rise (Figure 1.6, right frame) is followed by a deformation of the the ocean floor as a consequence of the change in the water load (Figure 1.8). This effect produces a complex pattern in the regional to global post–glacial sea level rise.

4. **Geoidal eustasy**. The equipotential surface of the ocean (i. e. the geoid) shows undulations which are related to local to regional variations of the Earth's gravitational field. The shape and the position of these deformations vary with time following the readjustment of the earth's gravitational field in response to the interior fluxes of matter and to the modification of the ice sheets configurations.

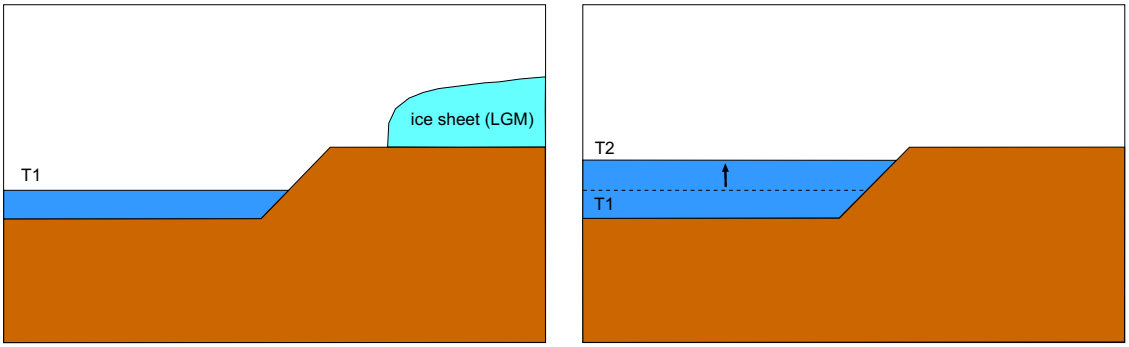

Figure 1.6: Glacio-eustasy. At the initial time T1, which refers to the LGM (left frame), the sea level is at a low–stand. After the end of melting (T2, right frame) the new sea level reaches a highstand.

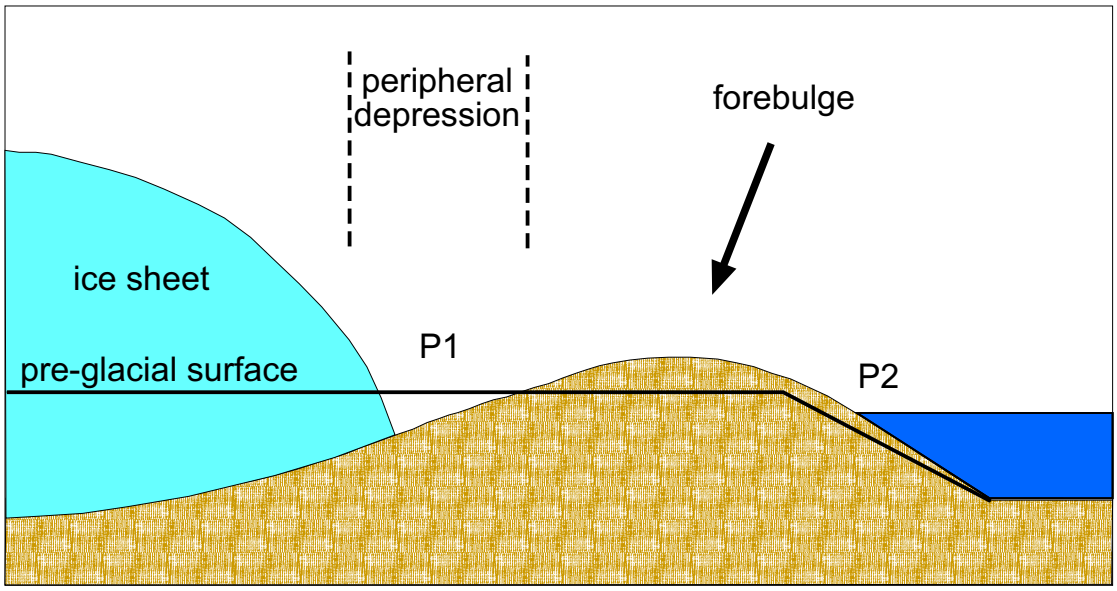

Figure 1.7: Glacio–isostasy. The rate of vertical uplift which affects both the previously covered region and the peripheral depression (P1) exceeds the rate of sea level rise ascribed to the ice melting, and results in a relative sea level drop. Subsidence of the forebulge region (P2) contributes to accelerate post–glacial sea level rise.

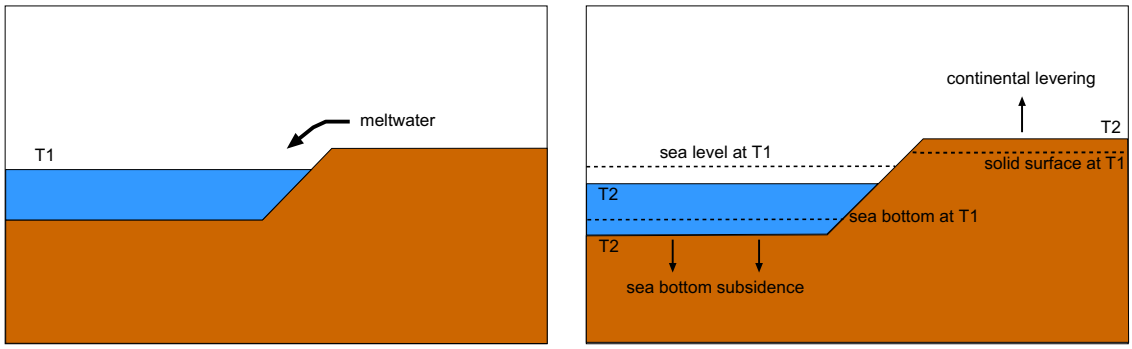

Figure 1.8: Hydro–isostasy. The addition of post–glacial meltwater to the ocean at time T1 causes subsidence of the sea bottom and a simultaneous uplift of continents (*continental levering*). The combined effects result in a sea level fall along the oceanic margins of the continents.

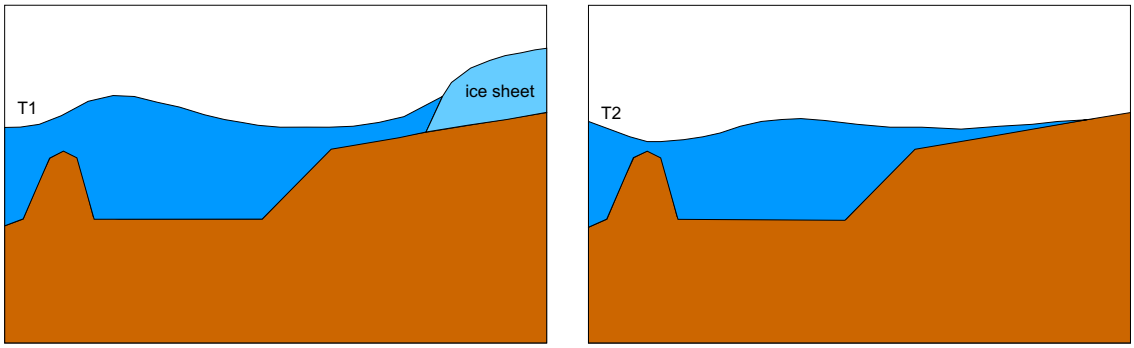

Figure 1.9: Geoidal eustasy. The surface of the ocean is subject to the gravitational attraction of the continental ice sheets and results in a regional sea level highstand around the ice masses (left frame). After the deglaciation sea level around the previous ice caps tends to fall (right frame).

The simultaneous forcing of the geophysical phenomena accompanying melting of continental glaciers results in a complex zonation of the global ocean based on the shape of post–glacial sea level curves. Figure 1.10 shows results of Clark and Lingle (1979) for an ice chronology lacking of Antarctic component. It is interesting to observe the differences between the eustatic sea level rise ending at 5,000 years BP and the curves pertaining to zones I–VI. Zone I encompasses regions once covered by Pleistocene ice sheets and exhibits a post–glacial sea level fall up to present–day as a consequence of uplift (see Figures 1.5 and 1.7). The forebulge regions pertain to Zone II where a monotonous sea level rise driven by a regional subsidence follows the end of melting (see Figure 1.7). Zones V and VI refer respectively to mid–ocean regions and continental borders. Both Zones show a sea level higher than present in correspondence to the end of melting (5.0 kyrs BP). The subsequent sea level fall of Zone VI is ascribed to continental levering (see also Figure 1.8) while in Zone V it results from a complex mechanism called *"equatorial ocean syphoning"* (Mitrovica and Milne, 2002) consisting in the combined effect of sea bottom subsidence and water migration from oceans to fill the gaps left by collapsing forebulge regions.

The general departure from eustasy and the zonal trends of sea level change after the end of melting are driven by the delayed viscous response of the Earth to deglaciation. Since the the last deglaciation ended about 6,000 years BP the GIA is still affecting the measured present–day sea level change and solid surface movements of Earth. Furthermore, because this melting phase lies in the range in which the radioactive carbon ^{14}C is applicable to provide chronological control of the recorded planetary response to this event, quantitatively constrained analyses of both solid Earth rheology and paleo–climatic dynamics may be performed by means of numerical models.

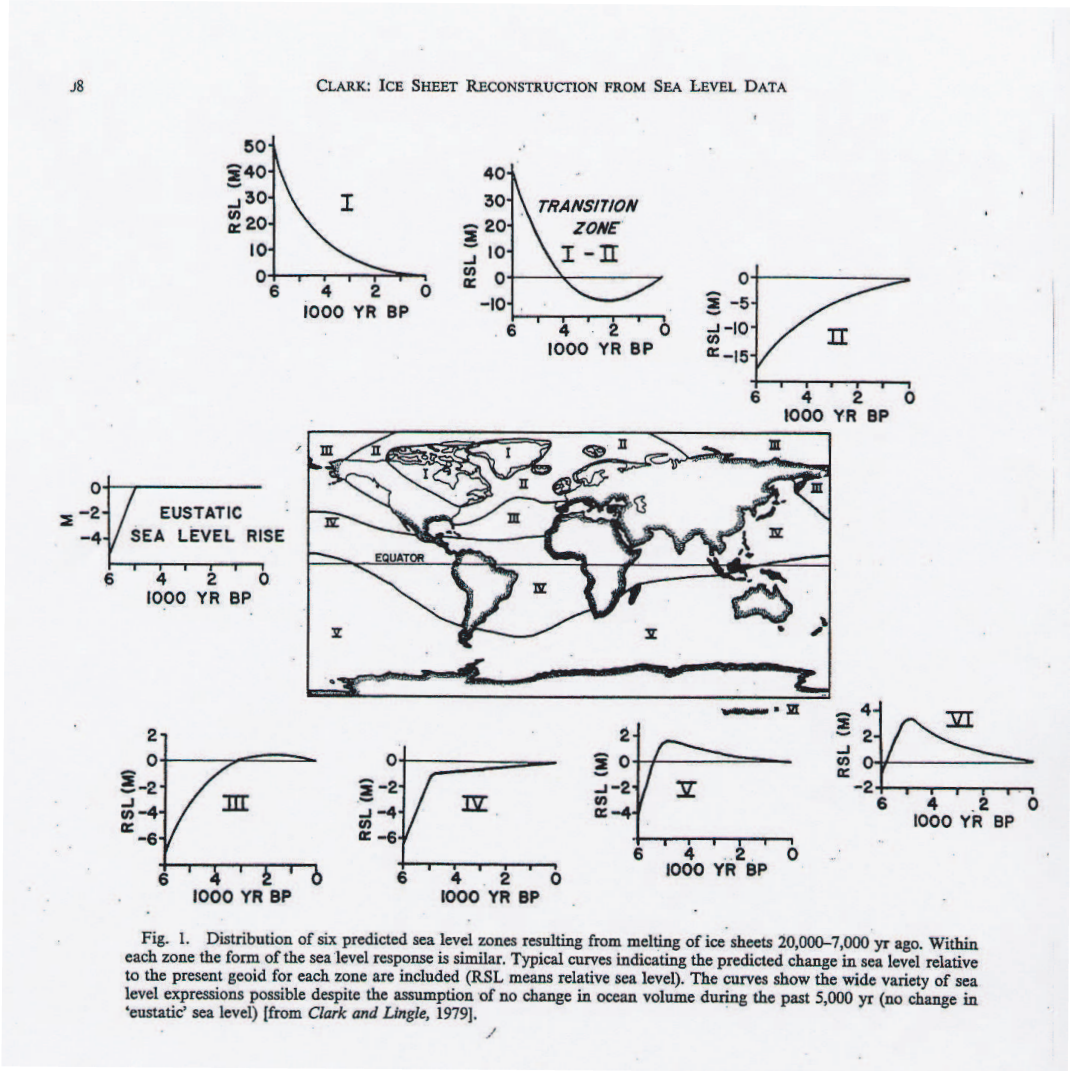

Fig. 1. Distribution of six predicted sea level zones resulting from melting of ice sheets 20,000–7,000 yr ago. Within each zone the form of the sea level response is similar. Typical curves indicating the predicted change in sea level relative to the present geoid for each zone are included (RSL means relative sea level). The curves show the wide variety of sea level expressions possible despite the assumption of no change in ocean volume during the past 5,000 yr (no change in 'eustatic' sea level) [from *Clark and Lingle*, 1979].

Figure 1.10: Clark's zones (after Clark and Lingle, 1979).

1.3 Research objectives

The present Doctoral Thesis work has been developed in the framework of the National Research Program PRIN2004: *"Global sea level variations and isostatic postglacial adjustment: effect of the rheological properties of the Earth mantle on the present rate of sea level rise"*. This project originated from the joint efforts of the two research groups, respectively pertaining to the Universities of Urbino and Bologna, which have been cooperating for a long time and have a specific experience on the topic of the post-glacial isostatic adjustment. As previously stated, this phenomenon has accompanied and followed the melting of the Pleistocene ice sheets and its implications have both a relevant scientific and a socio-economical impact. As testified by a broad scientific literature, a correct description of this phenomenon is a key for the understanding of a major planetary emergency: the progressive sea level rise in response to the increased mean surface temperature of the planet.

The link between isostatic adjustment, which is mainly a solid Earth process, and sea level rise, is apparent when one considers the problem of obtaining an eustatic signal from the longest available tide-gauge records, that represent the most valuable source of information about the present-day changes in the mean sea level. It is thus clear that a more accurate knowledge of the rheological properties of the mantle would allow to reliably correct to the tide-gauge derived rates and, in turn, for an improved estimate of the present-day sea level rise and for a the quantification of possible contributions of anthropic origin (enhanced greenhouse effect, urban warming, etc.).

In this work we have addressed the problem of postglacial isostatic adjustment by making use of innovative methods and also of alternative hypotheses for the Earth rheology. Following the general aim of improving our knowledge of both solid Earth and glacial dynamics, we have adopted advanced numerical modeling tools and considered available geological and geophysical data to constraining rheological properties and deformation mechanisms of the Earth, and inferring phenomenology

of the last deglaciation phase. We have faced various aspects of glacial isostatic adjustment, with the purpose of improving the usual approach to the problem, based on the hypothesis that Earth mantle materials obey to a linear rheology, and that the physical parameters of this rheology can be only characterized by their depth dependence. Getting through these assumptions and also through the "standard model" till now employed to study the GIA has demanded new modeling strategies and the development and distribution of new computing tools and theories finalized to the study of postglacial deformations and related phenomena. Therefore in the preliminary phase of this work we have developed a free source pseudo-spectral code (`SELEN`) aimed at the solution the Sea level Equation assuming a depth-dependent rheology (see Chapter 5). As previously mentioned in Section 1.1 the SLE is an integral equation that allows to predict the sea level variations accompanying glacial isostatic adjustment. By means of the "pseudo–spectral" solution method the SLE can be solved to obtain predictions of relative sea level variations and other geophysical quantities. The theory of the SLE (see Chapters 2, 3 and 4 of Part II) is based on these approximations:

1. the Earth is assumed to be radially stratified and incompressible, and the various layers are characterized by a linear viscoelastic rheology. This is a common approximation, but recent work has been done to include non–Newtonian rheologies and lateral viscosity variations in spherical Earth models (see e. g., Giunchi and Spada, 2000; Wu and Vanderwal, 2003),

2. it is assumed that the ocean function is constant, that implies fixed shorelines. The effect of allowing for time–dependent shorelines has been discussed in Johnston (1993),

3. we totally neglect the effects of rotation on the GIA–induced sea level variations. The reader is referred to Milne (1998) for the theoretical details concerning the rotational feedback and for the numerical evaluation of its consequences.

In view of the approximations above, our code provides a zeroth–order model for the postglacial sea level changes (see Chapter 6 for some applicative examples), that can be considerably improved in the future.

In the course of 2005 we have joined with `SELEN` in the SBL/GGFC project *"Standard model of present-day signals due to post-glacial rebound"* aimed at the definition of a *"standard GIA model"* (see Section 6.4 for further details). The theory described in Part II is a synthesis of a number of works that have been published in the course of the last three years (Spada et al., 2004; Spada and Stocchi, 2006; Spada and Stocchi, 2007).

Within the PRIN 2004 project, we have tested the potentialities of the PS method to investigate the GIA signatures in the Mediterranean Sea. By means of `SELEN` we have modeled and characterized the Holocene and present–day RSL changes ascribed to the melting of the remote Pleistocene ice sheets and of the Würm Alpine glacier. A fundamental part of this has task concerned the definition of a RSL reference database and of its resolving power of Holocene sea level variations in order to constrain the glacial chronology and the three–dimensional rheological structure of lithosphere and mantle. Part III of this dissertation describes the study of the Holocene and present–day sea level changes in the Mediterranean Sea and is a synthesis of published papers (Stocchi et al., 2005a, 2005b; Stocchi and Spada, 2006; Stocchi and Spada, 2007). The reader is referred to Section 7.2 and further Chapters in Part III for more details.

Part II

Glacial isostatic adjustment and sea level change

Chapter 2

The GIA problem

The first part of this chapter is devoted to the description of the Green's function approach in the context of the GIA theory. The Green's functions (henceafter GFs) provide a way to quantify the three dimensional displacements and the variation of the gravitational potential when a point–like, impulsive load is applied to the surface of a spherically symmetric, layered Earth model. The usefulness of the GFs technique is limited to the case of elastic or linear viscoelastic rheologies.

Except for models characterized by a very simple internal structure (Wu and Ni, 1996), the GFs cannot be established by means of purely analytical methods. For multi–layered models the GFs can only be computed numerically by means of the load–deformation coefficients (LDCs) obtained by the "normal modes" technique Peltier, 1974, 1985; Vermeersen and Sabadini, 1997; Spada et al., 2004).

Once the viscoelastic GFs have been constructed, the response of the Earth model to surface loads of arbitrary geometries and time–histories can be obtained by spatio–temporal convolutions. This will be explained in detail in Section 2.3, that is devoted to the solution of what we have called "simplified GIA problem", in which the water load is assumed to be uniformly distributed.

2.1 Green's functions

Here we introduce the GFs for the three components of the displacement field and for the incremental gravitational potential, in the case of rigid (Section 2.1.1), elastic (2.1.2), and viscoelastic (2.1.3) layered Earth models, respectively. The sea level GF, that constitutes one of the basic ingredients of the sea level equation, will be defined in Section 2.1.4.

2.1.1 Rigid Earth

We consider a localized point mass placed at the surface of a rigid, spherically symmetric Earth. We define the "dynamic" mass of the surface load as

$$\mu(t) = f(t)m_s, \tag{2.1}$$

where $f(t)$ describes its time–evolution, and m_s represents its intrinsic (or static) mass. For an impulsive load, $f(t) = \delta(t)$ where $\delta(t)$ is Dirac's delta, so that in this specific case the dynamic mass

$$\mu(t) = \delta(t)m_s \tag{2.2}$$

has dimensions of a mass per unit time.

The gravitational potential per unit time exerted by the localized mass at a point P on the Earth surface is

$$\phi^r(d,t) = \frac{\Gamma\mu(t)}{d}, \tag{2.3}$$

where Γ is Newton's constant, d is the distance between the mass and P, and the superscript r recalls that we are dealing with a rigid Earth. Since ϕ^r adds to the background potential of the Earth, we will refer to it as to the *incremental* gravitational potential.

By simple trigonometry,

$$d(\alpha) = 2a\sin(\alpha/2), \tag{2.4}$$

where α is the colatitude of P with respect to the point load and a is the radius of the Earth. This allows to write

$$\phi^r(\alpha, t) = \frac{a\gamma m_s \delta(t)}{2m_e \sin(\alpha/2)}, \tag{2.5}$$

where

$$\gamma = \frac{\Gamma m_e}{a^2} \tag{2.6}$$

is the surface gravity acceleration in spherical approximation, and m_e is the mass of the Earth.

Since ϕ^r only results from the gravitational attraction of the imposed point mass, it is sometimes referred to as *direct* potential. The GF for the incremental gravitational potential for a rigid Earth is defined as

$$G^r_\phi(\alpha, t) \equiv \frac{\phi^r(\alpha, t)}{m_s} = \frac{a\gamma\delta(t)}{2m_e \sin(\alpha/2)}, \tag{2.7}$$

where, by its own definition, $G^r_\phi(\alpha, t)$ has the dimensions of a gravitational potential per unit time and unit mass.

An equivalent expression for the GF can be obtained recalling the Legendre sum:

$$\sum_{l=0}^{\infty} P_l(\cos\alpha) = \frac{1}{2\sin(\alpha/2)}, \tag{2.8}$$

where $P_l(\cos\alpha)$ is the Legendre polynomial of harmonic degree l (Appendix B.1). Hence, from (2.7), the spectral form of G^r_ϕ is

$$G^r_\phi(\alpha, t) = \delta(t) \sum_{l=0}^{\infty} \phi^r_l P_l(\cos\alpha), \tag{2.9}$$

where

$$\phi^r_l \equiv \frac{a\gamma}{m_e}. \tag{2.10}$$

2.1.2 Elastic Earth

For an elastic Earth, the action of the impulsive mass (2.2) produces two related effects. First, the planet yields under the pressure exerted by the load. Second, there is a variation of the gravitational potential following the change of the shape of the Earth. In analogy with (2.9), the corresponding GF may be written as

$$G^e_\phi(\alpha,t) = \delta(t)\sum_{l=0}^{\infty}\phi^e_l P_l(\cos\alpha), \tag{2.11}$$

which is in phase with G^r_ϕ as a consequence of elasticity. Furthermore, since the Earth responds linearly to the imposed forces, the spectral coefficients ϕ^e_l are proportional degree-by-degree to ϕ^r_l:

$$\phi^e_l = k^e_l \phi^r_l, \tag{2.12}$$

where the non–dimensional number k^e_l is the elastic *load–deformation coefficient* (hereafter LDC) for the incremental gravitational potential.

The total GF for the incremental gravitational potential stems from a rigid and an elastic component

$$G_\phi(\alpha,t) = G^r_\phi(\alpha,t) + G^e_\phi(\alpha,t), \tag{2.13}$$

and, according to Eqs. (2.9-2.12) above, can be cast in the following spectral form

$$G_\phi(\alpha,t) = \delta(t)\frac{a\gamma}{m_e}\sum_{l=0}^{\infty}(1+k^e_l)P_l(\cos\alpha). \tag{2.14}$$

At the surface of the Earth, the elastic displacement induced by the applied load can be expressed as

$$\vec{u}(\alpha,t) = G_u(\alpha,t)\hat{r} + G_v(\alpha,t)\hat{\alpha}, \tag{2.15}$$

where $\hat{r}$ and $\hat{\alpha}$ are unit vectors in the directions of increasing radius and colatitude, and G_u and G_v are the GFs relative to the vertical and horizontal components of displacement, respectively. By virtue of the spherical symmetry of the Earth, the

longitudinal component of displacement – perpendicular to both $\hat{r}$ and $\hat{\alpha}$ – vanishes identically. Therefore, in analogy with (2.13), we write the displacement GFs as

$$G_u(\alpha,t) = G_u^r(\alpha,t) + G_u^e(\alpha,t), \tag{2.16}$$

and

$$G_v(\alpha,t) = G_v^r(\alpha,t) + G_v^e(\alpha,t), \tag{2.17}$$

where

$$G_u^r(\alpha,t) = G_v^r(\alpha,t) = 0 \tag{2.18}$$

since the Earth is rigid.

The vertical and horizontal components of displacement can be expressed in spectral form by means of appropriate LDCs. Following (2.11) we write

$$G_u^e(\alpha,t) = \delta(t)\sum_{l=0}^{\infty} u_l^e P_l(\cos\alpha) \tag{2.19}$$

$$G_v^e(\alpha,t) = \delta(t)\sum_{l=0}^{\infty} v_l^e \frac{\partial P_l(\cos\alpha)}{\partial\alpha}, \tag{2.20}$$

where

$$u_l = h_l^e \frac{\phi_l^r}{\gamma} \tag{2.21}$$

$$v_l = \ell_l^e \frac{\phi_l^r}{\gamma} \tag{2.22}$$

define the elastic LDCs h_l^e and ℓ_l^e.

From above, the GFs pertaining to vertical and horizontal displacement are

$$G_u^e(\alpha,t) = \delta(t)\frac{a}{m_e}\sum_{l=0}^{\infty} h_l^e P_l(\cos\alpha) \tag{2.23}$$

and

$$G_v^e(\alpha,t) = \delta(t)\frac{a}{m_e}\sum_{l=0}^{\infty} \ell_l^e \frac{\partial P_l(\cos\alpha)}{\partial\alpha}, \tag{2.24}$$

that with (2.14) constitute the basic set of GFs for an elastic Earth. We observe that G_u^e and G_v^e have dimensions of displacements per unit time and per unit mass.

2.1.3 Viscoelastic Earth

Viscoelasticity introduces a delayed response of the Earth to the surface load. As first shown by Peltier (1974) and later discussed in a number of papers, for a spherically symmetric layered and linear viscoelastic Earth, the GF relative to the total incremental gravitational potential reads

$$G_\phi(\alpha,t) = G^r_\phi(\alpha,t) + G^e_\phi(\alpha,t) + G^v_\phi(\alpha,t), \tag{2.25}$$

where the rigid and elastic components are given by (2.7) and (2.11), respectively, while the viscous part is

$$G^v_\phi(\alpha,t) = H(t)\frac{a\gamma}{m_e}\sum_{l=0}^{\infty}\left(\sum_{j=1}^{M} k_{lj}e^{s_{lj}t}\right)P_l(\cos\alpha), \tag{2.26}$$

where

$$H(t) = \begin{cases} 1, & t \geq 0 \\ 0, & t < 0 \end{cases} \tag{2.27}$$

is the Heaviside step function, k_{lj} are the *viscoelastic LDCs* for the incremental potential, and

$$s_{lj} = -1/\tau_{lj}, \tag{2.28}$$

where τ_{li} are the *relaxation times* of the Earth model that is being adopted. The couple $\{k_{lj}, s_{lj}\}$ $(l = 0, 1, \ldots; j = 1, 2, \ldots M)$ is referred to as the j–th *viscoelastic mode* of degree l. The *fluid LDCs* are

$$\left\{\begin{array}{c} k^f_l \\ h^f_l \\ \ell^f_l \end{array}\right\}(t) = \left\{\begin{array}{c} k^e_l \\ h^e_l \\ \ell^e_l \end{array}\right\} + \sum_{j=1}^{M}\tau_{lj}\left\{\begin{array}{c} k_{lj} \\ h_{lj} \\ \ell_{lj} \end{array}\right\}. \tag{2.29}$$

The number of viscoelastic modes M in (2.26) and (2.29) increases with increasing number of layers and also depends on the nature of the internal boundaries (Peltier and Andrews, 1976; Peltier, 1985; Spada et al., 1992). The reader is referred to Spada et al. (2003) for more details on how the modes can be numerically

determined. Using (2.14) and (2.26) in (2.25), the complete form of the viscoelastic GF for the incremental potential turns out to be

$$G_{\phi}(\alpha,t)=\frac{a\gamma}{m_e}\sum_{l=0}^{\infty}\left(\delta(t)(1+k_l^e)+H(t)\sum_{i=1}^{M}k_{li}e^{s_{li}t}\right)P_l(\cos\alpha). \tag{2.30}$$

The GFs pertaining to the vertical and horizontal components of displacement can be similarly written as the sum of elastic and viscoelastic parts, with

$$G_u(\alpha,t)=G_u^e(\alpha,t)+G_u^v(\alpha,t) \tag{2.31}$$

and

$$G_v(\alpha,t)=G_v^e(\alpha,t)+G_v^v(\alpha,t), \tag{2.32}$$

where we have used (2.18), the elastic components G_u^e and G_v^e are given by (2.23) and (2.24), respectively, and in analogy with (2.26) the viscous components are

$$G_u^v(\alpha,t)=H(t)\frac{a}{m_e}\sum_{l=0}^{\infty}\left(\sum_{j=1}^{M}h_{lj}e^{s_{lj}t}\right)P_l(\cos\alpha) \tag{2.33}$$

and

$$G_v^v(\alpha,t)=H(t)\frac{a}{m_e}\sum_{l=0}^{\infty}\left(\sum_{j=1}^{M}\ell_{lj}e^{s_{lj}t}\right)\frac{P_l(\cos\alpha)}{\partial\alpha}, \tag{2.34}$$

where h_{lj} and ℓ_{lj} are the viscoelastic LDCs relative to the radial and horizontal components of displacement, respectively (notice that the relaxation times are common to all of the three viscous GFs so far introduced). The total GFs for the components of displacement are thus

$$G_u(\alpha,t)=\frac{a}{m_e}\sum_{l=0}^{\infty}\left(\delta(t)h_l^e+H(t)\sum_{j=1}^{M}h_{lj}e^{s_{lj}t}\right)P_l(\cos\alpha) \tag{2.35}$$

and

$$G_v(\alpha,t)=\frac{a}{m_e}\sum_{l=0}^{\infty}\left(\delta(t)\ell_l^e+H(t)\sum_{j=1}^{M}\ell_{lj}e^{s_{lj}t}\right)\frac{P_l(\cos\alpha)}{\partial\alpha}. \tag{2.36}$$

A more compact form for the GFs can be established introducing the time–dependent LDCs:

$$\left\{ \begin{array}{c} k_l \\ h_l \\ \ell_l \end{array} \right\}(t) = \left\{ \begin{array}{c} 1+k_l^e \\ h_l^e \\ \ell_l^e \end{array} \right\}\delta(t) + \sum_{j=1}^{M} H(t) \left\{ \begin{array}{c} k_{lj} \\ h_{lj} \\ \ell_{lj} \end{array} \right\} e^{s_{lj}t}, \tag{2.37}$$

that finally allows to write

$$\left\{ \begin{array}{c} \frac{1}{\gamma}G_\phi \\ G_u \\ G_v \end{array} \right\}(\alpha,t) = \frac{a}{m_e}\sum_{l=0}^{\infty} \left\{ \begin{array}{c} k_l \\ h_l \\ \ell_l \end{array} \right\}(t) \left\{ \begin{array}{c} 1 \\ 1 \\ \partial_\alpha \end{array} \right\} P_l(\cos\alpha), \tag{2.38}$$

with $\partial_\alpha \equiv \frac{\partial}{\partial\alpha}$.

2.1.4 The sea level Green function

The *s*ea level GF G_s constitutes one of the essential ingredients of the SLE (see Section 3.3). Physically, G_s represents the offset between the Earth's geoid and the topography, hence its relevance in the context of sea level change. It is defined as

$$\frac{G_s}{\gamma}(\alpha,t) \equiv \frac{G_\phi}{\gamma} - G_u, \tag{2.39}$$

where G_ϕ and G_u are given (2.38). Using (2.25) and (2.31) into (2.39), we obtain

$$\frac{G_s}{\gamma}(\alpha,t) = \frac{G_\phi^r}{\gamma} + \left(\frac{G_\phi^e}{\gamma} - G_u^e\right) + \left(\frac{G_\phi^v}{\gamma} - G_u^v\right), \tag{2.40}$$

where the first, second, and third term represent the rigid, the elastic, and the viscous components of G_s, respectively.

In the discussion of Section 4.3.2, it will be convenient to write the sea level GF in the equivalent form

$$\frac{G_s}{\gamma}(\alpha,t) = \beta\Big(\psi^\delta(\alpha)\delta(t) + \psi^h(\alpha,t)H(t)\Big), \tag{2.41}$$

where

$$\psi^\delta(\alpha) \equiv \sum_{l=0}^{\infty}(1+k_l^e-h_l^e)P_l(\cos\alpha), \tag{2.42}$$

and

$$\psi^h(\alpha,t) \equiv \sum_{l=0}^{\infty}\left(\sum_{j=1}^{M}(k_{lj}-h_{lj})e^{s_{lj}t}\right)P_l(\cos\alpha), \tag{2.43}$$

with

$$\beta = \frac{a}{m_e}. \tag{2.44}$$

2.2 Surface loads

The response of the Earth to a localized impulsive load (i. e. the GFs), can be used to build the response to finite–size, time–evolving surface loads. In general, we can write the total load as

$$\mathcal{L}(\omega,t) = L_i + L_o, \tag{2.45}$$

where $\omega = (\theta,\lambda)$, θ and λ are colatitude and longitude, t is time, and L_i and L_o are the surface loads associated with changes of the weight of the ice sheets and of the oceans, respectively. These two terms are separately studied in the following sections.

2.2.1 Ice load

Given the ice thickness $T(\omega,t)$ at a point P of coordinates ω and at a given time t, the *ice thickness variation* is defined as

$$I(\omega,t) = T(\omega,t) - T_0, \tag{2.46}$$

where T_0 is the ice thickness at P at the remote reference time t_0. The *ice load* is

$$L_i(\omega,t) = \rho_i I(\omega,t), \tag{2.47}$$

where ρ_i is the ice density ($\rho_i = 931$ kg m^{-3}). By its own definition, L_i has units of mass per unit surface. The mass variation of the whole ice sheet is

$$m_i(t) = a^2\int_i d\omega L_i(\omega,t), \tag{2.48}$$

where

$$d\omega = \sin\theta d\theta d\lambda \tag{2.49}$$

and i is the region where $I(\omega, t) \neq 0$.

For an ice load with fixed margins, the following factorization is possible

$$L_i(\omega, t) = \sigma(\omega) f(t), \tag{2.50}$$

where $\sigma(\omega)$ is the *load function*, and $f(t)$ is the *load time–history* (the load function is defined for $\omega \in i$, and vanishes outside the ice margins). The more general case of a complex ice load with time–evolving margins can be dealt with by a combination of loads of the form (2.50).

The spectral form of the load function is

$$\sigma(\omega) = \sum_{lm} \sigma_{lm} \mathcal{Y}_{lm}(\omega), \tag{2.51}$$

where we have used the abbreviation

$$\sum_{lm} = \sum_{l=0}^{\infty} \sum_{m=-l}^{l} \tag{2.52}$$

and $\mathcal{Y}_{lm}(\omega)$ are the 4π–normalized complex spherical harmonics (B.3). Using (B.6), the coefficients σ_{lm} are

$$\sigma_{lm} = \frac{1}{4\pi} \int_{\Omega} d\omega \sigma(\omega) \mathcal{Y}^*_{lm}(\omega). \tag{2.53}$$

From (2.48) and (2.50) we observe that

$$m_i(t) = m_s f(t) \tag{2.54}$$

where the static mass of the load is

$$m_s = a^2 \int_i d\omega \sigma(\omega). \tag{2.55}$$

2.2.2 Water load

The growth or the melting of the ice sheets is accompanied by a variation of the mass of the oceans, that constitutes the *water load*. To define it, we need to introduce the sea level and the sea level change. With $r = r'_t$ we denote the radius of a point P of the Earth's solid surface of coordinates ω, while with $r = r'_g$ we indicate the radius of the projection of P to the surface of the geoid, at the same time. The (absolute) *sea level* at P is the difference

$$SL(\omega, t) = r'_g(\omega, t) - r'_t(\omega, t), \tag{2.56}$$

while the *sea level change* is

$$S(\omega, t) = SL(\omega, t) - SL_0, \tag{2.57}$$

where SL_0 is the sea level measured at ω at the reference time $t_0 \leq t$. Notice that SL and S are defined also across the continental masses, not only on the oceans. The sea level change defined by (2.57) results from (i) vertical displacements of the surface topography, (ii) alterations of the shape of the geoid, and (iii) changes of the amount of water contained within the oceans. These three geophysical processes are simultaneously described by the *sea lavel equation*, that will be introduced in the next chapter.

The water load is

$$L_o(\omega, t) = \rho_o S(\omega, t) \mathcal{O}(\omega), \tag{2.58}$$

where ρ_w is the density of water (ρ_w=1000 kg m^{-3}), and $\mathcal{O}(\omega)$ is the ocean function

$$\mathcal{O}(\omega) = \begin{cases} 1, & \omega \in \text{oceans} \\ 0, & \omega \notin \text{oceans}, \end{cases} \tag{2.59}$$

with spectral form

$$\mathcal{O}(\omega) = \sum_{lm} \mathcal{O}_{lm} \mathcal{Y}_{lm}(\omega), \tag{2.60}$$

and coefficients

$$\mathcal{O}_{lm} = \frac{1}{4\pi} \int_o d\omega \mathcal{Y}^*_{lm}(\omega), \tag{2.61}$$

where o is the surface of the oceans.

An estimate of L_o can obtained assuming that the Earth does not deform under the action of the loads (rigid Earth hypothesis), and that no geoid changes occur (Newton's constant is $\Gamma = 0$). In this case, the sea level changes are called *eustatic*, a word coined by Suess (1906). Given a change $m_i(t)$ in the ocean mass, eustasy imposes a spatially uniform sea level change of opposite sign

$$S(\omega, t) = -\frac{m_i(t)}{\rho_w A_o}, \tag{2.62}$$

that, according to (2.58) implies

$$L_o(\omega, t) = -\frac{m_i(t)}{A_o} \mathcal{O}(\omega). \tag{2.63}$$

2.3 The simplified GIA problem

The vertical displacement U and the variation of the gravitational potential Φ at a point ω and time t result from the displacements and potentials due to changes of the ice and of the oceanic mass distributions at any point ω' and times $t' \leq t$. This involves a spatial integration over the whole surface of the Earth and a time convolution which accounts for the load time–history and the time–dependent response of the viscoelastic mantle. Since the GFs for vertical displacement G_u and gravitational potential G_ϕ have similar forms,[1] the spatio–temporal convolutions can be compacted as

$$\left\{ \begin{array}{c} U \\ \Phi \end{array} \right\} (\omega, t) = \int_{-\infty}^{t} dt' \int_e dA' \left\{ \begin{array}{c} G_u \\ G_\phi \end{array} \right\} (\alpha, t - t') \mathcal{L}(\omega', t'), \tag{2.64}$$

[1] The computation of the horizontal component of displacement requires further considerations, that will be illustrated in Section 3.5.3.

where $\mathcal{L}$ is the total load,

$$dA \equiv a^2 \sin\theta d\theta d\lambda, \tag{2.65}$$

and α implicitly depends upon ω and ω' via the cosines formula

$$\cos\alpha = \cos\theta\cos\theta' + \sin\theta\sin\theta'\cos(\lambda' - \lambda). \tag{2.66}$$

It is useful to introduce the concise notation

$$(G \otimes_d L)(\omega, t) \equiv \int_{-\infty}^{t} dt' \int_d dA' G(\alpha, t - t') L(\omega', t'), \tag{2.67}$$

where here G and L are a generic GF and a generic load, respectively, and d is a subset of the Earth's surface. Hence, using (2.45), (2.64) reads

$$\left\{ \begin{array}{c} U \\ \Phi \end{array} \right\} (\omega, t) = \left\{ \begin{array}{c} G_u \\ G_\phi \end{array} \right\} \otimes_e \mathcal{L} = \left\{ \begin{array}{c} U_i + U_o \\ \Phi_i + \Phi_o \end{array} \right\}, \tag{2.68}$$

where

$$\left\{ \begin{array}{c} U_i \\ \Phi_i \end{array} \right\} (\omega, t) \equiv \left\{ \begin{array}{c} G_u \\ G_\phi \end{array} \right\} \otimes_i \rho_i I, \tag{2.69}$$

and

$$\left\{ \begin{array}{c} U_o \\ \Phi_o \end{array} \right\} (\omega, t) \equiv \left\{ \begin{array}{c} G_u \\ G_\phi \end{array} \right\} \otimes_o \rho_w S, \tag{2.70}$$

represent the ice and the oceanic components of the total response, and with $\otimes_i$ and $\otimes_o$ we indicate integrations over the ice sheets and the oceans, respectively.

By its own definition (see 2.45), the total load $\mathcal{L}$ depends both on the ice thickness and the sea level variations. While the former can be reasonably *assumed* to be known from geological or geophysical evidence, the latter will depend, beside on the amount of water exchanged between the ice sheets an the oceans, also on vertical displacement of the solid Earth and geoid height changes, which can only be determined once the sea level changes themselves are known! Here we will escape to this circularity assuming an eustatic ocean load, which leads to a simple – but possibly inaccurate – analytical solution for the responses. Once we will introduce the sea level equation in Chapter 3, the eustatic approximation will be abandoned.

2.3.1 Response to the ice load

Here we provide the details on the derivation of the "ice components" of the response of the Earth to the surface loads. Using (2.69) with (2.47) and (2.50), we obtain

$$\left\{ \begin{array}{c} U_i \\ \Phi_i \end{array} \right\}(\omega,t) = \int_{-\infty}^{t} dt' \int_i dA' \left\{ \begin{array}{c} G_u \\ G_\phi \end{array} \right\}(\alpha, t-t')\sigma(\omega')f(t'), \tag{2.71}$$

that with the expressions of G_u and G_ϕ (2.38) and the spectral decomposition of the load function (2.51), becomes

$$\begin{aligned} \left\{ \begin{array}{c} U_i \\ \frac{1}{\gamma}\Phi_i \end{array} \right\}(\omega,t) &= \frac{a^3}{m_e}\int_{-\infty}^{t} dt' f(t') \int_i dA' \sum_{l=0}^{\infty} \left\{ \begin{array}{c} h_l \\ k_l \end{array} \right\}(t-t') \times \\ &\times P_l(\cos\alpha) \sum_{l'm'} \sigma_{l'm'} \mathcal{Y}_{l'm'}(\omega'), \end{aligned} \tag{2.72}$$

which can be further transformed recalling the addition theorem for spherical harmonics (B.8) and integrating over the whole sphere – this is possible since $\sigma(\omega) = 0$ outside i:

$$\begin{aligned} \left\{ \begin{array}{c} U_i \\ \frac{1}{\gamma}\Phi_i \end{array} \right\}(\omega,t) &= \frac{a^3}{m_e}\int_{-\infty}^{t} dt' f(t') \int_\Omega d\omega' \sum_{l=0}^{\infty} \left\{ \begin{array}{c} h_l \\ k_l \end{array} \right\}(t-t') \times \\ &\times \frac{1}{2l+1} \sum_{m=-l}^{+l} \mathcal{Y}^*_{lm}(\omega')\mathcal{Y}_{lm}(\omega) \times \\ &\times \sum_{l'm'} \sigma_{l'm'} \mathcal{Y}_{l'm'}(\omega'), \end{aligned} \tag{2.73}$$

hence

$$\begin{aligned} \left\{ \begin{array}{c} U_i \\ \frac{1}{\gamma}\Phi_i \end{array} \right\}(\omega,t) &= \frac{a^3}{m_e} \sum_{lm}\sum_{l'm'} \frac{\sigma_{l'm'}}{2l+1} \left\{ \begin{array}{c} \overline{h}_l \\ \overline{k}_l \end{array} \right\}(t) \mathcal{Y}_{lm}(\omega) \times \\ &\times \int_\Omega d\omega' \mathcal{Y}^*_{lm}(\omega')\mathcal{Y}_{l'm'}(\omega'), \end{aligned} \tag{2.74}$$

where

$$\left\{ \begin{array}{c} \overline{h}_l \\ \overline{k}_l \end{array} \right\}(t) \equiv \int_{-\infty}^{t} dt' \left\{ \begin{array}{c} h_l \\ k_l \end{array} \right\}(t-t')f(t'). \tag{2.75}$$

Also taking into account the orthonormality relationship for the spherical harmonics (B.6) and introducing the average density of the Earth

$$\overline{\rho}_e = \frac{3m_e}{4\pi a^3} = 5511.57 \text{ kg m}^{-3} \tag{2.76}$$

from (2.74) we finally obtain

$$\left\{ \begin{array}{c} U_i \\ \frac{1}{\gamma}\Phi_i \end{array} \right\}(\omega,t) = \frac{3}{\overline{\rho}_e}\sum_{lm}\frac{\sigma_{lm}}{2l+1}\left\{ \begin{array}{c} \overline{h}_l \\ \overline{k}_l \end{array} \right\}(t)\mathcal{Y}_{lm}(\omega). \tag{2.77}$$

2.3.2 Response to the water load

Assuming an eustatic load (2.63), the "oceanic components" of the responses (2.70) read

$$\left\{ \begin{array}{c} U_o \\ \Phi_o \end{array} \right\}(\omega,t) = -\int_{-\infty}^{t} dt' \int_o dA' \left\{ \begin{array}{c} G_u \\ G_\phi \end{array} \right\}(\alpha, t-t')\frac{m_i(t')}{A_o} f(t'), \tag{2.78}$$

that can be rephrased recalling (2.54) and (2.38):

$$\begin{aligned} \left\{ \begin{array}{c} U_o \\ \frac{1}{\gamma}\Phi_o \end{array} \right\}(\omega,t) &= -\frac{m_s}{m_e}\frac{a^3}{A_o}\int_{-\infty}^{t} dt' f(t') \times \\ &\times \int_o \sum_{l=0}^{\infty} \left\{ \begin{array}{c} h_l \\ k_l \end{array} \right\}(t-t') P_l(\cos\alpha) d\omega'. \end{aligned} \tag{2.79}$$

With (2.75) and (B.8), we obtain

$$\begin{aligned} \left\{ \begin{array}{c} U_o \\ \frac{1}{\gamma}\Phi_o \end{array} \right\}(\omega,t) &= -\frac{m_s}{m_e}\frac{a^3}{A_o}\sum_{l=0}^{\infty}\frac{1}{2l+1}\left\{ \begin{array}{c} \overline{h}_l \\ \overline{k}_l \end{array} \right\}(t) \times \\ &\times \sum_{m=-l}^{+l} \mathcal{Y}_{lm}(\omega)\int_o d\omega' \mathcal{Y}^*_{lm}(\omega'), \end{aligned} \tag{2.80}$$

that, using (2.61), (2.52) and (2.76), provides the result:

$$\left\{ \begin{array}{c} U_o \\ \frac{1}{\gamma}\Phi_o \end{array} \right\}(\omega,t) = -\frac{3}{\overline{\rho}_e}\frac{m_s}{A_o}\sum_{lm}\left\{ \begin{array}{c} \overline{h}_l \\ \overline{k}_l \end{array} \right\}(t)\frac{\mathcal{O}_{lm}}{2l+1}\mathcal{Y}_{lm}(\omega). \tag{2.81}$$

2.3.3 Solution of the simplified GIA problem

According to (2.77) and (2.81), the vertical displacement and the change in the gravitational potential due to the combined action of the ice and of the ocean loads is

$$\left\{ \begin{array}{c} U \\ \frac{1}{\gamma}\Phi \end{array} \right\} (\omega, t) = \frac{3}{\overline{\rho}_e} \sum_{lm} \frac{\sigma'_{lm}}{2l+1} \left\{ \begin{array}{c} \overline{h}_l \\ \overline{k}_l \end{array} \right\} (t) \mathcal{Y}_{lm}(\omega), \tag{2.82}$$

where

$$\sigma'_{lm} = \sigma_{lm} - \frac{m_s}{A_o} \mathcal{O}_{lm}. \tag{2.83}$$

The expansions (2.82), that solve the simplified GIA problem, have been implemented in Spada (2003), and Spada et al. (2003) to account for various ice load time–histories and shapes. Since we have assumed an extremely simplified water load, we expect that these solutions may be somewhat inaccurate in the far field with respect to the former ice sheets, where the effects of the water and ice loads can be of comparable magnitude. The difficulty is circumvented introducing the sea level equation (SLE), that is the subject of the next chapter.

Chapter 3

The Sea Level Equation

This chapter is devoted to the study of the Sea Level Equation, that has been introduced in Sectionr̃efgia-sle of Chapter **??**. The theoretical aspects of our analysis are largely based on the manuscripts by Farrell and Clark (1976), and Wu and Peltier (1983).

The basic idea of the SLE dates back to 1888, when Woodward published his pioneering work on the *form and position of mean sea level* (Woodward, 1888), and later has been refined by Platzman (1971) and Farrell (1973) in the context of the study of the ocean tides. In the words of Wu and Peltier (1983), the solution of the SLE *yields the space– and time–dependent change of ocean bathymetry which is required to keep the gravitational potential of the sea surface constant for a specific deglaciation chronology and viscoelastic earth model*. This constitutes a significant improvement with respect to the approach of the last chapter, where we have assumed an eustatic water load to simplify the discussion.

3.1 Background

Consistently with the definitions of Section 2.2.2, the sea level at a point P of coordinates ω is the offset between the surface of the geoid and that of the solid

Earth (Figure 3.1b):

$$SL = SL(\omega, t) = r'_g - r'_s, \tag{3.1}$$

while the sea level change is

$$S(\omega, t) = SL - SL_0, \tag{3.2}$$

where SL_0 is a reference sea level, measured at the same point but at the remote time $t = t_0$ (Figure 3.1a):

$$SL_0 = r_g - r_s. \tag{3.3}$$

The quantity provided by (3.2) represents exactly the sea level variation that would be measured by a stick–meter at P (Figure 3.1), as described by Farrell and Clark Farrell and Clark (1976).

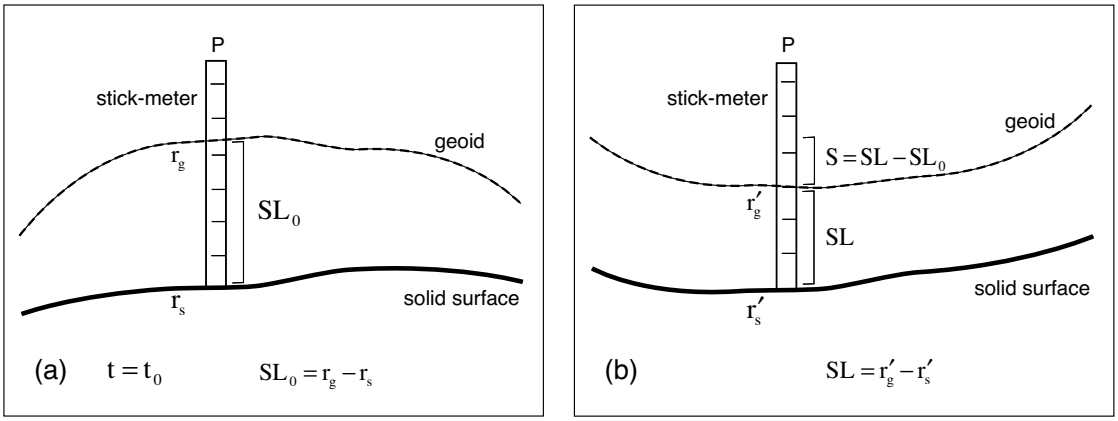

Figure 3.1: Sea level at a point P.

A particularly illuminating expression for $S(\omega, t)$ can be obtained combining (3.1) with (3.3):

$$S(\omega, t) = N - U, \tag{3.4}$$

where

$$N(\omega, t) = r'_g - r_g \tag{3.5}$$

is the *geoid height change*, and

$$U(\omega, t) = r'_s - r_s. \tag{3.6}$$

represents the *vertical displacement* of the solid surface of the Earth. Eq. (3.4) explicitly shows that the sea level change is determined by changes in the shape of the two surfaces that define the geoid and the solid Earth.

The sea level change (3.4) is defined on the whole surface of the sphere, since both N and U have a precise meaning also across the continents. However, it is convenient to define the *reduced sea level change*, that coincides with S on the surface of the oceans, and vanishes outside:

$$Z(\omega, t) = \mathcal{O}S, \tag{3.7}$$

where $\mathcal{O}$ is the ocean function (2.59). The reduced sea level change will play an important role in Chapter 4, that describes the "pseudo–spectral method" for solving the SLE

In our ensuing discussion, it is assumed that the Earth's solid surface and the geoid slightly depart from a sphere having of $r = r_0$ and the same mass m_e of the real Earth, but characterized by a radially varying density. In this quasi–spherical approximation, the gravity acceleration is

$$\vec{g} = -g_r \hat{r} + g_t \hat{t} \tag{3.8}$$

with

$$g_r = \gamma(r) + \delta g_r(\omega, r) \tag{3.9}$$

and

$$g_t = \delta g_t(\omega, r), \tag{3.10}$$

where the perturbations δg_r and δg_t are small compared to

$$\gamma(r) = \frac{\Gamma m_e}{r^2}, \tag{3.11}$$

that represents the modulus of the gravity field of the spherically symmetric Earth.

The total gravitational potential W includes contributions from the solid Earth, the oceans, and the ice sheets. It is related to the gravity field by

$$\vec{g} = \nabla W, \tag{3.12}$$

that from (3.8) implies

$$g_r = -\frac{\partial W}{\partial r}. \tag{3.13}$$

We now observe that if $r = r_{ep}$ is an equipotential surface close to the sphere $r = r_0$ and $\epsilon = \epsilon(\omega)$ is a small radius, we have

$$\begin{aligned} W(r_{ep} + \epsilon) - W(r_{ep}) &\simeq \epsilon \frac{\partial W}{\partial r}(r_{ep}) \\ &= -\epsilon g_r(r_{ep}) \\ &= -\epsilon(\gamma(r_{ep}) + \delta g_r(r_{ep})) \\ &\simeq -\epsilon\gamma(r_0) \\ &= -\epsilon\gamma \end{aligned} \tag{3.14}$$

where we have used (3.9) and (3.13), we have neglected terms of second order in the small quantities ϵ and δg_r, we have approximated $\epsilon\gamma(r_{ep})$ with $\epsilon\gamma(r_0)$, and

$$\gamma = \gamma(r_0). \tag{3.15}$$

In the particular case $\epsilon = c = \text{constant} \ll r_0$, from (3.14) we obtain

$$W(r_{ep} + c) = W(r_{ep}) - c\gamma, \tag{3.16}$$

showing that if $r = r_{ep}$ is an equipotential surface, $r = r_{ep} + c$ is an equipotential as well.

3.2 Obtaining the SLE

To obtain the SLE, we need first to evaluate how the surface of the geoid has changed from the reference state to the current state. Both states are characterized

by an arbitrary distribution of ice and ocean masses, and they differ by the mass contained in these reservoirs – the total mass being unaltered. Here we denote with $m_i(t)$ the ice mass variation, where conventionally a positive change denotes accretion. We recall that we are assuming fixed shorelines, so that the shape of the continents is unaltered by the exchange of mass between the ice sheets and the oceans.

We first observe that it is possible to determine a (non constant) small height $h = h(\omega)$ with $|h| \ll r_0$ such that the current gravitational potential at radius $r_g + h$ equals the potential in the reference state at $r = r_g$, i. e.:

$$W'(r_g + h) = W(r_g) = \text{constant}, \tag{3.17}$$

where the right–hand equality holds because $r = r_g$ is the geoid in the reference state. But from (3.14) we have

$$W'(r_g + h) \simeq W'(r_g) - h\gamma, \tag{3.18}$$

hence

$$h = \frac{W'(r_g) - W(r_g)}{\gamma} = \frac{\Phi(r_g)}{\gamma}, \tag{3.19}$$

where Φ is the variation of the total gravitational potential with respect to the reference state. Since the masses involved in the process of glacio–isostasy are small compared to the Earth mass, the potential Φ can be considered as a small quantity. Therefore, to a high degree of approximation we can write $\Phi(r_g) \simeq \Phi(r_0)$, that gives

$$h = \frac{\Phi(r_0)}{\gamma}, \tag{3.20}$$

where $\Phi(r_0)$ is given by (2.68) as a spatio–temporal convolution between the GF G_ϕ and the surface load: it results from variations of the ice load, of the water load, and from the deformations of the solid Earth in response to the varying surface loads.

The surface $r = r_g + h$ determined above is certainly an equipotential surface, but it does not necessarily coincide with the geoid. In fact, beside being an equipotential surface, the geoid must be constrained by the requirement of mass conservation.

Since from (3.16) we know that a new equipotential surface can be obtained by a uniform shift of a near by equipotential surface, we seek the current geoid in the form

$$r'_g = r_g + h + c, \tag{3.21}$$

where the small constant c will be determined below imposing mass conservation. As a consequence of (3.21) and (3.20), the geoid height variation (3.5) can be expressed as

$$N = \frac{\Phi}{\gamma} + c, \tag{3.22}$$

and according to the definition (3.2), the sea level change is

$$\begin{aligned} S &= SL - SL_0 \\ &= (r'_g - r'_s) - (r_g - r_s) \\ &= r_g + h + c - r'_s - r_g + r_s \\ &= h + c - (r'_s - r_s) \\ &= \frac{\Phi}{\gamma} - U + c, \end{aligned} \tag{3.23}$$

where U is the vertical displacement of the solid surface of the Earth (3.6), that is given by (2.68) in the form of a convolution between the appropriate GF and the surface load.

The requirement of mass conservation can be stated as

$$\Delta M = 0, \tag{3.24}$$

where the mass variation of the system ice + oceans is

$$\Delta M = m_i(t) + \int_o S\rho_w dA. \tag{3.25}$$

Using (3.24) with (3.25) and (3.23) we obtain

$$m_i(t) + \int_o \rho_w \left(\frac{\Phi}{\gamma} - U + c \right) dA = 0, \tag{3.26}$$

that gives

$$m_i(t) + c\rho_w \int_o dA + \rho_w \int_o \left(\frac{\Phi}{\gamma} - U\right) dA = 0, \tag{3.27}$$

where we have assumed a constant water density. Hence

$$m_i(t) + c\rho_w A_o + \rho_w A_o \overline{\left(\frac{\Phi}{\gamma} - U\right)} = 0, \tag{3.28}$$

where the overbar denotes the average over the surface of the oceans:

$$\overline{(\cdot)} \equiv \frac{1}{A_o} \int_o (\cdot) dA. \tag{3.29}$$

Solving (3.28) for the constant c gives

$$c = -\frac{m_i(t)}{\rho_w A_o} - \overline{\left(\frac{\Phi}{\gamma} - U\right)}, \tag{3.30}$$

that substituted into (3.23) finally provides

$$S = \left(\frac{\Phi}{\gamma} - U\right) - \frac{m_i(t)}{\rho_w A_o} - \overline{\left(\frac{\Phi}{\gamma} - U\right)}, \tag{3.31}$$

which represents the sea level equation.

3.3 "Gravitationally self–consistent" SLE

The SLE is an implicit equation. This can be seen recalling the expressions for the vertical displacement and the incremental gravitational potential (2.68), that give

$$\frac{\Phi}{\gamma} - U = \frac{\rho_i}{\gamma} G_s \otimes_i I + \frac{\rho_w}{\gamma} G_s \otimes_o S, \tag{3.32}$$

where G_s is the sea level GF (2.39). Upon substitution of (3.32) into (3.31), the SLE can be arranged as

$$S = \frac{\rho_i}{\gamma} G_s \otimes_i I + \frac{\rho_w}{\gamma} G_s \otimes_o S + S^E - \frac{\rho_i}{\gamma} \overline{G_s \otimes_i I} - \frac{\rho_w}{\gamma} \overline{G_s \otimes_o S}, \tag{3.33}$$

where

$$S^E = -\frac{m_i(t)}{\rho_w A_o} \tag{3.34}$$

represents the *eustatic term* of the SLE.

In the literature, the solution of the SLE in the form (3.33) is often referred to as "gravitationally self–consistent" solution, since it has been obtained imposing that the geoid is that particular equipotential surface constrained by the requirement of mass conservation. The water load is thus "consistent" with the gravity field.

The unknown sea level variation S appears explicitly to left–hand side of (3.33), but it is also embedded in spatio–temporal convolution products at the right–hand side. This makes the SLE a (linear) integral equation. We observe that, differently from the simplified rebound problem described in Section 2.3, the solution of (3.33) directly provides the sea level variations, that allows to make direct comparisons with geophysical observations, as discussed in Section 3.5 below. Once S has been determined, the vertical displacement of the solid surface of the Earth and the incremental gravitational potential can be obtained from (2.68), that do not imply an eustatic ocean load, as the approximate solution (2.82) does.

The solution of the SLE is a particularly challenging task and cannot be undertaken by means of analytical methods, except in the particular cases described in Section 3.4.2. The "pseudo–spectral method" that we will discuss in Chapter 4 takes advantage from an iterative approach, similar to the Neumann's method that is used in the context of the Fredholm integral equations (see e. g., Krasnov et al., 1977). As described in detail in Section 4.4, at first the test solution $S^{(0)} = S^E$ is substituted to S on the right–hand side of (3.33). In this way, a new estimate $S^{(1)}$ is obtained at the left–hand side, and the process is iterated. The experience has shown that this procedure quickly converges to a stable solution Peltier et al. (1978).

3.4 Approximate solutions of the SLE

Here we show that in some conditions the SLE can be reduced to a non–integral equation that can be solved without invoking the iterative method. These particular

solutions of the SLE should only be used in special circumstances, e. g., when the traditional Green's functions approach outlined in Chapter 2 is not viable due to the presence of lateral viscosity contrasts or non–Newtonian rheologies. The approximate solutions presented here are useful because they allow to better appreciate the physical meaning of the various terms that appear in the SLE. Some of them will be explicitly considered in the numerical examples of Chapter 6.

3.4.1 Eustatic solution

The eustatic term of the SLE

$$S^E(t) = -\frac{m_i(t)}{\rho_w A_o} \tag{3.35}$$

plays an important role in our discussion. From (3.31), we observe that the SLE has solution

$$S = S^E \tag{3.36}$$

provided that

$$U = 0, \tag{3.37}$$

and

$$\Phi = 0. \tag{3.38}$$

According to (2.68) and (2.31), the first implies

$$G_u^e = G_u^v = 0, \tag{3.39}$$

while from (2.25) the second yields

$$G_\phi^e = G_\phi^v = 0 \tag{3.40}$$

and

$$G_\phi^r = 0. \tag{3.41}$$

Eqs. (3.39) and (3.40) state that the Earth is rigid, while (3.41) implies that the variations of gravitational potential due to the rearrangement of the ice and ocean masses are neglected. From (2.40) we also observe that $G_s = 0$ in the eustatic approximation.

Since the real Earth is deformable and the Newton's constant is not zero, we must expect that the melting of the ice sheets produces spatially non–uniform sea level variations, which may significantly depart from eustasy. This is widely confirmed by the results published in the literature and will be fully appreciated in Chapter 6, where the SLE will solved numerically.

More insight into the meaning of the eustatic approximation can be gained taking the ocean–average of both sides of (3.31). Since $\overline{c} = c$ for any constant c, this yields

$$\overline{S} = \overline{\left(\frac{\Phi}{\gamma} - U\right)} + \overline{S^E} - \overline{\overline{\left(\frac{\Phi}{\gamma} - U\right)}} = S^E, \tag{3.42}$$

showing that the spatially–averaged sea level variations coincide with the eustatic term. This property holds independently from the ice sheets chronology and the shape of the shorelines.

3.4.2 Other rigid–Earth solutions

Woodward (1888) found an analytical solution of the SLE assuming that (i) the Earth is rigid, (ii) the mass load is localized and impulsive – so that in this problem we are faced with is the instantaneous freezing (or melting) of a point load –, (iii) the oceans cover uniformly the Earth, and (iv) variations in the ocean mass distribution do not affect the gravity field – i. e., the oceans are not "self–gravitating". Woodward's solution shows that the sea level changes can significantly depart from eustasy even when essential physical ingredients – such as the deformations of the solid Earth and the shape and self–gravitation of the oceans – are totally neglected.

Since the Earth is rigid, $U = 0$. Furthermore, since we are dealing with an impulsive point mass, we can identify the incremental potential Φ with the GF G^r_ϕ

given by (2.7). Accordingly, from (3.31) we write the SLE as

$$S^* = \frac{G^r_\phi}{\gamma} + S^{E*} - \frac{\overline{G^r_\phi}}{\gamma}, \tag{3.43}$$

where the asterisk indicates that the sea level changes are referred to a unit mass and unit time.

The three terms in (3.43) can be worked out analytically. Using (2.7), the first is simply

$$\frac{G^r_\phi}{\gamma} = \delta(t)\frac{a}{m_e}\frac{1}{2\sin(\alpha/2)}. \tag{3.44}$$

The second term – that represents the eustatic component of the SLE – can be transformed as follows

$$S^{E*} = -\frac{\delta(t)}{\rho_w A_o} = -\frac{\delta(t)}{4\pi a^2 \rho_w} = -\frac{\delta(t)}{\frac{3m_e}{a\overline{\rho}_e}\rho_w} - \delta(t)\frac{a}{m_e}\frac{\overline{\rho}_e}{3\rho_w}, \tag{3.45}$$

where we have set $m_i(t) = \delta(t)$, we have taken into account that the oceans cover uniformly the Earth, and we have used (2.76). The third term of (3.43) is

$$\begin{aligned} -\frac{\overline{G^r_\phi}}{\gamma} &\equiv -\frac{1}{A_o}\int_o dA \frac{G^r_\phi}{\gamma} \\ &= -\delta(t)\frac{1}{4\pi a^2 m_e} a^3 \int_0^{2\pi} d\lambda \int_0^{\pi} \frac{d\alpha \sin\alpha}{2\sin(\alpha/2)} \\ &= -\delta(t)\frac{a}{2m_e}\int_0^{\pi} d\alpha \cos(\alpha/2) \\ &= -\delta(t)\frac{a}{m_e}, \end{aligned} \tag{3.46}$$

where we have written the element of area as $dA = a^2 \sin\alpha d\alpha d\lambda$, where λ is longitude, and we have integrated over the uniform oceans.

Thus, from above, the solution of the Woodward's problem is

$$S^*(\alpha, t) = \delta(t)\frac{a}{m_e}\left(\frac{1}{2\sin(\alpha/2)} - \frac{\overline{\rho}_e}{3\rho_w} - 1\right), \tag{3.47}$$

showing that, as a consequence of the point–source approximation and of spherical symmetry, S^* only depend on the angular distance from the point mass.

It is also clear from (3.47) that Woodward's solution departs from eustasy: this is merely a consequence of the gravitational attraction exerted by the point mass on the uniform oceans. We observe in particular that (i) $S^* \geq S_E^*$ for $\alpha \leq 60^\circ$ and (ii) $S^* \geq 0$ if $\sin(\alpha/2) \leq (2(1+\overline{\rho}_e/3\rho_w))^{-1}$, that gives $\alpha \leq 10.2^\circ$ for $\overline{\rho}_e = 5511.57$ kg m^{-3} and $\rho_w = 1000$ kg m^{-3}. The singularity shown by (3.47) for $\alpha \mapsto 0$ disappears as soon as a finite–size ice sheets is employed.

The Woodward approach can be generalized to account (i) for realistic ice loads and shorelines distribution and (ii) for the self–gravitation of the oceans. Using (3.33) with $G_s = G_\phi^r$, in the first case the SLE takes the form

$$S = \frac{\rho_i}{\gamma} G_\phi^r \otimes_i I + S^E - \frac{\rho_i}{\gamma} \overline{G_\phi^r \otimes_i I}, \tag{3.48}$$

that immediately provides the solution (since the geometry of the ice sheets and of the shorelines are complex, the solution is not analytical). In the second case, to account for self–gravitation of the oceans we just modify (3.48) into

$$S = \frac{\rho_i}{\gamma} G_\phi^r \otimes_i I + \frac{\rho_w}{\gamma} G_\phi^r \otimes_o S + S^E - \frac{\rho_i}{\gamma} \overline{G_\phi^r \otimes_i I} - \frac{\rho_i}{\gamma} \overline{G_\phi^r \otimes_o S}, \tag{3.49}$$

that must be solved iteratively, since in this form the SLE is an integral equation.

3.4.3 Ice–free approach

In their 1976 manuscript, Farrell and Clark Farrell and Clark (1976) have considered the problem of solving the SLE in the absence of ice loads, assuming a purely elastic Earth. In their own words, ... *the mass is added* (to the oceans) *from outside the Earth, rather than coming from a melting ice sheet*. With $I = 0$, the SLE becomes

$$S = \frac{\rho_w}{\gamma} G_s \otimes_o S + S^E - \frac{\rho_w}{\gamma} \overline{G_s \otimes_i S}, \tag{3.50}$$

where in the sea level GF (2.40) the viscous terms are dropped. This ice–free version of the SLE was developed in order to show how the changes of sea level may depart from eustasy, even neglecting the deformations induced by the ice loads. Of

course, the viscous response of the Earth can be accounted for just substituting the complete form of G_s into (3.50). In Section (6.1) this "ice–free" solution of the SLE is compared to the gravitationally self–consistent solution in terms of relative sea level variations.

3.4.4 Explicit solutions

The SLE can be reduced to an explicit form also in the general case of a viscoelastic Earth and of spatially complex surface loads. The implied brute–force method of solution is based on the assumption of negligible water loads, and may be appropriate to describe the sea level variations after the end of the melting of the ice sheets. Due to the simple solution that we find in this case – that takes advantage from the approximate solution of the GIA of Section 2.3 – this may provide first guesses of postglacial sea level changes in the vicinity of the formerly glaciated areas, where the ice load effect is expected to dominate the water load effect.

In Section 3.2 we have determined the value of the constant c that allows to write the SLE in the form

$$S = \frac{\Phi}{\gamma} - U + c, \tag{3.51}$$

so that mass is conserved, with

$$\Delta M = m_i(t) + \int_o dAS\rho_w = 0. \tag{3.52}$$

From (3.52), here we observe that the constraint $\Delta M = 0$ can be also satisfied – for any value of c – provided that

$$m_i(t) = 0, \tag{3.53}$$

and

$$\rho_w = 0, \tag{3.54}$$

where (3.53) states that the mass of the ice load has not changed since the remote reference time, while with (3.54) the weight of the meltwater that has filled the

oceans is neglected. The indeterminacy of the constant c shows that the geoid cannot be unequivocally determined for a weightless ocean; for the sake of convenience, we choose $c = 0$, that minimizes the offset between the new and the former geoid. From (3.22), this condition gives

$$N = \frac{\Phi}{\gamma}, \tag{3.55}$$

while from (3.51) the SLE reduces to

$$S = \frac{\Phi}{\gamma} - U, \tag{3.56}$$

that still appears as an implicit equation, since both U and Φ in general depend on S itself (see 2.68). However, because of (3.54), the ocean components of U and Φ vanish (see 2.70), that gives the explicit solution

$$S = \frac{\Phi_i}{\gamma} - U_i, \tag{3.57}$$

where Φ_i and U_i are given by (2.69).

An even more drastic approach to the SLE consists in neglecting Φ_i in front of U_i, that leads to

$$N = 0 \tag{3.58}$$

and

$$S = -U_i. \tag{3.59}$$

This further approximation may be helpful for investigators employing finite elements techniques, that often do not allow for a straightforward implementation of the gravitational forces.

3.5 By–products of the SLE

Once the SLE has been solved for the sea level change, it is possible to compute a number of interesting geophysical quantities. In the following we discuss how they

can be derived. We first introduce the *relative sea level* and the *rate of sea level change*. Then, we discuss the *velocity field* and the time–variation of the *Stokes coefficients* of the gravity field.

3.5.1 Relative sea level variations

As previously discussed, the SLE does not provide absolute sea level variations, but rather it allows to compute sea level changes referred to a remote time. More specifically, if t_{BP} denotes a given time before present, solving the SLE yields the difference

$$S(\omega, t_{BP}) = SL(\omega, t_{BP}) - SL(\omega, t_r), \tag{3.60}$$

where SL is the (absolute) sea level, and t_r is a remote (and arbitrary) time BP; at the present time $t = t_p$, we can similarly write

$$S(\omega, t_p) = SL(\omega, t_p) - SL(\omega, t_r). \tag{3.61}$$

The *relative sea level* at a given epoch t_{BP} is defined as the past sea level referred to the present–day level:

$$RSL(\omega, t_p) = SL(\omega, t_{BP}) - SL(\omega, t_p), \tag{3.62}$$

that according to (3.60) and (3.61) can be directly related to the sea level change, i. e., the solution of the SLE:

$$RSL(\omega, t_{BP}) = S(\omega, t_{BP}) - S(\omega, t_p). \tag{3.63}$$

As discussed in e. g. Farrell and Clark (1976), the RSL observations are typically inferred from elevated beach terraces formed during the retreat of the late–Pleistocene ice sheets and from archaeological evidence in anciently populated areas. In Section 6 we will provide RSL predictions for some of the sites of the global database of Tushingham and Peltier (1992, 1993) for which radiocarbon–controlled data are available[1].

[1] http://www1.ncdc.noaa.gov/pub/data/paleo/paleocean/relative_sea_level/.

3.5.2 Present–day sea level changes

The currently observed rate of sea level change $\dot{\zeta}$ constitutes another important source of information in addition to the Holocene relative sea level variations. While the latter data set spans several thousand of years, the former only provides a snapshot of present–day changes:

$$\dot{\zeta}(\omega) = \frac{dS}{dt}(\omega, t_p), \tag{3.64}$$

that according to (3.63) represents the steepness of the RSL curve at present time. In Section 6.2 we will present predictions of $\dot{\zeta}$ for some of the tide–gauges of the database of the Permanent Service for the Mean Sea Level[2] (PSMSL), that provides changes in global sea level during the last two centuries.

3.5.3 Displacement and velocity fields

From Section 2.3 we recall that the vertical displacement is

$$U(\omega, t) = \rho_i G_u \otimes_i I + \rho_w G_u \otimes_o S, \tag{3.65}$$

where the GF G_u is given by (2.38). According to Spada et al. (2003), the horizontal components of displacements are

$$\left\{ \begin{array}{c} U_\theta \\ U_\lambda \end{array} \right\} (\omega, t) = \rho_i G_v \left\{ \begin{array}{c} \cos X \\ \sin X \end{array} \right\} \otimes_i I + \rho_w G_v \left\{ \begin{array}{c} \cos X \\ \sin X \end{array} \right\} \otimes_o S, \tag{3.66}$$

with

$$\cos X = \frac{\cos\theta' - \cos\theta\cos\alpha}{\sin\theta\sqrt{(1-\cos^2\alpha)}} \tag{3.67}$$

and

$$\sin X = \frac{\sin(\lambda - \lambda')\sin\theta'}{\sqrt{(1-\cos^2\alpha)}}, \tag{3.68}$$

where $\cos\alpha$ is given by (2.66).

[2]http://www.pol.ac.uk/psmsl/datainfo/rlr.trends.

The three components of the *velocity field* ($\dot{U}$, $\dot{U}_\theta$, $\dot{U}_\lambda$) are obtained from (3.65) and (3.66) by time differentiation. These quantities can be observed by modern geodetic techniques, such as GPS and VLBI, that allow for the determination of crustal velocities based on observations of relative displacements over finite time periods. If needed, the velocity field can be projected along the conventional unit vectors $(\hat{l}, \hat{t}, \hat{v})$ of the geodetic baseline that connects two sites. The relevant formulas are given by Spada (2003).

3.5.4 Geoid height variation and Stokes coefficients

When S and U have been obtained solving the SLE and from (3.65), respectively, the geoid height variation N can be easily deduced by (3.4), giving

$$N(\omega, t) = S + U, \tag{3.69}$$

that according to (3.22) allows to determine the incremental gravitational potential as

$$\frac{\Phi}{\gamma}(\omega, t) = N - c, \tag{3.70}$$

where the constant c is given by (3.30).

It is now useful to expand

$$\Phi(\omega, t) = \sum_{lm} \Phi_{lm} \mathcal{Y}_{lm}(\omega), \tag{3.71}$$

where the 4π–normalized, complex spherical harmonics are given by (B.3). Equivalently, we can represent the incremental potential in terms of real harmonics, with

$$\Phi(\omega, t) = \frac{\Gamma m_e}{a} \sum_{lm, l \geq 2} (\delta c_{lm} \cos m\lambda + \delta s_{lm} \sin m\lambda) P_{lm}(\cos\theta), \tag{3.72}$$

where a if the Earth's average radius, the associated Legendre functions $P_{lm}(\cos\theta)$ are given by (B.2), the sum is for orders $m \geq 0$, and the non–dimensional, time–dependent quantities $(\delta c_{lm}, \delta s_{lm})$ represent the variations of the Stokes coefficients

of the gravity field. The relationship between (δc_{2m}, δs_{2m}) and the change of the inertia tensor is given e. g. by Eqs. (2.102) and (2.103) of Spada (2003).

Since mass is conserved and we assume that the origin of the reference system coincides with the Earth's center of mass, the sum in (3.72) is restricted to degrees $l \geq 2$ (Spada et al., 2003). The constant c represents a term of harmonic degree $l = 0$, that from (3.70) implies

$$N_{lm} = \frac{\Phi_{lm}}{\gamma}, \quad l \geq 2, \tag{3.73}$$

where N_{lm} are the coefficients of the expansion of the geoid height change

$$N(\omega, t) = \sum_{lm} N_{lm} \mathcal{Y}_{lm}(\omega). \tag{3.74}$$

In geodynamics, it is particularly interesting to consider the trend of the Stokes coefficients, since this quantity can be observed by means of satellite geodetic techniques (Lambeck, 1988). Using (3.72), and (3.73), and proposition (5) of Spada et al. (2003), for $l \geq 2$ they are related with $\dot{N}_{lm}$ by

$$\left\{ \begin{array}{c} \delta\dot{c}_{lm} \\ \delta\dot{s}_{lm} \end{array} \right\} (t_p) = \frac{(2 - \delta_{0m})\mu_{lm}}{a} \left\{ \begin{array}{c} +\mathrm{Re} \\ -\mathrm{Im} \end{array} \right\} \dot{N}_{lm}(t_p), \tag{3.75}$$

where t_p is present time and μ_{lm} is given by (B.4).

Chapter 4

Solving the SLE: the Pseudo–Spectral approach

The "pseudo spectral" (PS) method for solving the SLE has been introduced by Mitrovica and Peltier (1991), and later revised and updated in a number of papers (see e. g., Mitrovica et al., 1994). It constitutes a significant improvement with respect to the "finite–element" method, that was originally introduced in Peltier et al. (1978). As discussed in Mitrovica et al. (1994), the PS approach allows to avoid the computation of coupling coefficients between sets of spherical harmonics (Dahlen, 1976), that may severely limit the maximum degree of the analysis.

In the illustration of the PS method we will largely follow the previous studies on this subject, but with the intent to facilitate the inexperienced readers we will provide a number of details that are often omitted. Section 4.1 shows how the SLE is transformed by the introduction of the reduced sea level change, while Sections 4.2 and 4.3 are devoted to the spatio–temporal discretization and to a step–by–step analysis of the various terms of the SLE, respectively. An iterative scheme for solving the SLE is proposed in Section 4.4.

4.1 Transforming the SLE

The key–point of the PS method is the introduction of the reduced sea level change Z (3.7), that allows to transform (3.33) into

$$S = \frac{\rho_i}{\gamma} G_s \otimes_e I + \frac{\rho_w}{\gamma} G_s \otimes_e Z + S^E - \frac{\rho_i}{\gamma} \overline{G_s \otimes_e I} - \frac{\rho_w}{\gamma} \overline{G_s \otimes_e Z}, \tag{4.1}$$

where we have substituted $G_s \otimes_i I$ with $G_s \otimes_e I$ (I vanishes outside the region i), and $G_s \otimes_o S$ with $G_s \otimes_e Z$, that follows from the definition of Z. Multiplying both sides of (4.1) by the ocean function gives

$$Z = \mathcal{O}\frac{\rho_i}{\gamma}\left(G_s \otimes_e I - \overline{G_s \otimes_e I}\right) + \mathcal{O}S^E + \mathcal{O}\frac{\rho_w}{\gamma}\left(G_s \otimes_e Z - \overline{G_s \otimes_e Z}\right), \tag{4.2}$$

that represents the new form of the SLE in the unknown Z. The vertical displacement (3.65) reads

$$U(\omega, t) = \rho_i G_u \otimes_i I + \rho_w G_u \otimes_o Z, \tag{4.3}$$

where G_u is given by (2.38).

For the ongoing discussion, it is convenient to introduce the new variables

$$\left\{ \begin{array}{c} A \\ B \end{array} \right\}(\omega, t) = \frac{1}{\gamma} \left\{ \begin{array}{c} \rho_i \\ \rho_w \end{array} \right\} G_s \otimes_e \left\{ \begin{array}{c} I \\ Z \end{array} \right\}, \tag{4.4}$$

so that the SLE (4.2) takes the form

$$Z = H + Z^E + K(Z), \tag{4.5}$$

where

$$Z^E = \mathcal{O}S^E, \tag{4.6}$$

and

$$H = \mathcal{O}(A - \overline{A}) \tag{4.7}$$

$$K(Z) = \mathcal{O}(B - \overline{B}). \tag{4.8}$$

In terms of the new variables, (4.1) becomes

$$S = A - \overline{A} + S^E + B - \overline{B}, \tag{4.9}$$

while (4.3) reads

$$U = A^U + B^U, \tag{4.10}$$

where A^U and B^U have the same form of the terms A and B in (4.4), with G_s/γ substituted by G_u.

4.2 Discretization

Before showing how the SLE can be written in a PS form, it is necessary to discretize the physical quantities involved. They are i) the ice thickness T and its variation I, ii) the sea level change S, the vertical displacement U and the change of geoid height N, iii) the reduced sea level change Z, and iv) the ocean function $\mathcal{O}$. The temporal discretization is made assuming that, at a given place on the Earth surface, these variables vary stepwise in time. At a given time, their spatial discretization is accomplished by spherical harmonics expansions.

4.2.1 Ice thickness

The basic input variable of the problem is the ice thickness $T(\omega, t)$, for which we adopt the discretization

$$T(\omega,t) = \begin{cases} T_0(\omega), & t < t_0 \\ T_k(\omega), & t_{k-1} \le t < t_k, \quad k = 1, 2, ..., N \\ T_{N+1}(\omega), & t \ge t_N, \end{cases} \tag{4.11}$$

where $N \ge 1$ is the number of time steps within the interval $0 \le t \le t_N$, and

$$t_k - t_{k-1} = \Delta = \frac{t_N}{N}, \tag{4.12}$$

where Δ is the length of each time step. The time discretization (4.11) is usually applied assuming that $t = t_N$ is present time, and that $t_0 = 0$ marks the beginning of the last deglaciation. This latter condition implies a complete isostatic equilibrium before the Last Glacial Maximum (LGM). However, it is clear that (4.11) can be employed to approximate any time–evolution of the ice load, possibly containing cycles of loading and unloading before the LGM. The discretization (4.11) characterizes most of the currently available ice thickness models, in which $T_k(\omega)$ has normally the form

$$T_k(\omega) = \begin{cases} H_k, & \omega \in D \\ 0, & \omega \notin D, \end{cases} \tag{4.13}$$

where H_k is a constant, and D is a subset of the sphere.

It is straightforward to verify that (4.11) is equivalent to

$$T(\omega, t) = T_0(\omega) + \sum_{k=0}^{N} \delta T_k(\omega) H(t - t_k), \tag{4.14}$$

where $H(t)$ is the Heaviside step function (2.27), and

$$\delta T_k(\omega) = T_{k+1}(\omega) - T_k(\omega), \quad k = 0, 1, ..., N, \tag{4.15}$$

represents the ice thickness variation at ω between two successive time steps. A time–history of the type (4.11) characterizes the two deglaciation models considered in this study, i. e., ICE1 (Peltier and Andrews, 1976) and ICE3G (Tushingham and Peltier, 1991). For both models, $T_k(\omega)$ has the form

$$T_k(\omega) = \sum_{e=1}^{N_e} H_{ke} \Theta_{D_e}(\omega) \tag{4.16}$$

where N_e is the number of ice elements that compose the aggregate, H_{ke} is ice thickness at time t_k within each subdomain of the sphere D_e, and Θ is the characteristic function

$$\Theta_D(\omega) = \begin{cases} 1, & \text{if } \omega \in D \\ 0, & \text{if } \omega \notin D. \end{cases} \tag{4.17}$$

In model ICE1 (for which $N_e = 153$), regions D_e are disjoint "spherical quadrilaterals", whereas in model ICE3G ($N_e = 808$) they are (in some case overlapping) circular disc (see Figure 5.4). Notice that where overlaps occur, according to Eq. (4.16) the total ice thickness results from the sum of individual discs thicknesses. We will return on this issue in Section

The spatial discretization of the functions $T_k(\omega)$ in (4.13) is accomplished by a spherical harmonics decomposition as

$$T_k(\omega) = \sum_{lm} T_{lm,k} \mathcal{Y}_{lm}(\omega), \quad k = 0, 1, \ldots N+1, \tag{4.18}$$

where the 4π–normalized harmonics $\mathcal{Y}_{lm}(\omega)$ are given by (B.3).

When $T_k(\omega)$ is assumed to be constant within circular discs (this is the case of ICE3G of Tushingham and Peltier, 1991), the spectral coefficients $T_{lm,k}$ of (4.18) can be computed analytically by virtue of the symmetry of the ice element. For more complex geometries (i. e., the quadrilateral elements of model ICE1 of Peltier and Andrews, 1976), it is necessary to evaluate numerically the coefficients with

$$T_{lm,k} = \frac{1}{4\pi} \int_\Omega T_k(\omega) \mathcal{Y}^*_{lm}(\omega) d\omega, \quad k = 0, 1, \ldots N+1, \tag{4.19}$$

that can be obtained by (4.18) and the orthogonality condition (B.6).

The relation (4.19) can be written as

$$T_{lm,k} = \sum_{e=1}^{N_e} f_{lme} H_{ke}, \tag{4.20}$$

with non–dimensional shape factors

$$f_{lme} = \int_{D_e} \mathcal{Y}^*_{lm}(\omega) d\omega \tag{4.21}$$

given explicitly in Section 5.3.1 for both ice chonologies.

Using (4.18), we finally observe that (4.15) can be expanded as

$$\delta T_k(\omega) = \sum_{lm} \Delta T_{lm,k} \mathcal{Y}_{lm}(\omega), \tag{4.22}$$

where

$$\Delta T_{lm,k} \equiv T_{lm,k+1} - T_{lm,k}, \quad k = 0, 1, \ldots N. \tag{4.23}$$

4.2.2 Ice thickness variations

Recalling (2.46), the ice thickness variation is

$$I(\omega, t) = T(\omega, t) - T_0(\omega), \tag{4.24}$$

where $T_0(\omega)$ is the ice thickness at the remote time t_0 (see Section 2.2.1). According to (4.14), $I(\omega, t)$ can be equivalently written as

$$I(\omega, t) = \sum_{k=0}^{N} \delta T_k(\omega) H(t - t_k), \tag{4.25}$$

with $\delta T_k(\omega)$ given by (4.15).

The ice thickness variation is spatially discretized writing

$$I(\omega, t) = \sum_{lm} I_{lm}(t) \mathcal{Y}_{lm}(\omega), \tag{4.26}$$

where, using (4.22) and (4.25), it can be easily verified that

$$I_{lm}(t) = \sum_{k=0}^{N} \Delta T_{lm,k} H(t - t_k). \tag{4.27}$$

If we further define

$$I_{lm,i} \equiv I_{lm}(t_i), \tag{4.28}$$

(4.27) gives

$$I_{lm,i} = \sum_{k=0}^{i} \Delta T_{lm,k}, \tag{4.29}$$

that implies

$$I_{lm,i} = \Delta T_{lm,i} + I_{lm,i-1}, \quad i = 0, 1, \ldots N, \tag{4.30}$$

with $I_{lm,-1} = 0$.

4.2.3 Sea level change, vertical displacement, and geoid

In analogy with (4.26), we assume the following spectral decomposition for the sea level change

$$S(\omega, t) = \sum_{lm} S_{lm}(t)\mathcal{Y}_{lm}(\omega), \tag{4.31}$$

where the coefficients $S_{lm}(t)$ will be determined solving the SLE. In a similar manner, the spherical harmonics expansions for the vertical displacement and the geoid height change are

$$U(\omega, t) = \sum_{lm} U_{lm}(t)\mathcal{Y}_{lm}(\omega), \tag{4.32}$$

and (3.74), respectively. Similarly to (4.28), with $S_{lm,i}$, $U_{lm,i}$, and $N_{lm,i}$ we indicate $S_{lm}(t_i)$, $U_{lm}(t_i)$, and $N_{lm}(t_i)$, respectively, where t_i is a given time.

4.2.4 Reduced sea level change

The reduced sea level change $Z(\omega, t)$, that represents the new unknown of the SLE (4.2), can be spectrally decomposed following the scheme outlined above. Similarly to (4.26) and (4.27), we write

$$Z(\omega, t) = \sum_{lm} Z_{lm}(t)\mathcal{Y}_{lm}(\omega), \tag{4.33}$$

where

$$Z_{lm}(t) = \sum_{k=0}^{N} \Delta W_{lm,k} H(t - t_k). \tag{4.34}$$

With $Z_{lm,i} = Z_{lm}(t_i)$, in analogy with (4.30), we have

$$Z_{lm,i} = \Delta W_{lm,i} + Z_{lm,i-1} \quad i = 0, 1, \ldots N, \tag{4.35}$$

with $Z_{lm,-1} = 0$.

4.2.5 Ocean function

Since we assume fixed shorelines, the ocean function $\mathcal{O}(\omega)$ (2.59) only needs to be spatially discretized. In terms of 4π–normalized harmonics, its spectral representation is already given by (2.60) with coefficients (2.61).

The issue of the numerical computation of $\mathcal{O}_{lm}$ will be addressed in Section 5.2 below. Here we only observe that the area of the surface of the oceans is

$$\begin{aligned} A_o &\equiv \int_o dA = \int_o a^2 d\omega = a^2 \int_\Omega \mathcal{O}(\omega) d\omega \\ &= a^2 \int_\Omega \sum_{lm} \mathcal{O}_{lm} \mathcal{Y}_{lm} d\omega \\ &= a^2 \sum_{lm} \mathcal{O}_{lm} \int_\Omega \mathcal{Y}_{lm} \mathcal{Y}^*_{00} d\omega \\ &= 4\pi a^2 \mathcal{O}_{00}, \end{aligned} \tag{4.36}$$

where we have used $\mathcal{Y}_{00} = 1$ (see Table B.3) and (B.6), that yields

$$\frac{a^2}{A_o} = \frac{1}{4\pi \mathcal{O}_{00}}. \tag{4.37}$$

4.3 The SLE term by term

This section is devoted to a term–by–term discussion of the SLE. Starting from (4.5), we will consider separately the terms Z^E, A and B, $(A - \overline{A})$ and $(B - \overline{B})$, H and K, and A^U and B^U. Our purpose is to find computationally convenient expressions of these quantities. Since the material that follows is admittedly boring, the reader may go directly to the PS form of the SLE (4.86).

4.3.1 Eustatic term

The (reduced) eustatic term of the SLE is given by (4.6). With (3.35) we can write

$$Z^E(\omega, t) = -\frac{m_i(t)}{\rho_w A_o} \mathcal{O}(\omega), \tag{4.38}$$

where $m_i(t)$ is the change of the mass of the ice load, ρ_w is the density of water, and A_o is the area of the surface of the oceans. In order to put Z^E in spectral form we first observe that using (4.26) $m_i(t)$ can be expressed in terms of the degree zero component of the change of the ice thickness:

$$\begin{aligned} m_i(t) &\equiv \rho_i \int_i dA I(\omega, t) \\ &= \rho_i a^2 \int_\Omega d\omega \sum_{lm} I_{lm}(t) \mathcal{Y}_{lm} \\ &= \rho_i a^2 \sum_{lm} I_{lm}(t) \int_\Omega d\omega \ \mathcal{Y}_{lm} \\ &= \rho_i a^2 \sum_{lm} I_{lm}(t) \int_\Omega d\omega \ \mathcal{Y}_{00}^* \mathcal{Y}_{lm} \\ &= 4\pi \rho_i a^2 \sum_{lm} I_{lm}(t) \delta_{l0} \delta_{m0} \\ &= 4\pi \rho_i a^2 I_{00}(t), \end{aligned} \tag{4.39}$$

where we have used $\mathcal{Y}_{00} = 1$ and (B.6). Substituting (4.39) into (4.38) gives

$$Z^E(\omega, t) = -\frac{\rho_i}{\rho_w} \frac{I_{00}(t)}{\mathcal{O}_{00}} \sum_{lm} \mathcal{O}_{lm} \mathcal{Y}_{lm}, \tag{4.40}$$

where we have used (4.37) and (2.60).

From above we conclude that, at a given time $t = t_i$ the (reduced) eustatic term is

$$Z^E(\omega, t_i) = \sum_{lm} Z^E_{lm,i} \mathcal{Y}_{lm}(\omega), \tag{4.41}$$

with

$$Z^E_{lm,i} = -\frac{\rho_i}{\rho_w} \frac{I_{00,i}}{\mathcal{O}_{00}} \mathcal{O}_{lm}, \tag{4.42}$$

and $I_{00,i} = I_{00}(t = t_i)$.

A direct consequence of (3.35) and of (4.39) is that the coefficients of the expansion

$$S^E(\omega, t_i) = \sum_{lm} S^E_{lm,i} \mathcal{Y}_{lm}(\omega) \tag{4.43}$$

are

$$S^E_{lm,i} = -\frac{\rho_i}{\rho_w}\frac{I_{lm,i}}{\mathcal{O}_{00}}\delta_{l0}\delta_{m0}. \tag{4.44}$$

4.3.2 The A term

According to (4.4) and (2.41), the A–term of the SLE can be decomposed as

$$A(\omega, t) = A_1 + A_2, \tag{4.45}$$

where

$$A_1(\omega, t) = \beta\rho_i\psi^\delta(\alpha)\delta(t) \otimes_e I \tag{4.46}$$

and

$$A_2(\omega, t) = \beta\rho_i(\psi^h(\alpha, t)H(t)) \otimes_e I, \tag{4.47}$$

where $\psi^\delta(\alpha)$ and $\psi^h(\alpha, t)$ are given by (2.42) and (2.43), respectively.

In the following pages, our purpose will be to determine the coefficients of the spherical harmonics expansion

$$A(\omega, t_i) = \sum_{lm} A_{lm,i}\mathcal{Y}_{lm}(\omega). \tag{4.48}$$

We will show that

$$A_{lm,i} = A_{1lm,i} + A_{2lm,i} \tag{4.49}$$

where

$$A_{1lm,i} = 3\frac{\rho_i}{\overline{\rho}_e}E_l I_{lm,i}, \tag{4.50}$$

and

$$A_{2lm,i} = -3\frac{\rho_i}{\overline{\rho}_e}\sum_{k=0}^{i}(I_{lm,k} - I_{lm,k-1})\beta_l(\Delta(i-k)), \tag{4.51}$$

with

$$E_l \equiv \frac{1 + k^e_l - h^e_l}{2l+1} \tag{4.52}$$

and

$$\beta_l(t) \equiv \frac{1}{2l+1}\sum_{j=1}^{M}\frac{k_{lj}-h_{lj}}{s_{lj}}(1-e^{s_{lj}t}). \tag{4.53}$$

(4.49):

$$A_{lm,i} = 3\frac{\rho_i}{\overline{\rho}_e}\bigg(E_l I_{lm,i} - \sum_{k=0}^{i}(I_{lm,k}-I_{lm,k-1})\beta_l(\Delta(i-k))\bigg). \tag{4.54}$$

The A_1 term

Using (4.46) and recalling (2.67), we get

$$\begin{aligned} A_1(\omega,t) &= \beta\int_{-\infty}^{t}dt'\int_e dA'\psi^{\delta}(\alpha)\delta(t-t')\rho_i I(\omega',t') \\ &= \beta\rho_i\int_e dA'\psi^{\delta}(\alpha)I(\omega',t), \end{aligned} \tag{4.55}$$

where we have used the basic property of the Dirac delta. With the aid of the addition theorem for spherical harmonics (B.8), from (2.42) $\psi^{\delta}(\alpha)$ can be expanded as follows

$$\begin{aligned} \psi^{\delta}(\alpha) &= \sum_{l=0}^{\infty}(1+k_l^e-h_l^e)P_l(\cos\alpha) \\ &= \sum_{l=0}^{\infty}\frac{1+k_l^e-h_l^e}{2l+1}\sum_{m=-l}^{l}\mathcal{Y}_{lm}^*(\omega')\mathcal{Y}_{lm}(\omega) \\ &= \sum_{lm}E_l\mathcal{Y}_{lm}^*(\omega')\mathcal{Y}_{lm}(\omega), \end{aligned} \tag{4.56}$$

where E_l is given by (4.52). Hence, substituting (4.56) into (4.55) and using (4.26), we obtain

$$\begin{aligned} A_1(\omega,t) &= \beta\rho_i\int_e dA'\bigg(\sum_{lm}E_l\mathcal{Y}_{lm}^*(\omega')\mathcal{Y}_{lm}(\omega)\bigg)\bigg(\sum_{l'm'}I_{l'm'}(t)\mathcal{Y}_{l'm'}(\omega')\bigg) \\ &= \beta\rho_i a^2\sum_{lm}E_l\sum_{l'm'}I_{l'm'}(t)\bigg(\int_\Omega d\omega'\ \mathcal{Y}_{lm}^*(\omega')\mathcal{Y}_{l'm'}(\omega')\bigg)\mathcal{Y}_{lm}(\omega) \\ &= 4\pi\beta\rho_i a^2\sum_{lm}E_l I_{lm}(t)\mathcal{Y}_{lm}(\omega), \end{aligned} \tag{4.57}$$

where we have also taken advantage from (B.6).

Thus, from (2.44) and (2.76), the spherical harmonics expansion of A_1 at time t_i is

$$A_1(\omega, t_i) = \sum_{lm} A_{1lm,i} \mathcal{Y}_{lm}(\omega), \tag{4.58}$$

with coefficients

$$A_{1lm,i} = 3\frac{\rho_i}{\overline{\rho}_e} E_l I_{lm,i}, \tag{4.59}$$

that proves our statement (4.50).

The A_2 term

From (4.47) and (2.67) we have

$$\begin{aligned} A_2(\omega, t) &= \beta \int_{-\infty}^{t} dt' \int_e dA' \psi^h(\alpha, t - t') H(t - t') \rho_i I(\omega', t') \\ &= \beta \rho_e \int_{-\infty}^{t} dt' \int_e dA' \psi^h(\alpha, t - t') I(\omega', t'), \end{aligned} \tag{4.60}$$

where we have used (2.27). Recalling (4.25), we obtain

$$\begin{aligned} A_2(\omega, t) &= \beta \rho_i \int_{-\infty}^{t} dt' \int_e dA' \psi^h(\alpha, t - t') \left(\sum_{k=0}^{N} \delta T_k(\omega') H(t' - t_k) \right) \\ &= \beta \rho_i \sum_{k=0}^{N} \int_e dA' \delta T_k(\omega') \int_{-\infty}^{t} dt' \psi^h(\alpha, t - t') H(t' - t_k), \end{aligned} \tag{4.61}$$

that with the new variable $\tau = t' - t_k$ becomes

$$A_2(\omega, t) = \beta \rho_i \sum_{k=0}^{N} \int_e dA' \delta T_k(\omega') \int_{-\infty}^{t - t_k} d\tau \psi^h(\alpha, t - t_k - \tau) H(\tau), \tag{4.62}$$

where, because of the term $H(\tau)$, the integral over time vanishes for $t - t_k < 0$ and can be otherwise restricted to the interval $0 \leq \tau \leq t - t_k$. Hence

$$\begin{aligned} A_2(\omega, t) &= \beta \rho_i \sum_{k=0}^{N} \int_e dA' \delta T_k(\omega') H(t - t_k) \int_{0}^{t - t_k} d\tau \psi^h(\alpha, t - t_k - \tau) \\ &= \beta \rho_i \sum_{k=0}^{N} \int_e dA' \delta T_k(\omega') \tilde{\psi}^h(\alpha, t - t_k), \end{aligned} \tag{4.63}$$

where we have defined

$$\tilde{\psi}^h(\alpha,t) \equiv H(t)\int_0^t d\tau \psi^h(\alpha,t-\tau). \tag{4.64}$$

Using (2.43) into (4.64) gives

$$\begin{aligned}
\tilde{\psi}^h(\alpha,t) &= H(t)\int_0^t d\tau \ \sum_{lj}(k_{lj}-h_{lj})e^{s_{lj}(t-\tau)}P_l(\cos\alpha) \\
&= H(t)\sum_{lj}(k_{lj}-h_{lj})\int_0^t d\tau \ e^{s_{lj}(t-\tau)}P_l(\cos\alpha) \\
&= -H(t)\sum_{lj}\frac{k_{lj}-h_{lj}}{s_{lj}}(1-e^{s_{lj}t})\frac{1}{2l+1}\sum_{m=-l}^{l}\mathcal{Y}^*_{lm}(\omega')\mathcal{Y}_{lm}(\omega) \\
&= -H(t)\sum_{lm}\beta_l(t)\mathcal{Y}^*_{lm}(\omega')\mathcal{Y}_{lm}(\omega),
\end{aligned} \tag{4.65}$$

where we have also used the addition theorem (B.6) and $\beta_l(t)$ is given by (4.53).

Substituting (4.65) into (4.63) we obtain

$$\begin{aligned}
A_2(\omega,t) =& \beta\rho_i\sum_{k=0}^{N}\int_e dA' \ \delta T_k(\omega')\tilde{\psi}^h(\alpha,t-t_k) \\
=& -\beta\rho_i\sum_{k=0}^{N}\int_e dA' \ \left(\sum_{l'm'}\Delta T_{l'm',k}\mathcal{Y}_{l'm'}(\omega')\right)\times \\
& \times\left(\sum_{lm}\beta_l(t-t_k)H(t-t_k)\mathcal{Y}^*_{lm}(\omega')\mathcal{Y}_{lm}(\omega)\right) \\
=& -\beta\rho_i a^2\sum_{lm}\left(\sum_{k=0}^{N}\beta_l(t-t_k)H(t-t_k)\sum_{l'm'}\Delta T_{l'm',k}\times\right. \\
& \left.\times\left(\int_\Omega d\omega' \ \mathcal{Y}_{l'm'}(\omega')\mathcal{Y}^*_{lm}(\omega')\right)\right)\mathcal{Y}_{lm}(\omega) \\
=& -3\frac{\rho_i}{\overline{\rho}_e}\sum_{lm}\left(\sum_{k=0}^{N}\Delta T_{lm,k}\beta_l(t-t_k)H(t-t_k)\right)\mathcal{Y}_{lm}(\omega),
\end{aligned} \tag{4.66}$$

where we have also taken advantage from (4.22), (2.44), (2.76), and (B.6). Thus, at time $t=t_i$, using (4.30) from above we obtain

$$A_2(\omega,t_i) \ = \ -3\frac{\rho_i}{\overline{\rho}_e}\sum_{lm}\left(\sum_{k=0}^{i}\Delta T_{lm,k}\beta_l(t_i-t_k)\right)\mathcal{Y}_{lm}(\omega)$$

$$
\begin{aligned}
&= -3\frac{\rho_i}{\overline{\rho}_e}\sum_{lm}\left(\sum_{k=0}^{i}(I_{lm,k}-I_{lm,k-1})\beta_l(\Delta(i-k))\right)\mathcal{Y}_{lm}(\omega) \\
&= \sum_{lm} A_{2lm,i}\mathcal{Y}_{lm}(\omega), \qquad (4.67)
\end{aligned}
$$

where $A_{2lm,i}$ is given by (4.51).

4.3.3 The B term

According to (4.4) this term of the SLE has exactly the same structure of A; its spectral decomposition follows immediately from (4.54) replacing ρ_i with ρ_w and $I_{lm,k}$ with $Z_{lm,k}$, respectively:

$$B(\omega,t_i)=\sum_{lm} B_{lm,i}\mathcal{Y}_{lm}(\omega), \qquad (4.68)$$

with

$$B_{lm,i}=3\frac{\rho_w}{\overline{\rho}_e}\left(E_l Z_{lm,i}-\sum_{k=0}^{i}(Z_{lm,k}-Z_{lm,k-1})\beta_l(\Delta(i-k))\right). \qquad (4.69)$$

4.3.4 The $(A-\overline{A})$ and $(B-\overline{B})$ terms

The SLE in the form (4.5) involves the differences $(A-\overline{A})$ and $(B-\overline{B})$, where the overbar denotes the average over the surface of the oceans. Here we determine the coefficients of the spherical harmonics expansion of these two terms. We first observe that if $f=f(\omega)$ denotes a given function defined on the unit sphere, with expansion

$$f(\omega)=\sum_{lm} f_{lm}\mathcal{Y}_{lm}(\omega), \qquad (4.70)$$

its average value can be written in terms of f_{lm} and $\mathcal{O}_{lm}$ as follows

$$
\begin{aligned}
\overline{f} &\equiv \frac{1}{A_o}\int_o f dA \qquad (4.71)\\
&= \frac{a^2}{A_o}\int_\Omega \mathcal{O}f\ d\omega
\end{aligned}
$$

$$\begin{aligned}
&= \frac{a^2}{A_o}\int_\Omega \mathcal{O}^* f\ d\omega \\
&= \frac{a^2}{A_o}\int_\Omega \left(\sum_{lm}\mathcal{O}^*_{lm}\mathcal{Y}^*_{lm}\right)\left(\sum_{l'm'} f_{l'm'}\mathcal{Y}_{l'm'}\right)d\omega \\
&= \frac{a^2}{A_o}\sum_{lm}\sum_{l'm'}\mathcal{O}^*_{lm}f_{l'm'}\int_\Omega \mathcal{Y}^*_{lm}\mathcal{Y}_{l'm'}d\omega \\
&= \frac{4\pi a^2}{A_o}\sum_{lm}\mathcal{O}^*_{lm}f_{lm} \\
&= \frac{1}{\mathcal{O}_{00}}\sum_{lm}\mathcal{O}^*_{lm}f_{lm}, \qquad (4.72)
\end{aligned}$$

where we have used (4.37) and (B.6). Hence,

$$\begin{aligned}
f-\overline{f} &= \sum_{lm} f_{lm}\mathcal{Y}_{lm} - \overline{f} \\
&= \sum_{lm} f_{lm}\mathcal{Y}_{lm} - \overline{f}\mathcal{Y}_{00} \\
&= \sum_{lm} f_{lm}\mathcal{Y}_{lm} - \overline{f}\sum_{lm}\delta_{l0}\delta_{m0}\mathcal{Y}_{lm} \\
&= \sum_{lm}(f_{lm}-\overline{f}\delta_{l0}\delta_{m0})\mathcal{Y}_{lm}. \qquad (4.73)
\end{aligned}$$

From above we conclude that

$$\left\{\begin{array}{c} A-\overline{A} \\ B-\overline{B}\end{array}\right\}(\omega,t_i) = \sum_{lm}\left\{\begin{array}{c} A'_{lm,i} \\ B'_{lm,i}\end{array}\right\}\mathcal{Y}_{lm}(\omega) \qquad (4.74)$$

with

$$\left\{\begin{array}{c} A'_{lm,i} \\ B'_{lm,i}\end{array}\right\} = \left\{\begin{array}{c} A_{lm,i} \\ B_{lm,i}\end{array}\right\} - \left\{\begin{array}{c} \overline{A}_i \\ \overline{B}_i\end{array}\right\}\delta_{l0}\delta_{m0} \qquad (4.75)$$

and

$$\left\{\begin{array}{c} \overline{A}_i \\ \overline{B}_i\end{array}\right\} = \frac{1}{\mathcal{O}_{00}}\sum_{lm}\mathcal{O}^*_{lm}\left\{\begin{array}{c} A_{lm,i} \\ B_{lm,i}\end{array}\right\}. \qquad (4.76)$$

4.3.5 The H and K terms

From the definitions of Section 4.1, we recall that $H = \mathcal{O}(A - \overline{A})$ and $K = \mathcal{O}(B - \overline{B})$, where $\mathcal{O}$ is the ocean function (2.59). We expand the H term

$$H(\omega, t_i) = \sum_{lm} H_{lm,i} \mathcal{Y}_{lm}(\omega), \tag{4.77}$$

where $H_{lm,i} \equiv H_{lm}(t = t_i)$ is ultimately to be determined by the knowledge of the coefficients of the expansion for $\mathcal{O}$ and $(A - \overline{A})$. Inverting (4.77), we obtain

$$H_{lm,i} = \frac{1}{4\pi} \int_{\Omega} d\omega H(\omega, t_i) \mathcal{Y}^*_{lm}(\omega), \tag{4.78}$$

that, according to property (5.1) of the pixelization scheme illustrated in Section 5.2, can be discretized as

$$H_{lm,i} = \frac{1}{N_p} \sum_{j=1}^{N_p} H(\omega_j, t_i) \mathcal{Y}^*_{lm}(\omega_j), \tag{4.79}$$

where N_p is the number pixels over the sphere, and ω_j are the coordinates of their centroids. But from (4.7) and (4.74),

$$\begin{aligned} H(\omega_j, t_i) &= \mathcal{O}(\omega_j)(A - \overline{A})(\omega_j, t_i) \\ &= \mathcal{O}(\omega_j) \sum_{pq} A'_{pq,i} \mathcal{Y}_{pq}(\omega_j), \end{aligned} \tag{4.80}$$

hence, from (4.79) and the definition of ocean function, we obtain

$$H_{lm,i} = \frac{1}{N_p} \sum_{j \in \text{oce}} \left(\sum_{pq} A'_{pq,i} \mathcal{Y}_{pq}(\omega_j) \right) \mathcal{Y}^*_{lm}(\omega_j), \tag{4.81}$$

that solves the problem of the spectral decomposition of $H(\omega, t)$. The coefficients of $K(\omega, t)$ follow immediately from (4.8):

$$K_{lm,i} = \frac{1}{N_p} \sum_{j \in \text{oce}} \left(\sum_{pq} B'_{pq,i} \mathcal{Y}_{pq}(\omega_j) \right) \mathcal{Y}^*_{lm}(\omega_j). \tag{4.82}$$

with $B'_{pq,i}$ given by (4.75).

4.3.6 The A^U and B^U terms

Based on the observations at the end of Section (4.1), the spherical harmonics expansions of the terms A^U and B^U are

$$\begin{Bmatrix} A_{lm,i} \\ B_{lm,i} \end{Bmatrix}^U = \frac{3}{\overline{\rho}_e} \begin{Bmatrix} \rho_i \\ \rho_w \end{Bmatrix} \Bigg(E_l^U \begin{Bmatrix} I_{lm,i} \\ Z_{lm,i} \end{Bmatrix} + - \sum_{k=0}^{i} \begin{Bmatrix} I_{lm,k} - I_{lm,k-1} \\ Z_{lm,k} - Z_{lm,k-1} \end{Bmatrix} \beta_l^U(\Delta(i-k)) \Bigg), \tag{4.83}$$

with

$$E_l^U \equiv \frac{h_l^e}{2l+1}, \tag{4.84}$$

and

$$\beta_l^U(t) \equiv \frac{1}{2l+1} \sum_{j=1}^{M} \frac{h_{lj}}{s_{lj}} (1 - e^{s_{lj}t}). \tag{4.85}$$

4.3.7 PS form of the SLE and related quantities

From the results so far obtained, it is possible to write the SLE (4.2) in a PS form as

$$Z_{lm,i} = H_{lm,i} + Z_{lm,i}^E + K_{lm,i}(Z_{pq,k}), \tag{4.86}$$

where the spectral coefficients $Z_{lm,i}^E$, $H_{lm,i}$, and $K_{lm,i}$ are given by (4.42), (4.81), and (4.82), respectively, and where we have emphasized that the harmonic components of K depend on all of the components of Z at all times, that reflects the integral nature of the SLE. The SLE in the form (4.86) is solved iteratively according to the scheme presented in Section 4.4.

Once $Z_{lm,i}$ is retrieved from (4.86), recalling (4.9), it is easy to recover the spectral coefficients of the usual sea level change:

$$S_{lm,i} = A'_{lm,i} + S_{lm,i}^E + B'_{lm,i}(Z_{pq,k}), \tag{4.87}$$

where $A'_{lm,i}$, and $B'_{lm,i}$ are given by (4.75), and $S^E_{lm,i}$ is obtained from (4.44). The spectral coefficients $S_{lm,i}$ can be used to compute the present–day rate of sea level change (see Section 6.2), and the Holocene relative sea level variations (Section 6.1).

From (4.10), the spectral coefficients for vertical displacement are

$$U_{lm,i} = A^U_{lm,i} + B^U_{lm,i}(Z_{pq,k}), \tag{4.88}$$

where $A^U_{lm,i}$ and $B^U_{lm,i}$ are given by (4.83). Using (4.88), it is possible to obtain predictions of the present–day vertical velocity, as it will be shown in Section 6.2 below.

Recalling the fundamental relationship (3.4) between S, U, and N, the spectral coefficients of the geoid height change are

$$N_{lm,i} = S_{lm,i} + U_{lm,i}, \tag{4.89}$$

where $S_{lm,i}$ and $U_{lm,i}$ are given by (4.87) and (4.88), respectively. Using (4.89), we will determine the present–day rate of change of the Stokes coefficients and of the geoid height (see Sections 6.3 and 6.4, respectively).

4.4 A solution scheme for the SLE

Here we propose a simple scheme for solving the SLE, in which the steps from 1 to 6 describe the preliminary procedures (the discretization of the spherical domain, the computation of the spherical harmonics coefficients of the ice sheets distribution, and the determination of the of the LDCs). More details on these steps can be found in Section 5.2. The iterative method for solving the SLE is described at step 7, while step 8 concerns the by–products of the SLE. Our numerical implementation of the SLE (Chapter 5) follows exactly the solution scheme described here.

1. According to the desired spatial resolution, (i) determine the maximum harmonic degree l_{max} of the analysis, (ii) determine the coordinates of the pixels centroids $\omega = \omega_j$ $(1 \leq j \leq N_p)$, where $N_p \geq l^2_{max}/3$ and l_{max} is the maximum harmonic degree, and (iii) separate wet (ocean) from dry (continental) pixels,

2. Compute a set of 4π–normalized harmonics of degree $0 \leq l \leq l_{max}$ at the centroids of the pixels ($\omega = \omega_j$),

3. Pixelize the ocean function (2.59) and determine numerically its harmonic coefficients for $0 \leq l \leq l_{max}$ using (5.2),

4. Choose one of the available ice sheets distributions, and determine (i) the shape factors f_{lme} ($1 \leq e \leq N_e$) (see Eq. 4.21), (ii) the harmonic coefficients $T_{lm,k}$ (4.19), $\Delta T_{lm,k}$ (4.23), and $I_{lm,k}$ (4.30) for $0 \leq l \leq l_{max}$, and $0 \leq k \leq N$,

5. Compute the LDCs and the arrays E_l (see 4.52), E_l^U (4.84), $\beta_l(t_i)$ (4.53), and $\beta_l^U(t_i)$ (4.85), for a spherically symmetric, viscoelastic Earth model,

6. Compute the spectral coefficients $Z_{lm,i}^E$ (4.42), $A_{lm,k}$ (see 4.54), $A'_{lm,k}$ (4.75), and $H_{lm,k}$ (4.81),

7. For $s = 1, 2, \ldots, s_{max}$ solve the SLE in the recursive form

$$Z_{lm,i}^{(s)} = H_{lm,i} + Z_{lm,i}^E + K_{lm,i}(Z_{pq,k}^{(s-1)}), \tag{4.90}$$

   with initial value

$$Z_{lm,i}^{(0)} = Z_{lm,i}^E, \tag{4.91}$$

   where $K_{lm,i}$ is given by (4.82), and where $B_{lm,i}$ and $B'_{lm,k}$ are obtained from (4.69) and (4.75), respectively,

8. Set $Z_{lm,i}$=$Z_{lm,i}^{(s_{max})}$, and compute $S_{lm,i}$, $U_{lm,i}$, and $N_{lm,i}$ from (4.87), (4.88), and (4.89), respectively.

Chapter 5

SELEN: a Fortran 90 program for solving the SLE

5.1 Introducing SELEN

SELEN is a collection of standard Fortran 90 programs and subroutines, and of GMT Wessel and Smith (1991)[1] and gnuplot[2] scripts, which are compiled and executed by the bash shell script selen.sh. The definition of constants and parameters used by all program units, with a short description, is given in the include file *data.inc* (a sample of this file is given in Appendix C.1). The user can easily modify it to prepare the input data or for setting a new problem. In the applications of Chapter 6 we will give examples on how to configure some of the relevant parameters.

The components of SELEN have been written from scratch, with the exception of (i) some routines from Numerical Recipes Press et al. (1992), (ii) the freely available pixelization code of Tegmark (1996) [3], (iii) some ALFPACK[4] routines for the evaluation of the associated Legendre functions, and (iv) the program TABOO[5] (Spada, 2003;

[1]Help is available at http://gmt.soest.hawaii.edu/.

[2]Gnuplot is a copyright by Thomas Williams, Colin Kelley, and many others.

[3]http://space.mit.edu/home/tegmark/icosahedron.html.

[4]http://www.cisl.ucar.edu/softlib/ALFPACK.html.

[5]http://samizdat.mines.edu/taboo.

Spada et al., 2004), which provides the LLNs for a suite of spherically symmetric Earth model.

SELEN has been developed using the IBM XL Fortran compiler and runs on a 1.5 GHz Macintosh Power PC G4. With minor modifications SELEN can be employed under other Unix or Linux environments with different Fortran 90 compilers. Efforts have been made throughout to use clearly written and testable algorithms, which can be easily modified according to the user's needs. The Fortran 90 routines are written in single precision, which safely allows to perform spherical harmonic expansions up to harmonic degree $l_{max} = 96$. If a finer spatial resolution is desired (i. e., a degree $l_{max} > 96$), the memory requirements of SELEN will exceed ~ 0.5 Gb (i. e., making the execution virtually impossible on a 1 Gb RAM Power PC), and the spherical harmonic codes (see description below) will need to be implemented in double precision.

All the numerical experiments performed in this study have been carried out using $l_{max} = 72$ and a geometrical resolution $r = 14$ in the Tegmark algorithm that generates the pixels coordinates (see Section 5.2.1 below). As shown in Figure 6.2, increasing l_{max} to 96 would not significantly affect the results. According to Tegmark (1996), the r value chosen here implies a number of pixels $N_p = 40r(r-1)+12 = 7292$ that largely exceeds, for $l_{max} = 72$, the minimum number $N_p^{min} = l_{max}^2/3 = 1728$ that ensures an optimal quadrature on the sphere. When model ICE3G is employed, the CPU time needed for fully solving the SLE, (i. e., for compiling the codes, for evaluating all the steps listed in Section 4.4 with $s_{max} = 3$, and for running all the graphical GMT and gnuplot procedures that can be scheduled by `selen.sh`) is of about 600 s, which reduces to ~ 400 s if all the graphical procedures are bypassed. Since a considerable fraction of CPU time for a single run (~ 120 s) is devoted to the computation of SH at the pixels coordinates, the CPU requirements can be further alleviated saving in a library the harmonics computed during previous runs. The CPU time sensibly increase, however, when ICE1 is employed, since the SH decomposition of the "rectangular" ice elements of this aggregate requires

numerical instead of analytical procedures (see Section 5.3.1).

The next Sections 5.2–5.5 follow the solution scheme proposed in Section 4.4. For each Section a case–sensitive list gives the main Fortran and `GMT` units of `SELEN`; its order reflects the order of execution of the programs, consistently with the script `selen.sh`. At each entry, we also mention other procedures directly connected to the main ones. The functions of the program units are summarized in Table C.2 (more details can be found in the files headers), while Table C.1 gives the names of their input files.

5.2 Preliminary steps

Solving the SLE demands the evaluation of the spectral coefficients of the ocean function $\mathcal{O}$ (2.61), as well as of the functions H and K (see Section 4.3.5). The implied numerical integrations have been performed using the hycosaedral pixelization of the sphere described by Tegmark (1996). This approach[6] is particularly convenient in the framework of the PS method, since it provides a set of equal–weight Gauss points that allow for a straightforward quadrature on the sphere. By the properties of the pixelization Tegmark (1996), the integral of any function $f(\omega)$ over a subset D of the unit sphere Ω can be discretized as follows

$$\int_D f(\omega) dA = \frac{1}{N_p} \sum_{\omega_j \in D} f(\omega_j), \tag{5.1}$$

where ω_j are the coordinates of the centroids of the pixels (see Figure 5.3), and N_p is their number. According with the Tegmark method, the resolution r must be chosen consistently with the desired minimum resolvable spatial wavelength λ, that in turn determines the maximum harmonic degree of the expansions $l_{max} = 2\pi a/\lambda$. The approximation of integrals on the surface of the sphere with discrete sums is exact as far as $N_p \geq l_{max}^2/3$ Tegmark (1996). With this in mind, for $\lambda \sim 500$ km, that is sufficient to describe the global pattern of relative sea level variations, l_{max} should be

[6]Free software is available at http://www.sns.ias.edu/∼max/icosahedron.html.

close to 80. Since the number of pixels for a given resolution is $N_p = 40r(r-1)+12$, this requires $N_p \geq 2200$, that is ensured as far as the resolution is $r \geq 8$. The global pixelization employed in this study, that has been obtained by the code of Max Tegmark with resolution $r = 14$, is shown in Figure 5.3. For such resolution, the number of pixels is $N_p = 7292$.

The ocean function $\mathcal{O}(\omega)$ (2.59) is pixelized running the GMT[7] utility `gmtselect` (see Wessel and Smith (1991)). The centroids of the wet and dry pixels are shown in Figure 5.2. The spherical harmonic coefficients of the ocean function $\mathcal{O}_{lm}$ are theoretically given by (2.61). According to (5.1), they can be determined numerically as

$$\mathcal{O}_{lm} = \frac{1}{N_p} \sum_{j \in \text{oce}} \mathcal{Y}^*_{lm}(\omega_j), \tag{5.2}$$

where ω_j denotes the coordinate of the centroids of the wet pixels. Some low–degree ($0 \leq l \leq 4$) coefficients of the ocean function are reported in Table 5.1. Figure 5.3 shows the ocean function reconstructed at degree $l_{max} = 72$ from the computed coefficients, using (5.2) into (2.60).

5.2.1 PX.F

`PX.F` executes substep (i) of step (1) of the algorithm outlined in Section 4.4. It computes the coordinates (i. e., longitude and colatitude) of the centroids of the pixels ω_j for $1 \leq j \leq N_p$ using the icosahedral discretization algorithm Tegmark (1996).For a given spatial resolution r, the number of pixels on the sphere is $N_p = 40r(r-1)+12$.

5.2.2 px.gmt

`px.gmt` is a `GMT` script that accomplishes substep (ii) of step (1) of the SLE algorithm in Section 4.4, separating ocean from continental pixels by the utility

[7]Help is available at http://gmt.soest.hawaii.edu/.

`gmtselect` (different sets of pixels may be obtained tuning the `-A` and `-D` options). The wet and dry pixelizations, as well as the global one generated by program `PX.F` (see above), may be visualized by `pxmap.gmt`.

5.2.3 SH.F

This program computes the 4π–normalized SH $\mathcal{Y}_{lm}(\omega_j)$ by Eq. (B.3) using the `ALFPACK` codes collected in the include file `SHTOOLS.F` (step (2) of the algorithm of Section 4.4).

5.2.4 WNW.F

In `SELEN`, the maximum degree of the analysis l_{max} must be such that $N_p \geq l_{max}^2/3$ to take advantage of the "window property" of the pixelization, which ensures that the orthonormality condition of the SH (B.6) holds numerically (Tegmark, 1996). On the basis of Eq. (5.1), program WNW.F evaluates the errors due to the spatial discretization and, in particular, it computes

$$\varepsilon_{lm}(\%) = \frac{\left|\sum_{j=1}^{N_p} \mathcal{Y}^*{}_{lm}(\omega_j)\mathcal{Y}_{lm}(\omega_j) - N_p\right|}{J_{max}} \times 100, \tag{5.3}$$

where $J_{max} = \frac{1}{2}(l_{max}+1)(l_{max}+2)$ is the number of spherical harmonics for degree l_{max}.

5.2.5 SH_OF.F

`SH_OF.F` computes the coefficients $\mathcal{O}_{lm}$ from Eq. (5.2) for degrees $0 \leq l \leq l_{max}$ (see step (3) of the algorithm of Section 4.4). The ocean function may be reconstructed at the pixels centroids using `REC_OF.F`, and visualized by `of.gmt`.

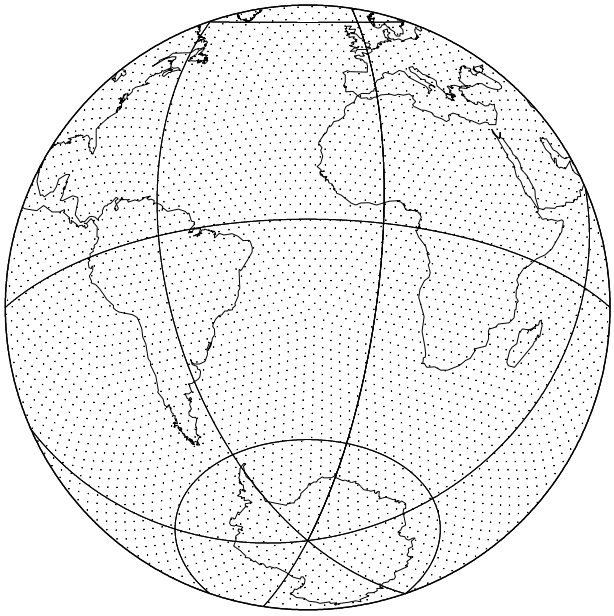

Figure 5.1: Spatial distribution of the centroids of the pixels obtained with $r = 14$ using the algorithm by Tegmark (1996). The distribution of pixels is quasi–uniform on the surface of the sphere.

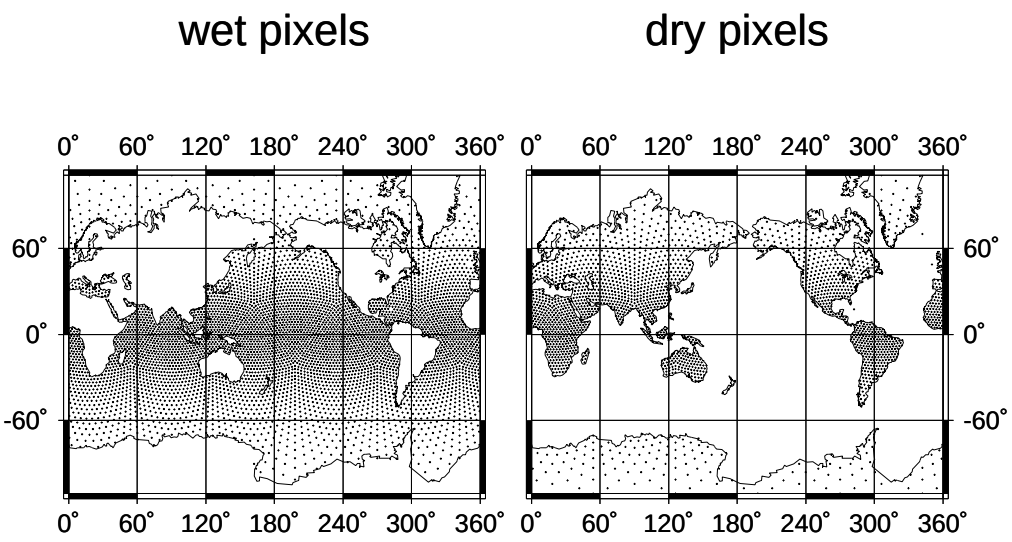

Figure 5.2: Wet and dry pixels distributions. The pixels coordinates have been obtained by the global distribution of Figure 5.3 using the utility `gmtselect` of GMT (Wessel and Smith, 1991).

Table 5.1: Complex coefficients of the spherical harmonics decomposition of the ocean function for degrees $0 \leq l \leq 4$. Here j stands for $l(l+1)/2 + m + 1$, where l and m are the degree and order, respectively.

j	l	m	$\mathrm{Re}(\mathcal{O}_{lm})$	$\mathrm{Im}(\mathcal{O}_{lm})$
1	0	0	+0.716	0.000
2	1	0	-0.111	0.000
3	2	1	+0.785E-01	-0.421E-01
4	2	0	-0.512E-01	0.000E+00
5	2	1	+0.294E-01	-0.445E-01
6	2	2	+0.257E-01	0.364E-02
7	3	0	+0.557E-01	0.000
8	3	1	-0.320E-01	-0.289E-01
9	3	2	+0.442E-01	0.643E-01
10	3	3	+0.656E-02	-0.571E-01
11	4	0	-0.240E-01	0.000
12	4	1	-0.258E-01	0.175E-01
13	4	2	+0.607E-01	0.160E-01
14	4	3	+0.349E-01	0.350E-02
15	4	4	+0.989E-02	0.699E-01

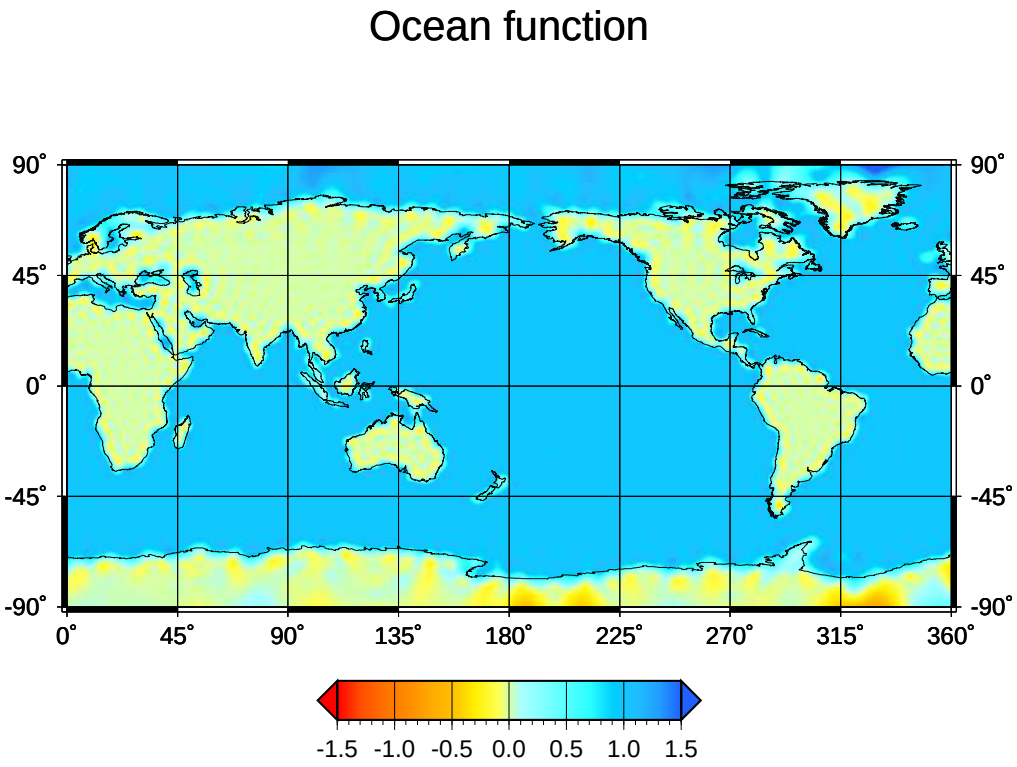

Figure 5.3: Ocean function obtained for $r = 14$ (see Table 5.1).

5.3 Ice sheets

In the current numerical implementation of the SLE, we have made use of the ICE3G chronology (Tushingham and Peltier, 1991), that is freely available and widely used in the literature. With a few changes, the code can also manage the ICE1 chronology (Peltier and Andrews, 1976) and can be easily modified to account for arbitrary chronologies. ICE3G comes in a discretized form where the whole load is seen as an aggregate of simple disc–shaped ice elements with a time–dependent thickness (see also Spada et al., 2003). The time–discretization of ICE3G follows the scheme (4.11) with $\Delta = 1$ kyr and $t_N = 18$ kyrs, so that this ice–sheets chronology can be very easily conveyed within our formalism.

The change of ice thickness is expanded in spherical harmonics taking advantage of the simple geometry of the discs, without the aid of the grid of pixels introduced above. The spherical harmonics expansion of each disc is first determined in the reference frame where the z axis is the axis of symmetry of the disc, and then transformed into the geographical reference frame Spada et al. (2003). This directly provides the coefficients $T_{lm,k}$ (see 4.18), and, from (4.23) and (4.29), the terms $I_{lm,k}$.

5.3.1 `SH3_C.F`, `SH3.F`

These two programs execute step (4) of the SLE algorithm outlined in Section 4.4. In particular, `SH3_C.F` computes the shape factors f_{lme} pertaining to the ICE3G global ice–sheets chronology Tushingham and Peltier (1991). The ice–sheet parameters for model ICE3G are read from the input file *ice3.dat*. Since ICE3G is composed of an aggregate of axis–symmetrical disk–shaped ice elements (see Figure 5.4), the computation of the shape factors is fully analytical. Taking advantage of the discs symmetry, one obtains

$$f_{lme} = \frac{1}{2(2l+1)} \mathcal{Y}^*{}_{lm}(\omega_e^{ice})[-P_{l+1}(\cos\alpha_e) + P_{l-1}(\cos\alpha_e)], \tag{5.4}$$

(Spada, 2003) where ω_e^{ice} denotes colatitude and longitude of the discs centers, and α_e is the half–amplitude of the ice elements. In other approaches to the solving of the

SLE (Hugo Schotman, personal communication, 2006), ICE3G is interpolated on a set of spherical quadrilaterals before being decomposed in spherical harmonics, with the advantage of eliminating the superpositions and the interstices inherent in the discs distribution (but with the disadvantage of an increased CPU time). Of course, the two methods may give slightly different results, with the largest discrepancies expected at the margins of the former ice–sheets.

In order to deal with the ICE1 chronology of Peltier and Andrews (1976), which already comes as an aggregate of spherical rectangles defined by meridians of longitudes λ_{1e} and λ_{2e}, and parallels of colatitudes θ_{1e} and θ_{2e}, with $\lambda_{2e}-\lambda_{1e}=\theta_{2e}-\theta_{1e}=5^\circ$ (see input file *ice1.dat* and Figure 5.4) the user can employ the routines `SH1_C.F` and `SH1.F` *in lieu* of `SH3_C.F` and `SH3.F`. Using the results of Spada (2003), `SH1_C.F` computes the shape factors

$$f_{lme}=\frac{1}{4\pi}\bar{\mu}_{lm}\epsilon_{me}\gamma_{lme}, \tag{5.5}$$

where

$$\epsilon_{me}=\begin{cases}\lambda_{2e}-\lambda_{1e}, & m=0\\ \dfrac{\sin m\lambda_{2e}-\sin m\lambda_{1e}}{m}+i\dfrac{\cos m\lambda_{2e}-\cos m\lambda_{1e}}{m}, & m\neq 0,\end{cases} \tag{5.6}$$

and

$$\gamma_{lme}=-\int_{\cos\theta_{1e}}^{\cos\theta_{2e}}P_{lm}(z)dz \tag{5.7}$$

For the two ice–sheets chronologies, the SH coefficients $T_{lm,k}$ and $I_{lm,k}$ in Eqs. (4.27) and (4.20) are computed by `SH3.F` and `SH1.F`, respectively. The two–character string *[k]* indicates the time elapsed since the Last Glacial Maximum (LGM), expressed in (uncalibtrated) kyrs. For models ICE1 and ICE3G the LGM was 18 kyrs BP.

Any of the two ice–sheet distributions may be reconstructed at a given time–step by `REC_ICE.F`, and portrayed running the script `ice3(1).gmt`, which provide images of the ice sheets.Examples of ice sheet reconstructions are given in Figure 5.5.

Although `SELEN` in its present form only includes ICE1 and ICE3G, it can be easily modified to deal with any other (publicly available) ice sheet model, provided that its form is described by either disk–shaped elements or spherical quadrilaterals.

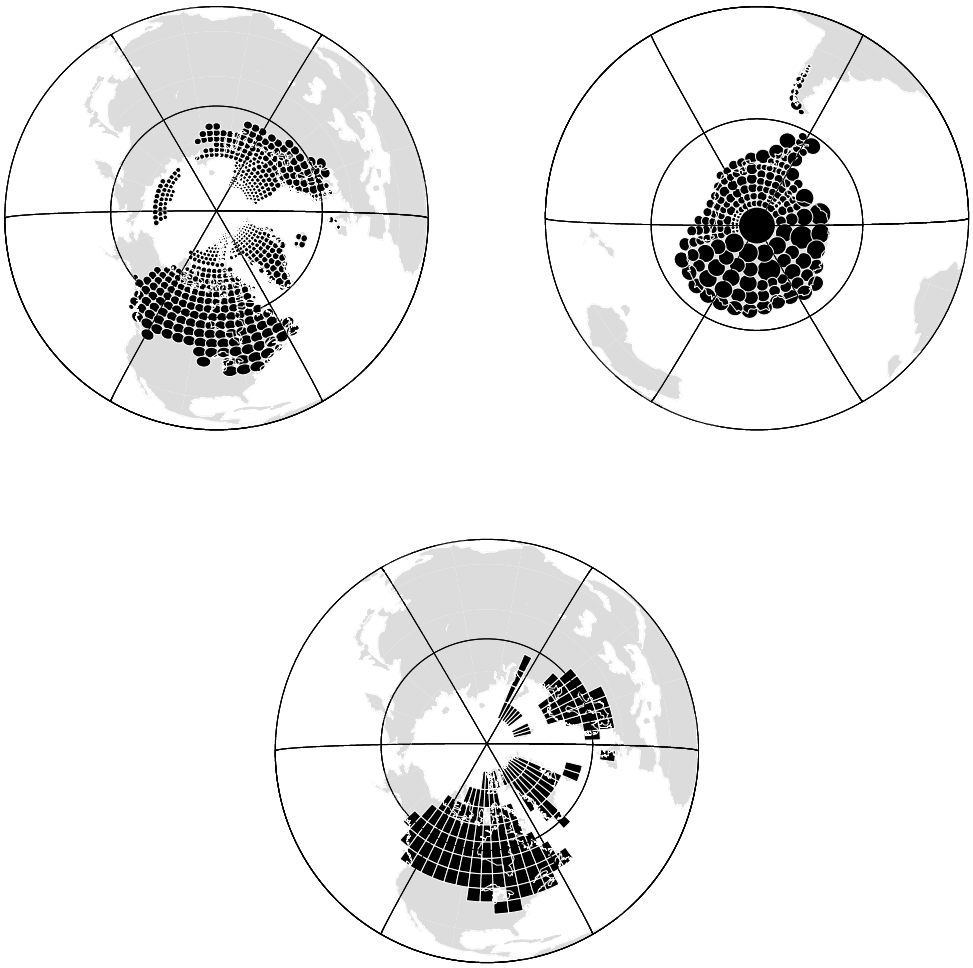

Figure 5.4: Spatial discretization of ICE3G (top, left and right) and of ICE1 (bottom), based on "discs" and "spherical quadrilaterals", respectively. In ICE1 Antarctica is stationary during Holocene.

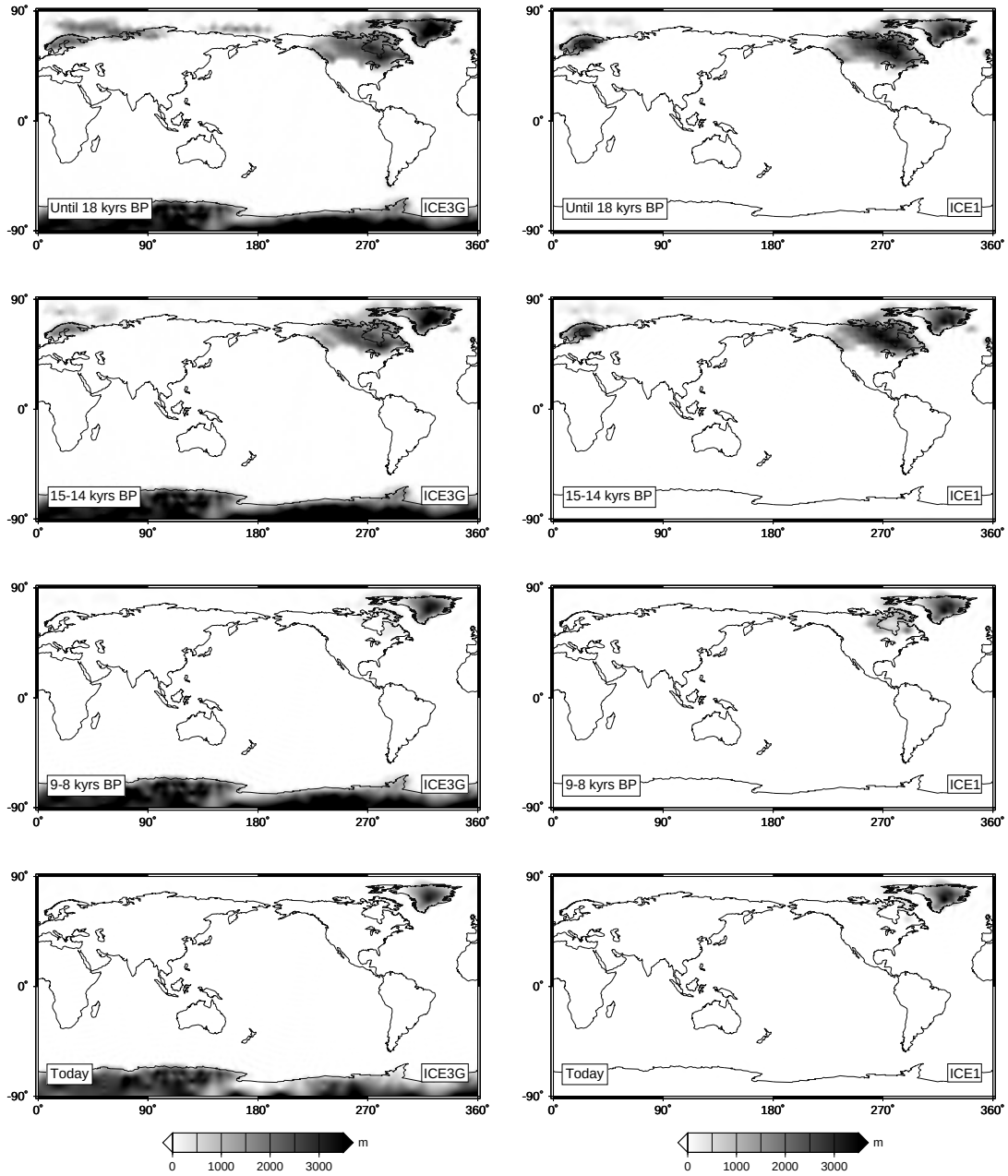

Figure 5.5: Reconstructed (LMAX=72) ice thickness for ICE3G (left) and ICE1 (right) at different time steps. Fringes particularly visible over Antarctica (left) reflect overlaps and gaps between disk–shaped ice elements of ICE3G (see Figure 5.4), which could be avoided by smoothing before SH decomposition.

5.4 Earth model

Before solving the SLE, it is necessary to choose an Earth model and to determine its elastic and viscous LDCs, that are needed to build the arrays E_l (see Eq. 4.52) and $\beta_l(t)$ (Eq. 4.53), respectively. This can be done using TABOO (Spada, 2003; Spada et al., 2004), a free Fortran 90 code that also solves the "simplified GIA problem" discussed in Section 2.3.

TABOO includes a set of built–in layered viscoelastic models whose parameters can be tuned to obtain the desired rheological profile. The LDCs are computed according to the 'normal modes' method (e. g., Peltier, 1985), based on the analytical form of the poloidal propagator matrix (Sabadini et al., 1982; Spada et al., 1992). At its present stage of development, TABOO only allows to deal with coarsely layered models. The forthcoming version of TABOO is planned to include models with an arbitrary number of layers (Spada and Boschi, 2006). All of the computations of this chapter are based on the rheological profile employed in Cianetti et al. (2002), that is reported in Table 5.2 (REF rheological profile).

The spectrum of relaxation, and the elastic and fluid LDCs as a function of the harmonic degree (see Section 2.1 for their definition), are shown in Figure 5.7.

5.4.1 `TB.F`

Program `TB.F` essentially duplicates the program `TABOO` (Spada, 2003). According to step (5) of the algorithm described in Section 4.4 above, `TB.F` computes the elastic (h_l^e, k_l^e), fluid (h_l^f, k_l^f), and viscoelastic (h_{lj}, k_{lj}) LDCs, as well as the relaxation times τ_{lj}, for a spherically symmetric, incompressible, self–gravitating Earth model (see Eq. 2.37). According to e. g., Spada and Boschi (2006), the fluid LDCs are defined by Eq. 2.29 and represent the long–term asymptotes of the LDCs relative to an Heaviside load. The number of mantle layers and the physical parameters of the Earth model (density, rigidity, and viscosity profiles), are controlled by the include file *data.inc* (see Appendix C.1 and the `TABOO` documentation). All of the

models available by TABOO include an elastic lithosphere and an inviscid homogeneous core. In addition, TB.F builds the arrays E_l (Eq. 4.52), E_l^U (4.84), $\beta_l(t)$ (Eq. 4.53), and $\beta_l^U(t)$ (Eq. 4.85).

Table 5.2: Earth model parameters employed in this study (REF, see Section 7.3). Layering, density and rigidity are from e. g. Cianetti et al. (2002). Viscosity is that implicit in model ICE3G Tushingham and Peltier (1991).

Layer	Range (km)	Density (kg m^{-3})	Rigidity (GPa)	Viscosity ($\times 10^{21}$ Pa $\cdot$ s)
LITHOSPHERE	$6251 - 6371$	4120	73	∞
UPPER MANTLE	$5951 - 6251$	4120	95	1
TRANSITION ZONE	$5701 - 5951$	4220	110	1
LOWER MANTLE	$3480 - 5701$	4508	200	2
CORE	$0 - 3480$	10925	0	0

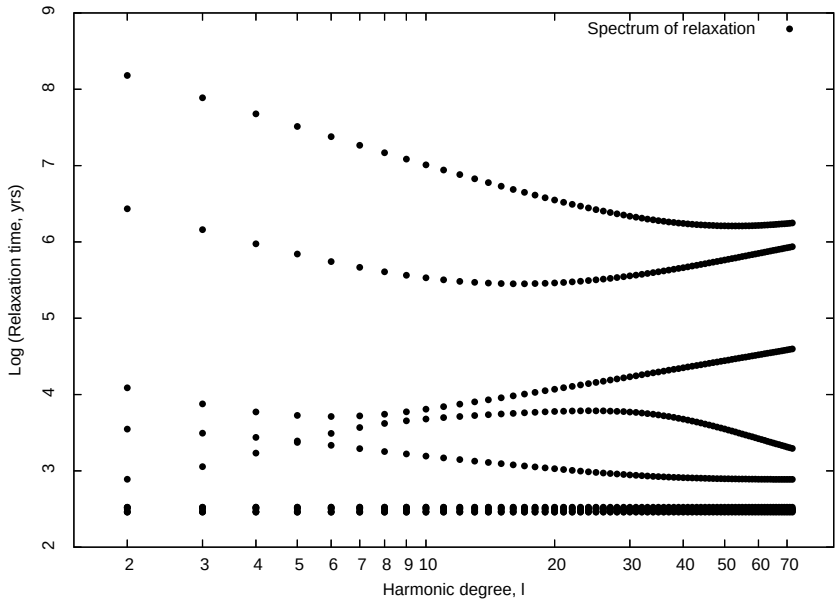

Figure 5.6: Relaxation spectrum, showing decay times τ_{lj} $(j = 1, \ldots, M)$ as a function of l, for the model of Table 5.2, which carries $M = 12$ modes.

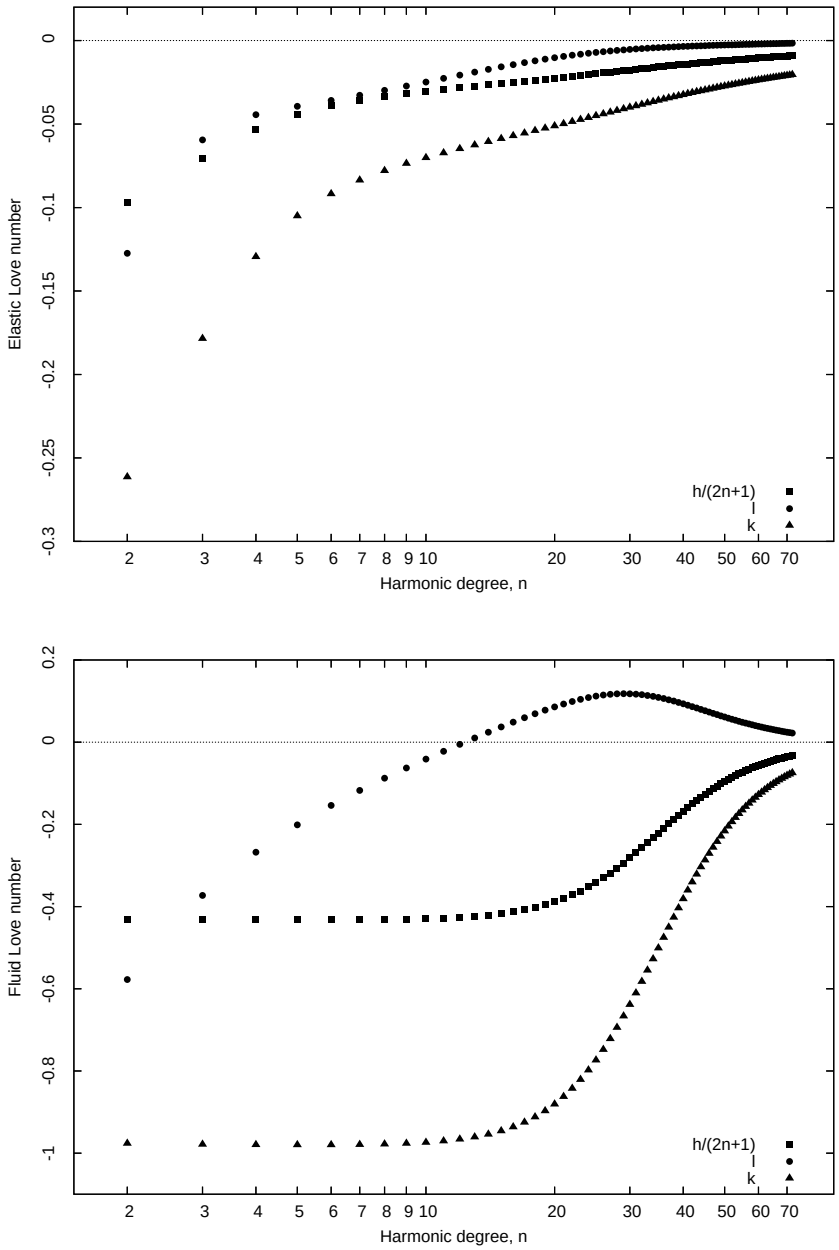

Figure 5.7: Top: elastic LDCs as a function of the harmonic degree for the model of Table 5.2. The h LDC (squares) is normalized by $2n+1$, where n is harmonic degree. Bottom: fluid LDCs. For low degrees, the k_l^f LDC is close to 1; a prefect isostatic compensation would, with $k_l^f = -1$ be attained in the absence of the elastic lithosphere.

5.5 Solution of the SLE and outputs

5.5.1 SLE.F

This program solves the recursive form of the SLE (Eq. 4.90) for the unknown $Z_{lm,k}$, and also determines the harmonic coefficients $S_{lm,i}$ (see Eq. 4.87), $U_{lm,i}$ (4.88), and $N_{lm,i}$ (4.89). This corresponds to steps (7) and (8) of the algorithm of Section 4.4 above. In order to show the role of each of the terms of the SLE, SLE.F can solve the equation in various possible forms, as described in Section 6.1 below. The particular form of the SLE and the number of iterations are defined by the switch IMODE and by the parameter SMAX and of the include file *data.inc*, respectively (see Appendix C.1).

5.5.2 SH_RSL.F, RSL.F

These programs determine the relative sea level curves for each site of the database of Tushingham and Peltier (1992, 1993) for which radiocarbon–controlled data are available[8] (the RSL sites and the observations are listed in the user–supplied input file *sealevel.dat*). More specifically, SH_RSL.F computes the SH at the RSL sites, $\mathcal{Y}(\omega_j^{rsl})$, whereas RSL.F determines the RSL curves by Eq. 3.63. Program RSL.F also computes individual and global χ^2 misfits between the observations and the model–based predictions.

5.5.3 GMAPS.F

Program GMAPS.F computes the rate of sea level change $\dot{S}$, the rate of vertical displacement $\dot{U}$, and the rate of change of the geoid height $\dot{N}$ at present time $t = t_p$ taking the discrete time–derivative of

$$R(\omega_j, t_p) = \sum_{lm} R_{lm,i} \mathcal{Y}(\omega_j), \tag{5.8}$$

[8] http://www1.ncdc.noaa.gov/pub/data/paleo/paleocean/relative_sea_level/.

where R represents any of the three scalar fields, and $R_{lm,i}$ are the corresponding harmonic coefficients. Maps of the three scalar fields can be obtained by the GMT script `gmaps.gmt`.

5.5.4 SH_PSMSL.F, PSMSL.F

These two codes compute the sea level secular trends at the sites of the database of the Permanent Service for the Mean Sea Level(the PSMSL sites and the observations are listed in the user–supplied input file *psmsl.dat*). `SH_PSMSL.F` computes the SH at the PSMSL sites, $\mathcal{Y}(\omega_j^{psm})$, while `PSMSL.F` computes the rates of sea level change at the sites by the discrete time–derivative

$$\dot{S}(\omega_j^{psm}, t_p) \approx \sum_{lm}^{l_{max}} \frac{S_{lm,N} - S_{lm,N-1}}{\Delta} \mathcal{Y}(\omega_j^{psm}). \tag{5.9}$$

5.5.5 STOKES.F

This program computes the time–derivatives of the cosine and sine Stokes coefficients of the gravity field at present time, in the range of degrees specified in the include file *data.inc* (see Appendix C.1). `STOKES.F` implements the formula

$$\left\{ \begin{array}{c} \dot{c}_{lm} \\ \dot{s}_{lm} \end{array} \right\} (t_p) \approx \frac{2 - \delta_{0m}}{a} \bar{\mu}_{lm} \left\{ \begin{array}{c} +\mathrm{Re} \\ -\mathrm{Im} \end{array} \right\} \frac{N_{lm,N} - N_{lm,N-1}}{\Delta}, \tag{5.10}$$

where Re and Im denote real and imaginaly parts, respectively.

Chapter 6

Applications of SELEN

To the purpose of illustrate the potentiality of the PS method for the SLE in the following sections we present three applications of SELEN that concern (i) predictions of the Holocene relative sea level variations for the Hudson bay region, (ii) estimates of the present–day rates of sea level variations, vertical deformations and geoid heights in the Mediterranean, and (iii) the determination of the time–derivatives of the Stokes coefficient of the gravity field. In Section 6.4 we show predictions of global GIA signatures which have been submitted to the Special Bureau for Loading.

In the following applications, the SLE will be normally solved in its gravitationally self–consistent form given by Eq. (4.5) for both the ICE1 and the ICE3G chronology (see Figure 5.5). However, in one of the proposed applications, we will solve the SLE in various simplified manners to appreciate the role of its individual components. The spatial resolution will be kept fixed to $r = 14$, (r corresponds to the parameter RES of the input file *data.inc*, see Appendix C.1), which implies $N_p = 7292$. The pixels distribution obtained for such resolution is shown in Figures 5.3 and 5.2.

In the ensuing computations, we will use the density and rigidity values of the REF rheological profile (see Table 5.2 in Chapter 5), but the shallow upper mantle and lower mantle viscosities will be changed accordingto our needs.

6.1 RSL curves for the Hudson Bay

This first example consists in the computation of RSL curves for the sites of the Hudson Bay region (see Figure 6.1). The purpose is to calibrate the method of solution and to analyze the sensitivity of RSL predictions to the settings of various free parameters.

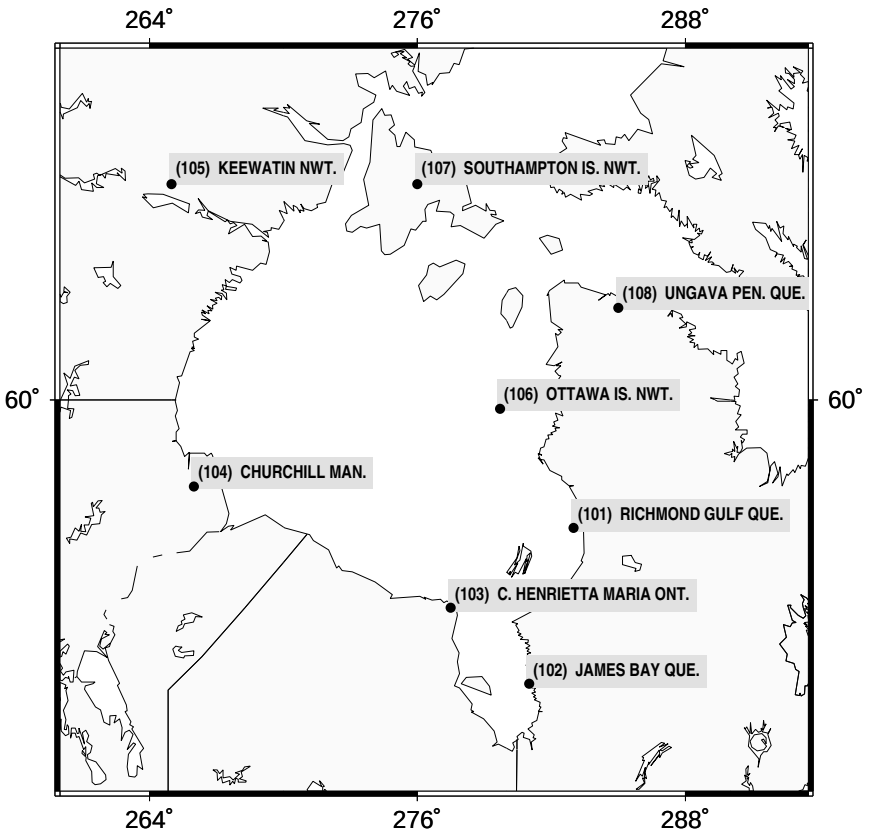

Figure 6.1: Hudson Bay RSL sites considered in this study, according to Tushingham and Peltier (1992, 1993). RSL predictions and observations for these sites are shown in Figures 6.2 and 6.3.

In the ensuing examples, the RSL has been computed according to Eq. (3.63), which is implemented in program `RSL.F` of `SELEN` (see Section 5.5).

In Figure 6.2 we consider various solutions of the SLE for the site of Ungava Peninsula, Quebec, for the mantle viscosity of Table 5.2 and the deglaciation chronology ICE3G (see Figure 5.5). In order to test the convergence of the recursive scheme in Eq. (4.90) in Figure 6.2a we show a set of RSL curves pertaining to different values of the SMAX parameter of *data.inc*, which determines the number of iterations s_{max}. The maximum harmonic degree, which is defined by LMAX parameter (see *data.inc*), here is $l_{max} = 72$. All the RSL curves shown have been obtained setting IMODE=1 in *data.inc*, which implies a "gravitationally self–consistent" approach to the SLE. The curve for SMAX=0 (dashed), corresponding to the eustatic solution of the SLE, is characterized by a monotonous sea level rise since the LGM, and is the same that we would obtain in the case of a rigid, non–self–gravitating Earth, i. e. setting IMODE=3 in *data.inc*. Other curves of the sequence show essentially a monotonous sea level fall. This trend is characteristic of the sites close to the center of the former ice–load (i. e. Clark's zone I, see Figure 1.10); RSL curves of different shapes are expected with increasing distance from this central region (Clark et al., 1978; Spada and Stocchi, 2006). It is apparent that the sequence quickly converges to a stable solution that is reached already for SMAX=3, consistently with Farrell and Clark (1976). For this same value of SMAX, and keeping fixed IMODE=1, Figure 6.2b shows the effect of choosing different values of LMAX, the maximum harmonic degree of the analysis. After a few oscillations, the solution converges for LMAX=72; a further increase of this parameter (i. e., LMAX=96) does not alter significantly the results. In Figure 6.2c we show the eustatic RSL curve (EUS) obtained setting IMODE=3 in *data.inc* and the converged gravitionally self–consistent one (thick line, GSC), reproduced from Figure 6.2b, which represent two end–members of the response of Earth to the surface loads. While the eustatic sea level changes is computed for a rigid, non–gravitating Earth, the latter accounts for both the elastic and the viscous response, and for the (gravitationally self–consistent) ocean load as

well. In terms of LDCs, the eustatic solution for a rigid Earth is obtained setting $1 + k_l^e - h_l^e \equiv 0$ and $k_{lj} = h_{lj} = 0$ in Eqs. (4.52) and (4.53), respectively, which implies $Z_{lm,i} = Z_{lm,i}^E$ in (4.90).

Figure 6.2c also shows another rigid–Earth solution (WOO), in which we only account for the gravitational interaction between the ice sheets and the ocean mass, with $k_l^e = h_l^e = k_{lj} = h_{lj} = 0$ in Eqs. (4.52) and (4.53), respectively, and IMODE=4 in *data.inc*. An analytical solution for this problem, valid for a point–like ice sheet, was originally found by Woodward (1888) (and reproduced by Farrell and Clark, 1976) in his pioneering work on the form and position of mean sea level. The RSL curve labeled by ILN shows the prediction obtained when the ice load is switched out in the GSC solution, obtained setting $I_{lm,i} = 0$ in Eq. (4.83) and IMODE=5 in *data.inc*. In this case, the postglacial sea level changes only result from the deformations driven by the ocean load and the associated geoid variations. The results obtained fall close to the eustatic curve. A similar approach, but limited to the elastic response, was proposed by Farrell and Clark (1976) to illustrate the physics of the SLE. As a final example, the RSL curve marked by ELA depicts the GSC solution when the viscous LDCs are neglected ($k_l^e = h_l^e = 0$ in Eq. (4.52), obtained setting IMODE=2 in *data.inc*). The comparison with the fully GSC result clearly shows how significant the contribution is of the delayed viscoelastic effects on RSL. With the exception of EUS, all the solutions shown in Figure 6.2 require an iterative approach to the SLE, according to Eq. (4.90). They have been obtained setting SMAX=3 and LMAX=72 in the configuration file *data.inc*. The whole set of RSL observations available form the Hudson Bay region are considered in Figure 6.3, where solid and dashed curves show the results of computations using the deglaciation chronologies of ICE3G and of ICE1, respectively. The particular ice chronology can be chosen in `selen.sh` before execution (see Section 5.3.1 above). In all of the cases considered in Figure 6.3, LMAX=72, and SMAX=3, and the gravitationally self–consistent solution of the SLE has been employed (IMODE=1). The input file *sealevel.dat* can be easily easily modified by the user.

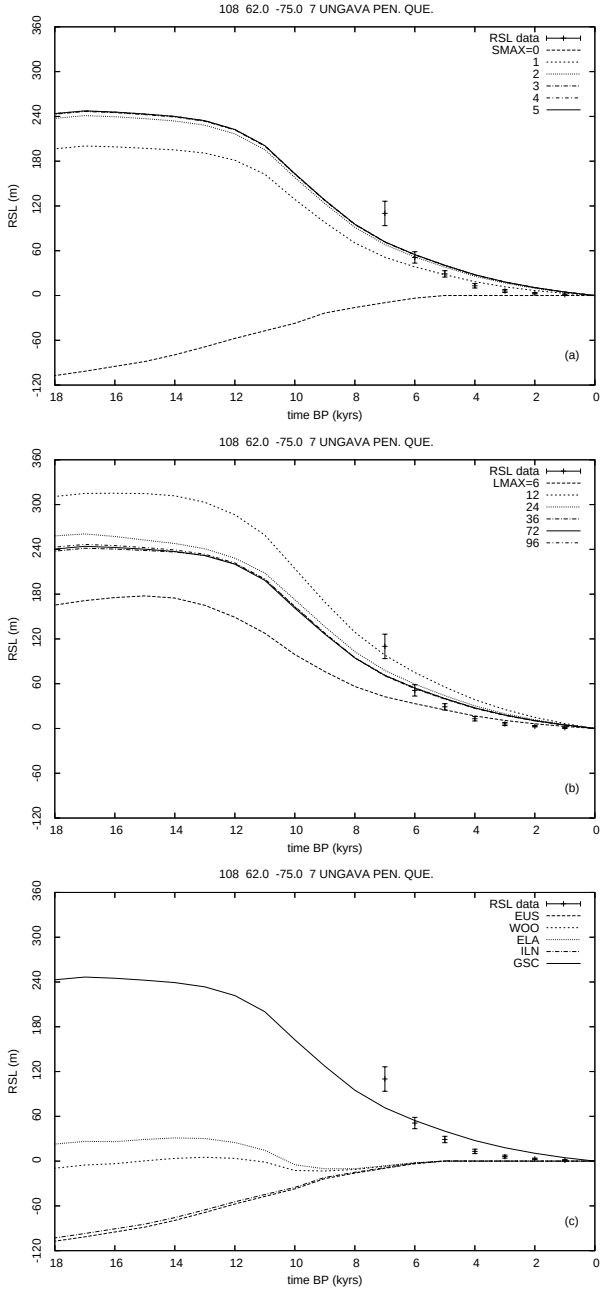

Figure 6.2: Predicted and observed RSL curves for Ungava Peninsula, Quebec. Frame (a) shows RSL curves corresponding to various SLE iterations, (b) illustrates how RSL curves are affected by varying LMAX, while in (c) we consider various possible SLE solutions (see text).

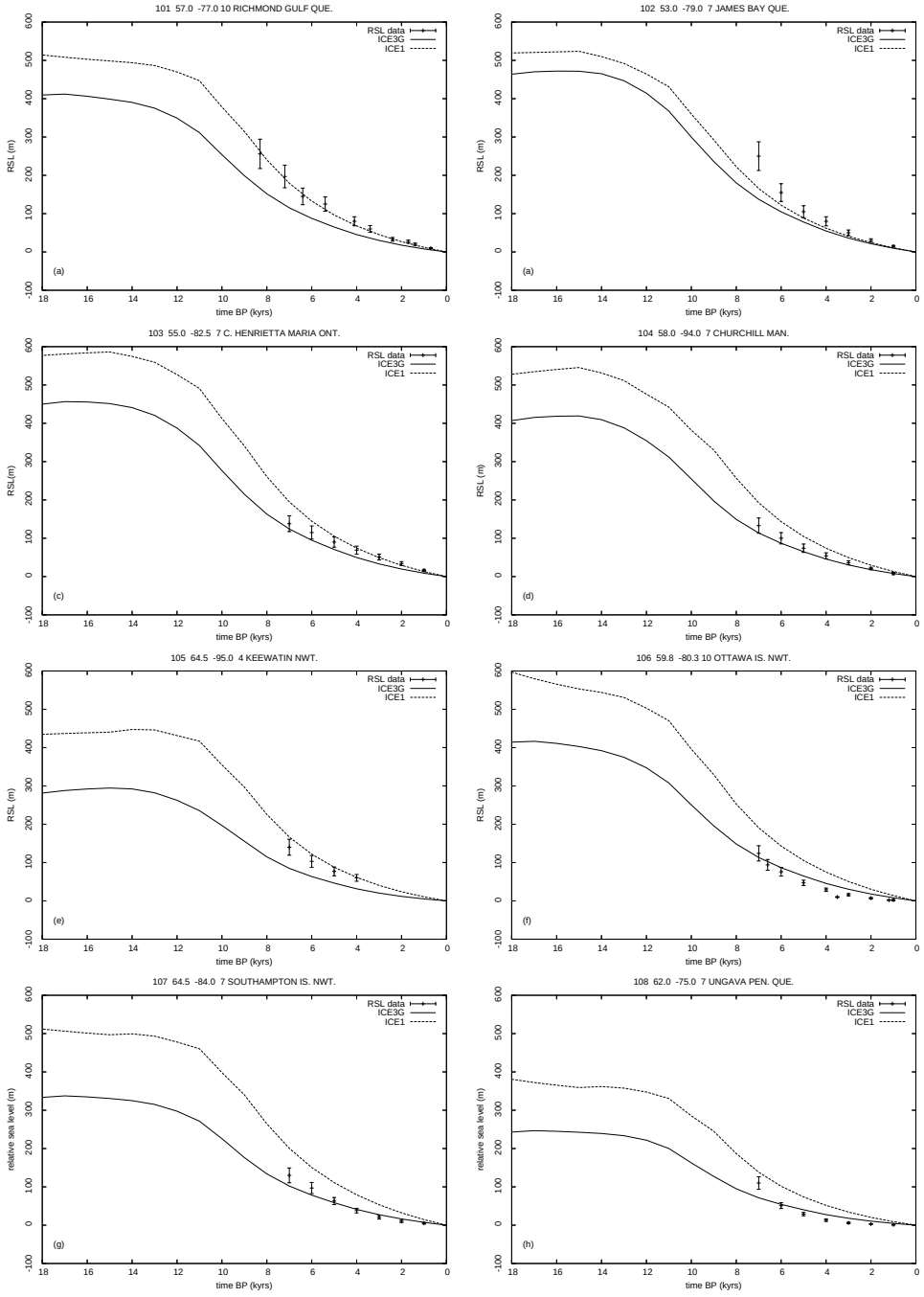

Figure 6.3: Observed and predicted RSL curves for sites of Figure 6.1. "Gravitationally self–consistent" computations using ICE3G and ICE1 are shown by solid and dashed curves, respectively (see Figure 5.5).

6.2 Present–day rate of sea level change in the Mediterranean

In Figure 6.4 we show the present–day rate of sea level change in the Mediterranean, computed for a shallow upper mantle viscosity of 0.5×10^{21} Pa $\cdot$ s and a transition zone viscosity of 10^{21} Pa $\cdot$ s. The lower mantle viscosity is 2×10^{21} Pa $\cdot$ s in frame (a) and 50×10^{21} Pa $\cdot$ s in frame (b), respectively. The other physical parameters of the Earth are given in Table 5.2. The rates of sea level change shown in Figure 6.4 have been obtained using `GMAPS.F`, which implements Eq. (5.8) with coefficients $R_{lm,i} = S_{lm,i}$. In all of the computations of this section, we have run `SELEN` using the deglaciation model ICE3G and the parameters IMODE=1, SMAX=3, RES=14, and LMAX=72 in file *data.inc*.

From the results of Figure 6.4a it is apparent that glacial–isostatic adjustment has the effect of producing a sea level rise in the central portion of the Mediterranean, with a maximum close to 0.45 mm yr^{-1}. However, for the viscosity values and ice chronology employed here, a sea level fall close to -0.1 mm yr^{-1} is predicted along most of the continental coasts of the Mediterranean. The pattern of sea level change shown in Figure 6.4, characteristic of the Mediterranean and other closed mid–latitude basins (Mitrovica and Milne, 2002), has been identified as a new "Clark's zone" (Clark et al., 1978) named Clark's zone VII (see Chapter 9 for further details). An increase of the viscosity of the lower mantle (Figure 6.4b, with 50×10^{21} Pa $\cdot$ s) has the effect of increasing the peak value of sea level rise to ~ 0.65 mm yr^{-1}, and to significantly narrow the regions characterized by a sea level fall that are now completely absent along the Tyrrhenian coast of France and Italy. This appears to be more consistent with the available observations of late–Holocene RSL variations changes in this regions (see Chapters 9 and 10).

For the same viscosity profile and parameters of Figure 6.4a, we show in Figure 6.5 the present–day rates of vertical velocity and geoid height change driven by glacial–isostatic adjustment in the Mediterranean. These scalar fields are computed

by `GMAPS.F` along with $\dot{S}$. According to Eq. (3.56), the fields $\dot{U}$ (frame a) and $\dot{N}$ (b) are related by $\dot{N} - \dot{U} = \dot{S}$, where $\dot{S}$ is shown in Figure 6.4a. We observe that $\dot{U}$ and $\dot{N}$ are both negative across the Mediterranean, to indicate that in this region the surface topography and the geoid are both subject to subsidence. However, while $\dot{U}$ is characterized by a significant spatial variability, $\dot{N}$ is almost constant, which reflects a larger content of long–wavelength harmonics. We also observe that in the Mediterranean $|\dot{N}|$ is not small with respect to $|\dot{U}|$, as we could expect in formerly glaciated regions, where sea level changes are mainly due to vertical deformations.

The issue of present–day sea level variations is considered more in detail for the Italian PSMSL sites shown in Figure 6.6. Using the programs `SH_PSMSL.F` and `PSMSL.F` and the same settings used to obtain Figure 6.4a, we have computed $\dot{S}$ as a function of lower mantle viscosity. The results, shown in Figure 6.7, clearly show that along the coasts of Italy the expected glacial–isostatic contribution to the currently observed sea level variations is generally positive, which indicates a sea level rise. Consistently with Figure 6.4a, a moderate sea level fall is predicted for the sites of northern Italy (Porto Maurizio, Genova, Porto Corsini, Venezia, and Trieste) provided that the lower mantle viscosity does not exceed $\sim 3 \times 10^{21}$ Pa $\cdot$ s. A horizontal asymptote of the $\dot{S}$ curves is only obtained for the unrealistically large viscosity of $\sim 10^{24}$ Pa $\cdot$ s which indicates that the observations for the Mediterranean are sensitive to the rheological properties of lower mantle for a wide range of possible mantle viscosities. The inverted parabola profile shown by the curves of Figure 6.7 as a function of lower mantle viscosity can be explained observing that for relatively low values of the viscosity of the lower mantle the Earth has already reached equilibrium at present time, while for relatively large viscosities it is always far from equilibrium on the time scales of glacial–isostatic adjustment. For intermediate viscosity values (close to 2×10^{22} Pa $\cdot$ s), a maximum is attained.

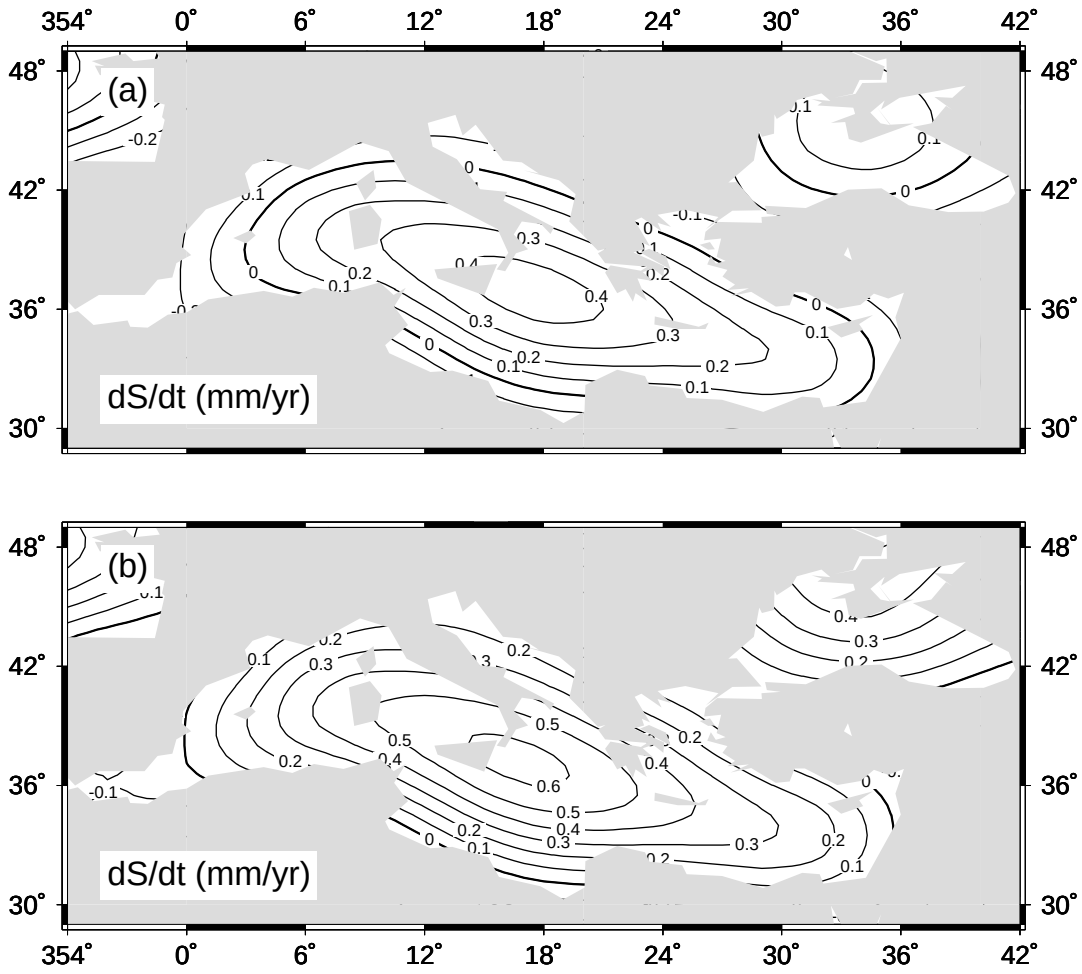

Figure 6.4: Rate of present–day Mediterranean sea level variations, for a low–viscosity lower mantle (2×10^{21} Pa $\cdot$ s, frame a) and a high–viscosity lower mantle (50×10^{21} Pa $\cdot$ s, b). Shallow upper mantle and transition zone viscosities are 0.5×10^{21} and 1×10^{21} Pa $\cdot$ s,respectively.

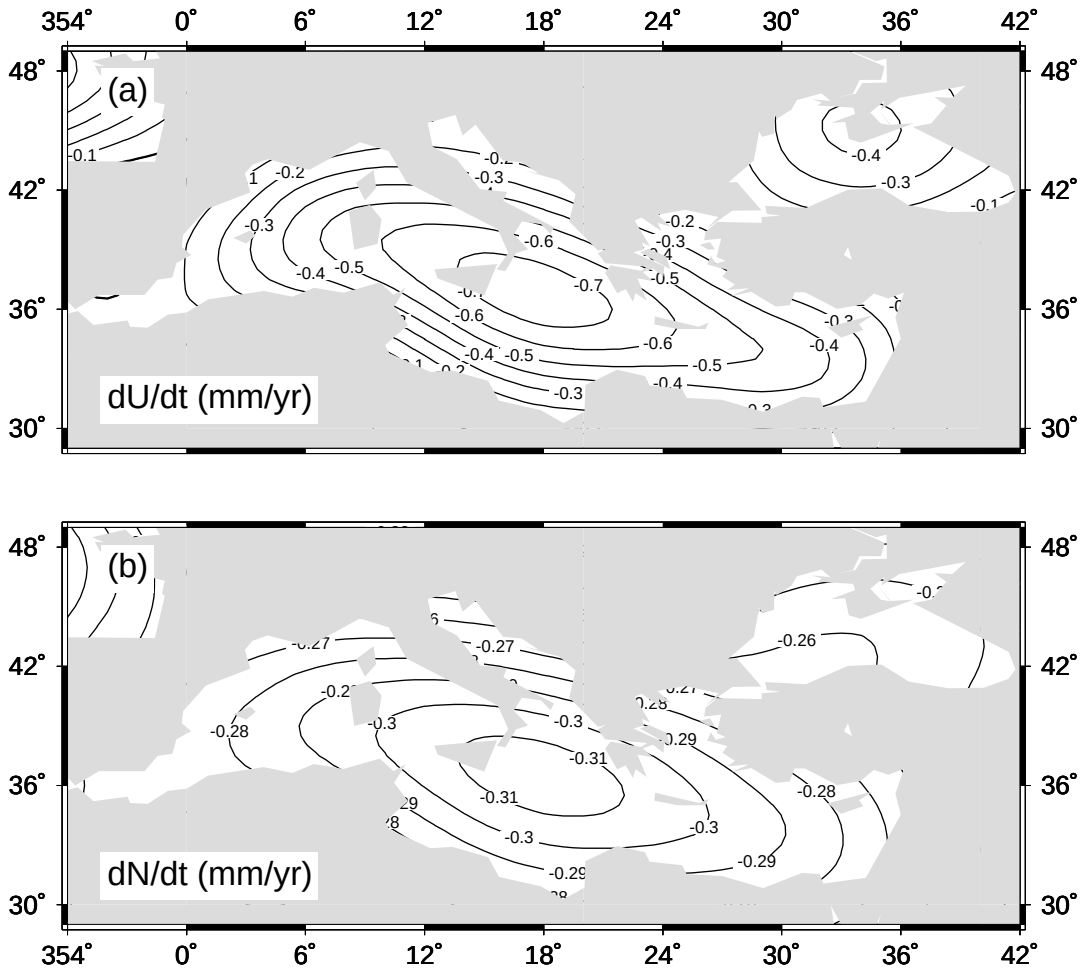

Figure 6.5: Present day Mediterranean rates of vertical uplift (a) and of geoid height change (b) with mantle viscosity as in Figure 6.4a.

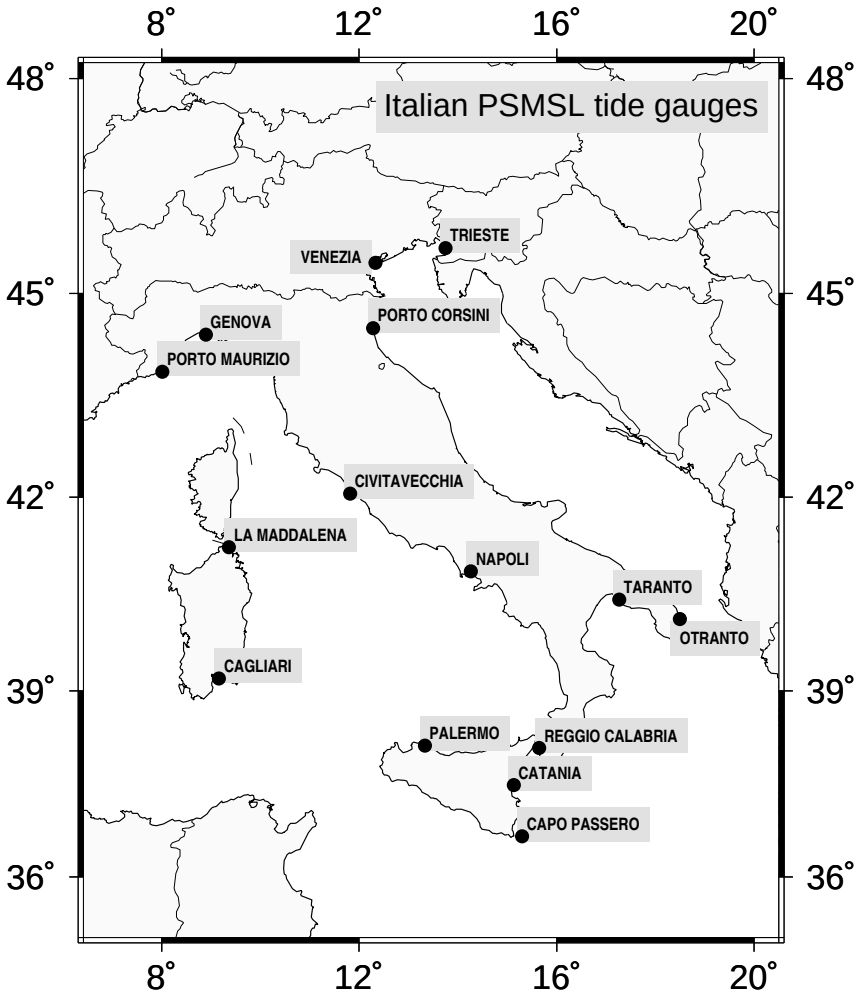

Figure 6.6: Italian PSMSL sites considered in Figure 6.7.

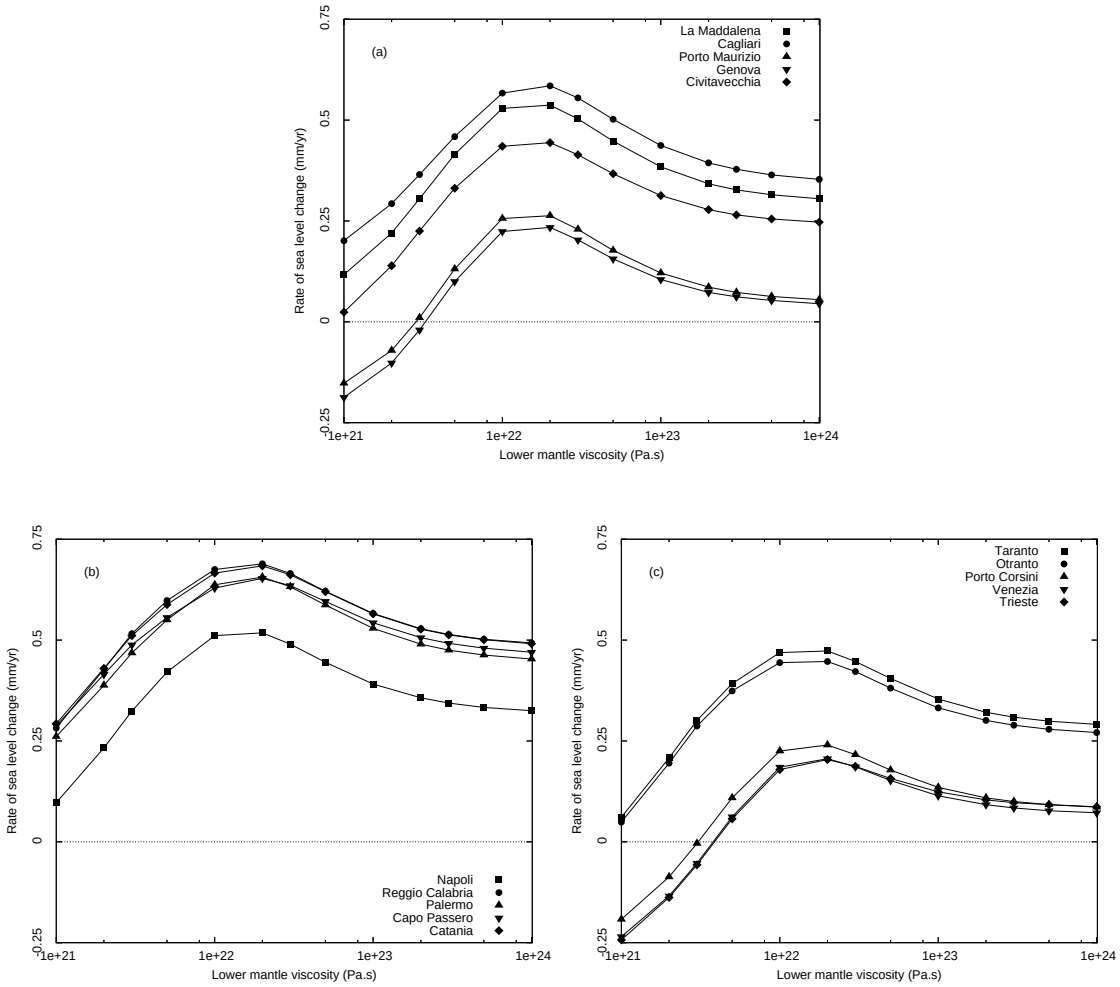

Figure 6.7: Present–day rate of sea level change for Italian PSMSL sites shown in Figure 6.6, as a function of lower mantle viscosity. Shallow upper mantle and transition zone viscosities are kept fixed to 0.5 and 1×10^{21} Pa $\cdot$ s, respectively.

6.3 Rates of variation of the Stokes coefficients

This last application of `SELEN` concerns a study of the effects of glacial–isostatic adjustment on the rates of variation of the Stokes coefficients of the gravity field $(\dot{c}_{lm}, \dot{s}_{lm})$, which are computed by the routine `STOKES.F` using Eq. (5.10) and the parameters of Table 5.2. The minimum and maximum harmonic degree of the Stokes coefficients to be computed is set by the parameters STMIN and STMAX of the include file *data.inc*, respectively.

Figure 6.8 shows some low–degree cosine and sine coefficients $\dot{c}_{lm}$ and $\dot{s}_{lm}$ obtained from the gravitationally self–consistent solution of the SLE (i. e., IMODE=1), with SMAX=3 and LMAX=72 in file *data.inc*. From the results shown, it is clear that the terms with $m = 0$ are those of largest amplitude, due to the strong zonal symmetry imposed by the spatial distribution of the ice sheets in model ICE3G (see Figure 5.5).

Among the Stokes coefficients, a particular role is played by c_{20}. Variations of this coefficient reflect variations of the inertia tensor of the Earth I_{ij}, being

$$c_{20} = -\frac{I_{33} - (I_{11} + I_{22})/2}{m_e a^2}, \tag{6.1}$$

(e. g., Lambeck, 1980). A positive value of $\dot{c}_{20}$ indicates that the shape of the Earth is progressively approaching that of a sphere, as a consequence of the global readjustment in response to the melting of the Holocene ice sheets. In view of the very long wavelength involved, the sensitivity of $\dot{c}_{20}$ to the lower mantle viscosity is known to be significant (see e. g., Spada et al., 1992).

To address this issue, we show in Figure 6.9 $\dot{c}_{20}$ for various values of the lower mantle viscosity. All of the three curves shown have been obtained by the gravitationally self–consistent solution and the same settings as in Figure 6.8. With filled squares we show the results obtained using all of the elements of the ice aggregate ICE3G, while the curve with open squares pertains to computations where we have not included in the Antarctic component of ICE3G (a partition of ICE3G in its regional components is available with the `TABOO` package of Spada, 2003). The ICE3G

results of Figure 6.9 are in good agreement with those obtained by Spada et al. (1992) (see their Figure 6, left frame), although in this latter the eustatic approximation was used for the water load, and a very coarse implementation of ICE3G was employed.

From Figure 6.9 it is clear that the Antarctic component of the whole deglaciation model accounts for a large fraction ($\approx 60\%$) of the total signal in the range of lower mantle viscosities considered. The curve with circles pertains to the deglaciation model ICE1, which assumes a zero antarctic ice aggregate (see Figure 5.5). The similarity between the results obtained with ICE1 and ICE3G–ANT confirms that at long–wavelengths the northern Hemisphere portions of the two aggregates have similar shapes and time–histories (see Figure 5.5). The inverted parabola profile shared by the three $\dot{c}_{20}$ curves as a function of lower mantle viscosity may be explained in the same manner as for the rates of sea level change shown in Figure 6.7.

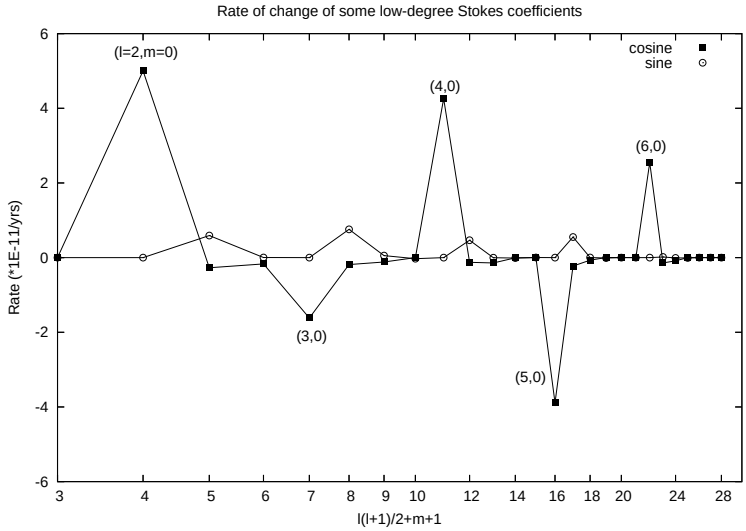

Figure 6.8: Present–day rate of variation of some low–degree Stokes coefficients. Cosine (squares) and sine (circles) coefficients are shown as a function of $l(l+1)/2+m+1$, where l is degree and m is order, for $l \leq 6$ and $|m| \leq l$. Here $\dot{c}_{20} = 5.00 \times 10^{-11}$ yrs^{-1}.

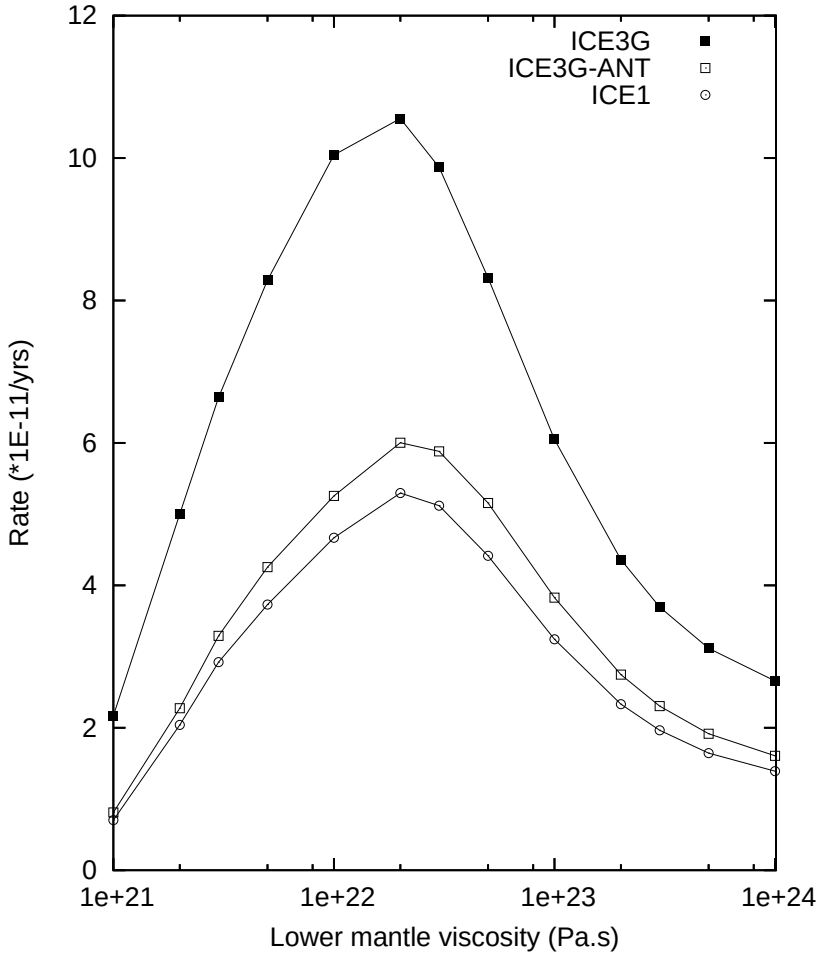

Figure 6.9: Present–day rate of variation of c_{20} as a function of lower mantle viscosity, for three different ice aggregates. Shallow upper mantle viscosity and other mantle parameters are given in Table 5.2.

6.4 Submission of post-glacial rebound predictions to the SBL

In the course of 2005 the Special Bureau for Loading (SBL)[1] of the Global Geophyscial Fluid Center (GGFC)[2] called for submission of predictions determined by geophysical models of the secular present–day 3–d motions of the surface of the Earth and secular variation of the gravitational field due to post–glacial rebound.[3] The SBL is one of the seven Special Bureaus of the GGFC, which in turn is a component of the International Earth Rotation and Reference Frame Service (IERS).[4] The SBL was set up in 2002 by the IERS to provide information and data products related to variations in shape, gravitational field and rotation of the Earth induced by surface mass loading. Until recently, the focus had been on the signals caused by present–day surface mass variations.

The IERS Conventions, which are the basis for the determination and monitoring of the International Terrestrial Reference Frame (ITRF)[5] consider three principal classes of models:

1. models that are recommended to be used in order to determine geodetic parameter estimates from raw space geodetic observations,

2. models that are purely conventional such as physical constants or models replacing physical specifications of properties of the reference frame,

3. models that are useful particularly for the interpretation of the results obtained from geodetic observations.

Class 3 models gain increasing importance for scientific and non–scientific applications requiring access to the ITRF. ITRF is gaining a wide–spread acceptance as

[1] http://www.sbl.statkart.no.
[2] http://bowie.gsfc.nasa.gov/ggfc/.
[3] http://www.sbl.statkart.no/projects/pgs/.
[4] http://www.iers.org.
[5] http://itrf.ensg.ign.fr/.

the global terrestrial reference frame, and many applications require that coordinates determined at different epochs can be compared directly or that the velocity field can be interpolated between ITRF points. Ultimately, this will require a detailed model of the Earth's surface kinematics, which would be a typical class 3 model.

The PGS is a global signal which regionally dominates the secular displacement field and significantly biases the rigid motion of the tectonic plates. Thus, it appears to be worthwhile to inter–compare the existing PGS models with the aim of quantifying the accuracy and documenting the inter–model differences. The SBL is taking the lead in an effort of the GGFC towards this goal and aims to identify a candidate for a class 3 model of the present–day PGS in the Earth's shape, gravitational field, and rotation, that can be used in space-geodetic studies e. g. as a conventional model for the correction of PGS or for the inclusion of PGS in a model of the present-day kinematics of the Earth's surface.

As a group active in the field of post-glacial rebound studies, we have fulfilled the request of the SBL for predictions of the present–day secular PGS in the shape of the Earth, the surface gravity field, and relative sea level. Our submission[6] included predictions of:

- RSL curves for the 392 sites included in the Tushingham and Peltier database (see also Section 6.1),
- rates of variation of the Stokes coefficients (see Section 6.3),
- present–day rates of sea level change at a number of selected tide gauges included in the PSMSL dataset,
- global velocity fields ($\dot{S}$, $\dot{U}$, and $\dot{N}$).

The maps of Figures 6.10, 6.11, and 6.12 show respectively the predicted present–day rate of sea level change $\dot{S}$, the vertical velocity $\dot{U}$, and the rate of change of the geoid height $\dot{N}$ for ICE3G and ICE1 models (Figure 5.4 and 5.5), respectively.

[6]http://www.sbl.statkart.no/projects/pgs/authors/.

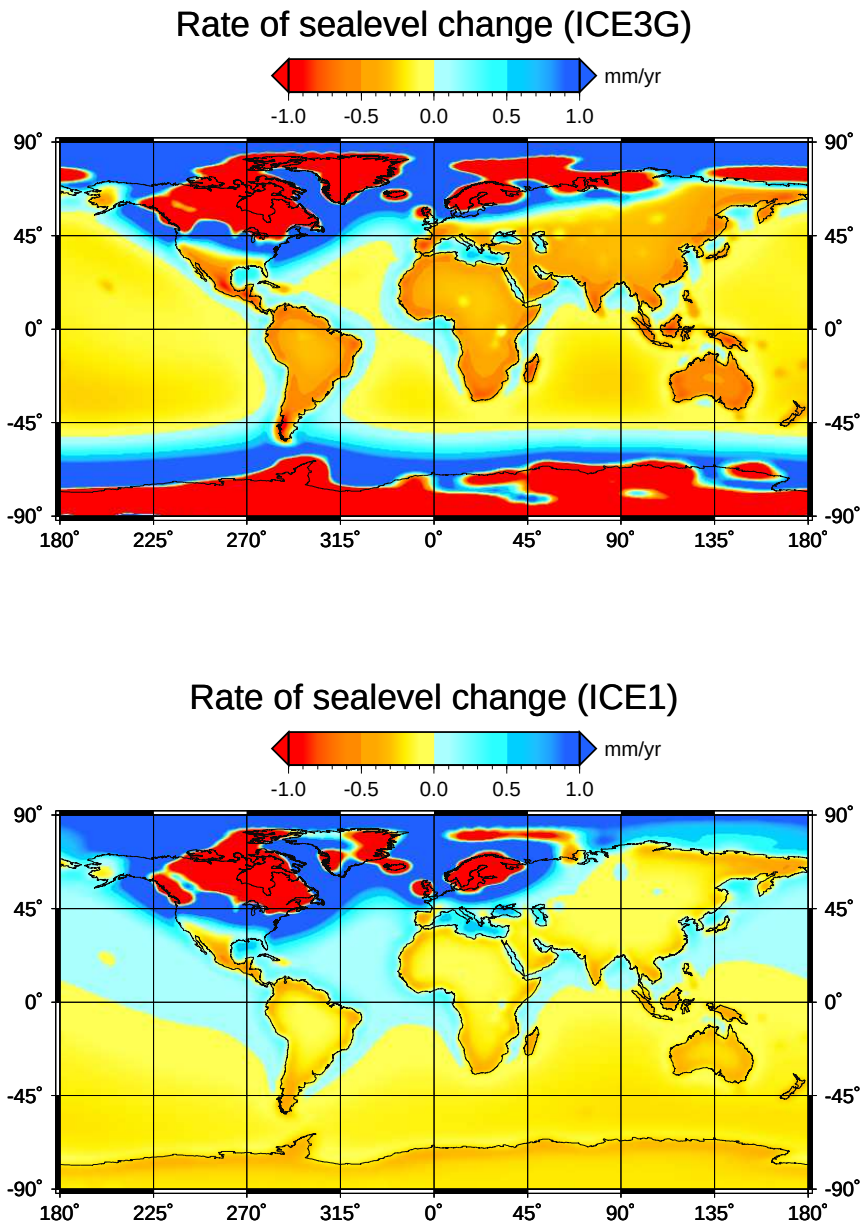

Figure 6.10: Present–day rate of sea level change $\dot{S}$ computed by means of models ICE3G and ICE1 using physical parameters of Table 5.2.

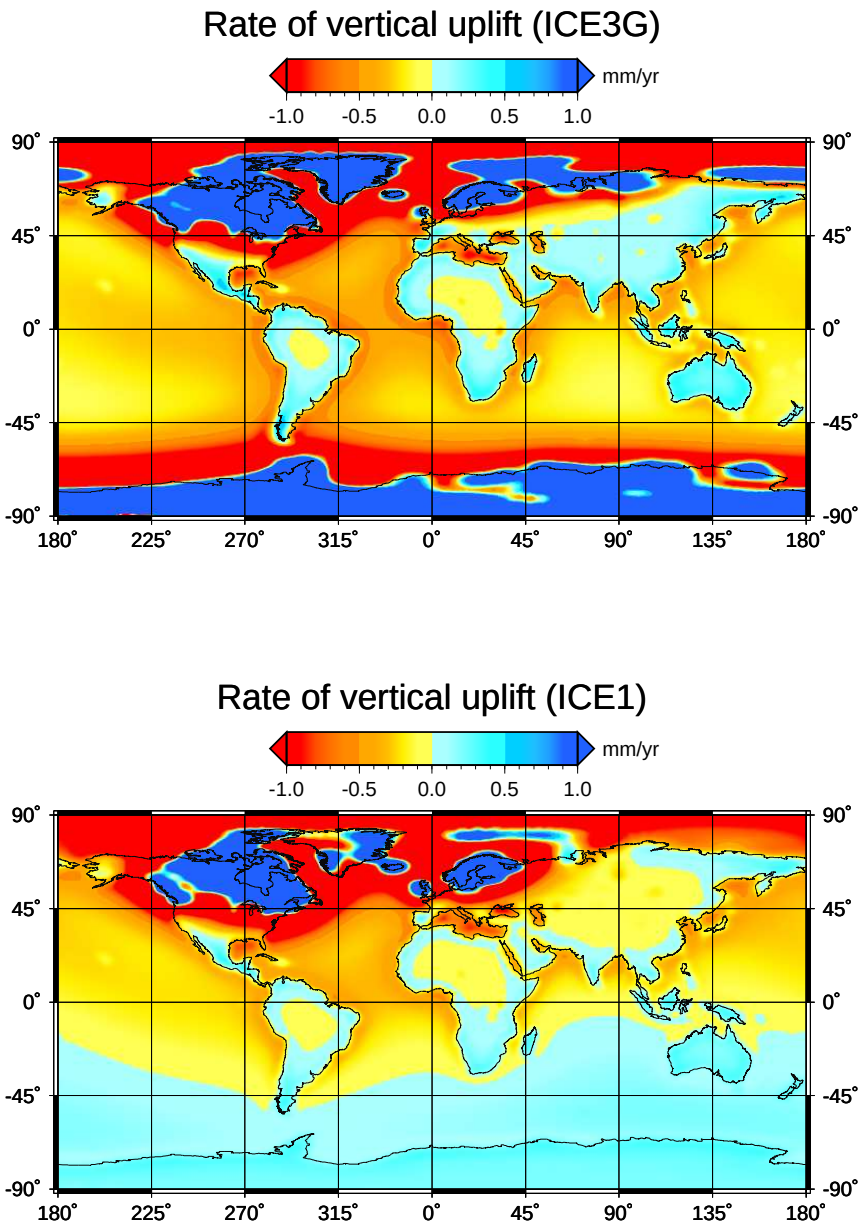

Figure 6.11: Present–day rate of vertical uplift $\dot{U}$ obtained using the same parameters as in Figure 6.10.

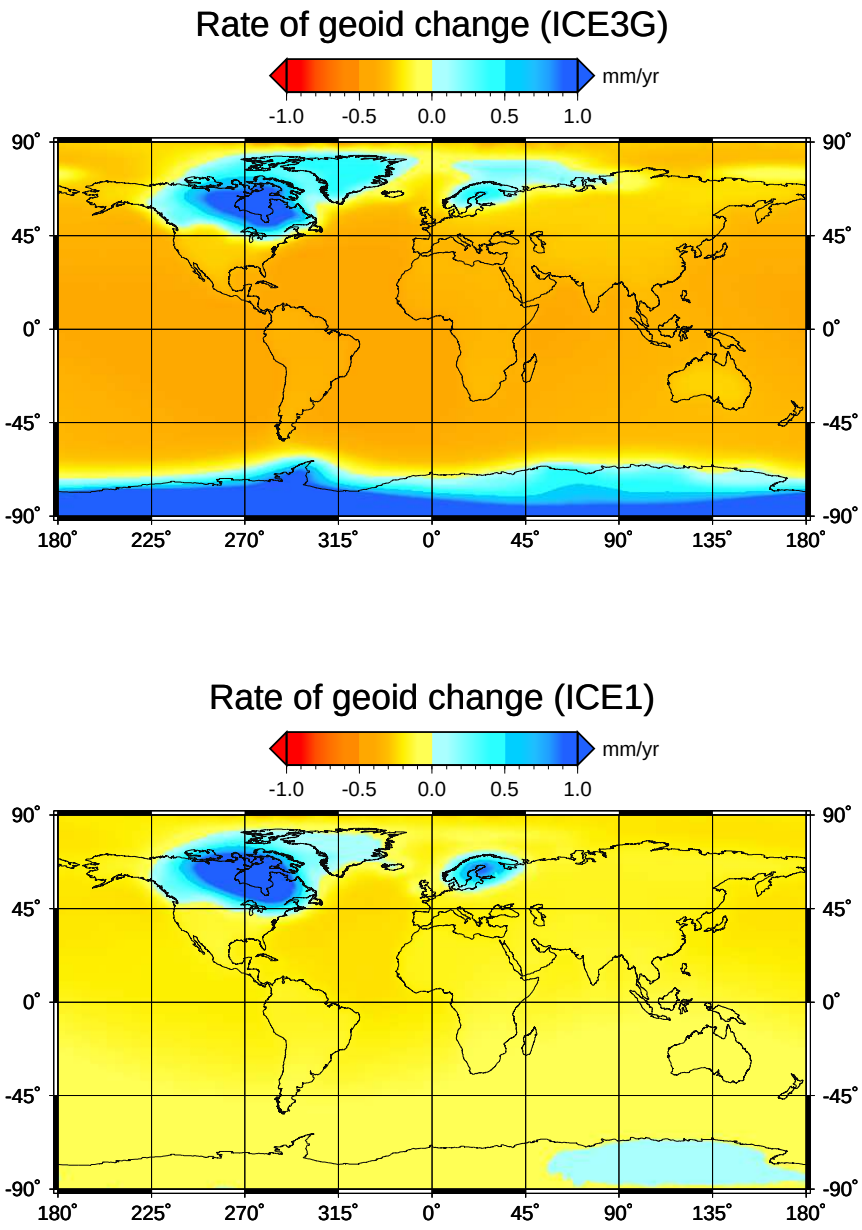

Figure 6.12: Present–day rate of change of the geoid height $\dot{N}$. Based on (3.4), this scalar field equals $\dot{S} + \dot{U}$, where $\dot{S}$ and $\dot{U}$ are shown in Figures 6.10 and 6.11, respectively.

6.5 Conclusions

We have presented and for the first time we have made available a simple Fortran 90 program (`SELEN`) for the computation of the sea level variations driven by the melting of the Holocene ice sheets. `SELEN` allows to solve the SLE in its gravitationally self–consistent form, but it is also possible to obtain the solution for some simplified versions of the SLE. Tuning the parameters of the include file *data.inc* and acting on the script `selen.sh`, it is possible to solve many problems in the context of GIA ranging from Holocene RSLvariations to present–day variations of the Stokes coefficients of the gravity field.

`SELEN` can be improved in a number of ways, with the implementation of time–dependent shorelines, mantle compressibility, a finely–layered mantle stratification, rotational feedbacks between sea level changes and Earth rotation, and horizontal deformations. However, in its present form, `SELEN` already performs well on a wide range of problems, giving results that are consistent with those already published in the literature. The programs that compose `SELEN` are designed to operate on a Mac OS X environment, and have been developed using the IBM XL Fortran compiler. However, the programs described herein can be easily ported to other hardware platforms. The source codes of the Fortran 90 and GMT procedures are publicly available upon request to the authors.

Part III

GIA signatures in the Mediterranean Sea

Chapter 7

Past and present–day sea level changes in the Mediterranean Sea

7.1 Studies on the Mediterranean sea level

Given the low tidal excursion and the presence of geological indicators and archaeological remains, the Mediterranean coasts are particularly suitable for the reconstruction of past sea levels (Flemming, 1972, 1978). The Holocene and the present–day sea level changes observed along the coasts of the Mediterranean basin stem for the contribution of several factors which span a wide range of space– and time–scales (Pirazzoli, 1991). The global glacio– and hydro–isostatic readjustment of the Earth to the melting of the late–Holocene ice–sheets is one of the most important long–term mechanisms, along with the vertical movements associated with subduction (Carminati et al., 2003) and marine sedimentation (Pirazzoli, 1991). On decadal to secular time–scales the sea level variations are affected by a climatological component (partly ascribed to an anthropogenic influence), which can be modeled as the sum of an eustatic and steric terms, both associated with the current climate changes, and of a local term due to human–driven subsidence (Carminati and Didonato, 1999; Pirazzoli, 1996).

The whole Mediterranean area is affected by a significant tectonic activity which contributes to a widespread coastal instability (Figure 7.1). Vertical movements, both sudden and continuous, have displaced, in the course of time, some coastal traits above or below the present–day sea level, preventing the depositional or erosional features from the destructive wave action. This spatially heterogeneous and short wavelength signal makes arduous the determination of a unique sea level curve representative of the Mediterranean region.

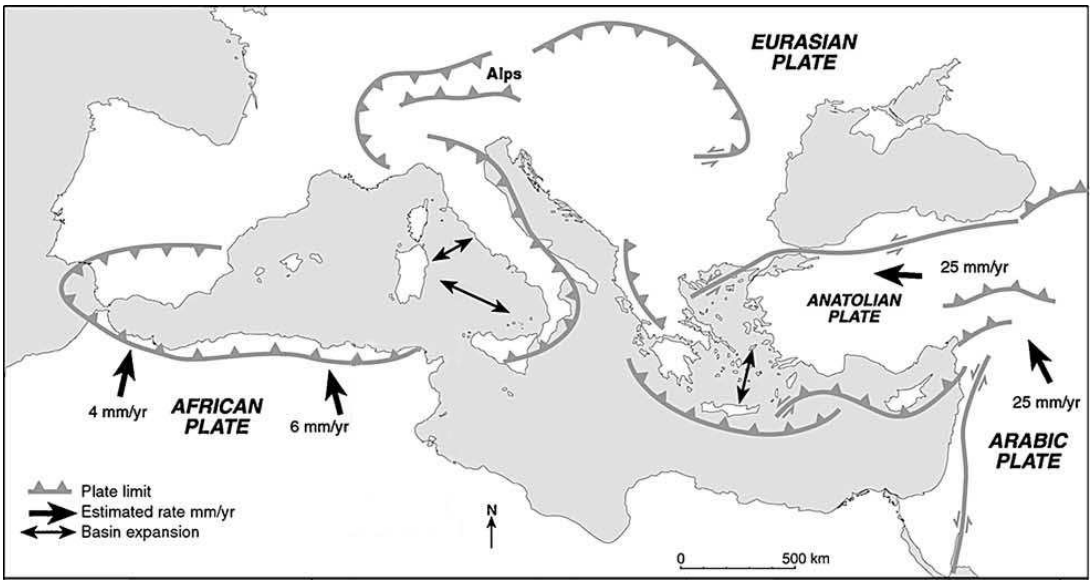

Figure 7.1: Mediterranean tectonic settings (from Morhange and Pirazzoli, 2005).

Our knowledge of the role played by the Holocene deglaciation on the relative sea level variations in the Mediterranean Sea mainly comes from numerous regional analyses aimed to the interpretation of various geological observations. Due to the significant evidence of past sea level changes, a number of these studies have dealt with the northern Mediterranean coasts (e. g., Lambeck and Bard2000). These are, potentially, the most affected by the process of isostatic adjustment due to the relatively small distance from the Fennoscandian and Alpine ice sheets (Figures 7.2 and 8.1). In general the glacio-isostatic term is a dominant factor in shaping the

overall pattern of apparent land subsidence within a distance of typically 40° to 60° of the ice centres (Lambeck and Johnston, 1995).

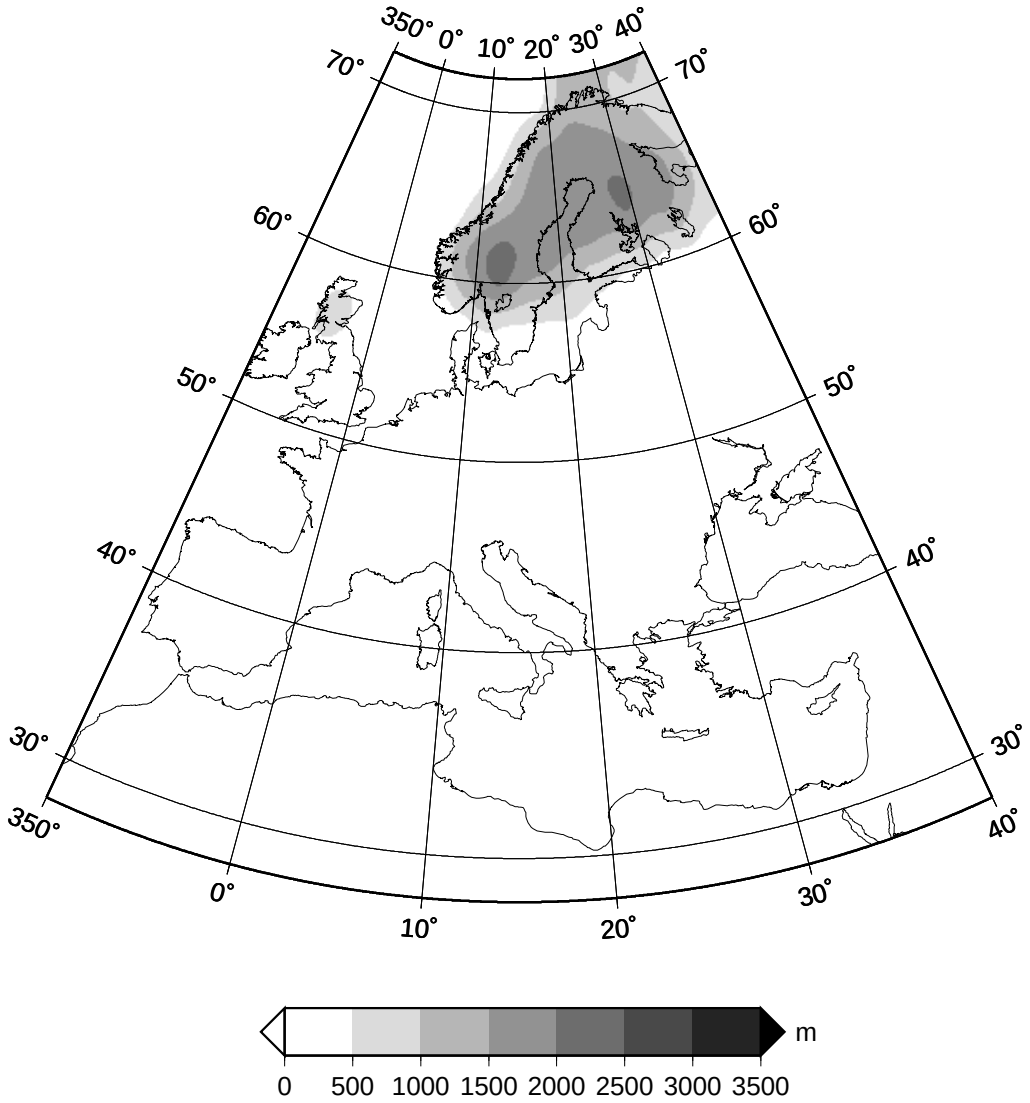

Figure 7.2: Position of the Fennoscandian and British components of the ICE3G model relative to the Mediterranean coasts.

Other investigations considered the interplay between tectonic and postglacial isostatic uplift in the central Mediterranean region (e. g., Pirazzoli et al. 1997; Lambeck 1995), and more remote regions, such as the coasts of Tunisia (Jedoui et al., 1998), and of Israel (Sivan et al., 2001). For a comprehensive review of the available Holocene observations, the reader is referred to Pirazzoli (1991) and Pirazzoli (1996). More recently, Pirazzoli (2003) compiled a collection of the existing investigations relative to the Mediterranean area, also including a discussion about eustatic, isostatic and tectonic contributions for a number of selected sites. Due to the relevance held by sea level variations in the context of the present–day climate change, recent geological and geomorphological investigations have been complemented by geodetic, palaeontological and archaeological evidence (Lambeck et al., 2004a). The latter have allowed us to better constrain the age of the paleo–sea level indicators available and to address the influence of tectonic motions upon the observed uplift. Quantitative interpretations of the data based upon global models of glacio–isostatic adjustment have been recently proposed by Lambeck and Purcell (2005), and Pirazzoli (2005).

7.2 Application of the PS method to the Mediterranean Sea

The need of an improved comprehension of both past– and present–day observed sea level changes along the Mediterranean coasts has motivated our study of the GIA related signatures. By means of our code for the solution of the SLE (see Chapter 5) we have investigated the effects of the melting of the Pleistocene glaciers on past and present–day observed sea level trends. A fundamental part of this work has regarded the collection and the revision all the available and updated observations concerning the sea level change in the Mediterranean (i. e. RSL curves, tide gauges time–series, and GPS vertical velocities). By analyzing and comparing the available data with the solutions of the Sea Level Equation for a Maxwell Earth we have

tested the sensitivity of RSL data to the melting of remote ice sheets (i. e., North America, Fennoscandia, Antarctica) and to the near field Würm Alpine glacier. Following the original work of Clark et al. (1978) we have investigated the existence in the Mediterranean Sea of regions characterized by similar RSL curves (see Figure 1.10). Furthermore we have tested the sensitivity of the observations to different values of the earth rheological parameters (i. e. lithospheric thickness and vertical viscosity profile), and to the time–history of the remote ice sheets. This latter task has been accomplished by modifying the pre–existing ice models on the basis of the Mediterranean evidences to obtain a revised and improved global ice chronology.

The following chapters describe the main published and submitted results of this investigation:

- Chapter 8 shows the study of the response of the Earth to the melting of the Würm Alpine glacier (Stocchi et al., 2005a; Stocchi et al., 2005b). In particular it describes the results of the computation of the glacio– and hydro–isostatic effects which affect the post–glacial RSL curves and the present–day vertical velocities in the Mediterranean basin,

- Chapter 9 concerns the investigation of the Clark's zones (Figure 1.10) in the Mediterranean Sea and describes the role of the remote ice sheets and of the Earth parameters (Stocchi and Spada, 2006) . In particular it focuses on the role of Antarctica and on the sensitivity of the Tunisian coast to this particular ice sheet,

- Chapter 10 describes the analysis of the sensitivity of the Holocene sea level record for SE Tunisia to the time–history of the Antarctic ice sheet. In particular, it shows that the mismatch between predictions and observations improves for a reduced and impulsive melting of Antarctica (Stocchi and Spada, 2007).

7.3 Methods

The present investigation has been carried out by means of code `SELEN` (Chapter 5) which solves the Sea Level Equation (Chapter 3) through the pseudo–spectral approach (Chapter 4). The following paragraph describes the general settings of the program and the input data that we have chosen in our investigations.

7.3.1 SLE solver configuration

Pixelization

We have kept the spatial resolution fixed to $r = 14$, which implies a global number of pixels of $N_p = 7292$ (Tegmark, 1996). The wet and dry pixels distribution over the Mediterranean area obtained for such resolution is shown in Figure 7.3. For the maximum harmonic degree of the expansions we have chosen a value of $l_{max} = 72$. This choice represents a good compromise in terms of resolution and CPU time.

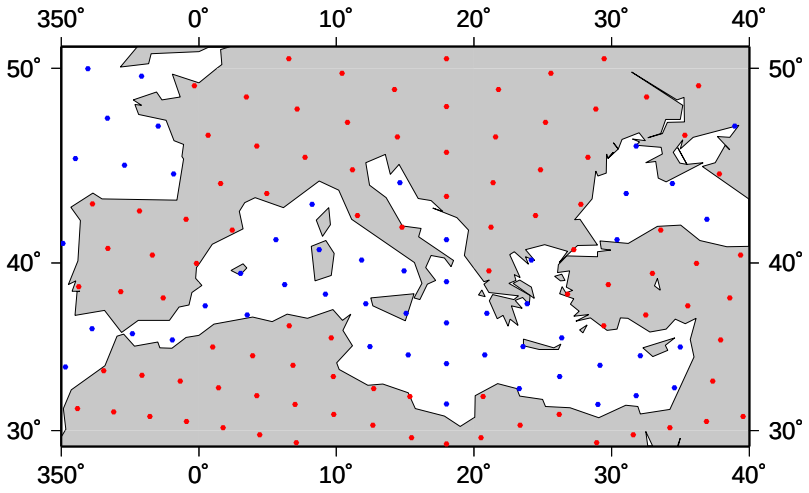

Figure 7.3: Wet (blue) and dry (red) pixels. See Figures 5.3 and 5.2 in Chapter 5 for the global distribution of pixels.

Ice models

In our investigations we have considered two distinct global ice sheets chronologies: ICE1 Peltier and Andrews (1976) and ICE3G Tushingham and Peltier (1991), shown in frames (a) and (b) of Figure 7.4, respectively, at the epoch of the Last Glacial Maximum (LGM, 18 kyrs BP). ICE1 describes the retreat of the northern Hemisphere ice sheets according to geological and geomorphological evidence, and stores $\sim$ 78 m of equivalent sea level (ESL) at the LGM (see Figure 7.4d, solid curve). Differently from ICE1, ICE3G has been built to improve the fit to the global RSL data in the near field assuming the REF rheological profile described in Table 7.3.1 (Tushingham and Peltier, 1991, 1992). While ICE1 assumes stationary southern Hemisphere ice masses, ICE3G accounts for the chronologies of Antarctica and South America, and consequently stores a larger water volume at the LGM, with an ESL of $\sim$ 113.5 m (see Figure 7.4d). The Antarctic component of ICE3G stores $\sim$ 28 m of ESL at the LGM and its volume is constant until 10 kyrs BP. Its deglaciation occurs between 10 and 5 kyrs BP, when the North American and the Fennoscandian ice aggregates had already lost most of their mass.

With the purpose of evaluating the sensitivity of the Mediterranean Clark zones to the time–history of remote Holocene ice aggregates, in the computations of Chapters 9 and 10 we have also considered alternative chronologies for the Antarctic ice sheet.

The spatially minor but important Würm Alpine glacier (see Figure 8.1) is considered in Chapter 8 (Stocchi et al., 2005a) were we have analyzed the effects of its melting on the Mediterranean sea level.

Earth model parameters

The Earth model employed in this work (REF rheological profile) has been previously introduced in Chapter 5 (see Table 5.2). As discussed above the value of the lithospheric thickness and the viscosity profile have been assumed by Tushingham and Peltier (1991, 1992) to build the ICE3G model.

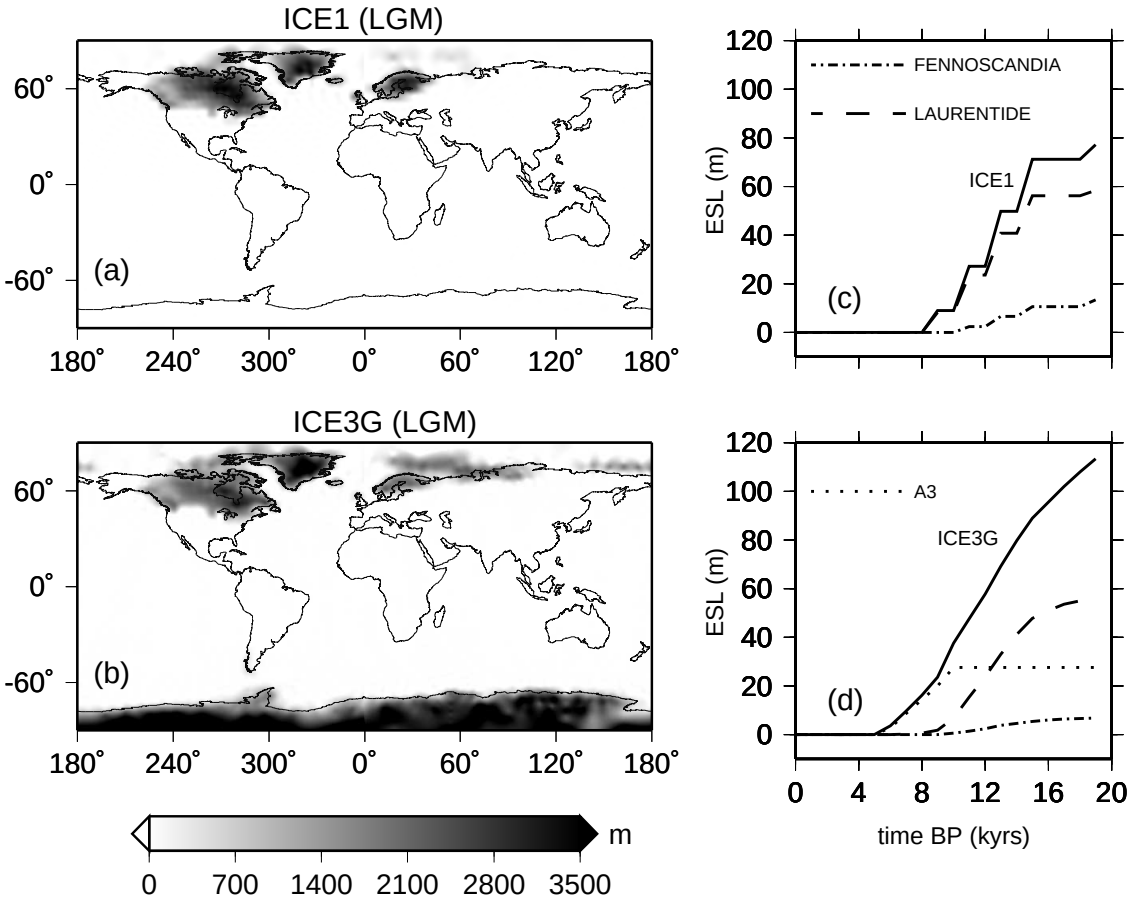

Figure 7.4: Global ice thickness distribution according to ICE1 (a) and ICE3G (b) at the Last Glacial Maximum. Frames (c) and (d) show the equivalent sea level (ESL) of ICE1 and ICE3G and of their largest components: Fennoscandia (dashed–dotted), North America (dashed), and Antarctica (A3, dotted, only included in ICE3G). Notice that in ICE1 and ICE3G the end of deglaciation occurs 8.0 and 5.0 kyrs BP, respectively.

SLE solution

The solution of the SLE has always been obtained for a number of iterations SMAX = 3 through the "gravitationally self–consistent" approach (IMODE=1 in *data.inc*, see Appendix C.1). For the computation of the ESL curves showed in Figures 7.4 and 9.8 the solution is obtained switching IMODE=3, which implies the eustatic solution (see Section 3.4 in Chapter 3).

Furthermore, in the analyses of Section 9.2.3 we have considered separately the ice– and ocean–load induced sea level variations. Following Mitrovica and Milne (2002), we write the total "reduced" sea level change as

$$Z = \mathcal{O}(S^{ICE} + S^{EUS} + S^{OCE}), \tag{7.1}$$

where S^{ICE}, S^{EUS} (see Eq. 3.34), and S^{OCE} account for glacio–isostasy, eustasy, and hydro–isostasy, respectively, with

$$S^{ICE} = \frac{\rho_i}{\gamma}\Big(G_s * I - \overline{G_s * I}\Big), \tag{7.2}$$

and

$$S^{OCE} = \frac{\rho_w}{\gamma}\Big(G_s * Z - \overline{G_s * Z}\Big) \tag{7.3}$$

where Z represents the solution of the SLE (4.2) in its complete form. As discussed in Mitrovica and Milne (2002), another measure exists of the ocean load–induced sea level variation, namely that arising from the meltwater loading in the total absence of ice–loading effects. Such 'hypothetical' sea level variation is computed assuming that the mass is added to the oceans from outside the Earth, rather than coming from a surface load (Farrell and Clark, 1976). Using $\rho_i = 0$ in (4.2), and indicating with Z^{HYP} the solution of the SLE so obtained, one gets

$$S^{HYP} = S^{EUS} + \frac{\rho_w}{\gamma}\Big(G_s * Z^{HYP} - \overline{G_s * Z^{HYP}}\Big) \tag{7.4}$$

that differs from (7.3), since the latter brings information about ice–loading effects through Z. Since S^{HYP} and S^{OCE} have largely similar patterns in the far–field of the former ice sheets (Mitrovica and Milne, 2002), in our ensuing discussion we have employed (7.3) as a measure of the ocean–load induced sea level change.

Chapter 8

Isostatic rebound following the Alpine deglaciation

8.1 Introduction

In all of the studies published so far, the RSL changes have been predicted by postglacial rebound models that account for the major ice–sheets at the last glacial maximum (LGM), i. e., the Fennoscandian, the Laurentian, the Greenland, and the Antarctica ice sheets (Denton and Hughes, 1981). However, a potentially important contribution to the Holocene and present–day vertical movements in the Mediterranean area could be played by the isostatic rebound caused by the melting of the Würm Alpine glacier (Pirazzoli et al., 1997; Lambeck and Bard, 2000; Stewart et al., 2000; Lambeck et al., 2004a). To date, the only study that explicitly modeled the effects of the Alpine ice sheet is by Gudmundsson (1994), who focused on the vertical movements in the Swiss Alps region. Despite of the simplified rebound model adopted, based on a flat–Earth approximation and on an axis–symmetric ice–sheet, the deformations computed by Gudmundsson (1994) indicate that, for a range of plausible rheological parameters, the Alpine deglaciation may significantly contribute to the geodetically determined present–day uplift rates of the Swiss Alps.

The results attained by Gudmundsson (1994) and the increased amount of observations, spanning from RSL to geodetic data, have justified the present investigation aimed to study the effects of Alpine deglaciation on a wide set of geophysical observables. Here we have abandoned the axis–symmetric load description to introduce a more realistic geometry, constrained by the geological and glaciological information. While the simplified disc load employed by Gudmundsson (1994) is certainly appropriate to describe the present–day postglacial deformations close to the center of the former Alpine ice–sheet, a more refined description was needed here since we were also concerned with the response of the solid viscoelastic Earth outside the load margins, where significant geophysical data are available.

The forward approach to the postglacial rebound problem would require two basic inputs: the chronology of the ice load imposed at the Earth surface and the rheological profile of the mantle. However, our knowledge of these inputs is seldom exact, so that it is generally by inverse approaches that we can get information about the ice chronology and the viscosity of the Earth mantle (Mitrovica and Peltier, 1995; Johnston and Lambeck, 2000; Cianetti et al., 2002). The purpose of this work was not to provide bounds on the extent and time history of the Alpine deglaciation nor to infer the rheology of the mantle. Rather, we have intended to use available geological evidence and a reasonable viscosity profile (REF rheological profile, see Table 5.2) to assess the relevance of the melting of the Alpine glacier on the Holocene and present–day deformations in the Mediterranean region, where the effects are expected to be the largest. We have accomplished this goal through a suite of forward computations (see Chapter 5) based on a spherically layered Earth model including both the Alpine glacier and the major Holocene ice sheets.

8.2 History of the Alpine glacier

With a width of ~ 600 km and a length of ~ 200 km, the Alpine glacier was the largest among the southern Europe local glaciers at the LGM. Other ice aggregates

of smaller extent partly covered the Pyrenees and other European mountain ranges (Denton and Hughes, 1981), but their reconstruction is still incomplete (Clapperton, 1995). In view of the scarce information about the advance and retreat of these secondary aggregates, and since most of the geophysical data currently available pertain to the central Alps and to the immediately surrounding coastlines, in the following we have restricted our attention to the combined effects of the Alpine glaciation and of the major remote Pleistocene ice sheets. Due to the linearity of the problem, the contribution from other glaciers have been computed separately and linearly added to the results presented here.

While the boundaries of the Alpine glacier at the LGM are quite well constrained, the thickness and the melting chronology are uncertain. According to the synthesis of Gudmundsson (1994) and to Florineth and Schlüchter (2000), the last phase of expansion prior to the LGM begun ~ 25 kyrs ago. Differently from Fennoscandia and other local European ice aggregates, the Alpine expansion was preceded by a ~ 30 kyrs long warm period during which the ice was limited to the central portion of the glacier. After LGM, the Alpine glacier has been characterized by a complex pattern of deglaciation. This has been well documented by geomorphological investigations in the Swiss Alps (Ehlers, 1996) and in the eastern Alps (Van Husen, 1997), which indicate alternate phases of advance and retreat of relatively short duration. The thickness of the Alpine glacier during the various phases outlined above is far from being completely reconstructed. As indicated by the available trimline data (Florineth and Schlüchter, 2000), the central Alpine ice cap showed a considerable complexity, characterized by several individual ice domes with a maximum thickness as large as 3000 m. It is recognized that the ice coverage at the LGM may have been characterized by a strongly variable thickness, with steep gradients and ice–free regions of considerable extent (Florineth and Schlüchter, 2000). While it appears plausible that the ice may have reached a thickness in excess of 1 km in the Alpine valleys, in the Alpine foreland the maximum ice thickness is unlikely to have exceeded few hundred meters (see Gudmundsson 1994).

The extent of the Alpine glacier at the LGM has been recently reviewed by Florineth and Schlüchter (2000) and is still the subject of active research.[1]

In the attempt to merge the available geological and geomorphological information, we have constructed the ice sheet model shown in Figure 8.1, hereafter referred as to model ALPS1. The contours of ALPS1, shown here at the LGM (i. e., during the Late Würm period, 20 to 18 kyrs BP), are consistent with those of Gudmundsson (1994), that are based on previous climatological and glaciological evidence (see Denton and Hughes1981 and Gudmundsson1994 and references therein). Each of the crosses in Figure 8.1 shows the centroid of the hexagonal finite elements used to discretize the Earth surface, as explained in Section 5.2. The black, gray and light gray crosses in Figure 8.1 show the thickness of each ice element at the LGM, being 1000, 500, and 250 m, respectively. To mimic the shrinkage of the glacier, these elements are subject to a constant rate of deglaciation, and disappear at 11, 12, and 13 kyrs BP, respectively. For ALPS1, we have conventionally placed the LGM at 18 kyrs BP, and we have assumed isostatic equilibrium prior to that epoch. To test the sensitivity of near–field sea level variations to the shape and to the chronology of the Alpine ice sheet, in some of the ensuing computations we have also considered an extremely simplified Alpine glacier (ALPS2) in which all the ice elements have a thickness of 500 m at the LGM (18 kyrs BP) and melt synchronously following a linear time–history until they disappear 12 kyrs BP. As for ALPS1, isostatic equilibrium prior to the LGM is assumed for ALPS2. The volume of ALPS1 and ALPS2 at the LGM is close to 0.09×10^6 km^3, i. e., roughly two times that employed by Gudmundsson (1994), who adopted a uniform thickness of 250 m for the simplified small-size disk load that was meant to be representative of the Swiss portion of the whole glacier.

In addition to the Alpine glacier, we have also included the major remote Pleistocene ice–sheets. Among the currently available chronologies, we have alternatively adopted ICE1 by Peltier and Andrews (1976) (see Figure 7.4 top), which is indepen-

[1] see http://www.skq.ch/IT/LGM.html.

dent from specific assumptions about the mantle viscosity profile (see also Spada, 2001) and ICE3G (Tushingham and Peltier, 1991), more accurate in reproducing the geometry and chronology of the ice aggregates (see Figure 7.4 bottom). The relatively coarse structure of ICE1 and ICE3G may constitute a problem if one is concerned with the response of the Earth at specific RSL or geodetic sites placed in the vicinity of the ice margins. This is not the case here, since the Fennoscandian ice–sheet is sufficiently distant from the region of interest.

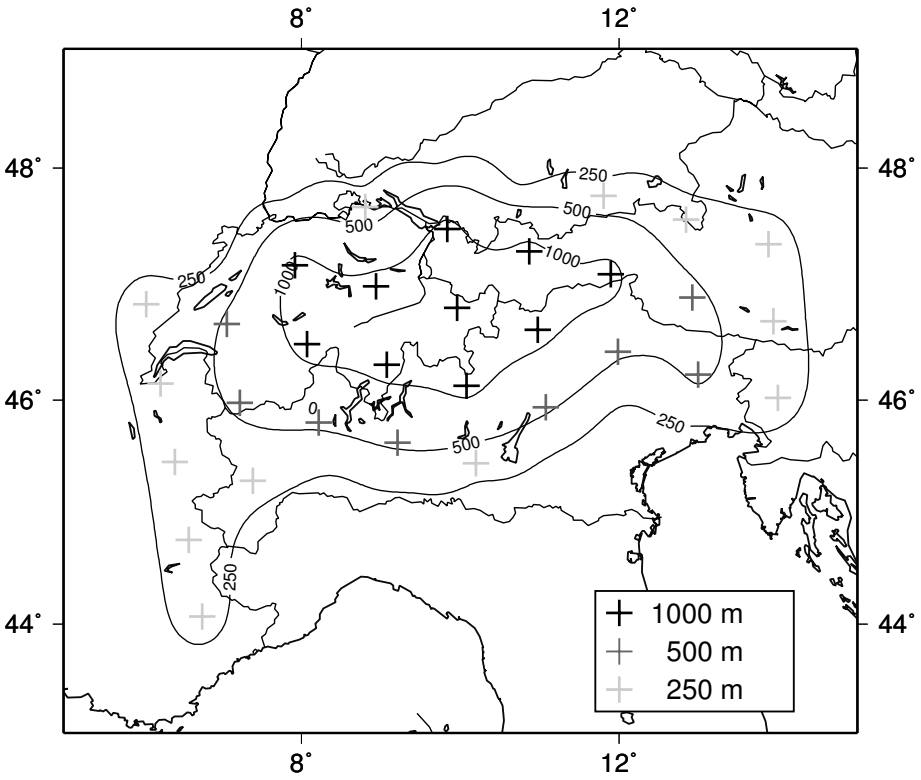

Figure 8.1: Contour lines showing the thickness of the ALPS1 model for the Alpine deglaciation at the LGM (e. g., 18 kyrs BP). The crosses show the centers of the single hexagonal ice elements that compose the aggregate, whose thickness is shown in the inset.

8.3 Results

8.3.1 Holocene sea level variations

The impact of the melting of the Alpine glacier on sea level changes in the Mediterranean Sea is shown in Figure 8.2, where we have employed the deglaciation model ALPS1 described above. Here and in the ensuing computations, the RSL curves are obtained by the solution of the SLE (Eq. 3.33) according to Eq. 3.63 (see Section 3.5). To focus on the effects of the small alpine glacier, the remote ice masses have not been included in our modelization at this stage. We have first considered the Mediterranean RSL sites included in the database of Tushingham and Peltier (1993), evidenced by the open circles of Figure 8.2a (see also Section 6.1). The predicted RSL curves, shown in Figure 8.2b, confirm the intuition that the melting of the Alpine glacier has had mainly a regional influence. In fact, amongst the sites considered here, the largest effects are predicted for the southern France sites of Marseilles and Roussillon, for Civitavecchia (central Italy), and Catania (Sicily). A monotonous sea level fall is predicted for the three Tyrrhenian sites, to indicate that the melting of the Alpine glacier has produced a significant uplift on a broad region spanning several hundreds of kilometers, that amounts to ~ 7.0 m and to ~ 3.5 m since the LGM for Marseilles and Civitavecchia, respectively. Although Roussillon and Civitavecchia are placed at comparable distances from the centroid of the former Alpine glacier (see Figure 8.2), the amplitude of the computed RSL are distinctly different in the two cases as a consequence of the non–axially symmetric contour of the glacier (see Figure 8.1). Since the actual geological observations clearly indicate a monotonous sea level rise both along the coasts of southern France and along the Tyrrhenian coasts of Italy (Schmiedt, 1972; Lambeck and Bard, 2000), from the results of Figure 8.2b we have concluded that if the chronology employed here for the Alpine glacier is correct and the viscosity profile of the mantle that we have adopted is appropriate for this region, the melting of the Würm Alpine glacier has counteracted the general Holocene sea level rise that is observed in this region. In

the case of Catania (Sicily) we have predicted a monotonous sea level rise of ~ 1 m since the LGM, that can be mainly attributed to the collapse of the small peripheral topographic bulge associated with the Alpine glacier.

As shown in Figure 8.2b, in the remaining sites of the Mediterranean area, the sea level variations driven by the melting of the Alpine glacier ALPS1 have been much less pronounced than in southern France and central Italy and in some case characterized by a non–monotonous behavior. An absolute RSL variation of less than 1 m is predicted at all of these sites since the LGM.

Due to the proximity of the former Alpine glacier, we expect that sites along the coasts of the northern Adriatic sea have been affected to some extent by the Alpine deglaciation (see Figure 8.1). A precise assessment of postglacial sea level variations at these sites is particularly important in view of efforts aimed to separate natural and anthropogenic movements on a secular scale in this area (see e. g., Carminati and Didonato, 1999). This issue is addressed in Figure 8.2c, where we have focused on the predictions of long–term RSL variations for three relevant sites of the Adriatic Sea, namely Venice, Trieste, and Porto Corsini (these sites are marked by stars in Figure 8.2a). According to the results shown by solid lines, the melting of ALPS1 has produced a monotonous sea level fall at these three sites. The effect is significantly enhanced with respect to southern France (see Figure 8.2b), with ~ 30 m for Venice and ~ 20 m for Porto Corsini and Trieste since the LGM. To test the sensitivity of the computed RSL curves to the shape and to the chronology of the Alpine aggregate, we have also shown in Figure 8.2c the results obtained using the uniform–thickness ice model ALPS2 (dashed curves). The introduction of ALPS2 has the effect of slightly diminishing the sea level variations: the RSL curve for Venice is roughly scaled by 15%, while for Trieste and Porto Corsini the effect is close to 5%, showing that the sensitivity to the geometry and chronology of the Alpine ice load is moderate even at this near–field sites. Since Holocene RSL data analogous to those available for southern France are not at our disposal, the computations that we have done here have merely an illustrative character. However, it is clear from these results that

the melting of the Alpine glacier has mitigated the postglacial rise of sea level in northern Adriatic. Judging from Figure 8.2c, this reduction has been between 1 and 2 m since the end of the melting of the Holocene ice–sheets, that occurred 5 kyrs ago according to the chronology of model ICE3G (Tushingham and Peltier, 1991). The role of the melting of the Alpine glacier in this region will be further addressed in Section 8.3.2, that is devoted to the present–day sea level changes.

The analysis of Figure 8.2 supports the observations by Lambeck et al. (2004a), who suggested that in the last 12 kyrs the contribution to sea level change from the melting of the Alpine glaciers could have been potentially significant only for the northern Mediterranean sites. However, the RSL variations effectively observed along the coast of the Mediterranean Sea stem from the contribution of all the ice sheets active during the Holocene. To study quantitatively how the melting of the Alpine glacier could have interfered with the action of the remote ice sheets and to analyze the sensitivity of the available RSL data to uncertainties in the global ice sheets distribution, we have considered the results of Figure 8.3. Here we present RSL predictions for the sites Roussillon, Marseilles, and Civitavecchia that, according to Figure 8.2b, are mostly affected by the melting of the Alpine glacier. The chosen time window is large enough to include all the RSL data available in the database by Tushingham and Peltier (1993) along with their uncertainties.

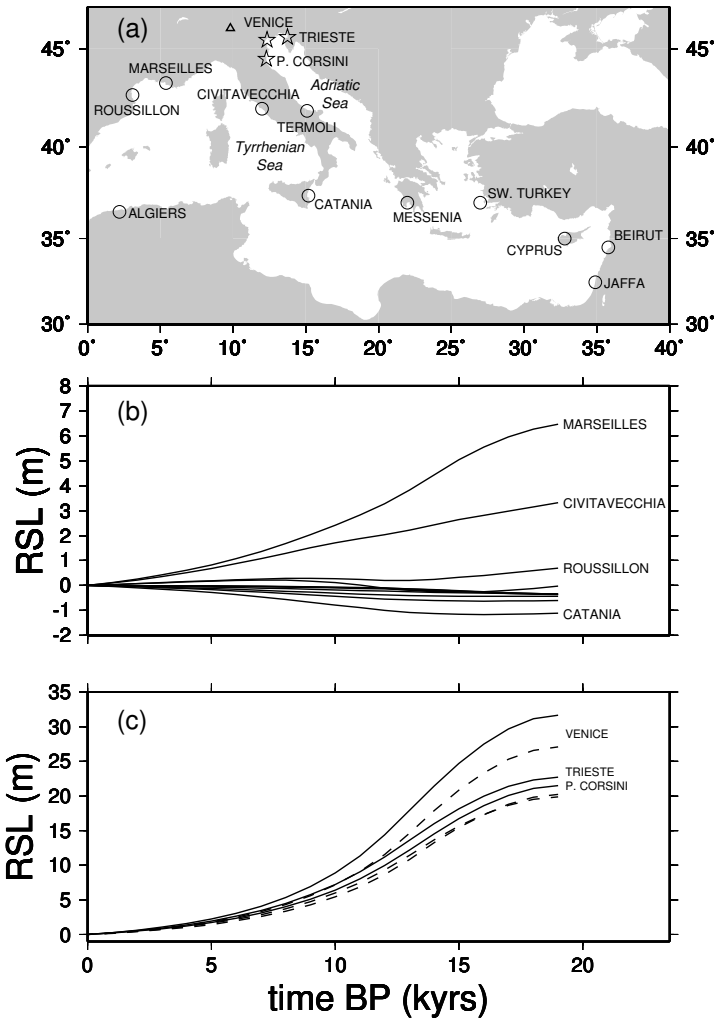

Figure 8.2: (a): the circles show the Mediterranean RSL sites included in the database by Tushingham and Peltier (1993). Three relevant northern Adriatic sites are marked by stars. The triangle shows the centroid of the former Alpine glacier. Frames (b) and (c): predicted RSL curves for sites marked with circles and stars, respectively. In both cases, solid curves only account for the effects of the Alpine glacier ALPS1. Dashed lines in (c) portray the results obtained using model ALPS2.

Dashed lines in Figure 8.3 portray the RSL curves predicted for model ICE3G, while those that account for the combined effects of ICE3G and ALPS1 are depicted by solid curves. As shown in Figure 8.3a for Roussillon, the eustatic portion of the RSL curve is dominated by the effect of the remote ice sheets that compose ICE3G, very large in comparison to the small size of the Alpine glacier. Furthermore the inset of Figure 8.3a evidences that the sensitivity to the melting of ALPS1 is modest since 5 kyrs BP, the time that marks the end of deglaciation for ICE3G (compare dashed with solid curves). Although this sensitivity is more enhanced when the RSL sites of Marseilles and Civitavecchia are considered (Figure 8.3b and 8.3c), both the ICE3G and the ICE3G+ALPS1 predictions fall within the error bars of the available RSL data. It is remarkable that, since the LGM, the melting of ALPS1 appears to produce significant variations of the steepness of the RSL curves relative to Marseilles and Civitavecchia, thus suggesting a possible role of the rebound driven by the Alpine glacier on the present–day sea level changes at these locations (this issue will be addressed in Section 8.3.2 below).

The results shown by dash–dotted curves in Figure 8.3 pertain to the combined effects of the ICE1 and ALPS1 models. The rough time discretization of ICE1 compared to ICE3G is responsible for the saw–tooth behavior of the RSL curves during the phase dominated by the eustatic sea level rise (see Figure 8.3a). Two features are noticeable. First, comparing solid with dash–dotted curves, we observe that a variation of the global structure of the ice load produces effects that largely exceed those produced by the glacier ALPS1 on the three RSL sites considered in Figure 8.3. Second, for the French sites, we observe that predictions based on model ICE1+ALPS1 well agree with the observed monotonous sea level rise that is supported by all of the data sets currently available in this region since the LGM (Morhange et al., 2001; Lambeck and Bard, 2000). This shows the inadequacy of ICE3G to model the RSL curves relative to southern France, a feature that is shared with the more recent global chronology ICE4G (Peltier, 1994), as already evidenced by Morhange et al. (2001). In the case of Civitavecchia, both the ICE1 and ICE3G

predictions agree with the available datum, that indicates a sea level rise of ~ 50 cm in the last 2 kyrs. Recent investigations based on archaeological evidence in the central Mediterranean however indicate a significantly larger sea level change at this site since 2 kyrs BP, close to 1.4 m (Lambeck et al., 2004b).

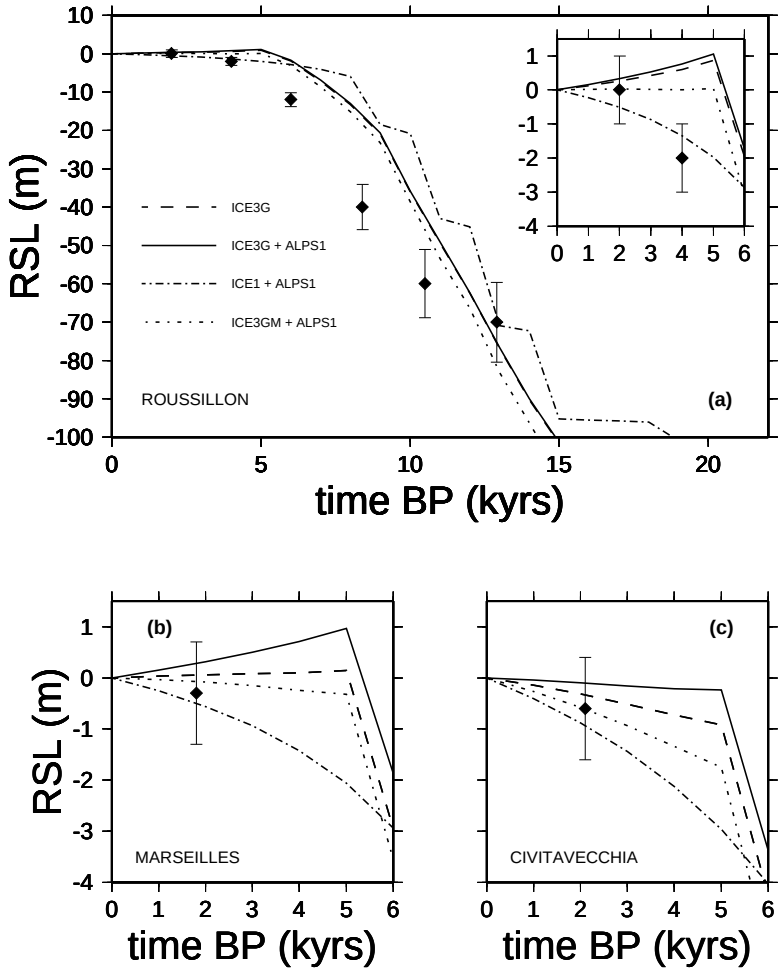

Figure 8.3: Observed and synthetic RSL curves for Roussillon (a), Marseilles (b), and Civitavecchia (c) (see Figure 8.2a). The predictions have been performed using four distinct ice aggregates, as described in the inset of the top frame.

In an attempt to understand the reasons for the disagreement between observations and predictions obtained using ICE3G in southern France, we have performed further computations in which the Fennoscandian portion of ICE3G has been replaced by that of ICE1. The deglaciation model so obtained is denoted by ICE3GM. The results show that when this hybrid ice model is employed, the synthetic RSL curves do not show the clear decreasing trend exhibited by ICE3G, but rather a stationary (Roussillon) or marginally increasing trend (Marseilles). This supports the idea that the anomalous trend of the RSL curves in southern France is to be at least partly attributed to the chronology of the Fennoscandian sub–aggregate of ICE3G.

A further point concerning the differences in the predictions obtained by ICE1 and ICE3G is addressed in Figure 8.4, where the RSL curves for Roussillon, Marseilles, and Civitavecchia have been obtained using Eq. (3.63) with $S = S^{OCE}$, where S^{OCE} (see Eq. 7.3) is the sea level change arising from the deformation and gravitational effects due to the loading of ocean meltwater in the total absence of ice–loading effects Mitrovica and Milne (2002). The term S^{OCE} thus represents the sea level variation that we would observe if the meltwater were gradually transferred into the ocean basins from a source placed at an infinite distance from the Earth instead of coming from the vanishing ice–sheets (see also Farrell and Clark, 1976). The results show that in the three sites considered the ocean load produces signals of varying amplitude, with predictions based on ICE3G+ALPS1 in excess to those pertaining to ICE1+ALPS1 due to the larger volume of the former. However, in both cases, the RSL curves indicate a sea level fall and share a similar trend. This is not the case when the effects of the ice load are accounted for as done in Figure 8.3, where both the amplitudes and the trends of the RSL curves depend significantly from the ice load employed (compare solid with dash–dotted curves). This shows that, despite of the distance from the centers of the remote ice aggregates, the ice–load term (and particularly its Fennoscandian component) is the major cause of the distinct RSL trend obtained in this region when the two chronologies are considered.

From the results of Figure 8.3 and Figure 8.4 we can estimate that the contribution of the meltwater accounts for about 1/3 of the observed discrepancies between ICE3G and ICE1 in these Mediterranean sites since 5 kyrs BP.

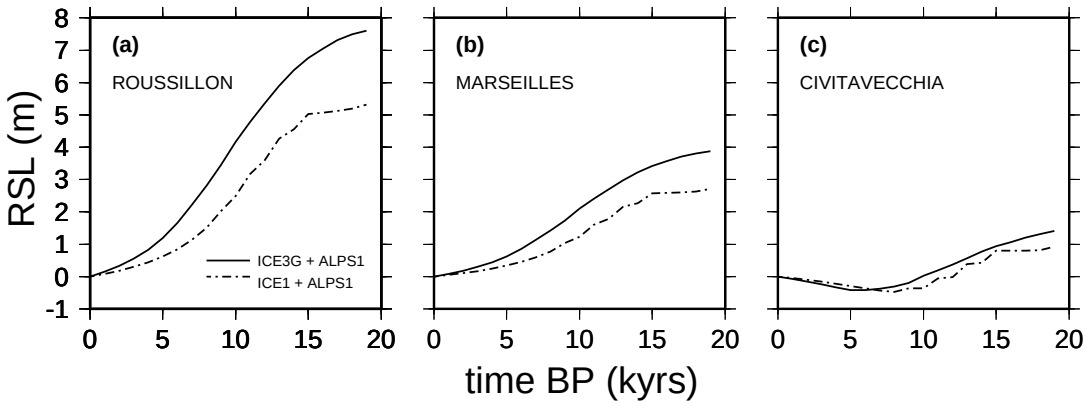

Figure 8.4: RSL predictions for the three sites of Roussillon Marseilles, and Civitavecchia when the ice load is completely neglected. See text for further details.

To complete our analysis, in Figure 8.5 we have considered the remaining subset of Mediterranean RSL curves available in the database of Tushingham and Peltier (1993). Due to the large distance between the former Alpine glacier and these sites, we do not observe any significant effect on the RSL curves neither on their steepness at present time (compare dashed with solid curves). Furthermore, the offset between (ICE3G+ALPS1) and (ICE3GM+ALPS1) markedly tends to decrease with increasing distance from the Fennoscandia ice aggregate. This indicates that the RSL curves at these sites are mostly determined by the chronology and large–scale structure of the deglaciation model ICE3G, that also shows a better overall fit with the available observations. Significant differences in the predictions based on ICE1 and ICE3G are visible in the whole set of frames.

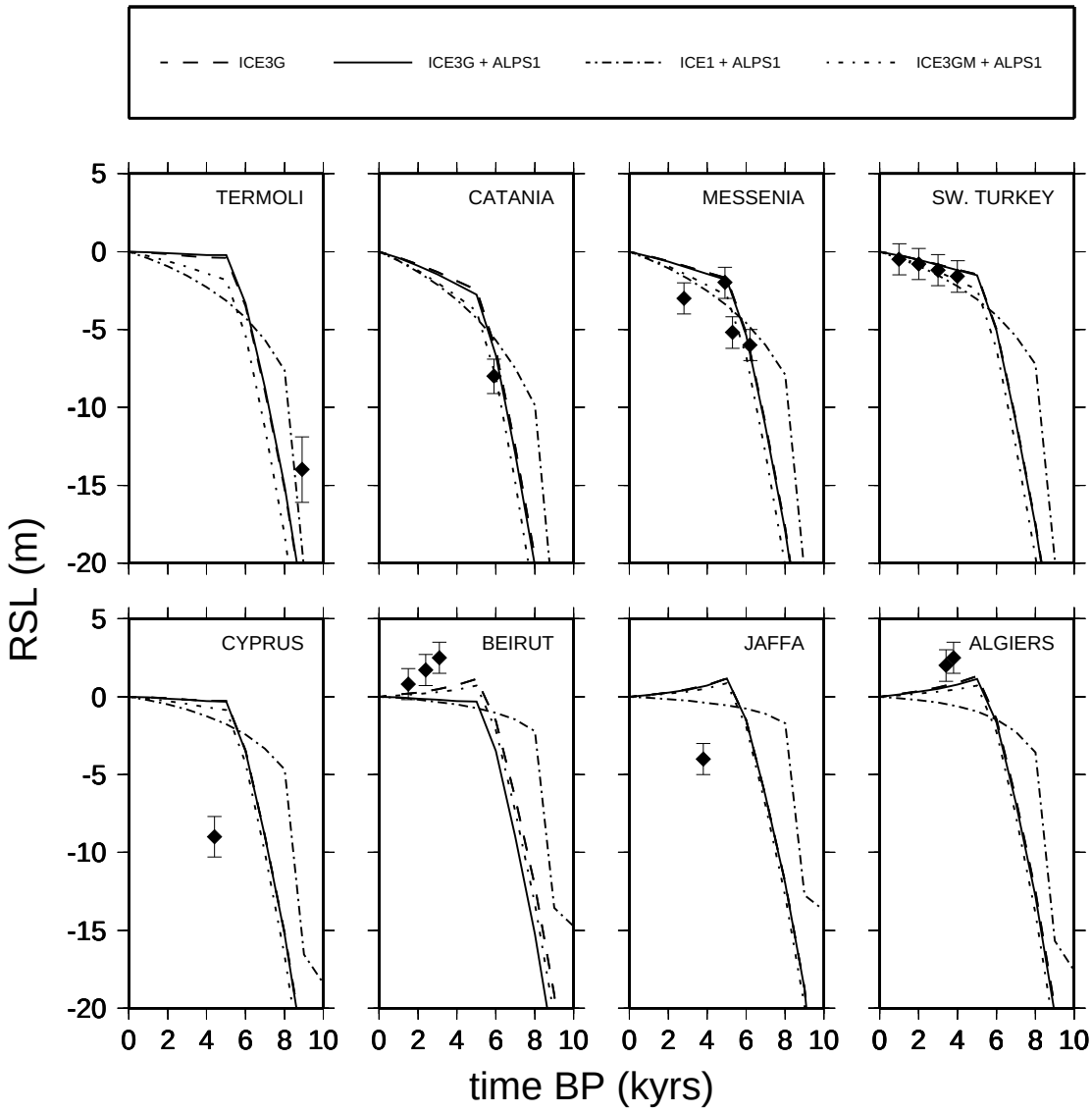

Figure 8.5: Observed and synthetic RSL curves for the other sites contained in the Peltier RSL database (see Figure 8.2a). The frames are ordered clockwise from Termoli (Italy) to Algiers. The same models of Figure 8.3 have been employed.

8.3.2 Present–day sea level change and crustal movements

The analysis of the previous section has suggested that the melting of the Alpine glacier may play a role in the present–day land movements and sea level changes in the Mediterranean area. This has been guessed by looking at the sensitivity of the steepness of the RSL curves to the imposed surface loads (see in particular Figure 8.3 above). More quantitative results are reported in Figure 8.6, showing from top to bottom the rate of sea level change expected in the Mediterranean area in response to the melting of the ALPS1 ice load alone (a), of ICE1+ALPS1 (b), and of ICE3G+ALPS1 (c), respectively. Frame (d) shows the rate of sea level change along the A1–A2 arc depicted in frame (a).

The rates have been computed by time–differentiation of the solution of the SLE (see Eq. 3.64). The signal associated with ALPS1 is negative (indicating a sea level fall) across a nearly–circular region with a radius of $\sim$ 800 km centered on the former ice load (this can be better appreciated in frame (d)). A negligible sea level rise is predicted outside this region. The sea level fall associated to the melting of the Alpine glacier is substantially due to the ongoing postglacial uplift in this region. An explanation for the considerable extent of the uplift region is given below. When the effects of the remote ice aggregates ICE1 and ICE3G are included (middle and bottom frames, respectively), the trends of the rate of sea level change show similar patterns on a Mediterranean scale, characterized by a maximum of about 0.4 mm/yr southeast of Italy, and by a significant spatial variability (see also frame d). When ICE3G+ALPS1 is employed, negative sea level trends are predicted in the northern Adriatic sea and along the coasts of southern France. As it can be deduced by Figure 8.3, the melting of the Alpine glacier enhances the sea level fall in these regions, that is also predicted when ICE3G alone is employed.

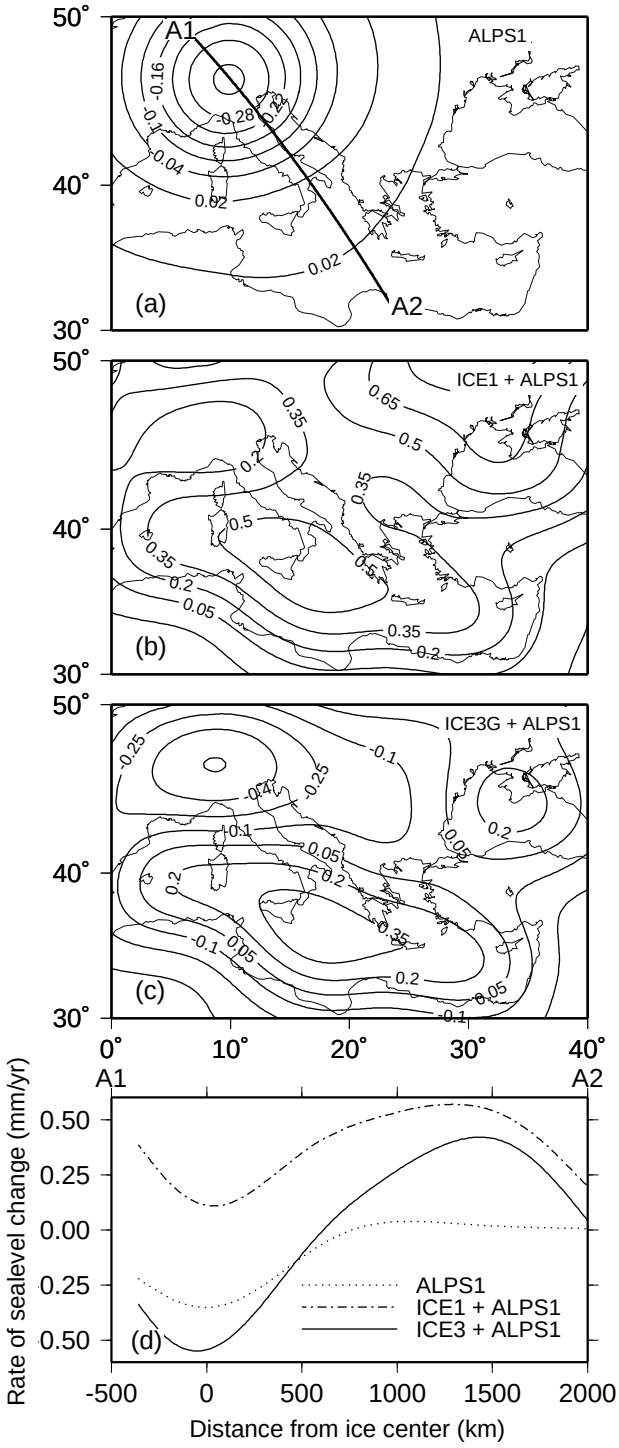

Figure 8.6: Predicted present–day rate of sea level change in the Mediterranean region when the melting chronologies of ALPS1 (a), ICE1+ALPS1 (b), and ICE3G+ALPS1 (c) are employed. Frame (d) shows the results projected along the arc A1–A2 shown in (a).

In Figure 8.7 we show predictions of the present–day rate of sea level change at specific PSMSL sites (see Section 3.5) along the coasts of the Mediterranean Sea. We have only considered sites for which at least four decades of data are available, so that the observed sea level trend from these sites is expected to be representative of actual secular trends. The predictions based on ICE1+ALPS1 and ICE3G+ALPS1 (solid lines) are characterized by opposite signs, and in both cases they poorly explain the available data. The glacially–induced sea level variations have a distinct long–wavelength character, that is in contrast with the spatially varying tide–gauge observations. This points to a significant role of local effects, that are particularly evident for Venice, where anthropogenic vertical movements are indeed important (e. g., Carminati and Didonato, 1999). It is noteworthy that for Venice the melting of the Alpine glacier counteracts the observed sea level rise (see the dotted curve and Figure 8.6a). When the deglaciation model ALPS2 is considered (dashed lines), the predicted rates of sea level change are only slightly modified at all of the sites considered, showing that the observations made at these sites are not significantly affected by the shape and melting time–history of the glacier.

Once the SLE is solved for S (see Eq. 3.33), and thus the gravitationally self–consistent ocean load is determined, other geophysical observables such as the vertical displacement U and the variations in the geoid height N can be easily obtained. The first can be computed according to $U = \rho_i \, G_u * _i I + \rho_w \, G_u * _o S$ (Eq. 3.65), where G_u is the Green function appropriate for vertical displacement. A similar expression holds for N, with G_u substituted by the geoid Green function G_g. The fundamental relationship $S = N - U$ (Eq. 3.4) exists between sea level change, the vertical uplift, and the geoid height change (e. g., Mitrovica and Milne, 2002). The uplift rate $\dot{U}$ in the Mediterranean region is shown in Figure 8.8 for the three different ice aggregates already considered in Figure 8.6.

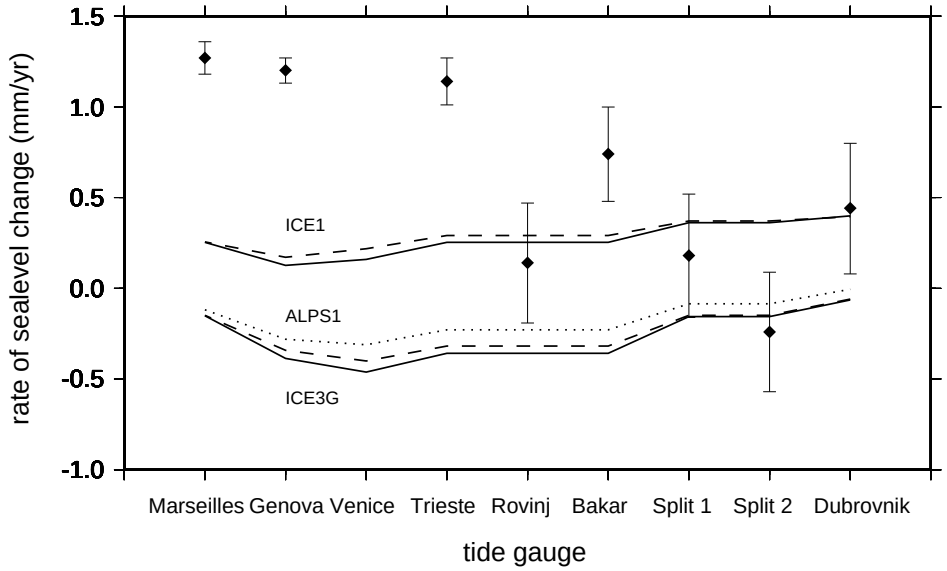

Figure 8.7: Present–day rate of sea level change at nine PSMSL sites located in the northern Mediterranean area. The dotted curve shows the predictions based on model ALPS1, while for the solid ones we have also included the contribution of the remote aggregates ICE1 and ICE3G. The dashed curves show the results obtained when the deglaciation model ALPS1 is substituted by ALPS2. The datum of Venice (2.40 ± 0.16 mm/yr) falls out of scale.

In the proximity of the former Alpine ice–sheet, we observe an uplift rate pattern that closely matches that of $-\dot{S}$ shown in the top frame of Figure 8.6, that implies a rate of geoid change $\dot{N} \sim 0$ (compare also frames (d) of these two figures). This is in general to be expected in the near field of the former ice loads, where the topographic contribution $\dot{U}$ to the sea level changes dominates. Since the Mediterranean region is in the far field with respect of the major Pleistocene ice sheets, we expect a significant contribution of $\dot{N}$ to the predicted rates of sea level change when the ice aggregates ICE1+ALPS1 or ICE3G+ALPS1 are considered. This is confirmed by the results of Figure 8.8. In particular, comparing Figure 8.8c with the corresponding frame of Figure 8.6, we notice the rate of geoid change accounts for a large fraction of the

rate of sea level change, with $|\dot{N}| \simeq \dot{S}/2$ in the central portion of the Mediterranean region. A similar result is obtained when ICE1+ALPS1 is considered (Figure 8.8b).

A noticeable feature of Figure 8.8a is the broad region of uplift caused by the melting of the small Alpine ice–sheet, that extends as far as southern Italy. To understand the physical reasons of this uplift pattern, we have considered a simplified axis–symmetric rebound model, in which an ice–load with parabolic profile has a constant height until 18 kyrs BP, and then melts at a constant rate until it disappears 6 krs BP. Here we mantaine the same rheological profile, and to focus on the basic physics of the problem, we do not account for the gravitationally self–consistent ocean load. The computations have been performed using a recently published public domain software (Spada et al., 2004), that has been benchmarked against independent methods.[2] The results are shown in Figure 8.9, where frame (a) shows the lateral extent β of the region of present–day uplift as a function of the half–amplitude of the load, α. The thickness T_{LGM} of the load at the LGM (18 kyrs ago) is imposed to scale with α, with $T_{LGM} = 3500$ m for $\alpha = 15^\circ$ km (this load has a size comparable with that of the Laurentian ice dome at its maximum extent). It is clear from frame (a) that, for a small glacier, the size of the uplifting region sensibly exceeds that of the ice load, in qualitative agreement with the results obtained above in Figure 8.8a in the case of the Alpine glacier, characterized by $\alpha \simeq 2.5^\circ$. With increasing α, the ratio β/α approaches unity (dashed line). The anomalously large β values obtained for small α can be explained observing that the vertical deformations induced by a small load are mostly determined by the properties of the uppermost portions of the mantle, that behaves elastically according to our assumptions. The load is supported by the lithosphere, that bends over large distances and promotes uplift regions of large extent at present time. Conversely, when the size of the load is large if compared to the thickness of the lithosphere, the viscoelastic properties of the mantle dominate, and the deformations are focused on a narrower range, that decreases the ratio β/α.

[2] http://geo.mff.cuni.cz/gia–benchmark/results.html.

According to the results of Figure 8.9, for extremely large values of α, the spatial scale of the present–day uplifting region reflects the size of the former ice sheets, the elastic lithosphere being almost transparent at large wavelengths.

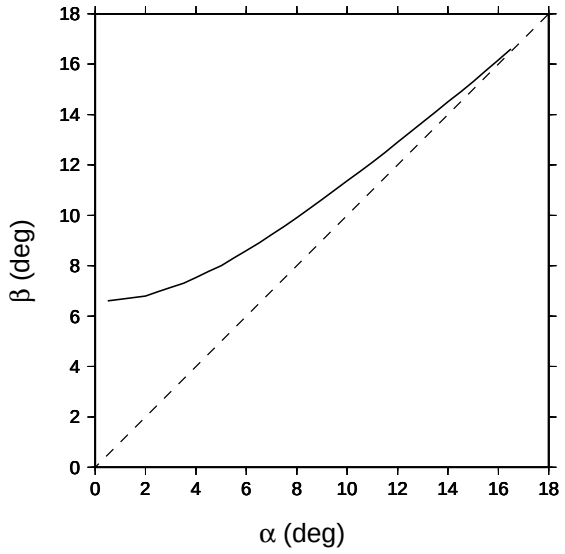

Figure 8.9: Half amplitude β of the region of uplift as a function of the half–amplitude α of the disk load according to the semplified rebound model described in the text.

From Figure 8.8, it is noteworthy to observe that the vertical motions in the Alpine region vary significantly according to the remote ice aggregates. The subsidence expected for ICE1+ALPS1 (Figure 8.8b) is turned into uplift when ICE3G is employed (Figure 8.8c). This finding may have an impact on the interpretation of vertical motions detected in the Alpine region, and may possibly hinder attempts to separate the glacio–isostatic from tectonic contributions. As a specific example, we consider the observations made by the permanent GPS REGAL network and by other European national institutions, that are available from the REGAL web site.[3] Here we only consider the vertical datum, since from a suite of test computations

[3]http://kreiz.unice.fr/regal/.

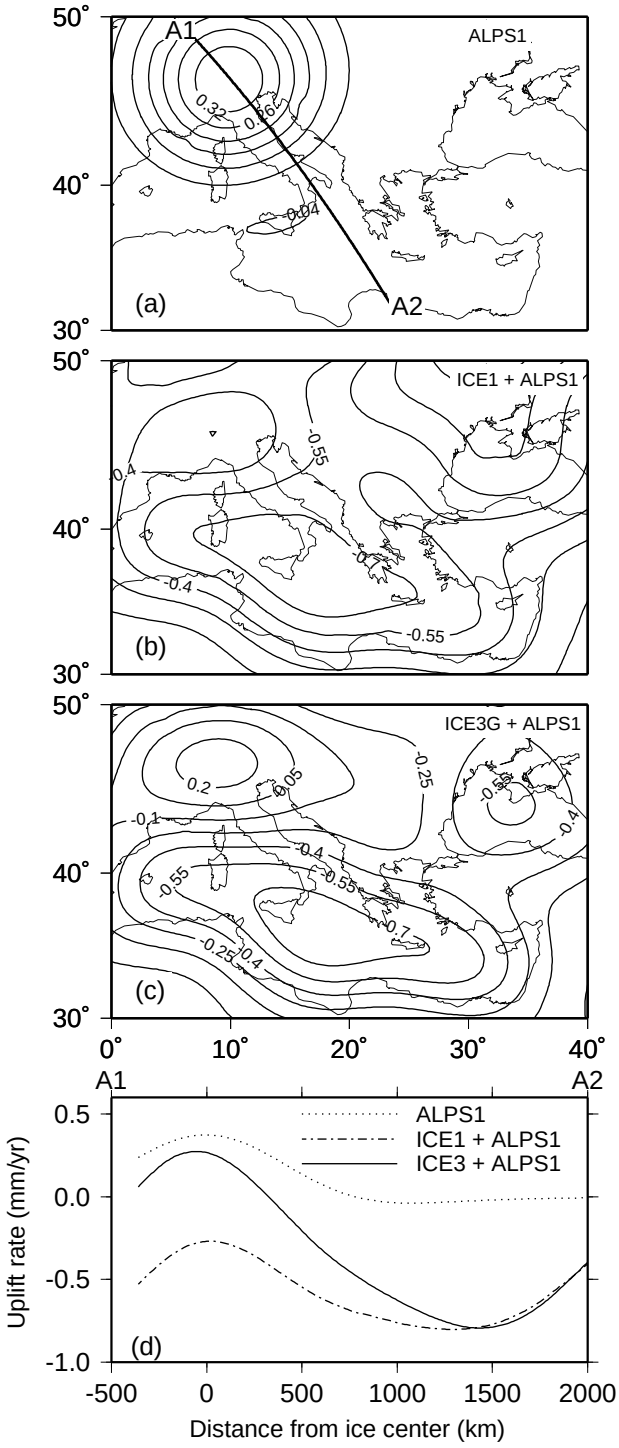

Figure 8.8: Predicted present–day uplift rate of the solid Earth in response to the deglaciation models ALPS1 (a), ICE1+ALPS1 (b), and ICE3G+ALPS1 (c), respectively. In frame (d) the uplift rates have been drawn along the arc shown in (a).

we have verified that in this region the typical GIA–induced rates of horizontal deformations do not exceed 0.15 mm/yr, negligible in front of the observed velocities, that range between 3 and 5 mm/yr when corrected for the motion of the Eurasian plate (Vigny et al., 2002). The reason for the small GIA– induced horizontal motions can be explained by their peculiar pattern, characterized by a vanishing amplitude close to the center of the rebound, and by a maximum close to the periphery of the ice load, where divergent motions are expected (see e. g., Spada, 2001). The large distance from the location of the former Fennoscandian ice dome of most of the stations of the REGAL network, their vicinity to the center of the Alpine ice–sheet, and the small size of the latter, are all factors that concur to produce very modest rates of postglacial horizontal deformation in the Alpine region.

The vertical velocity data, shown in Figure 8.10 along with their uncertainties, indicate the existence of two broad regions dominated by uplift and subsidence, respectively. The first (hereafter region I) encompasses the western portion of the Alps and the conterminous regions (black arrows), while the second (region II) mainly includes the Italian peninsula and the coasts of southern France (gray arrows). From inspection of Figure 8.8, we observe that this pattern qualitatively agrees with the predictions based on the deglaciation model ICE3G+ALPS1, while it is in contrast with that based on ICE1+ALPS1, that shows subsidence in region I. The measured rates of deformations are as large as a few millimeters per year at some sites, considerably larger than the values expected from the melting of the ice sheets (see Figure 8.8) in both regions.

A more quantitative analysis is shown in Figure 8.11, where the GPS observations for regions I and II are compared with the predictions based on the same three ice models considered in Figure 8.8. The x–axes of this figure report the names of the stations, ordered for increasing East longitude. For both regions, the long–wavelength signals associated with the postglacial rebound are in contrast with the observed trends, that show a larger spatial variability. If the melting of the Alpine glacier were the only source of deformation, it would produce an average uplift

at the level of 0.1-0.2 mm/yr of the GPS stations of both regions. When model ICE3G+ALPS1 is employed in region I (Figure 8.11a), the glacial isostatic adjustment is expected to produce an effect that averages to zero, while ICE1+ALPS1 produces a spatially uniform subsidence close to 0.4 mm/yr in the whole region, that has the tendency to counteract the observed uplifts. In region II (Figure 8.11b), both ICE3G+ALPS1 and ICE1+ALPS1 drive subsidence, coherently with most of the GPS observations in this area.

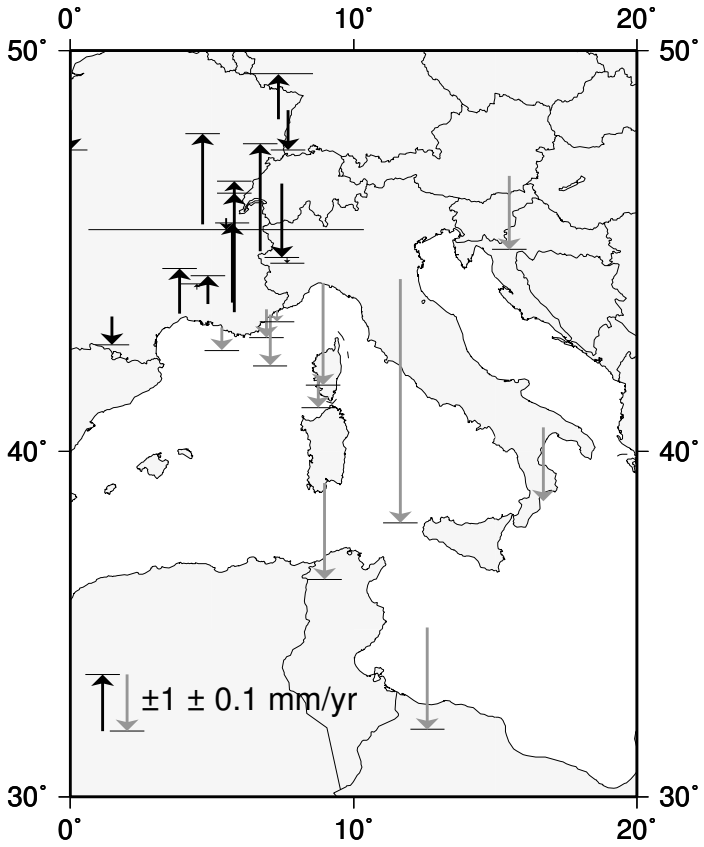

Figure 8.10: Vertical component of velocity field at some of the REGAL GPS network sites. Black and gray arrows show the data pertaining to regions I and II, respectively (see text for further details).

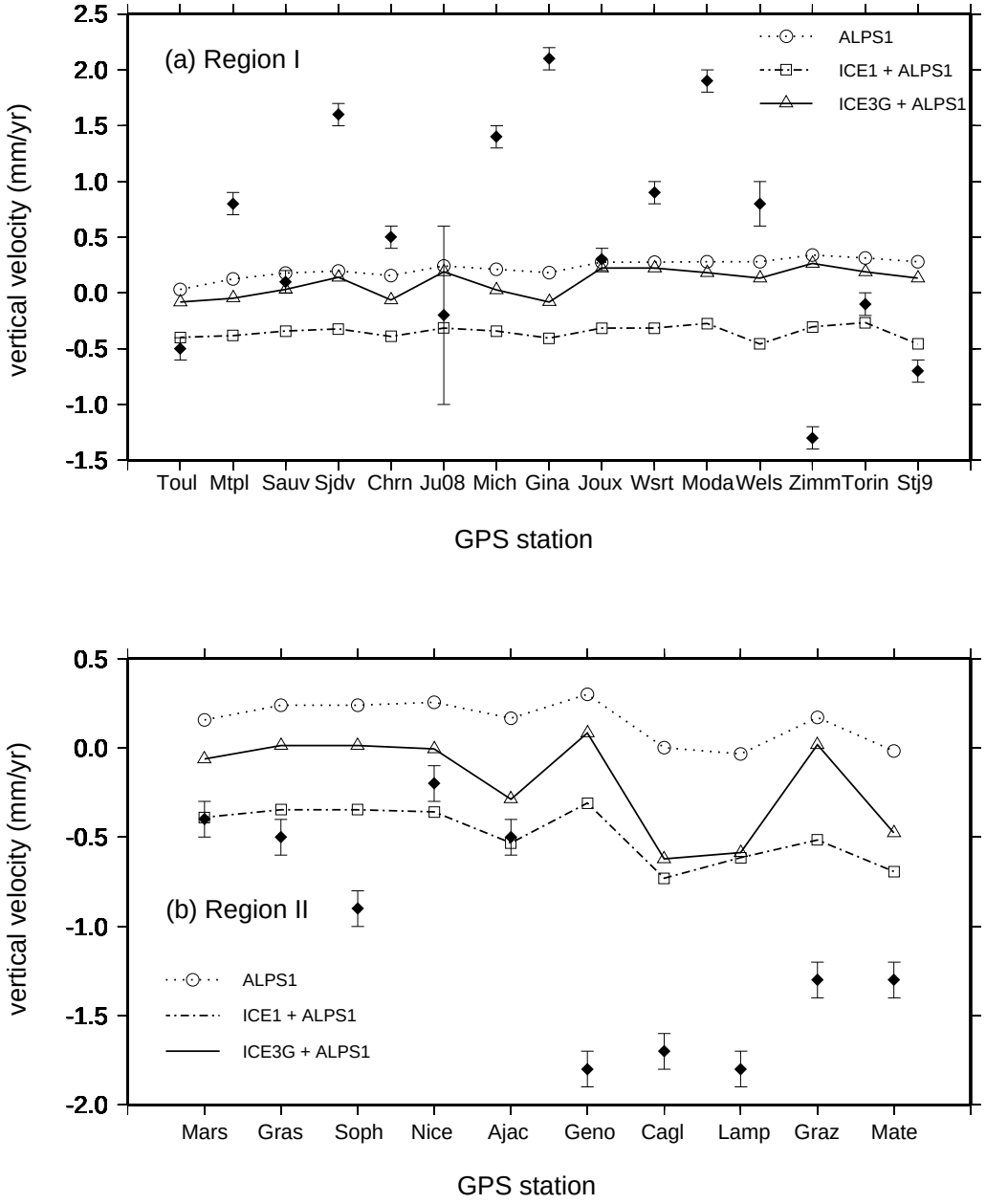

Figure 8.11: Predictions of glacially–induced uplift rate at the REGAL network sites (see Figure 8.10). Frames (a) and (b) refer to regions I and II, respectively.

8.4 Conclusions

In this work we have analyzed the effects of the melting of the Alpine glacier on a suite of geophysical observations across the Mediterranean Sea. Up to now, these observations were solely interpreted in terms of tectonic deformations, of glacially–induced movements associated with the melting of remote ice sheets, and anthropogenic effects. Our findings can be summarized as follows.

1. The melting of the Alpine glacier has mainly affected the Holocene sea level variations at the sites of Marseilles and Civitavecchia, with sea level falls of ~ 7 and ~ 3.5 m since the LGM, respectively. Minor effects are predicted for the other sites of the Mediterranean. When the postglacial RSL variations at Roussillon, Marseilles, and Civitavecchia are considered, we have found that it is not possible to resolve the effects of the melting of the Alpine glacier, mainly because of the large data uncertainties and to the small glacial mass involved. From a suite of forward computations, we have verified that the RSL data are by far more sensitive to the time–history of the remote ice sheets than to the melting of the former Alpine glacier. In particular, we have confirmed previous findings suggesting the inadequacy of the deglaciation model ICE3G to model the southern France data of postglacial RSL curves, and we have evidenced that the failure of ICE3G may be mostly attributed to its Fennoscandian component.

2. Due to the delayed postglacial uplift, the melting of the Alpine glacier is presently driving a sea level fall as large as 0.1–0.3 mm/yr along the coasts of southern France and of the northern Adriatic Sea. However, as previously observed, a correct estimate of sea level rate change in these areas cannot be obtained by means of the deglaciation model ICE3G, which also fails in predicting the observed Holocene sea level fall in these regions. When the deglaciation model ICE1 is used in conjunction with model ALPS1, a long–term sea level rise in the range 0.2–0.4 mm/yr is to be expected at a number of

representative Mediterranean PSMSL stations. As we have explicitly shown, the present–day postglacial sea level rate change at the Mediterranean scale cannot be simply explained as the result of the ongoing vertical deformations. A relevant role is played by glacially–induced changes of geoid height, which confirms the importance of a self–consistent modelization of the ocean load in the far–field of the Holocene ice sheets (Mitrovica and Milne, 2002).

3. The melting of the Alpine glacier may account for uplift rates as large as 0.2 mm/yr at the sites of the permanent GPS REGAL network (see Figures 8.10 and 8.11), whereas the horizontal motions are negligible in front of the observations. As in the case of the present–day sea level changes, the effective contribution of the postglacial deformations varies significantly according to the remote ice aggregate employed. An upper bound for the effect is obtained using model ICE1, that in conjunction with ALPS1 provides an average rate of subsidence close to 0.5 mm/yr. This value amounts to up to $\sim 1/3$ of the typical observed rates, indicating that present–day vertical deformations in the Alps and surrounding regions may be significantly affected by postglacial uplift induced by the Alpine and the remote glaciers. However, due to uncertainties in the deglaciation chronologies of both, a separation of the observed deformations in glacial and tectonic components must await for further investigations.

Chapter 9

Clark's zones in the Mediterranean Sea

9.1 Introduction

In the previous chapter we have verified that the melting of the Holocene remote ice sheets and the subsequent global glacio– and hydro–isostatic readjustment profoundly modified the geological environment of the Mediterranean. While the sea level signals caused by tectonic forces and other local mechanisms may exhibit a complex spatial and temporal variability (see e. g., Carminati and Didonato (1999) for a regional case study), those associated to glacio–isostatic adjustment are characterized by a smooth, long–wavelength pattern (see Figures 6.4, 6.5 in Section 6.2, and Figures 8.7, 8.11 in Section 8.3.2) that, on a global scale, allows to identify various regions (or zones) sharing the same relative sea level signatures (see Figure 1.10 in Section 1.2) and named after Clark (Clark et al., 1978; Clark and Lingle, 1979). The mechanisms that determine the shape of the Clark's zones can be identified solving the "gravitationally self–consistent" sea level equation (Eq. 3.33). Due to the limited computing resources, the early determinations of the Clark's zones (Farrell and Clark, 1976) failed to resolve important details of their global pattern,

including their contours and their possible fine structure in the Mediterranean basin (see Figure 1.10 in Section 1.2). The recent high–resolution approach of Mitrovica and Milne (2002) has shed new light on the mechanisms that determine the shape of the Clarks' zones on a global scale. Using the ice sheet chronology ICE3G Tushingham and Peltier (1991) and assuming a moderate increase of mantle viscosity across the 670 km depth discontinuity, Mitrovica and Milne have shown that the bulk of the Mediterranean and of other mid–latitude basins is presently subject to a sea level rise of postglacial origin. However, no attempts have been carried out to date to interpret quantitatively these findings nor to investigate the details of the Clark's zones along the continental margins of the Mediterranean. Furthermore, for this region, the sensitivity of the Clark's zones to the time–history of the Pleistocene ice aggregates and to the Earth's rheological parameters is still unknown. In the present investigation we have addressed these points by a straightforward approach based on the solution of the sea level equation. Our knowledge of the chronology of the Antarctic ice sheet since the Last Glacial Maximum is still affected by large uncertainties. During the last two decades geological and geomorphological evidence supported by glaciological and glacio–isostatic adjustment modeling and ice core analysis have yielded several (and sometimes divergent) estimates of the Antarctic contribution to global sea level (see e. g., Kaufmann, 2002 and references therein). We have considered several plausible models for the Holocene time–history of Antarctica and we have evaluated the consequences on the relative sea level observations in the Mediterranean. This has been motivated by our preliminary results concerning the sensitivity of the relative sea level observations along the coast of North Africa to the time–history of remote ice sheets and particularly of Antarctica (Stocchi et al., 2005c).

Here we have first qualitatively characterized the relative sea level variations in the Mediterranean Sea by studying the shape of the Clark zones and then we have compared the results based on ICE1 and ICE3G with the observations available from the database of Tushingham and Peltier (1993). The pattern of sea level change in

the Mediterranean has also been discussed by considering separately the oceanand the ice–load components S^{OCE} and S^{ICE}, and evaluating the role of individual regional components of the two global ice sheet distributions. An in–depth analysis of the sensitivity of the Mediterranean relative sea level variations to the ice sheets chronology and to mantle rheology is presented in the discussion section with the aid of further sea level indicators.

9.2 Results

9.2.1 Pattern of Clark zones for the Mediterranean Sea

As shown in Figure 9.1, the solution of the SLE discloses complex patterns of RSL change across the Mediterranean that strongly depend upon the assumptions about the ice sheets chronology of the far–field ice sheets. Model ICE3G (frame a) implies a late–Holocene highstand that marks the end of deglaciation (5.0 kyrs BP) along most of the Mediterranean coasts, with the exception of southern Italy, Greece and part of the coasts of Algeria, Lybia and of the southern Levant, while submergence is predicted in the bulk of the basin. The regions of emergence and submergence are separated by narrow transition zones in which sea level nearly follows the eustatic curve. The pattern of sea level change predicted in the Mediterranean Sea using model ICE3G might be mistakenly interpreted as a match of Clark's zones VI and II (see Figure 1.10), that characterize the far–field continental shorelines as a consequence of 'continental levering' and the collapsing forebulge regions, respectively (Walcott, 1972; Clark et al., 1978). However, as shown by Mitrovica and Milne (2002) and Lambeck and Purcell (2005) (and independently confirmed by our computations), submergence in the central Mediterranean Sea mainly stems from hydro–isostasy, being the glacio–isostatic effects of the northern Hemisphere aggregates, characteristic of zone II, confined to the coasts of France and northern Italy. In general, Clark's zones of type VI show up as bands of offshore sea level rise and onshore sea level fall, with the size of the submerging areas that show signif-

icant spatial variability with the tendency to increase for concave coastlines (this is clearly visible in the map of Figure 1 of Mitrovica and Milne, 2002). When the shorelines close on themselves to define a relatively small basin, as in the Mediterranean, the area of submergence tend to cover the central portion of the basin (this is also observed for the Black Sea and in other mid–latitude basins in the global map of Mitrovica and Milne), possibly leaving narrow regions of highstand onshore. To characterize the peculiar RSL pattern predicted for these mid–latitude basins, where zone VI is manifest as a central submergence region contoured by a narrow highstand zone, we propose the name of Clark's zone VII.

When model ICE1 is considered (see Figure 9.1b) the portion of zone VII characterized by highstands is narrowed significantly, being only present along the coasts of Spain, Northern Morocco, Tunisia and Lybia. Furthermore, the two transition regions of Figure 9.1(a) are not observed. Differently than in ICE3G, in ICE1 it is assumed that the Antarctic ice sheet is stationary during the Holocene, but the two aggregates also differ for the details of the melting chronologies of the North American and Fennoscandian ice aggregates (see Figure 7.4). To understand the origin of the distinct patterns in Figures 9.1(a) and 9.1(b), in Figure 9.1(c) we consider the ICE3G-A3 chronology, in which ICE3G is deprived of its Antarctic component. The pattern obtained is strikingly similar to that of ICE1 (b), indicating that the existence of late–Holocene highstand in the Mediterranean mainly result from the melting of the Antarctic ice aggregate as it is implemented in model ICE3G. When Antarctica is built into model ICE1 (Figure 9.1(d), model ICE1+A3), the configuration of Clark zones closely matches that of ICE3G (a). Significant difference between the results obtained for ICE3G and ICE1+A3, visible along the northern Adriatic and Tyrrhenian coasts, can be attributed to differences in the time–histories of the northern Hemisphere components of ICE3G and ICE1, with the relatively contiguous Fennoscandian ice sheet that is likely to play a major role. In terms of Clark zones, for model ICE1+A3 zone II counteracts the highstand of zone VII and merges with its core approximately North of the 42° N parallel. If

the Antarctic component of ICE3G were acting alone (frame e, deglaciation model A3), zone VII would disappear from the Mediterranean region leaving an ubiquitous late–Holocene highstand that, as we have verified, would extend north of the 45° S parallel.

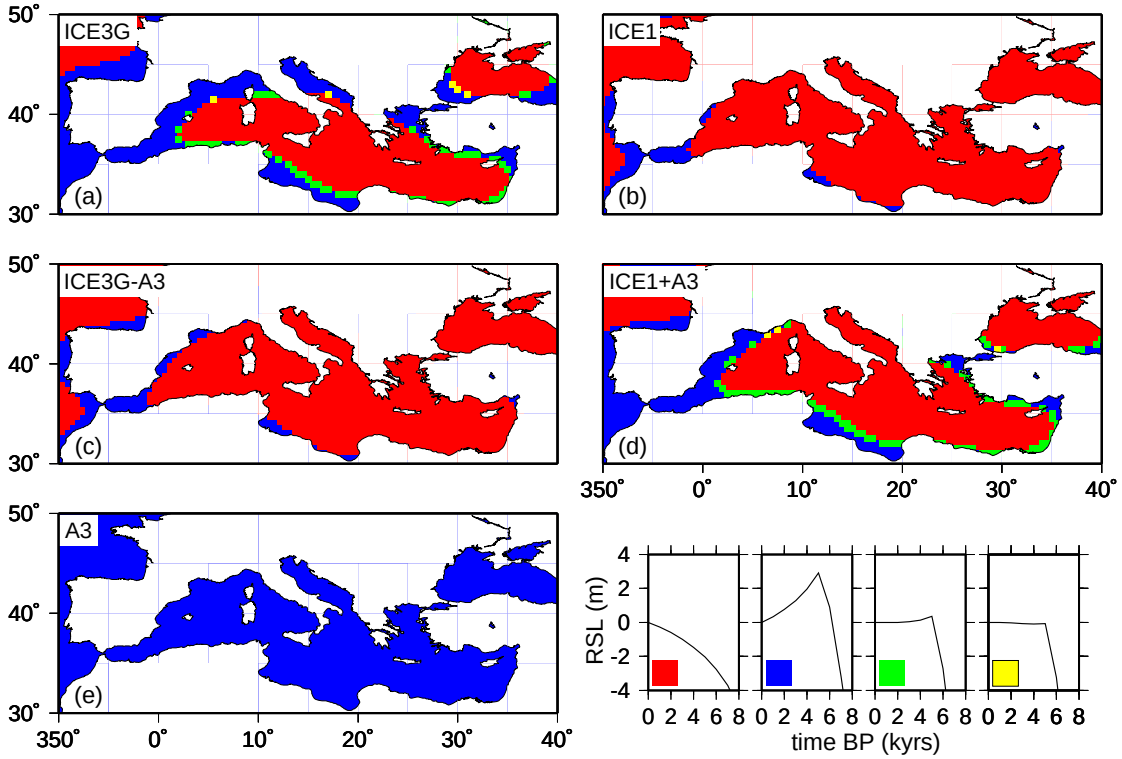

Figure 9.1: Shape of the Mediterranean Clark zones for models ICE3G (a), ICE1 (b), ICE3G-A3 (c), ICE1+A3 (d), and A3 (e). The RSL variations expected within each zone, qualitatively shown in the bottom right frame, include a monotonous submergence (red), a late–Holocene emergence characterized by a marked highstand of a few meters (blue), and two narrow transition zones (green and yellow). In all of the computations shown here, the SLE has been solved using the REF rheological model described in the text.

9.2.2 Observed and synthetic RSL curves

Figure 9.2(a) shows the location of the RSL Mediterranean sites pertaining to the publicly available database of Tushingham and Peltier (1993), while the data are displayed in Figure 9.2(b). Since ICE3G has been built to improve the fit with the available RSL observations, the database is an integral part of this ice sheets chronology. The RSL sites are quite evenly distributed across the Mediterranean, but since in the database only one datum is available for the coasts of North Africa (i. e., Algiers, site 12), we have included in our analysis the site of Djerba (Tunisia), based on the work of Jedoui et al. (1998). According to Figure 9.2(b), the only observations that indicates a sea level highstand in the late Holocene are those relative to Beirut (9), Djerba (11) and Algiers (12). While data from Beirut and Algiers are generally supposed to be influenced by local tectonic deformations (see Figure 9.3 top and bottom, respectively from Meghraoui et al., 2004, and Pirazzoli, 2005) the observations from Tunisia are mainly thought to reflect glacio– and hydro–isostatic RSL variations (Morhange and Pirazzoli, 2005). We observe that sites showing an highstand are only situated along the southern and eastern continental Mediterranean coasts. This is qualitatively consistent with the pattern of Clark's zones that we have obtained for models ICE1 and ICE1+A3, while it appears to be at variance with predictions based upon ICE3G (see Figure 9.1).

To better assess the role of Antarctica in the determination of the RSL variations in the Mediterranean, in Figure 9.4 we compare individual RSL observations with model calculations based on ICE3G (solid lines), ICE1 (dashed), ICE1+A3 (dotted) and A3 (dash–dotted). Consistently with the qualitative study of Figure 9.1(e), the RSL variations driven by the melting of A3 show a clear highstand at 5 kyrs BP in all of the sites considered, with a peak amplitude varying between ~ 2 m (Roussillon, frame 1) and ~ 1 m (Messenia, 4). For models ICE3G and ICE1+A3, predicted RSL curves are characterized by a knee at 5.0 kyrs BP caused by their Antarctic components that with the sole exception of the Aegean sites of Messenia (6) and SW Turkey (7) corresponds to a sea level highstand.

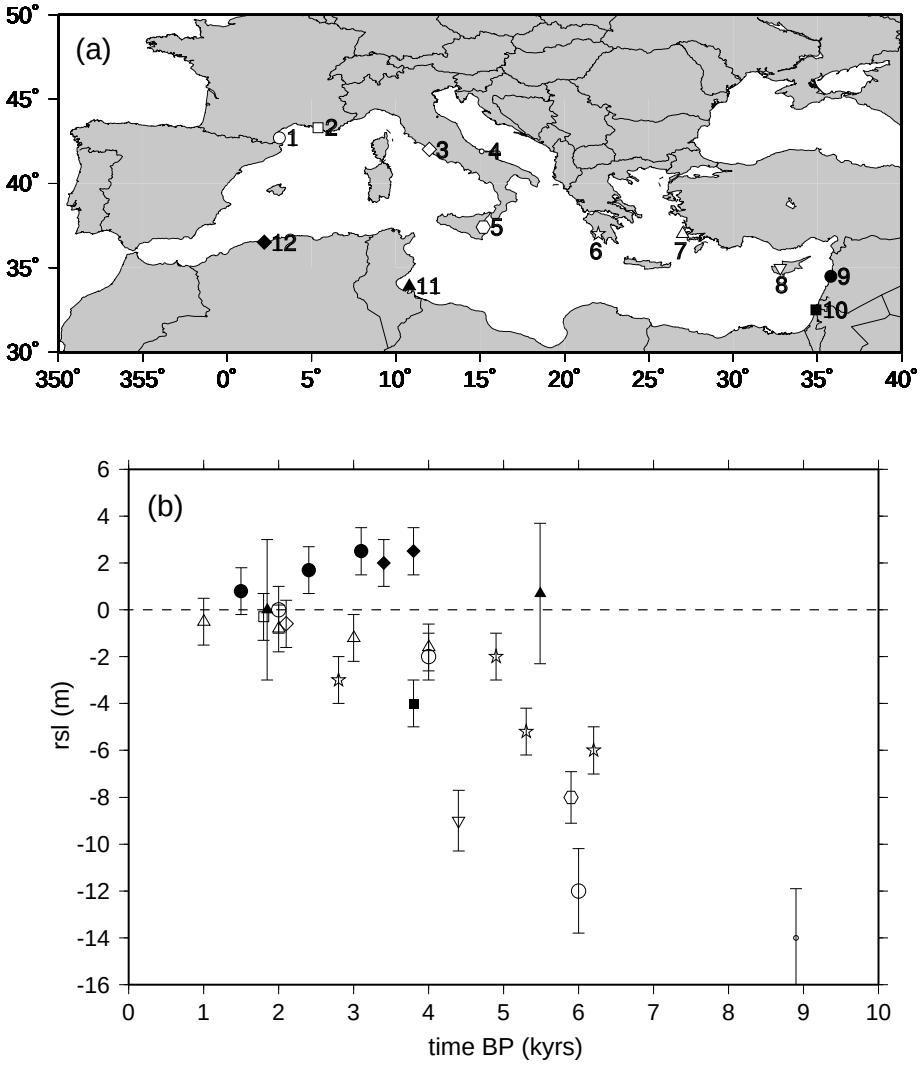

Figure 9.2: Top: location of the RSL sites considered in the analysis of Section 9.2.2, namely Roussillon (1), Marseilles (2), Civitavecchia (3), Termoli (4), Catania (5), Messenia (6), SW Turkey (7), Cyprus (8), Beirut (9), Jaffa (10), Djerba (11), and Algiers (12). With the exception of Djerba (filled triangle), all the sites shown here belong to the RSL database of Tushingham and Peltier (1993). Bottom: full set of RSL observations available for the sites considered in (a) during the last 10 kyrs, where filled symbols denote observations from North Africa and the Levant Sea.

Figure 9.3: Top: elevated shoreline in Lebanon formed as a consequence of a coseismic uplift (possibly at the time of the devastating earthquake of 9 July, 551 AD). Bottom: coseismic coastal uplift at Le Figuier (Algeria) associated with the M_w = 6.8 Zemmouri earthquake of 21 May, 2003 (see text for references).

When ICE1 is considered instead (dashed), the curves clearly show a monotonous sea level rise that broadly agrees with the trend of the Tushingham and Peltier observations from France, Italy and SW Turkey. In Roussillon (1), Marseilles (2) and Civitavecchia (3), the offset between the ICE1+A3 and the ICE3G predictions reflect differences in the time–history of the northern Hemisphere ice sheets. At lower latitudes, with increasing distance from the former margins of Fennoscandia, the gap between solid and dotted curves tends to diminish. In the case of Djerba (8), ICE1 implies a highstand of a few centimeters at 5.0 kyrs BP, and the predictions by A3, ICE1+A3, and ICE3G almost overlap, to indicate that RSL observations at this site are virtually sensitive to the sole Antarctic component of the Holocene ice sheets. Although evidence in favor of a late–Holocene highstand at Djerba is weak due to the large data uncertainties, the sensitivity of North Africa RSL observations to the chronology of Antarctica merits further investigations (see Section 9.3.2). Even a cursory inspection of Figure 9.4 reveals that in general model ICE3G provides a poor fit to the RSL observations in the Mediterranean. Conversely, with the sole exception of sites belonging to tectonically unstable regions such as Beirut (6) and Algiers (12) (Figure9.3 top and bottom respectively), the ICE1 chronology always matches the observed RSL trends. The results strongly suggest that the Antarctic component is the main responsible of the disagreement between predictions and observations, but it is also possible that the rheological profile REF impled in model ICE3G is not fully suitable to describe the RSL variations in the Mediterranean. We will return to these issues in depth in Sections 9.3.2 and 9.3.3, respectively.

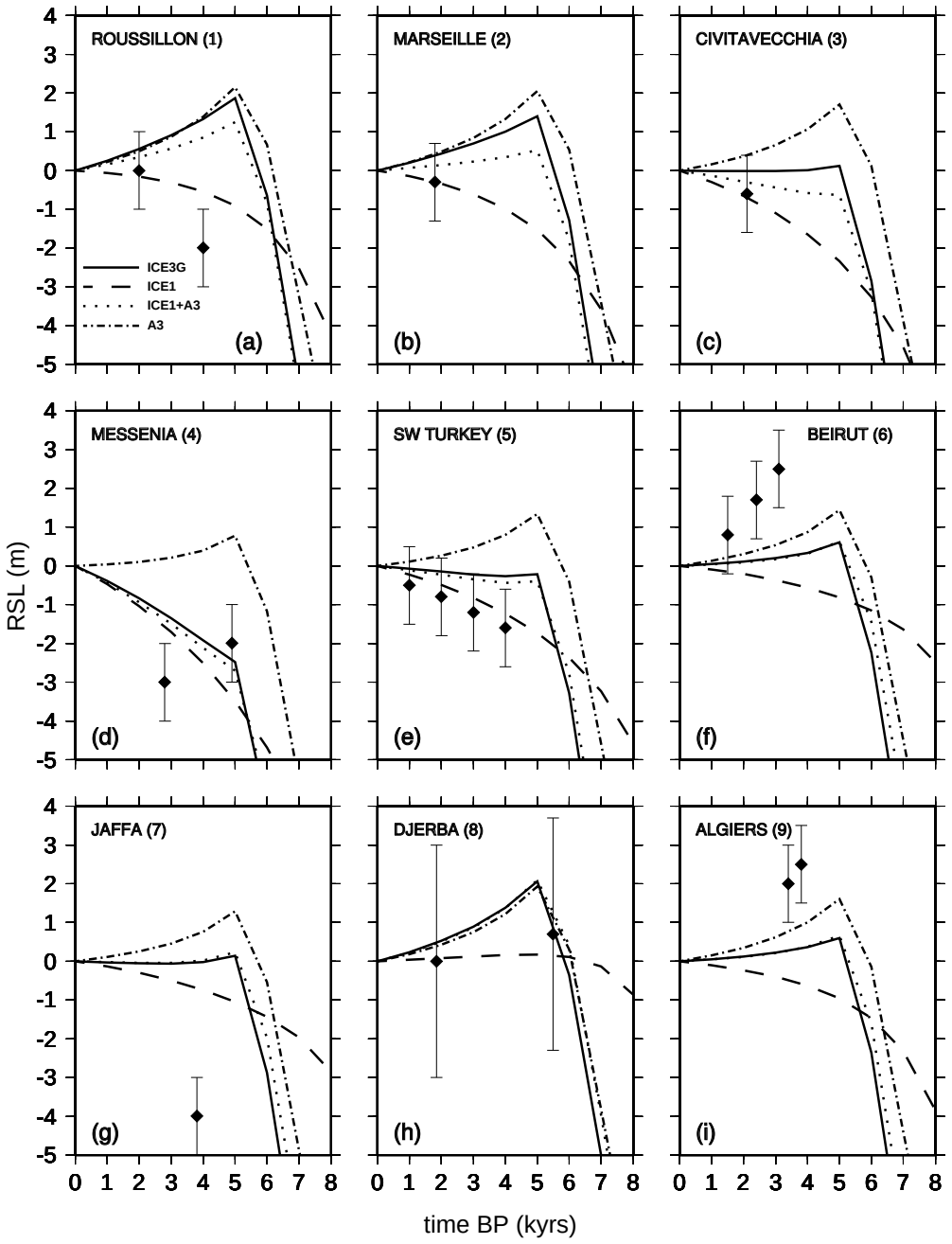

Figure 9.4: Observed and synthetic RSL observations during the last 8.0 kyrs for some of the sites of Figure 9.2a. The predictions have been obtained using the rheological model REF and the ice sheets models ICE3G, ICE1+A3, ICE1, and A3 (see inset of frame a). The RSL observations and their error bars are taken from the database of Tushingham and Peltier (1993) with the sole exception of Djerba (Jedoui et al., 1998). In this site melting of Antarctica provides virtually the whole signal during the last 6 kyrs (compare solid with dash–dotted curve in frame h).

9.2.3 Ocean and ice–induced RSL variations

Since the Mediterranean is moderately distant from the former late–Pleistocene ice sheets, the ice–induced RSL variations in this region are not expected to dominate the ocean components, as it is the case in the near–field Clark's zones I and II (Lambeck and Purcell, 2005). To address this point, using the rheological model REF, in Figure 9.5 we have separately considered the RSL variations of glacio–isostatic and hydro–isostatic origin at the three sites of Roussillon, Jaffa and Djerba, representative of the northern, eastern, and southern coasts of the Mediterranean basin, respectively (see Figure 9.2). Dashed and dotted lines show ocean– and ice–induced RSL components, obtained using Eq. (3.63) with $S = S^{OCE}$ (see Eq. 7.3) and $S = S^{ICE}$ (see Eq. 7.2), respectively. Since $S^{EUS} = 0$ after the end of deglaciation, in this time period the RSL variations are solely given by a combination of the ocean– and ice–load induced effects. For both the ice sheets chronologies considered here, the trend of the ice–induced component of RSL (dotted) does not change across the Mediterranean, being mostly determined by long–wavelength deformations driven by distant sources. However, the ice–load induced RSL variations are clearly sensitive to the ice sheets time–histories adopted, with a sea level fall for ICE3G (top frames) and a sea level rise for ICE1 (bottom). As discussed below, this diametrically opposite trend is to be attributed to the sea level changes driven by the melting of Antarctica in ICE3G. Differently from the ice term, the ocean term in Figure 9.5 (dashed) shows a significant spatial variability, with a clear sea level fall in Roussillon and Djerba, and a moderate sea level rise in Jaffa. Such variability is caused by the sensitivity of this component of RSL to local effects related to the irregular shape of the shorelines (e. g., Mitrovica and Milne, 2002; Lambeck and Purcell, 2005). The trend of the hydro–isostatic term is the same for both ice sheets, but its amplitude tends to be larger for ICE3G, due to the effect of the extra water load provided by its Antarctic component.

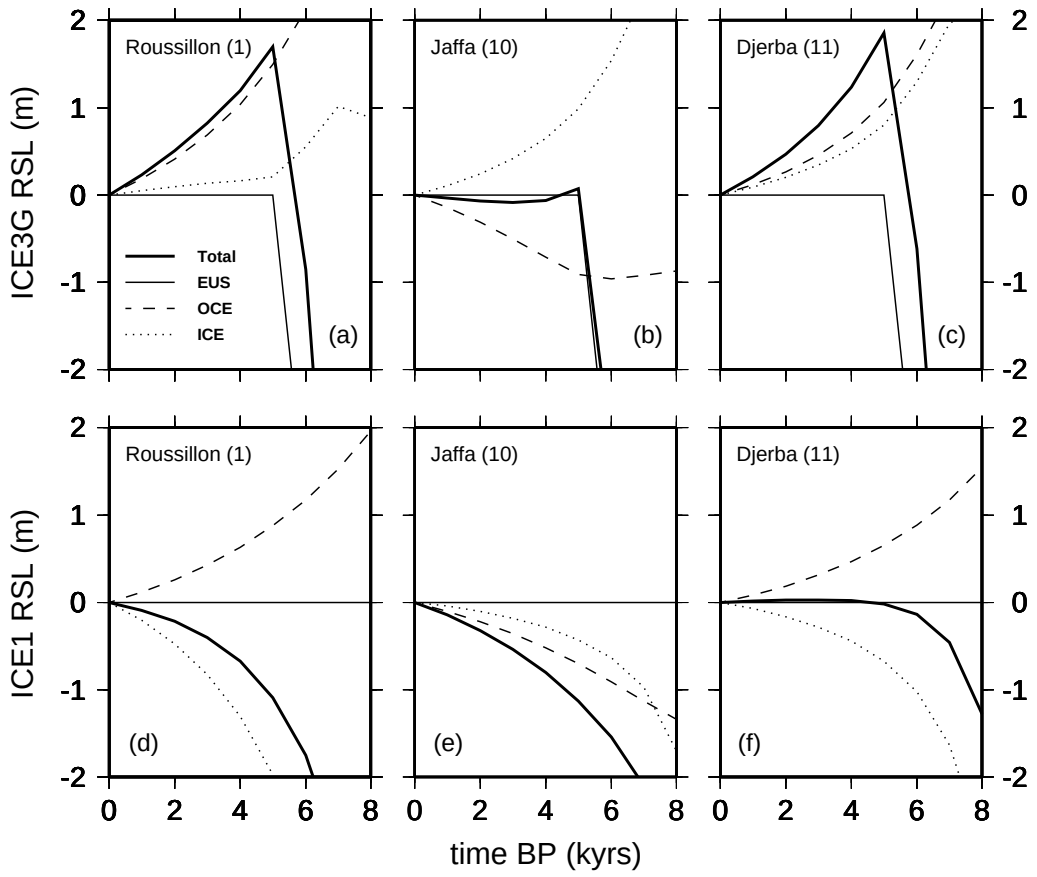

Figure 9.5: Ice– and ocean–load induced components of RSL for the sites of Roussillon, Jaffa, and Djerba (the sites location is shown in Figure 9.2(a)), using ICE3G (top) and ICE1 (bottom). Since in ICE1 the end of deglaciation occurs 8.0 kyrs BP (see Figure 7.4), its eustatic component vanishes in this time window.

In Figure 9.6 the expected RSL variations are decomposed into contributions of the major late–Pleistocene ice sheets, namely North America, Fennoscandia, and Antarctica (minor constituents of ICE3G and ICE1 are not considered here). The results obtained clearly illustrate how the distance from the former ice sheets affects the total response. In the case of Roussillon, the sea level rise produced by the relatively nearby Fennoscandian component of ICE3G is counteracted by Antarctica

and North America to produce a marked late–Holocene highstand . This feature is only barely visible in the predictions for Jaffa, since during the last 5.0 kyrs the melting of the northern Hemisphere aggregates almost exactly compensates the effects from the southern Hemisphere. Finally, for Djerba, in the last 6.0 kyrs, the North American and Fennoscandian ice sheets have produced equal but opposite trends for both ICE1 and ICE3G that make the RSL observations from the coasts of Tunisia particularly sensitive to the deglaciation of Antarctica, as already anticipated in Section 9.2.2.

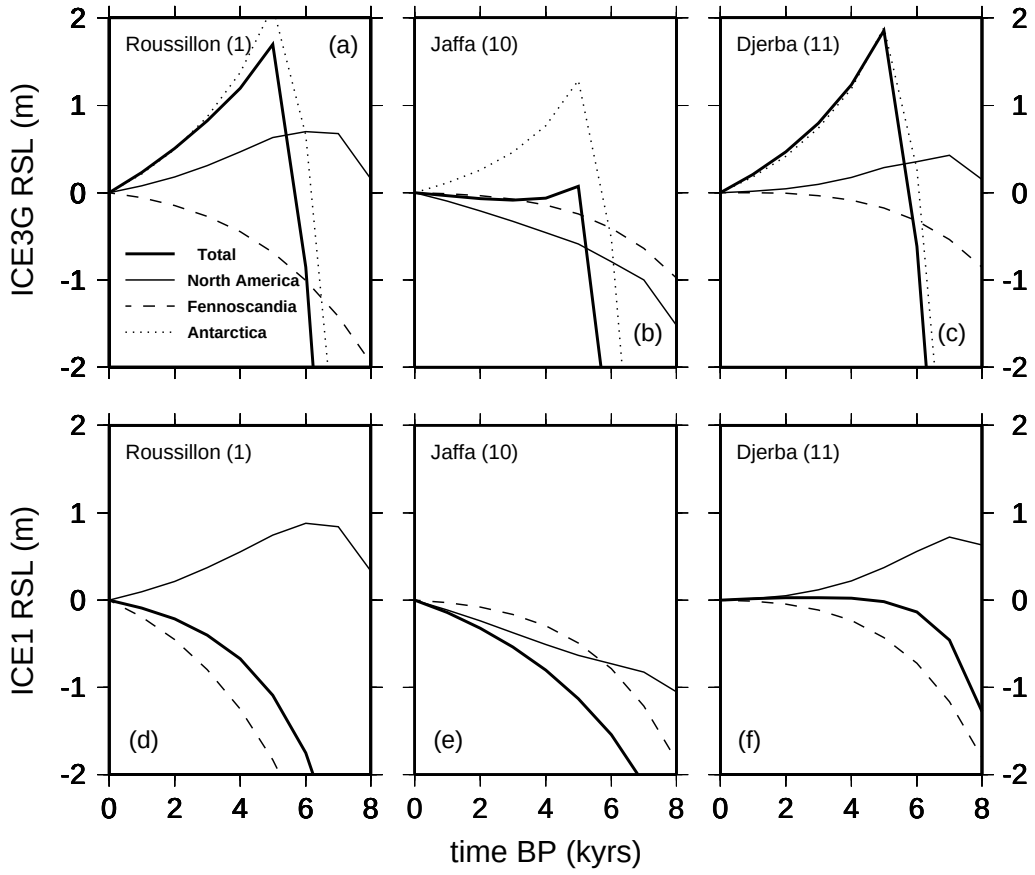

Figure 9.6: Contributions to RSL from individual components of ICE3G (top frames) and ICE1 (bottom) at Roussillon, Jaffa, and Djerba (see Figure 9.2a).

9.3 Discussion

Assuming ICE3G and REF as *a–priori* models for the late–Pleistocene ice sheets and for the Earth's rheological profile, respectively, in the previous sections we have confirmed that Antarctica significantly affects the Holocene sea level variations in the Mediterranean through the mechanism of continental levering. However, from the results obtained (see in particular Figure 9.4) it is apparent that ICE3G provides a poor fit to the field observations in this area, that are qualitatively better reproduced by ICE1, a model that assumes a stationary Antarctic ice sheet during the whole Holocene. In an attempt to reconcile the Mediterranean RSL observations with a global ice sheets chronologies that account for a non–stationary Antarctic ice sheet, we have first reviewed some of the available models of the deglaciation of Antarctica and then we have assessed their impact on the sea level observed in the Mediterranean without modifying the REF rheological profile. Since the ice model ICE3G is biased from the Earth viscosity profile used in its reconstruction (i. e., the same REF viscosity profile that we have employed so far), in a second step we have also assessed the effect of varying the mantle viscosity profile upon the RSL predictions, which have been compared with field observations from various locations along the coasts of the Mediterranean Sea, digitalized from the compilation of Pirazzoli (1991) and from more recent sources. With respect to the database of Tushingham and Peltier (1991), the sea level indicators used here provide a better spatial coverage for the regions that have been investigated starting from Section 9.3.2.

9.3.1 Three ice models for Antarctica

In the following, we have modified the original ice model ICE3G by including the three distinct melting chronologies for Antarctica that in Figure 9.8 are denoted by S, G, and D, respectively. All of them contribute 14 m of equivalent sea level (i. e., $\sim$ one half of the ICE3G value). Considering the distance of the Mediterranean

from the margins of the former Antarctic ice sheet, here we have modeled this ice sheet by a disc load of rectangular cross–section having an half–amplitude of 20° and a thickness of $\sim$ 355 m at the LGM (see figure 9.7). To fit the $\sim$ 113 m lowstand predicted by ICE3G in the far– field sites at the LGM (see Figure 7.4(d)), we have increased the volume of the northern Hemisphere ICE3G aggregates at this epoch keeping their isochrons unaltered.

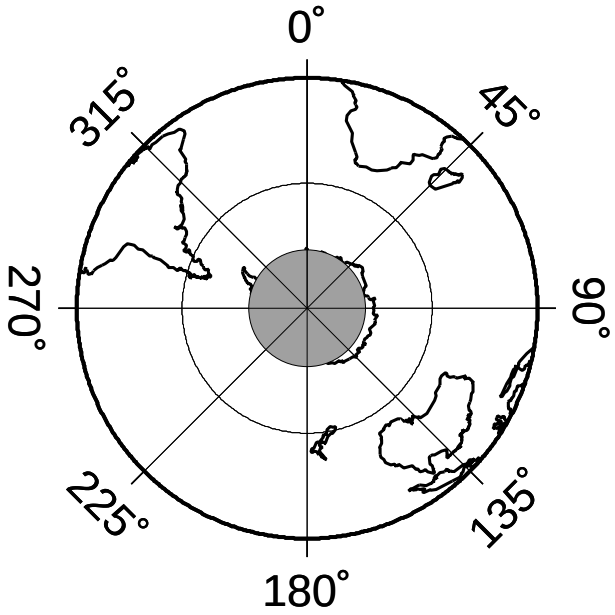

Figure 9.7: Antarctic disc model.

The chronologies so obtained are named ICE3G(S), ICE3G(G), and ICE3G(D), respectively. Evidence in support of the chosen ESL for Antarctica comes from a number of sources. In his review about the volume of Antarctica at the LGM, Bentley (1999) has proposed an ESL in the range of 6.1–13.1 m that matches the 12 m estimate of Huybrechts (1992) based on glaciological modeling. Through a 3–D

thermo–mechanical modeling, recently Huybrechts (2002) has derived an ESL in the range of 14–18, consistent with the value of 14 m obtained from geologic constraints by Denton and Hughes (2002), whereas from an ice–dynamical approach Bintanja et al. (2002) have estimated that Antarctica has contributed ~ 5 m of ESL since the LGM. These ESL predictions for Antarctica are consistently smaller (by at least a factor of 2) than former values based on the classical reconstruction of Denton and Hughes (1981), and of the ICE3G figure (~ 27 m). As we will show in the following, a reduced ESL for Antarctica improves the fit with the RSL observations in the Mediterranean, mainly because the amplitude of the late–Holocene highstand is significantly reduced. The simplest of the three time–histories considered for Antarctica (solid curve labeled by S in Figure 9.8) is characterized by a constant rate of melting between 12.0 and 5.0 kyrs BP, when geological evidence indicate that the Antarctic deglaciation was complete (Goodwin, 1996). However, a few global models suggest that some additional meltwater was still added to the ocean during the last 6.0 kyrs. Since the main source of this late–Holocene additional global sea level rise of ~ 3 m is assumed to be the Antarctic ice sheet (Nakada and Lambeck, 1988), we have also implemented a delayed (D) melting phase (dotted). This second chronology follows S until 7.0 kyrs BP but subsequently the rate of deglaciation decreases and the eustatic curve reaches the present–day sea level 1.0 kyrs BP. The D chronology provides a late–Holocene water release sufficient to increase sea level by about 3 m since 6 kyrs BP (Lambeck and Bard, 2000), while its contribution since 3.0 kyrs BP is less than 1 m (Fleming et al., 1998). Various evidence indicate a mid– to late–Holocene sea level highstand in the South Pacific, Indian Ocean and in parts of the Northern Atlantic and Pacific Oceans. The subsequent sea level fall is generally attributed to the "ocean siphoning" (Mitrovica and Milne, 2002). However, based on glaciological and geological field evidences, Goodwin (1998) suggested that a late–Holocene increase of the Antarctic ice volume may be partly responsible for this sea level fall. According to this hypothesis, the expansion of mountain glaciers, ice sheet margins and the thickening of the ice sheet interior could account for ~ 1.0 m of the

sea level fall on mid–oceanic islands. Hence, differently from D, the G chronology, shown by a dashed line in Figure 9.8, is characterized by a late–Holocene ice sheet re–advance causing a general eustatic sea level fall of $\sim$ 1.0 m since 5.0 kyrs BP, with $\sim$ 0.7 m of sea level fall between 4.0 and 2.0 kyrs BP (Goodwin, 1998).

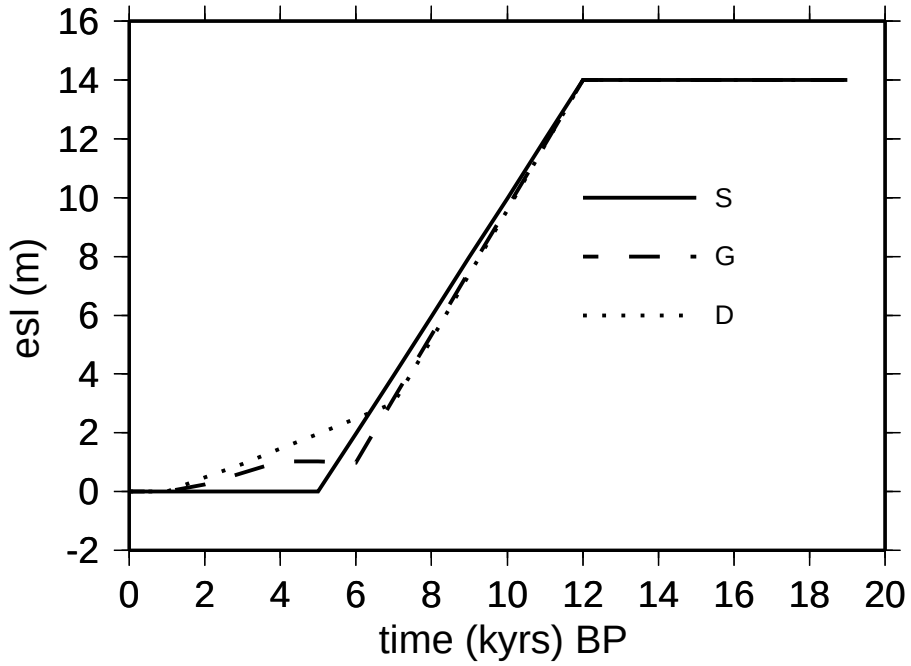

Figure 9.8: Time–histories of the Antarctic component of ICE3G according to the S, G, and D models described in the text. They are constituted by a simple disc–shaped ice element that stores an equivalent sea level of 14 m before the beginning of melting (12.0 kyrs BP).

9.3.2 RSL data and predictions

French coasts

From the collection of sea level field observations of Pirazzoli (1991), we have borrowed data from nine sites along the Golfe du Lion and the coasts of Corsica, ranging from Roussillon (1) to South Corsica (9). The sites locations are shown by filled circles in Figure 9.9.

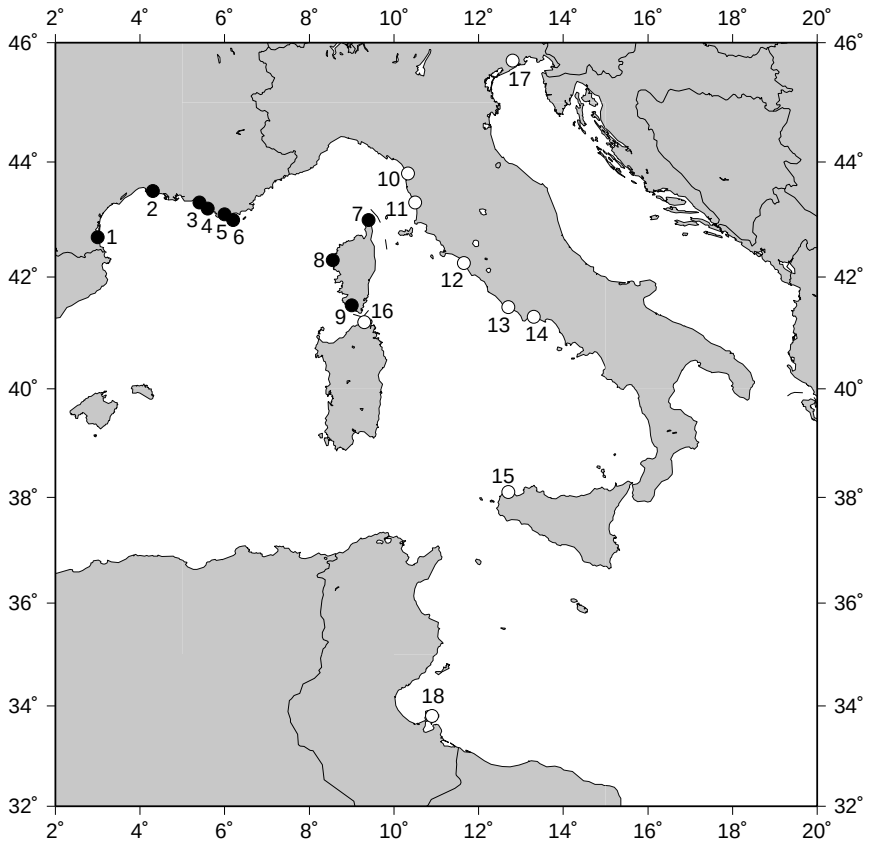

Figure 9.9: Sites from southern France and Corsica (sites 1–9), the Tyrrhenian coast of Italy (sites 10–16), northern Adriatic (17), and Tunisia (18).

In the original compilation of Pirazzoli (1991), only two sites show some indication of a late–Holocene highstand, with an emergence of ~ 2.0 m near Cap Romarin between 5 and 4 kyrs BP (Aloisi et al., 1978), and a highstand in the range of 2 to 4 m ~ 4 kyrs BP deduced from undated beach deposits in the Nice area and in the surroundings (Dubar, 1987). From a reexamination of the available record, Lambeck and Bard (2000) concluded that along the French coast Holocene sea levels have never exceeded the present level, being the highstand marked in the erosional notch at cap Romarin of pleistocenic age (Laborel et al., 1998). Some further evidence against a late–Holocene highstand comes from archaeological excavations of the ancient harbor of Marseilles, which have provided a new set of high–precision data for the past 4 kyrs (Morhange et al., 2001), and from the preservation of half–submerged Paleolithic paintings on a wall of the Cosquer cave near Marseilles (Vouvet et al., 1996), showing that during the Holocene sea level never has never exceeded its present–day level. In our previous calculations of Figure 9.1, the ice models ICE3G and ICE1+A3 have evidenced a late–Holocene emergence along the Mediterranean coast of France. As shown in Figure 9.10, different results are obtained when the three modified Antarctic chronologies of Figure 9.8 are implemented in ICE3G. The solution for ICE3G(S) (solid lines) evidences a sea level highstand of ~ 1 m at 5 kyrs BP both in Roussillon and in the Rhone Delta region. Due to the reduced ESL of ICE3G(S) and to the 2 kyrs anticipation of the melting inception of its Antarctic component (see Figure 9.8), the maximum transgression is diminished by about a factor of 2 with respect to the original ICE3G (compare with Figure 9.4).

The amplitude of the highstand diminishes eastward until it vanishes at Port Cros (site 6); in Corsica (sites 7–9) the highstand is canceled by the submergence that characterizes Clark zone VII in the bulk of the Mediterranean. Model ICE3G(S) generally provides a poor fit to the data. The late–Holocene re–advance of the Antarctic ice sheet, implied in the ICE3G(G) chronology (dashed lines), enhances the development of highstands. Those with largest amplitude (~ 1.5 m) are observed at Roussillon (1) and in the Rhone Delta (2). The predictions for this hypothetical

chronology of Antarctica systematically lie above those based upon ICE3G(S) (solid) and are found to be in clear disagreement with the field observations from southern France. The ICE3G(D) chronology (dotted lines) implies a smooth sea level rise through the late Holocene, similar to that predicted by ICE1 and ICE3G-A3 (see Figures 9.1(a) and 9.1(b)) and a subsequent barely visible sea level fall ending between 2 and 1 kyrs BP. The general agreement of the ICE3G(D) predictions with the sea level observations from this region is apparent.

Tyrrhenian and northern Adriatic coasts of Italy

The pioneering investigations of Alfieri and Caputo (Schmiedt, 1972) have shown the importance of the archaeological remains as sea level indicators of past sea levels along the Tyrrhenian coasts of Italy. For this region, they estimated a sea level rise of $\sim$ 1.7 mm yr^{-1} between 600 BC and 100 AD; in particular, dating Roman fish tanks and submerged harbors, they showed that between 100 years BC and 100 years AD the sea level was $\sim$ 1.0 m lower than present. Subsequently, the radiocarbon–based RSL curve of Antonioli and Frezzotti (1989) has evidenced, for the southern coasts of Lazio, a sea level similar to the present one between 7 and 5.4 kyrs BP, followed by a slight oscillation below present level (Pirazzoli, 1991), while the cumulative Tyrrhenian sea level curve of Alessio et al. (1994) confirmed that, during the Holocene, sea level has never been above the present datum. From the recently published RSL data set of Lambeck et al. (2004a) we have selected the field observations in the tectonically stable Tyrrhenian sites marked by open circles in Figure 9.9. The observations shown in Figure 9.11 clearly indicate a monotonous submergence since 8 kyrs BP with no evidence of highstands. With the exception of the northern Adriatic (site 17), the results based upon the ICE3G(D) deglaciation model (dotted curves) systematically overestimate the RSL observations but reproduce correctly their trends. In qualitative agreement with the results obtained for southern France (see Figure 9.10), the two alternative chronologies ICE3G(S) and ICE3G(G) do not improve the fit with the observations.

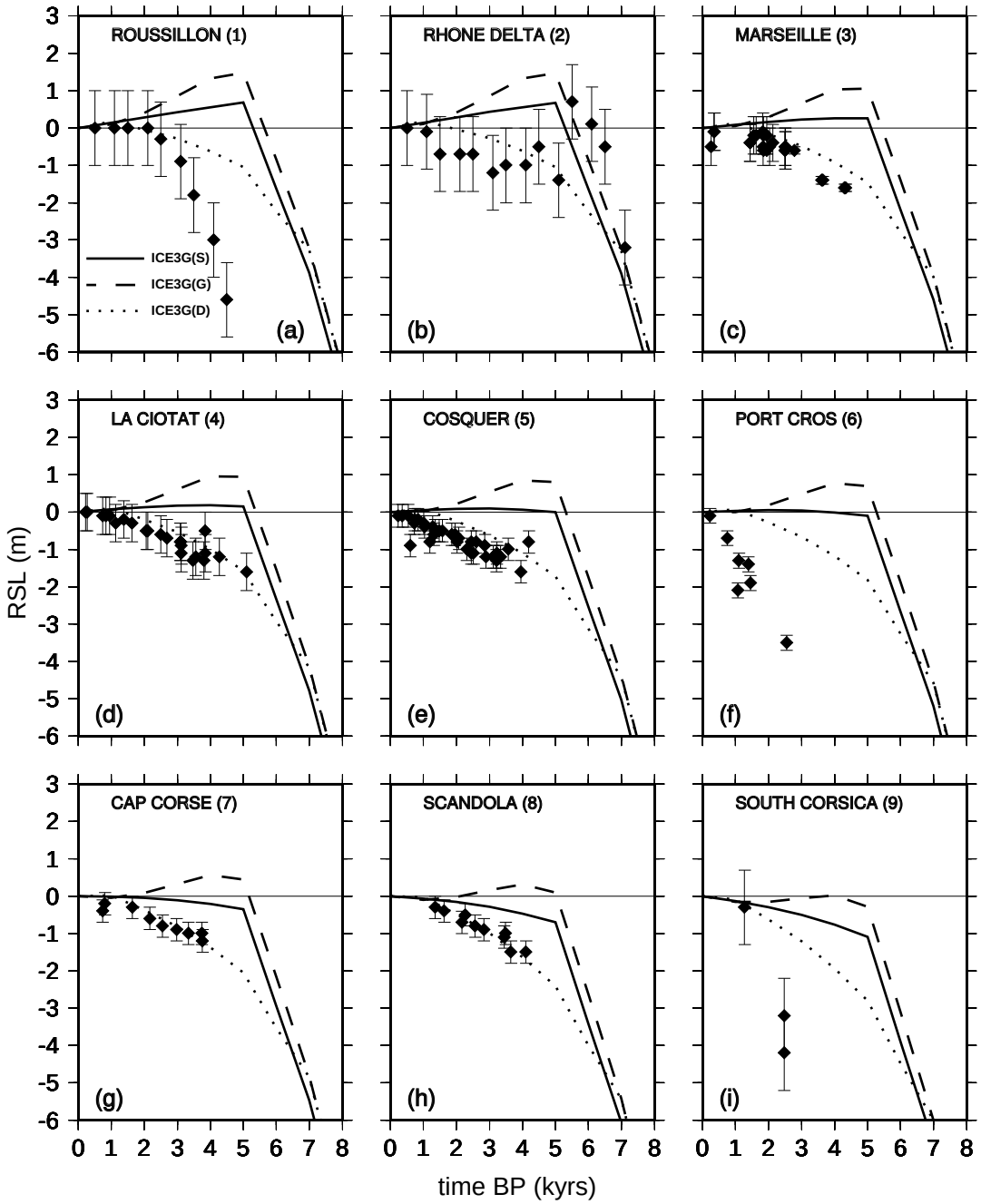

Figure 9.10: Relative sea level observations from southern France and Corsica according to the compilation of Pirazzoli (1991), to which the reader is referred for the original sources. Data uncertainties are taken from the original contributions with the exception of Roussillon (1) and the Rhone Delta (2), to which a standard deviation of 1 m has been arbitrarily assigned. Solid, dashed, and dotted curves show the results obtained for model ICE3G(S), ICE3G(G), and ICE3G(D), respectively.

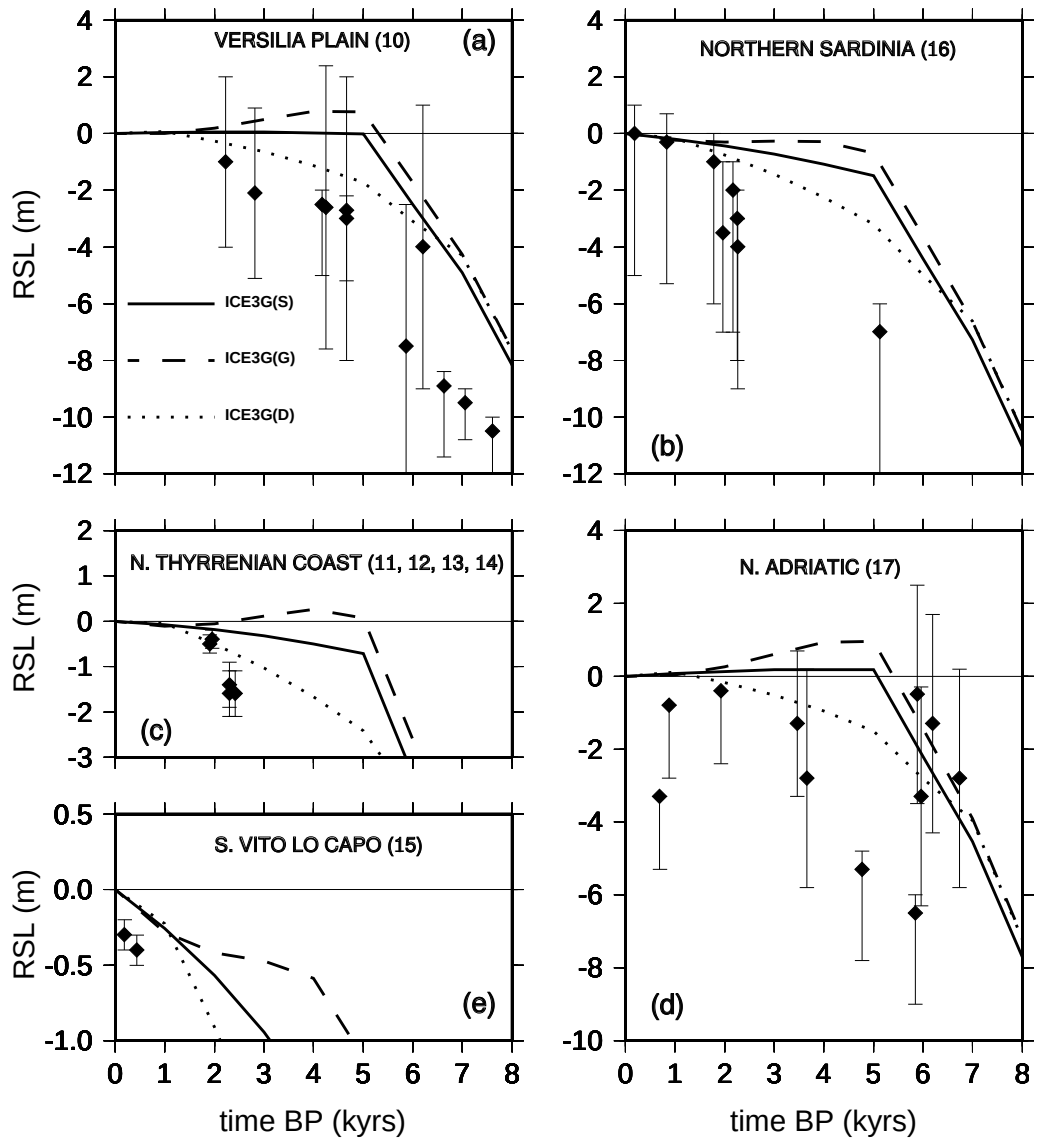

Figure 9.11: Relative sea level observations and uncertainties from the Tyrrhenian coasts of Italy (sites 10–16) and from the northern Adriatic (17) according to Lambeck et al. (2004a). The data are compared with predictions based on the three variants of model ICE3G described in Figure 9.8.

Gulf of Gabes, Tunisia

Paskoff and Sanlaville (1983) proposed a tentative sea level curve for the southern coasts of Tunisia in the last 8.0 kyrs (see also Pirazzoli, 1991). The fluctuating RSL curve of Paskoff and Sanlaville, relative to Djerba (site 18) and reproduced in Figure 9.12 by filled squares, shows a transgression peak of ~ 1.7 m between 6.5 and 4.5 kyrs BP and a second minor highstand at ~ 3.0 kyrs BP. The subsequent study of Jedoui et al. (1998) evidenced two fossilized bioclastic beaches at different elevations (see the diamonds in Figure 9.12a). The older paleobeach deposit (~ 5.3 kyrs BP), is found at an elevation of about 40 to 100 cm above the present sea level, while the younger deposit, dated ~ 1.85 kyrs BP, lies at the present sea level. Uncertainties on the interpretation of past sea level indicators from this area have been discussed by Pirazzoli (1987) and Lambeck et al. (2004a). Recently Morhange and Pirazzoli (2005) have published a tentative sea level curve for SE Tunisia based on new indicators collected between the Gulf of Gabes and the Libyan border. The curve, reproduced by open circles in Figure 9.12, shows a transgression peak of $\sim 2.0 \pm 0.10$ m between $6,000$ and $5,000$ ^{14}C years BP.

In Figure 9.12 we compare RSL observations from Djerba with predictions based on the three modified ICE3G chronologies described in Section 9.3.1. While ICE3G(S) (solid line) and ICE3G(G) (dashed) support the late–Holocene highstand suggested by the tentative curves of Morhange and Pirazzoli (2005) and Paskoff and Sanlaville (1983) in the last ~ 5.0 kyrs, the predictions obtained by ICE3G(D) (dotted) show a monotonous sea level rise that is in contrast with these observations. However, since confidence bands for the tentative curves are lacking, it is difficult to judge the misfit of the predictions presented here. Provided that the data uncertainties reported by Jedoui et al. (1998) are reliable, Figure 9.12 clearly shows that none of the three time–histories considered is indeed in contrast with the observations. In every instance, from the results obtained for this region it is clear that improved RSL observations for the coasts of Tunisia could significantly contribute to constrain the time–history of Antarctica in the last 6.0 kyrs. The cancellation of the effects

from the northern Hemisphere ice sheets that occurs in this region is apparent, observing that the ICE3G(D) results basically reproduce the effect from the sole Antarctic component of this ice sheet (dash–dotted curve). The reader is referred to Chapter 10 for further investigations concerning the sensitivity of SE Tunisia to the Antarctic melting.

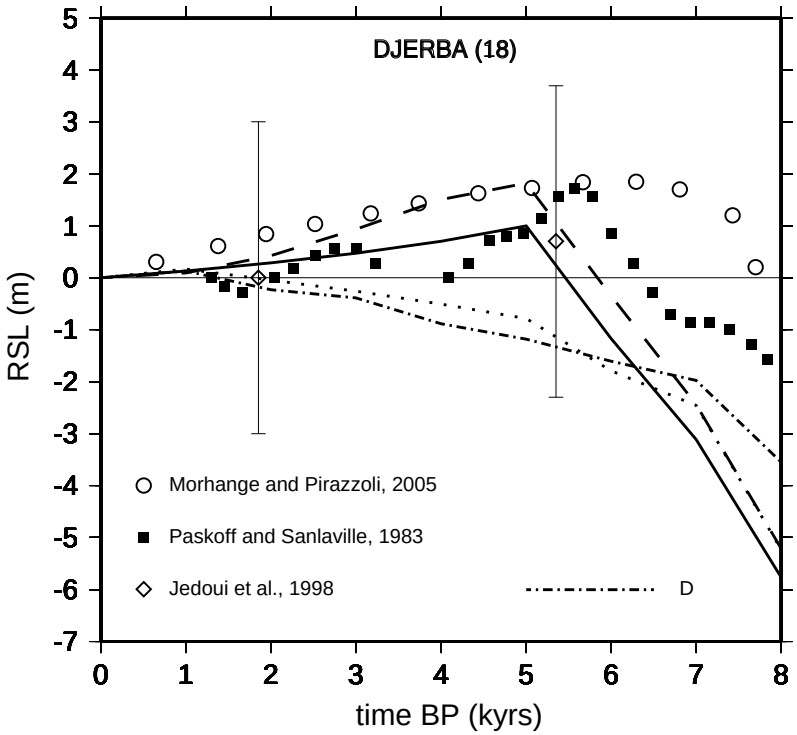

Figure 9.12: Relative sea level observations for Djerba and model predictions obtained using the ice model ICE3G(S) (solid line), ICE3G(G) (dashed), and ICE3G(D)(dotted). The dash–dotted RSL curve shows the results obtained assuming that the Antarctic ice sheet model D of Figure 9.8 is the only active load since the LGM.

The Levant sea, Israel

Evidence for late Holocene sea level higher than present in Israel (see Figure 9.13) has been reported by Sneh and Klein (1984) and by Raban and Galili (1985) who have derived two similar sea level curves for the site of Dor, showing sea level fluctuations of over 2.0 m of amplitude Pirazzoli (1991) as portrayed in Figure 9.14(a). In a subsequent study, Nir and Eldar (1987) proposed a curve characterized by small oscillations for the last 2.5 kyrs. From the investigation of submerged archaeological remains along the continental shelf of Israel, between Haifa and Atlit, (Galili et al., 1988) obtained the RSL curve shown by a dashed line in Figure 9.14(a), indicating a monotonous and smooth sea level rise until $\sim$ 1 kyrs BP (Pirazzoli, 1991). As shown in frame (b), archaeological evidences from the sites of Tel Nami (20), Dor (21), Michmoret (23) and Yavne Yam (24), indicate that at 6 kyrs BP the sea level was $\sim$ 4 m lower than today and that it reached the present–day level between 3 and 2 kyrs BP Sivan et al. (2001). The observational limits derived from the coastal water wells in Caesarea Maritima (site 22) have extended the record of the late Holocene sea level change to 1300 AD (Sivan et al., 2004) and suggest that during the Byzantine period sea level was higher by $\sim$ 30 cm than today. The RSL curve obtained using ICE3G(G) (dashed curve in Figure 9.14(b)) shows an high-stand between 5 and 4 kyrs BP, followed by a sea level fall and lastly by a negative oscillation. When the ICE3G(S) and the ICE3G(D) ice chronologies are considered (solid and dotted lines, respectively), the predicted late Holocene sea level curves define a narrow band broadly consistent with the archaeological evidence until $\sim$ 2 kyrs BP. These latter predictions do not match the more recent sea level data and clearly cannot explain the higher than present sea level between 2 and 1 kyr BP observed at Caesarea Maritima according to Sivan et al. (2004).

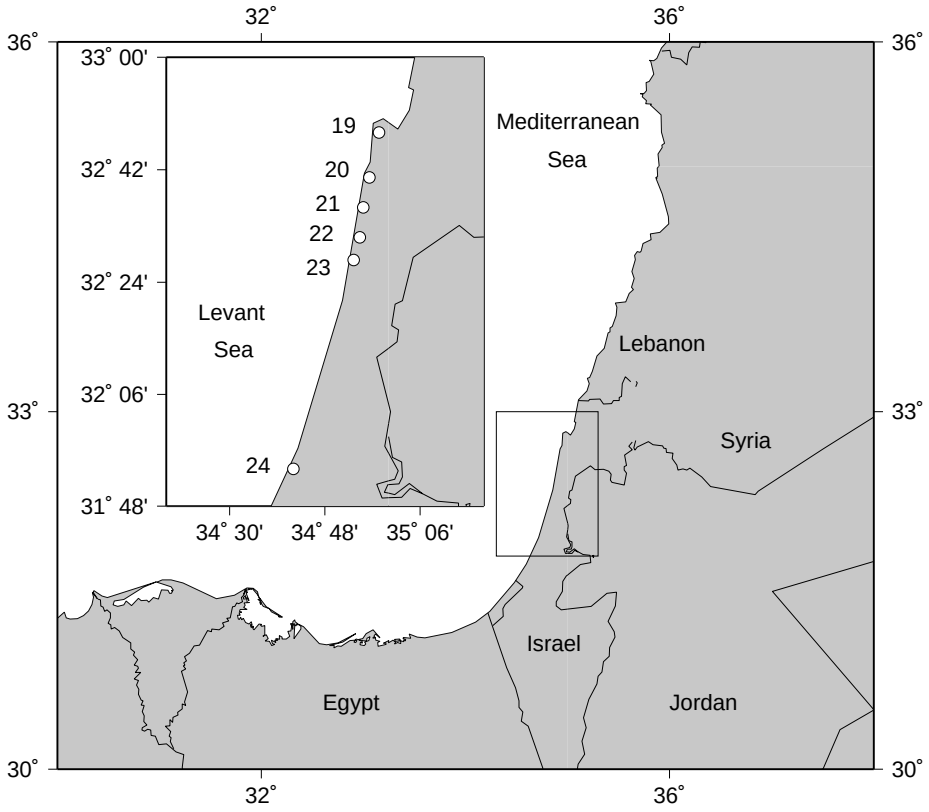

Figure 9.13: Sites along the coast of Israel, ranging between Haifa (site 21) and Yavne Yam (24). Predictions for these RSL sites are shown in Figures 9.14.

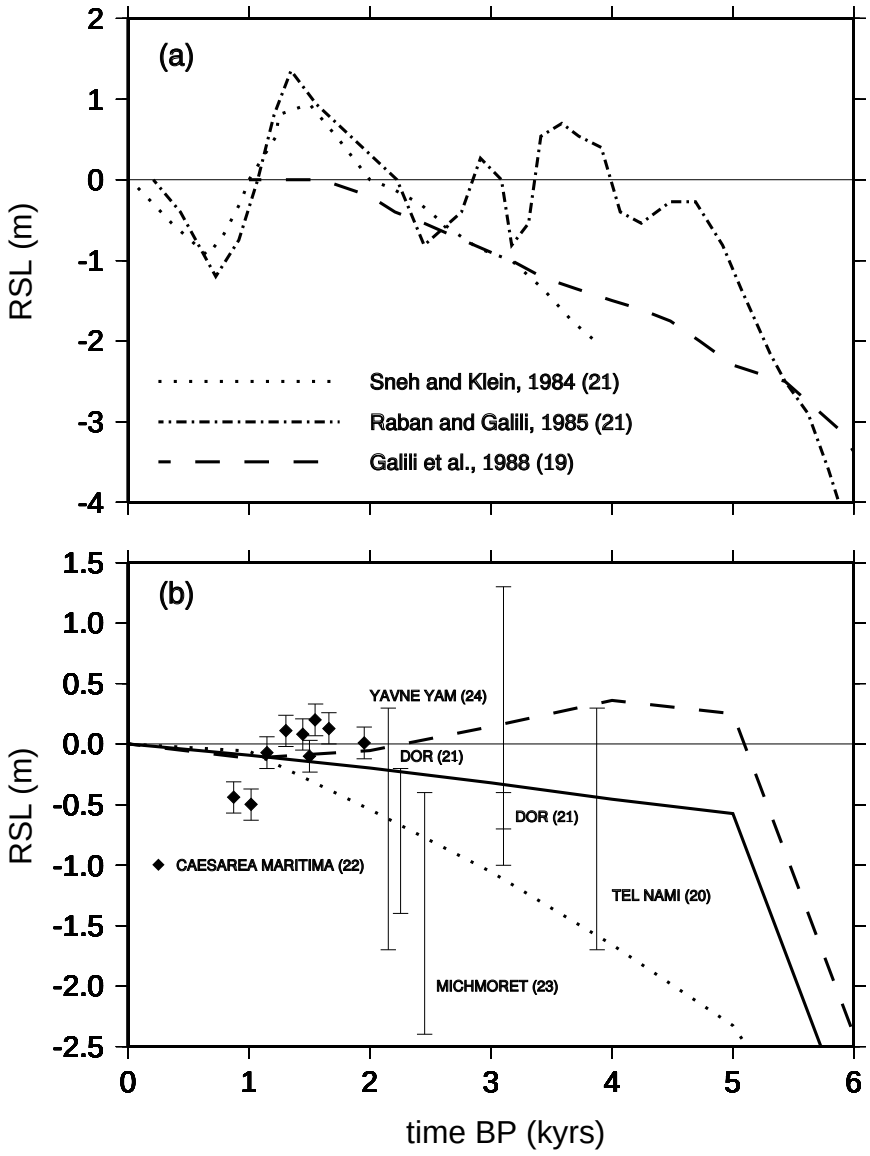

Figure 9.14: Relative sea level observations from a number of sites along the coasts of Israel, ranging between Haifa (site 21) and Yavne Yam (24) (see left frame). In (a) we have reproduced tentative RSL curves from the existing literature, while in (b) we compare the data of Sivan et al. (2001) and Sivan et al. (2004) with results based on the same models previously considered in Figure 9.12.

9.3.3 Effects of mantle rheology

Up to now, we have assumed that the REF viscosity profile, based on the work of Tushingham and Peltier (1991), provides a correct picture of mantle rheology. However, the REF viscosity profile has been recently challenged by various evidence related with GIA both on a regional and on a global scale, suggesting an upper mantle viscosity between 0.2 and 0.5×10^{21} Pa $\cdot$ s, well below the traditional (REF) value of 10^{21} Pa $\cdot$ s (Forte and Mitrovica 1996, Mitrovica 1996, Peltier 1996, Vermeersen et al. 1998, Lambeck et al. 1998, Spada 2001, Cianetti et al. 2002). Estimates of the lower mantle viscosity range between 5 and 50×10^{21} Pa $\cdot$ s (Nakada and Lambeck 1989, Mitrovica and Forte 1997, Lambeck et al. 1998).

Consistently with the above studies, we have adopted a new viscosity profile (different from REF) where the shallow upper mantle and the transition zone viscosities are kept fixed to $\eta_{SM} = 0.5 \times 10^{21}$ and $\eta_{TZ} = \times 10^{21}$, respectively. For the lower mantle, we have explored the effects of large viscosity values, with $\eta_{LM} = 10^{22}$ Pa $\cdot$ s. The purpose of this analysis is to show the trade–off between the choice of the viscosity profile and of the time chronology of the surface ice sheets. The results, shown in Figure 9.15 for a set of four different ice sheets chronologies (namely, ICE3G, ICE1+A3, ICE3G(S), and ICE1(S)), indicate that for a high–viscosity contrast across the mantle, all the ice models employed imply a clear submergence in the sites of Marseilles, Cap Corse, and Northern Adriatic, with no highstands predicted. The results obtained for Marseilles are qualitatively consistent with those by Lambeck and Purcell (2005), although here we are using different ice sheets chronologies. In these three sites, the predicted RSL curves vary in a range bounded by models ICE3G and ICE1(S) that among those considered show the largest contrasts in their Antarctic and Fennoscandian components. As we have verified, the disappearance of highstands when η_{LM} is increased to the current value is due to the variation of the trend of sea level change driven by the ice–load effects of the North America ice sheets, that changes from emergence to submergence. We have also verified that the contribution of Antarctica is almost unchanged with respect to the REF model,

since the comparatively smaller size of this ice aggregate implies a reduced sensitivity to a viscosity increase in the lower mantle. As shown in Figure 9.15, the large data uncertainties for sites (a–c) does not allow us to identify a preferred ice sheet chronology, although for the viscosity profile employed here ICE3G appears to be superior to the others in Marseilles and Cape Corse. The improved agreement of ICE3G with the observations along the coasts of France and Corsica is essentially due to the disappearance of the highstand that characterize the REF viscosity profile employed in our previous computations (see e. g., Figure 9.4), whose existence is clearly not supported by data.

Among those considered here, the only site showing an highstand is Djerba (see panel d) when ice models including an ESL of 27 m for Antarctica are employed (i. e., models ICE3G and ICE1+A3). For this site, an essentially stationary RSL curve since the end of deglaciation is obtained reducing the Antarctic ESL to 14 m (models ICE3G(S) and ICE1(S)). As we have already observed in Section 9.2.2 using the rheological profile REF, RSL observations in Djerba virtually only reflect the effects of Antarctica. Figure 9.15 shows that this is also true for a stiff lower mantle. This is illustrated by the small offset between predictions based on models ICE3G and ICE1+A3 (compare solid with dashed), that share the same Anctartic ice sheet but differ from the melting histories of other far–field aggregates. In a similar manner, changing the Antarctic time–history to S (dotted with dash–dotted), the predictions obtained are very similar to one another. By a suite of further computations (see Chapter 10) we have verified that the sensitivity to the chronology of Antarctica is indeed significant in the range of longitudes between $\sim$ 10 and $\sim$ 20°E, i. e. approximately between the Gulf of Gabes and the Gulf of Sirte, a region that has not shown a significant tectonic activity in the last $130,000$ years (see Morhange and Pirazzoli (2005) and references therein).

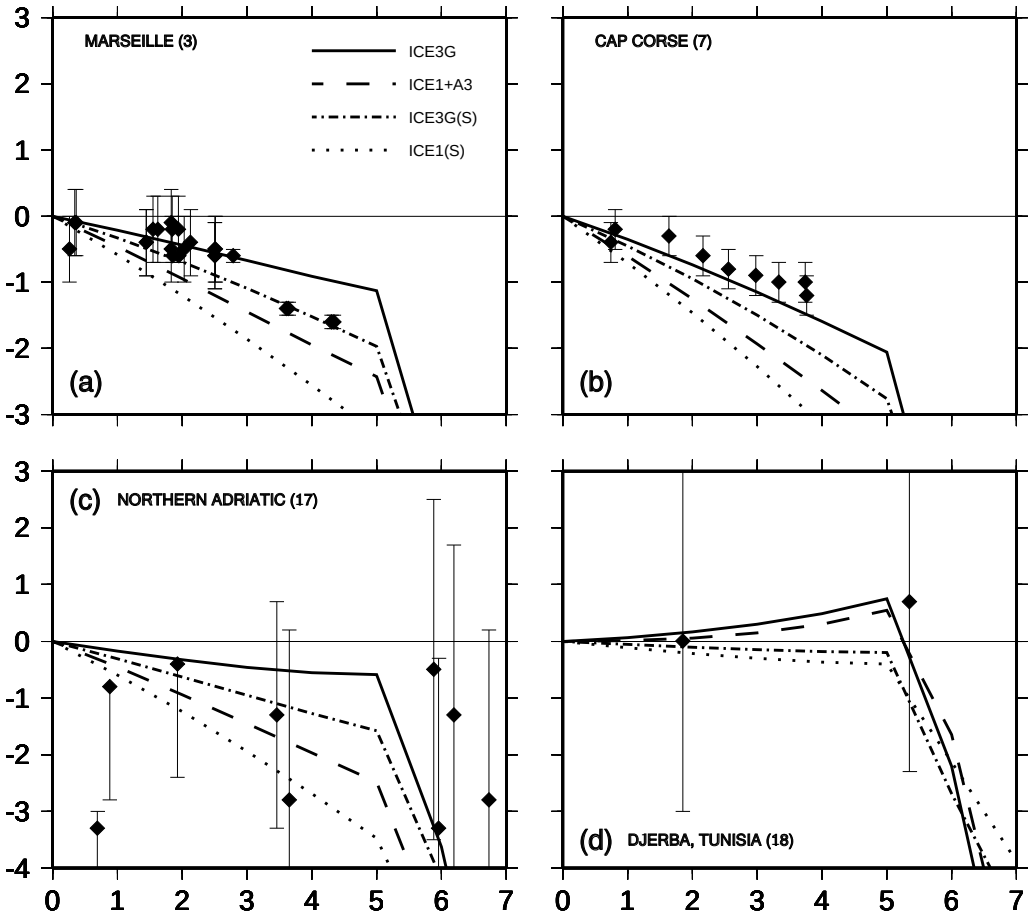

Figure 9.15: Relative sea level observations for Marseille (a), Cap Corse (b), northern Adriatic (c), and Djerba (d), compared to model computations based on mantle rheological profile characterized by a stiff lower mantle (see text).

9.4 Conclusions

Our analysis confirmed that the postglacial sea level changes across the Mediterranean exhibit a complex spatio–temporal variability through the Holocene Lambeck and Purcell (2005). By a straightforward analysis based on the solution of the Sea Level Equation, we have systematically explored the relative importance of some of the key factors that contribute to this variability, namely, the melting history of remote ice sheets (and particularly of Antarctica), and the viscosity of the lower mantle. The main results can be summarized as follows.

1. The pattern of sea level change in the Mediterranean can be described by means of two types of RSL curves. The first denotes a rising sea level through the late Holocene, while the second exhibits a late Holocene highstand that implies a sea level fall in the last ~ 5.0 kyrs. The extent of the so–called Clark's regions characterized by these distinct sea level patterns is strongly dependent upon the assumptions about the time–history of the late–Pleistocene ice sheets surrounding the Mediterranean. When the ICE3G chronology of Tushingham and Peltier is employed, a well developed highstand region is expected to surround the Mediterranean coasts, while the submergence region covers the bulk of the basin. Such peculiar pattern for closed basins has been named here as "Clark's zone VII". The assumption of a stationary Antarctic ice sheet and the enhanced effect of the melting of Fennoscandia disrupt zone VII when ICE1 is employed, leaving highstand zones along the indented coastlines of the Alboran Sea and South Tunisia. This clearly shows the significant role played by the melting of Antarctica upon the Holocene sea level variations in the Mediterranean.

2. Using model ICE3G, we have shown that along the coasts of South Tunisia (i. e., at Djerba) the effects due to the melting of Fennoscandia are almost exactly counterbalanced by that of North America. Such fortuitous cancellation make the highstand of ~ 2.0 m predicted in this region for this ice-sheets chronology

only sensitive to the effects of the remote Antarctica ice sheet. An highstand is indeed suggested by both the available RSL observations and tentative RSL curves at Djerba, but their resolving power is not sufficient to constrain its amplitude unequivocally. Incorporating within ICE3G a suite of plausible models for the melting of Antarctica during the last 6.0 kyrs, all characterized by a sensibly reduced ESL at the LGM, it has been possible to fully enlighten the sensitivity of RSL observations from South Tunisia to the details of the time–history. A late–Holocene highstand of ~ 1 m in this region is predicted when Antarctica is assumed to melt at a constant rate between 12.0 and 5.0 kyrs BP, and its amplitude is enhanced (nearly doubled) if a late ice re–advance is assumed. On the contrary, a delayed melting of Antarctica until 1 kyr BP is responsible for a regular sea level rise since 6.0 kyrs BP. Only an improved spatial coverage and sampling frequency of the RSL data, made difficult by the large tidal excursions in the Gulf of Gabes Sammari et al. (2006), could help to put tight bounds on the details of the melting chronology of Antarctica.

3. In the last part of the manuscript we have studied the impact of uncertainties on lower mantle viscosity on the results previously obtained. An increase of η_{LM} from 2×10^{21} to 10^{22}, a value more appropriate according to a number of authors, has a significant influence in the predicted RSL curves for the Mediterranean. In particular, this implies the disappearance of the late–Holocene highstand from the coasts of South France, that would improve the agreement with the observations available from this region. In general, an increase in lower mantle viscosity limits the variability of the predicted RSL curves corresponding to different assumptions about the chronology of Antarctica. For the revised viscosity profile, the confirmation of the existence of a late–Holocene highstand in Djerba would indicate for Antarctica an ESL consistent with the value implicit in ICE3G, whereas an essentially stationary sea level would be suggestive of a sensibly reduced ESL.

Chapter 10

Holocene deglaciation of Antarctica

10.1 Introduction

The geological evidences showed in Figure 9.12 and reviewed in Section 10.2.2 below (Figure 10.6), indicate that in SE Tunisia sea level has been continuously falling during the mid– to late–Holocene, and that a peak of $\sim$ 2.0 m above the present datum was reached between 6.0 and 7.0 kyrs BP[1]. Since no significant tectonic activity has been reported in this area during the last $\sim$ 130 kyrs (see Morhange and Pirazzoli, 2005 and references therein), the observed relative sea level variations are thought to only reflect the effects of hydro–isostatic adjustment.

In the previous Chapter we have noticed that the observed mid– to late–Holocene sharp highstand in SE Tunisia mostly reflects the history of melting of the Antarctic ice sheet, since contributions to relative sea level from the two major northern Hemisphere ice sheets (Laurentia and Fennoscandia) have opposite sign and almost

[1]Here and in the following, unless differently stated, the RSL data published in the literature have been converted from ^{14}C to calendar time scale using the radiocarbon calibration program available at http://radiocarbon.ldeo.columbia.edu research/radcarbcal.htm by Fairbanks et al. (2005).

cancel out each other in this particular region. Starting from the evidence in SE Tunisia, we have elaborated on the previous results of Chapter 9, in an attempt to constrain the melting history of Antarctica from available RSL observations. We have found that to explain amplitude and timing of SE Tunisia sea level highstand, the total equivalent sea level (ESL) of Antarctica may be reduced approximately by a factor of two relative to the global deglaciation model ICE3G (Tushingham and Peltier, 1991), provided that melting is allowed to occur catastrophically between 7.0 and 8.0 kyrs BP. This revised ESL and melting history for Antarctica is compatible with evidence from antarctic studies (Bentley, 1999) and, as it is shown here for the first time, with RSL observations ranging from a global to a Mediterranean scale.

The scenario that has emerged from this study is at variance with the Shepard school of thought, which suggests a nearly continuous (monotonous) sea level rise since 18.0 kyrs BP (see e. g., Kidson, 1982). Rather, it agrees with the Fairbridge school that favors a more episodic sea level rise (Fairbridge, 1961). Along these lines, Ruddiman (1987) has proposed and compared three different deglaciation models:

1. the "smooth deglaciation model",
2. the "french two–step" deglaciaton model, with maximum rates from $14,000$ to $12,000$ and from $10,000$ to $7,000$ radiocarbon years BP,
3. the"younger Dryas" deglaciation model which differs from (2) by a mid–deglacial reversal with significant ice growth at $11,000$–$10,000$ radiocarbon years BP.

Evidence in support of two surges in melt water at about $14,000$ (referred to as MPW–1A) and $11,000$ radiocarbon years BP (MPW–1B) came from the fundamental work of Fairbanks (1989), who extended an existing coral–reef sea level curve for Barbados to the last glacial maximum (Figure 10.1). Fairbanks et al. (1992) and Blanchon and Shaw (1995) argued that MWP–1A and MWP–2A may relate to a two step–wise collapse of Laurentide. While according to Bassett et al. (2005)

a sudden melting of Antarctica could be the "prime mover" of MWP–1A, Peltier (2005) rejects a significant role of this ice sheet.

Sea level records from drowned *Acropora palmata* in the Caribbean analyzed by Blanchon and Shaw (1995) have documented three other possible catastrophic rise events (CREs):

1. CRE1 (with an amplitude of 13.5 m, 14.2 kyrs BP),

2. CRE2 (7.5 m, 11.5 kyrs BP),

3. CRE3 (6.5 m, 7, 6 kyrs BP).

CRE1 and CRE2 are synchronous to the two collapse events possibly experienced by Laurentide during deglaciation (Bond et al., 1992, 1993), and their timing coincides with that of MWP–1A and MWP–1B, respectively (see Table 1 of the review of Bentley, 1999).

More specifically, on the basis of terrestrial and submerged diamictons, Kaufman et al. (1993) have indicated the possibility of collapses of the Labrador Dome 14 and 11.5 kyrs BP, which further supports a North American origin for CRE1 and CRE2. As pointed by Blanchon and Shaw (1995), due to the small volume of ice remaining in the northern Hemisphere at the epoch of CRE3, its origin could be explained invoking a role of the Antarctic ice sheet. In this study, we have shown that allowing for a CRE3 of Antarctic origin helps to explain the RSL records in the Mediterranean during the last 8.0 kyrs. The traditional, monotonously melting ICE3G is in fact unable to simultaneously account for RSL observations in SE Tunisia and in the northern Mediterranean. As discussed in the following, the melting scenario proposed here also constitutes an improvement, in the Mediterranean region, with respect to competing models characterized by a delayed melting phase (Nakada and Lambeck, 1988) or by an ice re–advance during the late–Holocene (Goodwin, 1998).

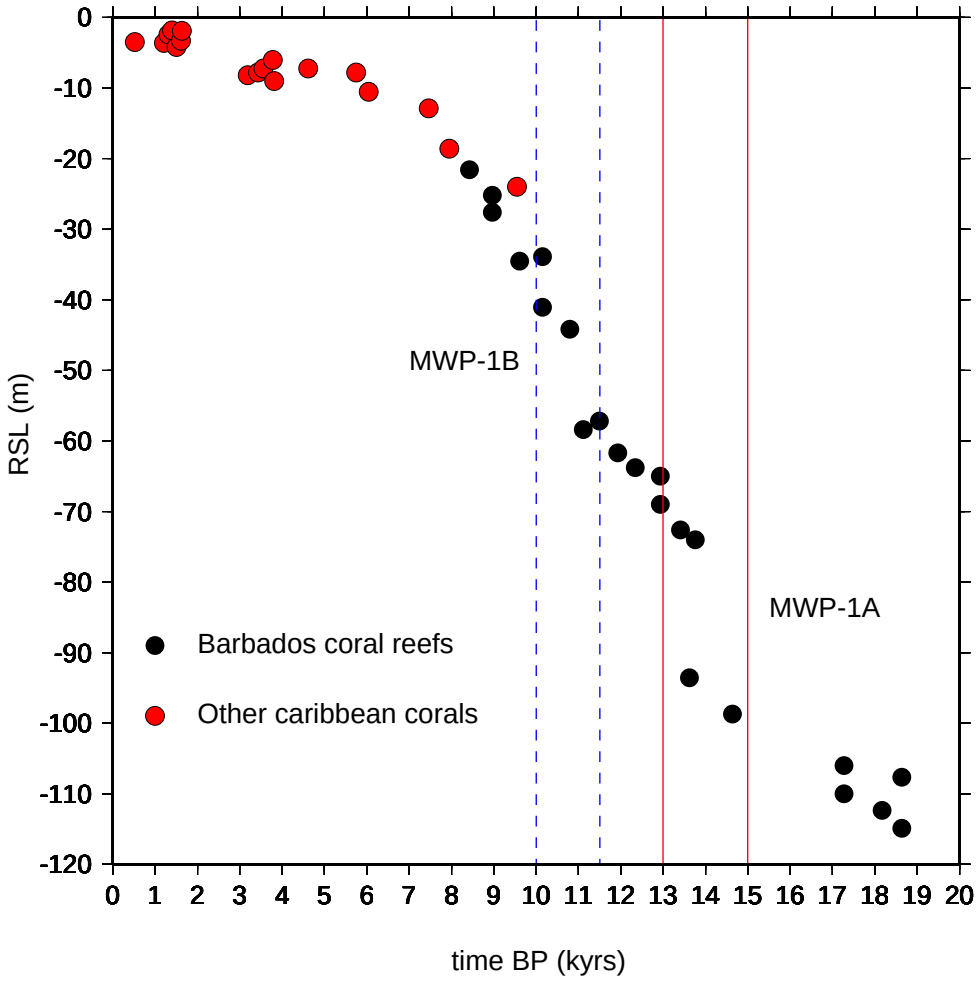

Figure 10.1: Barbados sea level curve (adapted and calibrated from the original curve of Fairbanks, 1989).

10.2 RSL curves for North Africa

10.2.1 Model predictions

The shape of the coastlines is important in determining the trend of postglacial RSL curves since this factor tunes the amplitude of the "continental levering" effect (Mitrovica and Milne, 2002), the process that mostly contributes to RSL variations in the Mediterranean (see Section 9.2). Since the Gulf of Gabes and the Gulf of Sirte have comparable shapes and latitudes (see Figure 10.2), we expect that solving the SLE provides similar patterns of sea level change.

This is confirmed in Figure 10.4 (top), where we show the RSL curves expected at Djerba, representative of the Gulf of Gabes, and Gulf of Sirte, when the ICE3G chronology is employed (the two sites are marked by a cross and a black dot in Figure 10.2). The major feature of solid curves is a sharp highstand at the end of deglaciation, with a peak amplitude of ~ 2 m at both sites. Dashed curves show that for model ICE3G–A3, in which ICE3G is deprived of its Antarctic component, no significant RSL variations are expected during the last ~ 6.0 kyrs. Thus, at these North African sites, during the mid– to late–Holocene the sea level has evolved *as if* Antarctica was the only active ice sheet (see dotted curves). Frames (c) and (d) pertain to the model ICE1. Since ICE1+A3 substantially reproduces ICE3G (top), at these sites RSL is basically insensitive to the history of deglaciation of the northern Hemisphere ice aggregates, in spite of significant differences between the Fennoscandian components of models ICE3G and ICE1 (see Figure 10.3 and Section 9.3). Dashed curves, relative to ICE1, show no RSL change during the last 5.0 kyrs, similarly to ICE3G–A3 (top). The peculiarity of the two sites considered in Figure 10.4 can be better appreciated in Figure 10.5, showing the highstand amplitude at $t = 5.0$ kyrs BP for all the North African sites marked by open circles and in Figure 10.2. For model ICE3G (solid), the highstand region ranges in the interval of longitudes between $\sim 10^\circ$ and $\sim 22^\circ$E, corresponding to sites from 12 to 44, respectively.

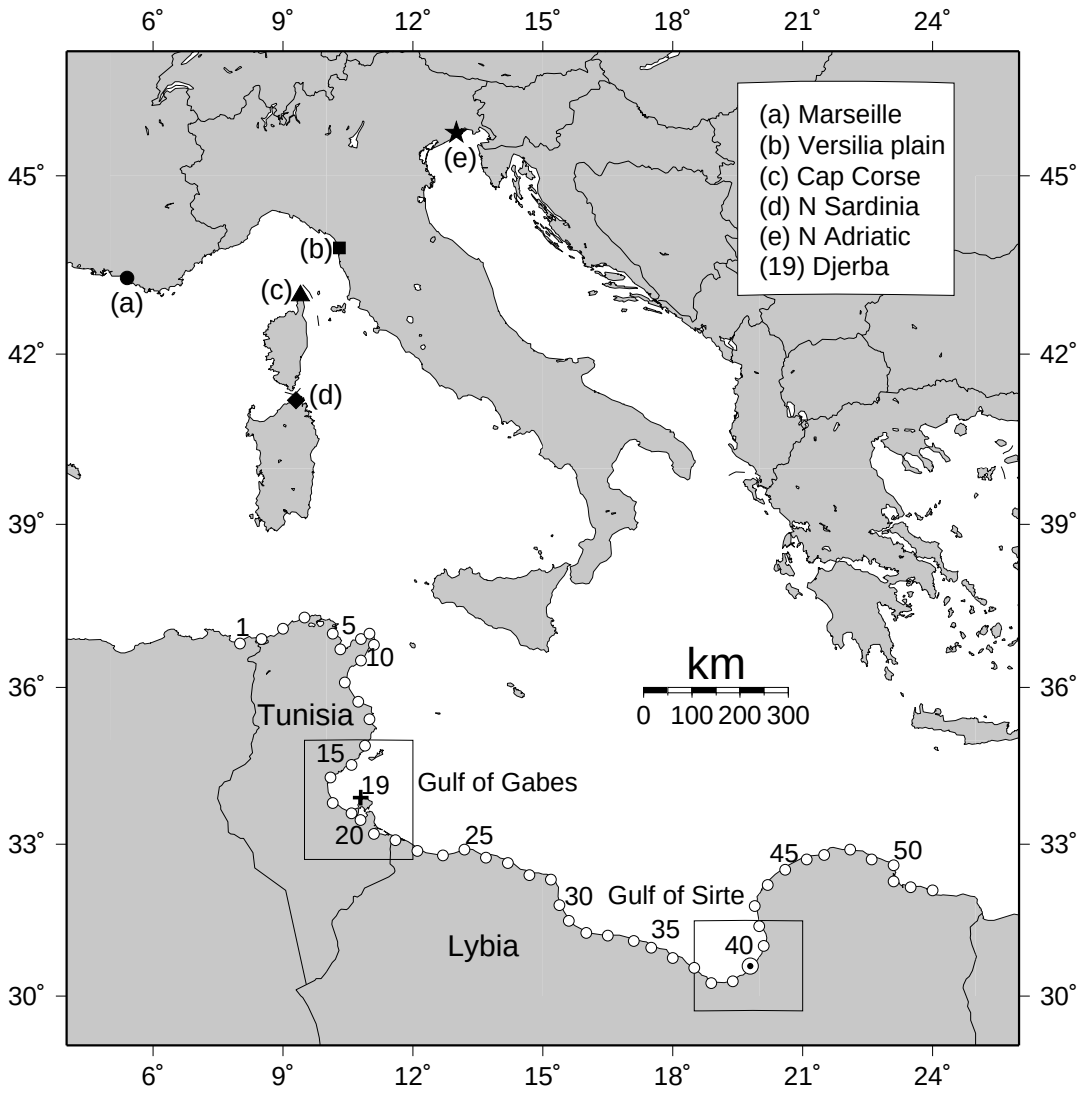

Figure 10.2: Map of the tudy region showing the RSL sites of Djerba (site 19, cross) and Gulf of Sirte (40, filled circle), as well as a number of other equidistant test sites (open circles). Also shown are the northern Mediterranean RSL sites considered in the analyses of Figures 10.10 and 10.11.

By further computations, we have verified that beyond these limits the RSL curves show no highstands, but rather a monotonous submergence with a kink at the time corresponding to the end of deglaciation. Where the dashed curve (ICE3G–A3), crosses the horizontal axis, RSL only stems from the contribution of Antarctica (dotted). Djerba is close to one of these points, and another is found at the center of the Gulf of Sirte (site 40 in Figure 10.2), consistent with the observation that "continental levering" is magnified at deep inlets (Mitrovica and Milne, 2002).

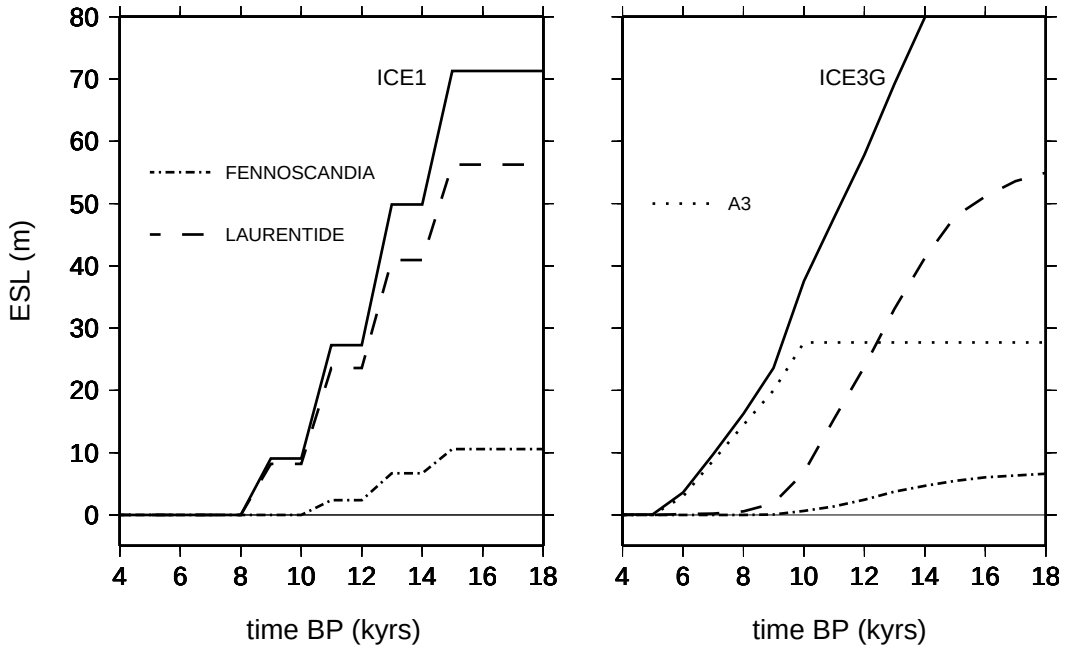

Figure 10.3: ESL for models ICE1 (left) and ICE3G (right) and relevant aggregates (readapted from Figure 7.4). Other minor components of ICE1 and ICE3G are not considered. Notice that both in ICE1 and in ICE3G ESL varies in a stepwise manner.

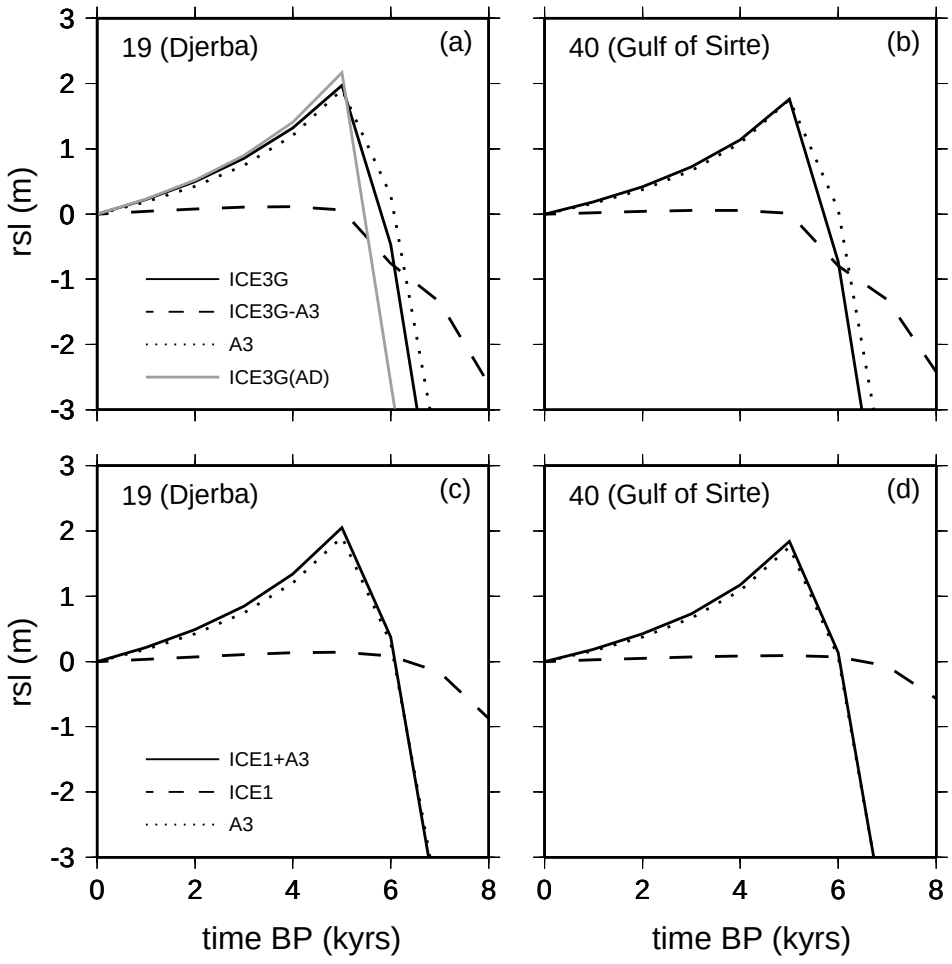

Figure 10.4: RSL histories predicted at Djerba (left) and Gulf of Sirte (right). In the top frames we use the ICE3G ice sheets chronology of Tushingham and Peltier (1991), ICE3G–A3 (i. e., ICE3G deprived of its Antarctic component A3), and A3. In the bottom frames, we employ the old ICE1 model of Peltier and Andrews (1976), ICE1+A3, and again A3. A marked highstand at 5.0 kyrs BP is visible as far as A3 is accounted for. The grey curve in frame (a) shows the results obtained using the simplified AD model of Antarctica introduced in Section 10.2.3.

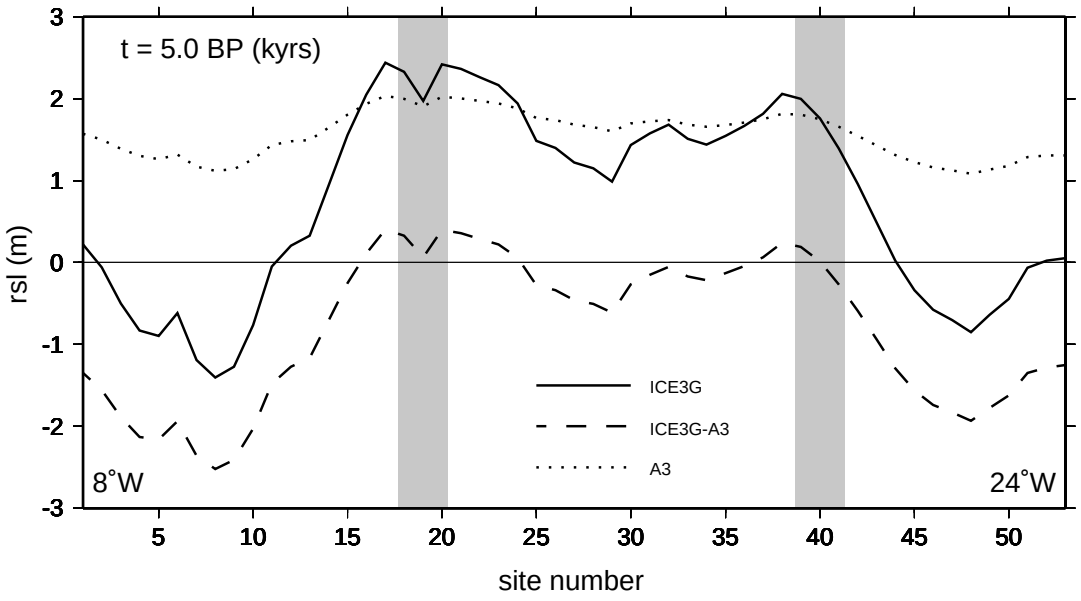

Figure 10.5: RSL at time $t = 5.0$ kyrs BP along the coasts of Tunisia and Libya in the range of longitudes between 8° and 24° W; numbers on the horizontal axis denote sites shown in Figure 10.2. Ice models are the same as in Figure 10.4 (top). Vertical shaded bars denote the location of Djerba and Gulf of Sirte, respectively.

10.2.2 RSL observations

From the analysis of previous section, the presence of a late–Holocene highstand is expected to be a stable feature along a significant portion of the coasts of Tunisia and Lybia (see Figure 10.5). This is confirmed by the available field observations for the Gulf of Gabes which are reported in Figure 10.6 (as far as we know no RSL observation is available to date for the Gulf of Sirte). As pointed by Sammari et al. (2006), the relatively large error bars which characterize some of the RSL data can be attributed to the considerable tidal excursions in this region.

As previously described in Section 9.3 the tentative RSL curve of Paskoff and Sanlaville (1983) (Figure 10.6, solid), suggests a maximum transgression of ~ 1.7 m between 6.4 and 4.3 kyrs BP, with the subsequent sea level fall which follows an erratic curve. Evidence from two fossilized bioclastic beaches (Jedoui et al. 1998, diamonds) also indicates the existence of a late–Holocene highstand, but the amplitude of emergence is only weakly constrained due to the large error bars. From a review of previous evidence and new indicators along the coast of the Gulf of Gabes, Morhange and Pirazzoli (2005) have recently published a quite detailed RSL history for Tunisia for the last 8.0 kyrs. Here we have analyzed and calibrated the single measurements of Morhange and Pirazzoli (2005) reproduced by solid circles in Figure 10.6. The observations are of improved precision relative to Paskoff and Sanlaville (1983) and Jedoui et al. (1998), and clearly indicate an anticipated marine transgression between 7.0 and 8.0 kyrs BP culminating in a sea level highstand between 6.0 and 7.0 kyrs BP, and followed by a quite irregular sea level fall. The best–fitting RSL history suggested by Morhange and Pirazzoli, here reproduced by a dashed curve (see also Figure 9.12, open circles), suggests a peak highstand of ~ 2 m at 6.0 kyrs BP. Finally, the recent study of Lakhdar et al. (2006), based on sedimentary record, also indicates the occurrence of a marine transgression at ~ 7.0 kyrs BP followed by a mid–Holocene highstand and provides a further tentative RSL curve for SE Tunisia, consistent with that of Paskoff and Sanlaville (1983) (gray curve in Figure 10.6). To summarize, all the available data and indicators

relative to the region of Gulf of Gabes denote, albeit sometimes weakly, a sea level highstand of 1–2 m between 5.0 and 7.0 kyrs BP. In the ensuing subsection, we will study how the timing and the amplitude of the highstand can be useful to constrain the melting history of Antarctica.

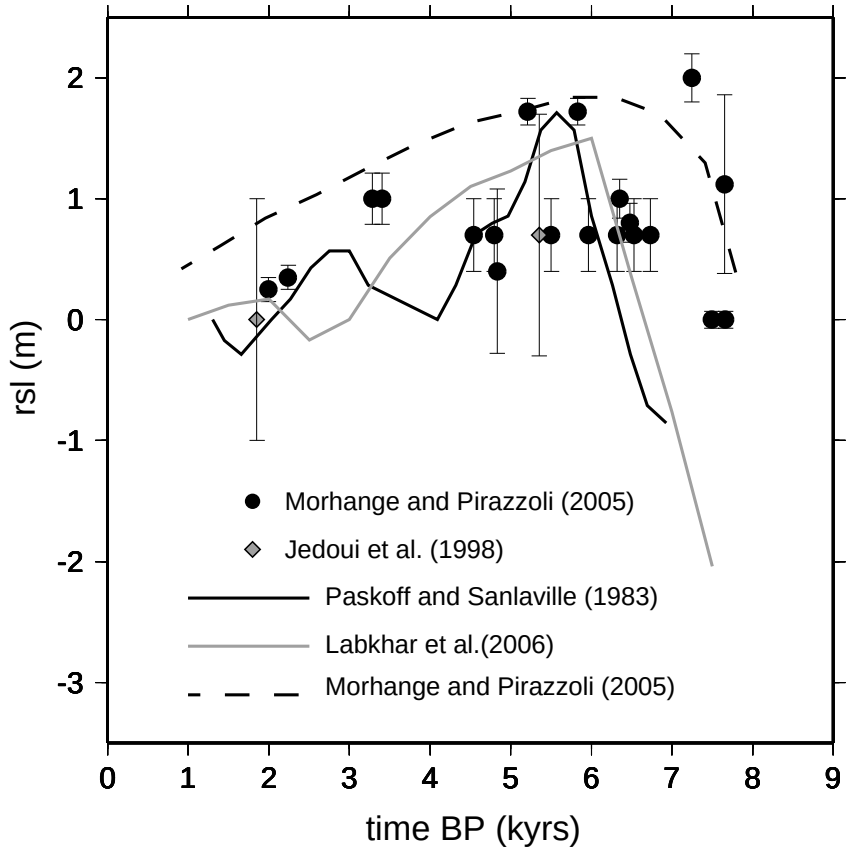

Figure 10.6: RSL data for SE Tunisia according to various authors. All the sources indicate the presence of a mid– to late–Holocene highstand in this region, with an amplitude between 1 and 2 m.

10.2.3 Sensitivity analysis

Since the Gulf of Gabes is in the far–field of Antarctica, it is appropriate to model this ice sheet by a simple disc of constant thickness and radius. Its time–history reproduces the main features of ice sheet A3 (the Antarctic portion of ICE3G), i. e., a quiescence until time $t = t_i$ kyrs BP followed by a complete deglaciation at a constant rate until time $t = t_f$ kyrs BP. For the A3 ice sheet, $t_i \sim 10.0$, $t_f \sim 5.0$ kyrs BP and the equivalent sea level is ESL ~ 28 m, comparable with the figure of 24 m proposed in the classical work of Denton and Hughes (1981) (see Figure 10.3). The simplified Antarctic ice model proposed here will be henceafter referred to as AD model, while with RAD we will indicate a disc model with a total equivalent sea level ESL(RAD)=ESL(AD)/2 $\approx$ 14 m. The equivalence between ICE3G and ICE3G(AD) can be quantitatively appreciated by inspection of the grey curve in Figure 10.4a.

In Figure 10.7, contour lines show the highstand peak amplitude HS_{max} predicted at Djerba (site 19 in Figure 10.2) for $0 \leq t_f \leq t_i$, while shades of gray in the background denote values of t_{HS}, the highstand epoch (see caption on top). Insets show the time–history of AD (left) and RAD (right), which here represent the Antarctic components of the global time–history of deglaciation (i. e., ICE3G, top), and ICE1 (bottom). Since $HS_{max} > 0$ it is apparent that an highstand is always predicted at Djerba. However, its maximum amplitude is greatly sensitive to the value of t_i and t_f, and increases towards the line $t_i = t_f$, corresponding to a sudden melting of the Antarctica. In particular, for ICE3G(AD), a value $HS_{max} \simeq 4.3$ m is obtained for $t_i = 6$ and $t_f = 5.0$ kyrs BP (not visible in figure). A qualitatively similar pattern is observed for ICE1+AD (c), with $HS_{max} \simeq 4.5$ m and a slight anticipation of melting ($t_i = 7.0, t_f = 6.0$ kyrs BP). Differences between frames (a) and (c) are only due to the distinct time–histories of the northern Hemisphere ice sheets in ICE3G and ICE1, respectively.

Circles and diamonds in Figure 10.7 indicate HS_{max} and t_{HS} values that agree with the qualitative curve of Morhange and Pirazzoli (2005) (MP05) and with the

observations of Paskoff and Sanlaville (1983) (PS83), respectively (see Figure 10.6). Peak amplitudes of the PS83 and MP05 highstands differ by $\sim$ 30 cm, with the former delayed by $\sim$ 1 kyr relative to the latter. From frame (a) we observe that to explain the PS83 highstand by the Antarctic model AD, the beginning of melting must be shifted backward of $\sim$ 1 kyr with respect to A3 (triangle), while t_f must not be significantly modified. An opposite trend is observed for the MP05 highstand, which requires a $\sim$ 2 kyrs anticipation of the termination melting that implies a significant shortening of the melting phase of Antarctica.

In order to fit the MP05 highstand using model ICE1+AD (frame c), the beginning of melting must be anticipated by $\sim$ 3 kyrs with respect to A3, and similarly the end of melting must be anticipated by $\sim$ 2 kyrs. By a suitable adjustment of the two free parameters t_i and t_f, it is also possible to fit the PS83 highstand (diamond). Thus, from frames (a) and (c) of Figure 10.7 it is apparent that by a simplified representation of A3, the HS_{max} and t_{HS} values suggested by the RSL curves of PS83 and MP05 can be always be fitted satisfactorily. As the geometry of the contour lines and the shaded regions indicate, the t_i and t_f values can be simultaneously constrained only by knowledge of both HS_{max} and t_{HS} for a given highstand (i. e., MP05 or PS83).

The sensitivity of North Africa RSL observations to the time–history of Antarctica, already addressed in Figure 10.4, motivates this analysis shown in frames (b) and (d) of Figure 10.7 where we use the RAD model of Antarctica, with ESL(RAD)=ESL(AD)/2 (see inset). Evidence in support to RAD comes from a wide spectrum of observations ranging from paleo–climatology to thermo–mechanical modeling of ice dynamics (see e. g., Bentley 1999 and Denton and Hughes 2002). When RAD is employed (b), HS_{max} is reduced by approximately a factor of 2 with respect to AD (a), that is, it scales with the amount of melt water released from Antarctica (a perfect scaling would indicate that the site of Djerba is in fact only affected by the melting of this remote glacier). While ICE3G(RAD) can only account for the PS83 highstand (diamond), ICE1+RAD can also explain MP05 (circle).

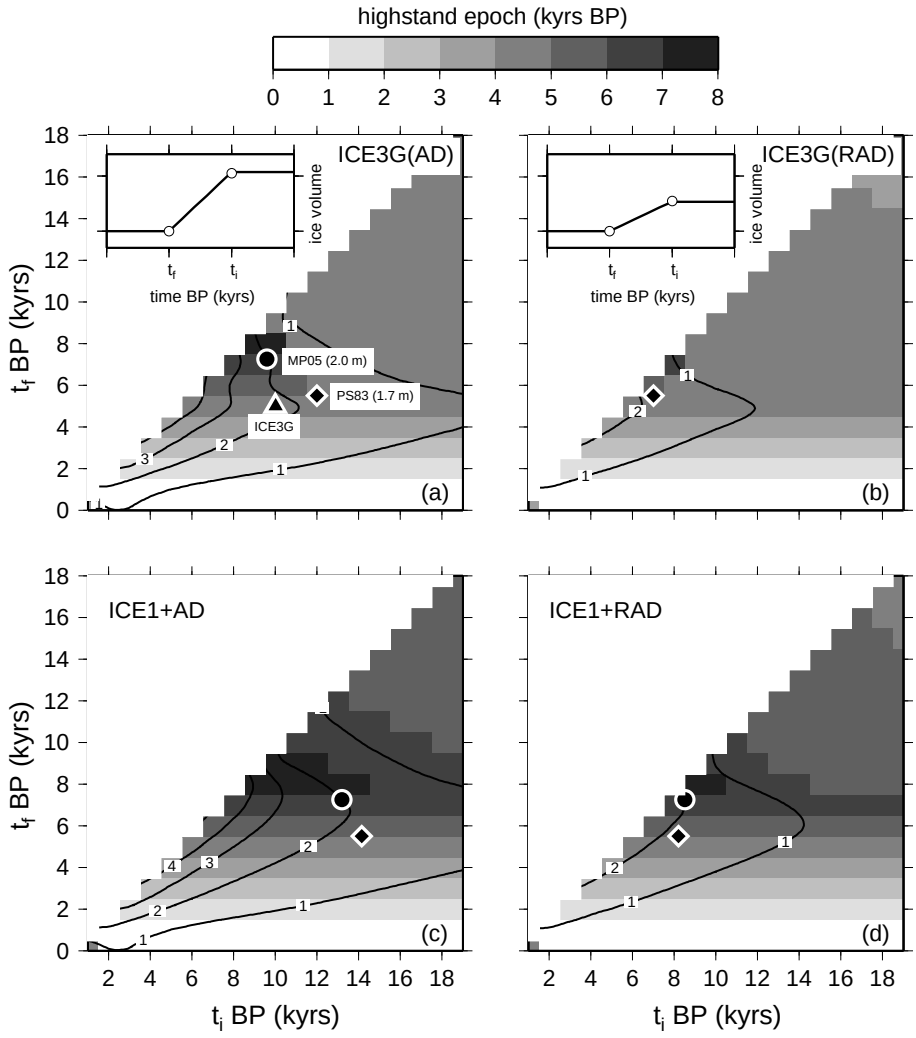

Figure 10.7: Highstand amplitude HS_{max} (contour lines, in meters) and highstand epoch t_{HS} (shades of gray) predicted at Djerba for all the possible values of parameters t_i and t_f, which describe the simplified time–history of Antarctica. Left and right frames pertain to the geometrically simplified models AD and RAD for Antarctica (their time–histories are shown in the insets). In top and bottom frames the chronologies of the northern Hemisphere ice sheets follow ICE3G and ICE1, respectively. Circles and diamonds show HS_{max} and t_{HS} values from the observations of MP05 and PS83, respectively (see text).

It is however clear from these diagrams that, for ICE1+RAD it is necessary to allow for a $\sim$ 1 kyr long melting phase from Antarctica to explain the observed highstand. Due to the coarse time discretization employed, the duration of this possible melting episode cannot be constrained more precisely.

10.3 Discussion

The study above has indicated that a drastic reduction of the ESL of Antarctica to 14 m may be reconciled with RSL observations in the Gulf of Gabes choosing appropriate t_i and t_f values. Also on the basis of the mentioned supporting evidence from Antarctic studies, this finding motivates us to test wether such revised melting history may improve the agreement with other rls observations on a regional or on a global scale. Here we will consider separately two facets of the problem, i. e., (i) the determination of an optimum ESL for Antarctica and (ii) the plausibility of a catastrophic rise episode that is suggested by the diagrams in Figures 10.7b and 10.7d.

The first issue is addressed in Figure 10.8, where we consider the chi–square misfit between data and predictions relative to various data sets, computed as in Spada et al. (2006). Since a full statistical study of the misfits obtained is not our purpose here, we proceed heuristically, leaving more rigorous analyses to future work. The misfit is computed as a function of the scaling factor $F(\%)$, which modulates ESL(A3). The C curves in Figure 10.8 refer to computations in which the ESL reduction of Antarctica is compensated by a uniform re–scaling of the volumes of all the other components of ICE3G to preserve its total ESL of $\sim$ 113.5 m. The figure shows results obtained for all of the 392 observations of the Tushingham and Peltier (1993) RSL database (hereafter "TP database", solid), and potentially interesting groups of data as well. In particular, we separately consider a set of TP sites located along the coasts of Antarctica (dotted, 4 sites) and in the Pacific Islands region (dashed, 30 sites). In addition, we employ two data sets pertaining

to the Mediterranean Sea (dash-dotted): the first includes nine out of the eleven TP observations for this region (the sites of Algiers and Beirut are excluded because of their recognized tectonic instability, see Meghraoui et al., 2004; Morhange et al., 2006), while the second collects independent RSL observations taken mostly from Lambeck et al. (2004a) and scrutinized in Chapter 9.

The solid curve in Figure 10.8 indicates that the agreement with the global TP observations improves with F, with the minimum misfit obtained when Antarctica is assumed to be stationary during the whole Holocene ($F = 0$), as in the ancestor ICE1 model of Peltier and Andrews (1976). As expected, the maximum sensitivity to variations of ESL(A3) is observed for the sites located along the coasts of Antarctica (dotted), suggesting a $\sim 60\%$ ESL reduction with respect to the ICE3G value of 28 m. Qualitatively similar results are obtained for the other regional curves, showing a minimum for F between ~ 30 to $\sim 40\%$. It is clear that when the global database is considered (solid), the sensitivity to modifications of the ESL of Antarctica is less pronounced than for the regional datasets. This is can be explained by the significant weight, in the full TP database, of sites belonging to Clark zones I and II (Farrell and Clark, 1976), which are the most influenced by the effects near–field glaciers. It is interesting to note that regardless of the F value, the revised Mediterranean set implies misfit values considerably smaller than for Med TP that may indicate an improved coherence of these RSL observations. The new data set also shows an improved sensitivity to variations of ESL, with the optimum value comparable with that inverted from the Antarctic records (dotted). This is a confirmation of our previous findings (see Chapter 9) regarding the value of improved Mediterranean RSL observations in constraining the mass balance of far–field ice sheets, and particularly of Antarctica.

Inspection of the "C" curve relative to the full TP database in Figure 10.8, reveals that a uniform scaling of the ESL of the ICE3G aggregates that compensates for the ESL reduction of Antarctica deteriorates the misfit relative to the previous computations (solid).

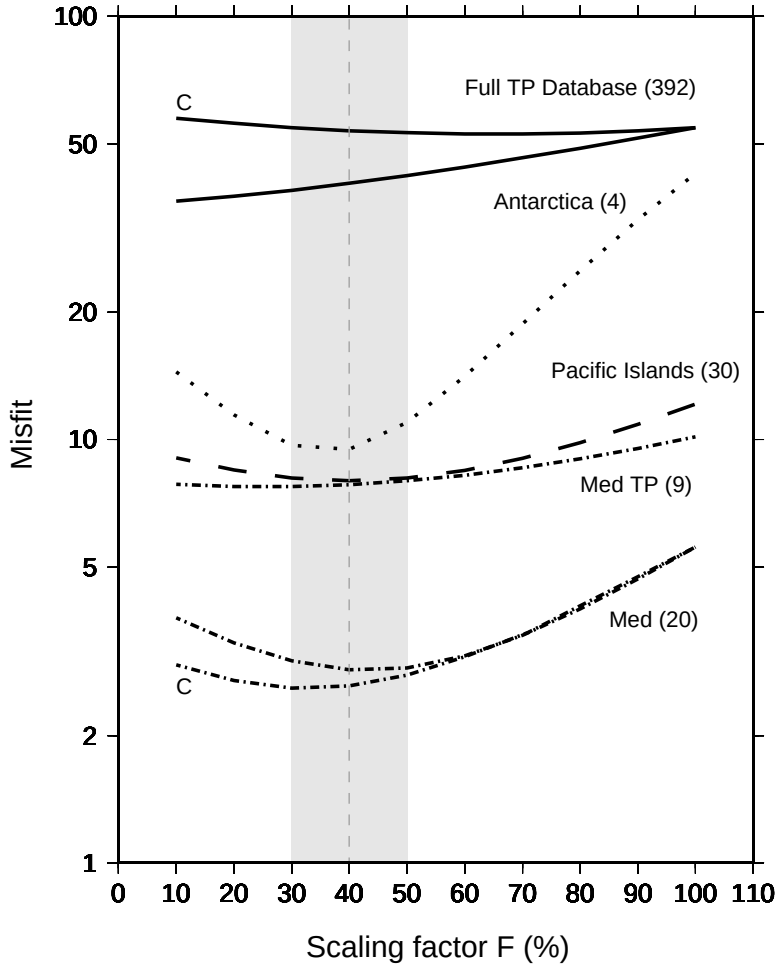

Figure 10.8: Effect of varying the ESL of model A3 of Antarctica on the misfit between observations and predictions on a global (solid line) and a regional scale. The preferred value of the scaling factor F is close to 40%, as evidenced by the shaded region. The two curves labeled by "C" refer to the case in which the ESL reduction of Antarctica is compensated by an equal and opposite uniform ESL increase over the other ICE3G ice elements. Notice that the misfit scale is logarithmic.

As we have directly verified, the reason is that an increase of the volumes of Laurentia and Fennoscandia does not help to better reproduce the RSL observations in these regions. As shown, the C curve is found to be basically insensitive to variations of the scaling factor F. In the case of the Med (20) dataset, imposing the eustatic constraint of ICE3G slightly alters the misft curve, now showing a minimum for $F \sim 30\%$. This possibly indicates that the revised Mediterranean observations can benefit from a simultaneous reduction of the ESL of Antarctica and a modification of the ICE3G chronology of Fennoscandia, the closest ice aggregate. The need of a revised chronology of Fennoscandia is also consistent with the findings of Lambeck et al. (2004a) and Chapter 9. Since mass conservation could not be attained unambiguously, in the ensuing computations od this section we have chosen not to compensate for the ESL reduction of Antarctica, also following Bassett et al. (2005). Possible explanations for the "missing water" problem, discussed by Bentley (1999), support the idea that at least some of the estimates of ice sheets volumes are not correct. The second issue, i. e., the details of the melting history of Antarctica, is addressed in Figure 10.9 by a misfit study aimed to constrain the t_i and t_f parameters of model RAD (see inset of Figure 10.7). Here RSL sites from the TP database and the Pacific Islands are considered in frames (a) and (b), respectively. In both cases we employ model ICE3G(RAD), in which the ESL of Antarctica is reduced from the reference value used so far of 14 m to the best–fitting value of 11.2 m, in agreement with the analysis of Figure 10.8. Using the full dataset (a), the best agreement with observations is met for $t_i = 15$ and $t_f = 14$ kyrs BP. This epoch approximately corresponds to the rapid melting event known as melt water pulse 1 (MWP–1A), first evidenced by Fairbanks (1989). This result supports a scenario in which Antarctica has been the main cause of the water pulse, consistently with the recent work of Bassett et al. (2005). While these authors have considered a limited set of far–field observations and a significantly different viscosity value for the lower mantle (see model VP2 of Table 5.2), here the plausibility of MWP–1A appears even from a global dataset.

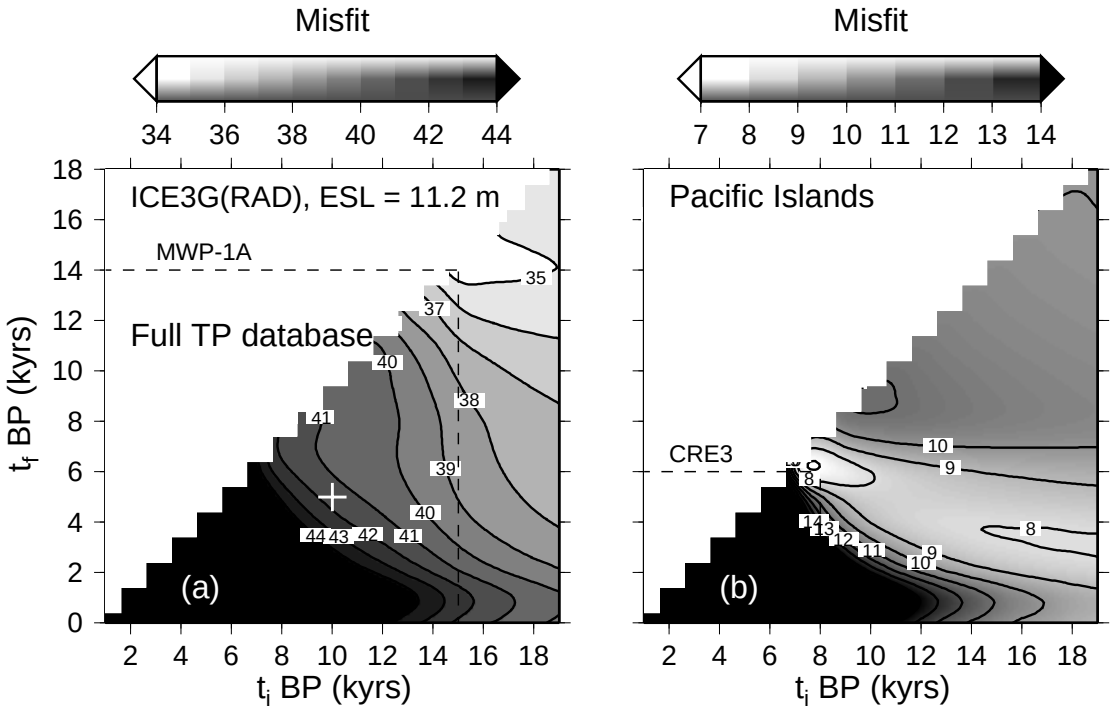

Figure 10.9: Misfit between predictions and observations on a global scale (left) and for the Pacific Islands (right), for various couples of the temporal parameters t_i and t_f of model RAD. The ESL of Antarctica is kept fixed to 11.2 m, according to Figure 10.8. The epoch of possible melt water pulses (MWP–1A and CRE3) are shown. A white cross shows the misfit obtained using the A3 time parameters.

However, since the misfit reduction that we obtain with respect to a RAD model with the same temporal parameters of ice sheet A3 (white cross in Figure 10.9) is not dramatically large, estimates of t_i and t_f from this search should be taken cautiously. Varying the ensemble of RSL observations may significantly affect values of the best–fitting parameters t_i and t_f. In the case study shown in Figure 10.9b, relative to the Pacific islands, the region of minimum misfit extends diagonally from point $\sim (t_i = 18, t_f = 3)$ kyrs to $\sim (t_i = 8, t_f = 7)$ kyrs, where the deepest minimum is met. Such elongated valley in the parameters space indeed provides a very weak constraint on the duration of the melting phase of Antarctica, which may range from ~ 15 to ~ 1 kyrs. We note that the region of plausible parameters contains the Antarctic melting phase of the original A3 model (namely, $t_i = 10, t_f = 5$ kyrs). This study shows that a water pulse cannot be rejected from the analysis of these Pacific Islands observations, but its epoch (~ 8 kyrs BP) is shifted onward significantly with respect to MWP–1A (compare with Figure 10.9a). This melt water pulse may coincide with the catastrophic rise event 3 (CRE3) discussed by Blanchon and Shaw (1995), the last of a sequence of three episodes the first of which corresponds to MWP–1A (CRE1).

The issue of how the melting scenarios for Antarctica suggested by Figures 10.7 and 10.9 may influence the Holocene RSL variations across the Mediterranean basin is addressed in Figure 10.10. Instead of considering the Med data as a whole, as previously done in Figure 10.9, here we discuss in detail six representative sets of observations (sites locations are shown in Figure 10.2). With the sole exception of Djerba, data and error bars are taken from the work of Lambeck et al. (2004a). By a trial–and–error approach, we have subsequently scrutinized five possible chronologies for the remote ice sheets, suggested by the results of Figure 10.9 (see inset in Figure 10.10a). The first is the classical ICE3G model (solid curves), which has been employed as a reference scenario since the onset of our discussion. In addition to ICE3G, here we deal with other ice models characterized by various RAD chronologies. Numbers in brackets following the ice sheets names indicate values of

t_i and t_f, in kyrs BP, pertinent to the RAD time history. In particular, a melt water pulse is accounted for by models ICE3G[15–14] (MWP–1A), ICE3G[8–7](CRE3) and ICE1[8-7](CRE3). In this analysis, we also considered model ICE3G[18–3], the chronology characterized by the very long melting phase suggested by the results of Figure 10.9b. This particular model, in which Antarctica is subject to a delayed melting with respect to A3, is broadly similar to the one termed "ANT 3a" by Nakada and Lambeck (1988), characterized by a significant melting (ESL $\sim$ 3 m) over the past 6 kyrs. Here we have not analyzed other competing chonologies that support an ice sheet re–advance during the late–Holocene (Goodwin, 1998). The re–advance would cause a global highstand followed by a sea level fall that cannot explain the observations in the northern Mediterranean (see Chapter 9). To accomplish the analytical results of Figures 10.10, Figure 10.11 summarizes misfit values at each site for the ice models tested.

Even from a cursory inspection of Figure 10.10 shows that ICE3G is unfit to describe the Holocene sea level rise at the Mediterranean sites considered, which confirms the pristine observations of Chapters 8 and 9. In particular, it fails both in predicting the slow and monotonous trend of sea level rise observed in the sites of Marseilles and N. Adriatic (a, e), and it is also inappropriate at Cap Corse (c), where data suggest a rapid sea level rise in the last 5.0 kyrs. While the agreement with the observations is qualitatively acceptable for Versilia Plain (b) and N Sardinia (d), in the case of Djerba (f) ICE3G produces an highstand of the correct amplitude, but significantly delayed (of about 2 kyrs) with respect to that observed by Morhange and Pirazzoli (2005) (see also Figure 10.7). The overall inadequacy of ICE3G is also apparent from Figure 10.11, where misfits from individual sites are shown by dashed lines, whereas thick solid curves show average misfit values for the viscosity profile VP1 and for the rheological profile of Bassett et al. (2005) (VP2) (see Table 5.2). Introducing a melt water pulse that mimics MWP–1A (i. e., model ICE3G[15–14], dotted), greatly improves the performance in Marseilles, Cap Corse, and N. Adriatic (see also Figure 10.11), while for Versilia and N Sardinia

the agreement with observations improves in the last $\sim$ 5 kyrs but it grows worse prior to this period. In Djerba, ICE3G[15–14] basically reproduces the ICE3G–A3 results of Figure 10.4a, since an early deglaciation of Antarctica enhances the effects of northern Hemisphere aggregates at a later time. The late pulse CRE3 implicit in model ICE3G[8–7] deteriorates, with respect to ICE3G[15–14], the agreement with observations in Marseilles, Cap Corse, N. Adriatic, and Versilia Plain as quantitatively confirmed in Figure 10.11. However, the match is improved for N Sardinia and Djerba. In this latter case, the impulse anticipates the transgression, thus providing a better fit to the observed RSL.

Results on the effects of glacial isostatic movements in northern Italy and southern France (Chapter 8) have enlightened the sensitivity of vertical uplift in these regions to the time–history of the former northern Europe ice sheets. To shed light on this issue, in Figure 10.10 we also show results based on the ICE1 history of deglaciation, which differs from ICE3G for the melting history of Fennoscandia and, most importantly in this context, for an anticipated cessation ($\sim$ 2 kyrs) of the melting phase (Peltier and Andrews, 1976; Tushingham and Peltier, 1991) (see Figure 10.3). According to Figure 10.10f, this feature of ICE1 has a significant effect at Djerba, where model ICE1[8–7] now reproduces the observed highstand satisfactorily (grey, dashed). This is also observed for Marseilles (a), Cap Corse (c), and N. Adriatic (e), where improvements relative to ICE3G[15–14] are apparent for all the available observations (see also Figure 10.11). A close inspection of the results relative to Versilia in Figure 10.10b reveals that ICE1[8–7] helps to better explain the kink suggested by the RSL observation at $t \sim 8$ kyrs BP, which may be interpreted as a signature of CRE3. At the same epoch, ICE1[8–7] is also compatible with the data relative to N Sardinia. Finally, with dash–dotted curves we test the sensitivity of the Mediterranean records to an extended melting phase for Antarctica using model ICE3G[18–3]. While this model is generally fit to explain the northern Mediterranean sea level indicators, it clearly fails along the coasts of SE Tunisia (f), where the evidences support of a late–Holocene highstand of hydro–isostatic origin.

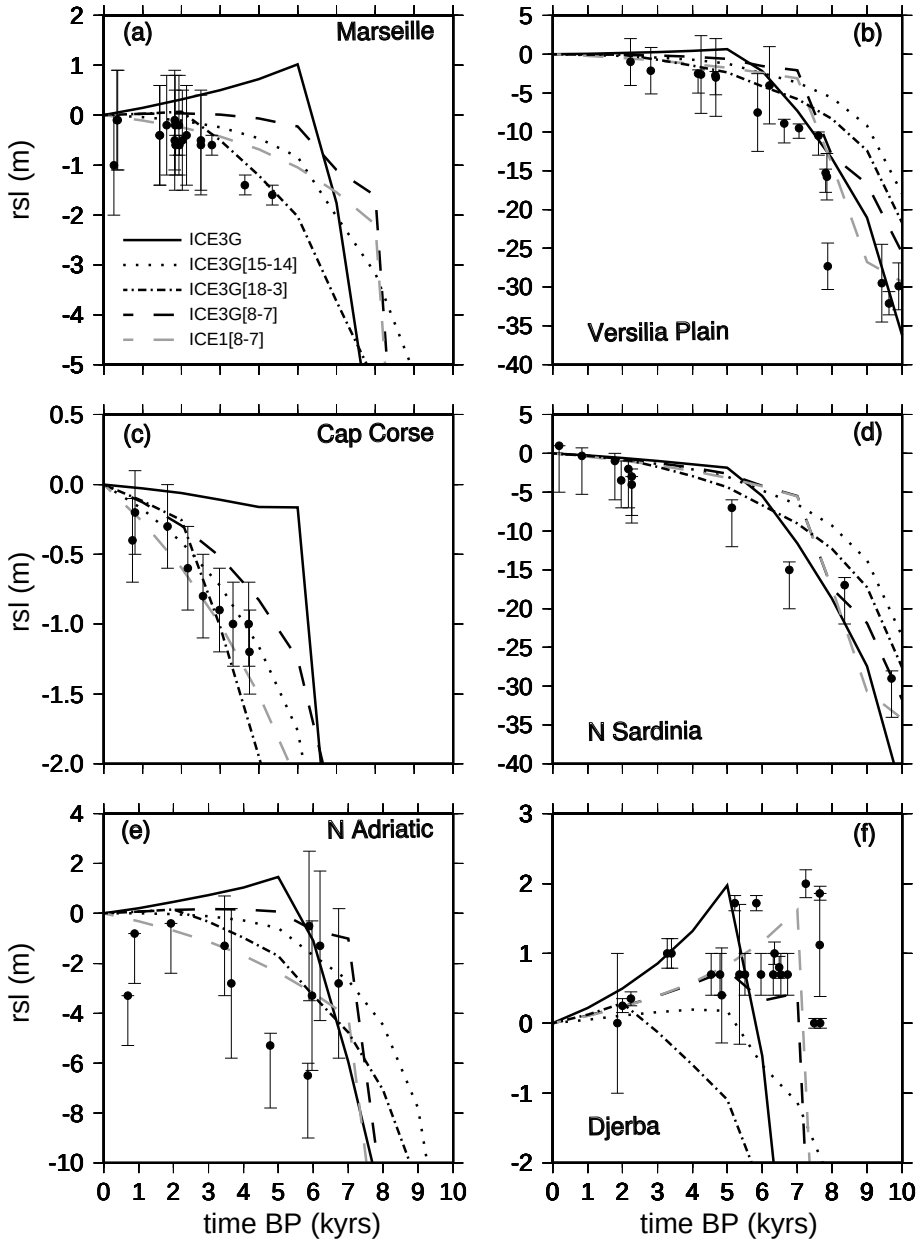

Figure 10.10: Observations and predictions relative to significant RSL sites from the revised Mediterranean data set (sites locations are shown in Figure 10.2). Here we use model ICE3G and four chronologies based upon ICE3G and ICE1, with "$[t_i$–$t_f]$" indicating the beginning and end of melting, respectively, in kyrs BP.

As shown in Figure 10.11 (thick black), the failure of ICE3G[18–3] in SE Tunisia produces a misfit increase with respect to the melt water pulse models.

To test the robustness of our results to variations of the viscosity profile, we have repeated the analysis of Figure 10.10 using the viscosity values suggested by Bassett et al. (2005), in which lower mantle viscosity exceeds the sublithospheric upper mantle viscosity by a factor of 80 (see model VP2 In Table 5.2). The results, summarized by thick gray curves in Figure 10.11, confirm that introducing a melt water pulse improves the agreement with the observations in the Mediterranean with respect to the classical ICE3G model. However, the overall misfit values are increased relative to the reference viscosity model VP1. As we have verified, this is mainly to be attributed to the inadequacy of VP2 to reproduce the observed highstand in Djerba.

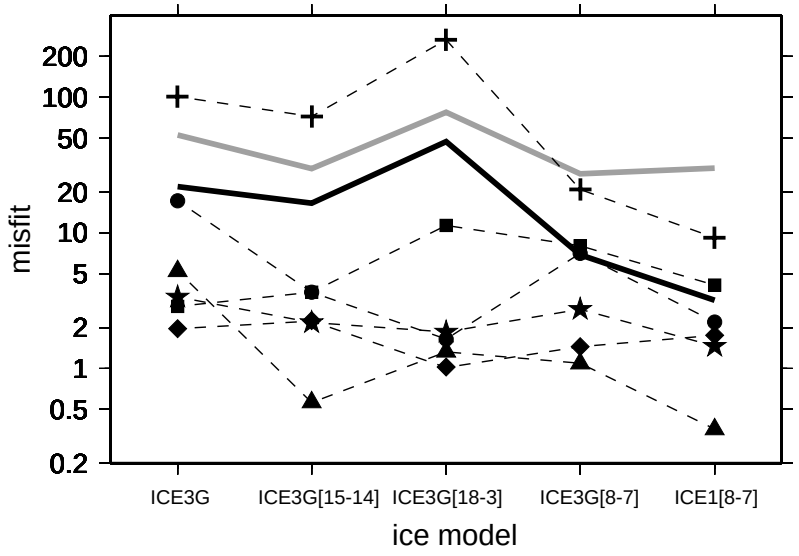

Figure 10.11: Misfist values computed for each of the ice models considered in Figure 10.10. Symbols used to denote the sites locations in Figure 10.2 are also employed here to label the misfit trends. Solid curves show average misfit values representative for all the sites considered. A thick gray line shows results obtained using the viscosity profile VP2 of Table 5.2.

10.4 Conclusions

The Holocene sea level record of SE Tunisia provide a unique opprtunity for calibrating competing models for the history of deglaciation of Antarctica. Our conclusions can be summarized as follows.

1. Forward computations based on the sea level equation confirm previous findings of Chapter 9 that at the sites of SE Tunisia and Gulf of Sirte the RSL variations in the last 8 kyrs are mostly determined by the melting of the remote Antarctic ice sheet, due to the mutual cancellation of the contributions from the northern emisphere. Attempts to identify other sites worldwide sharing this features with SE Tunisia were unsuccessful. The RSL curves expected in this region for the deglaciation model ICE3G are characterized by a neat late–Holocene highstand, which broadly matches a suite of observations and geological indicators.

2. In a sensitivity analysis we have established how the choice of the temporal parameter describing the deglaciation of Antarctica affects the highstand amplitude and timing. Such analysis has shown that a sensibly reduced ESL for Antarctica, compatible with recent reassessments of the Holocene mass budget of this ice sheet (see e. g., Bentley, 1999, and Denton and Hughes, 2002), may lead to the observed highstands in the study region. In this latter case, however, a sudden melting model is preferred for Antarctica, in which a melt water pulse occurs between 8 and 6 kyrs BP, possibly coinciding with the CRE3 episode discussed by Blanchon and Shaw (1995).

3. To test the reliability of the results obtained from SE Tunisia, we have performed a further analysis aimed to constrain the ESL reduction of Antarctica from RSL observations on a global to regional scale. We have found that a $\sim$ 60% ESL reduction relative to ICE3G implies a general misfit reduction when observations from Antarctica, Pacific Islands, and the Mediterranean

are considered. When we consider the global TP RSL database, the best fit with the observations is obtained assuming a stationary Antarctic ice sheet through the Holocene. A further misfit reduction is achieved allowing for modifications of the time–history of Antarctica, and particularly introducing melt water pulses that have been found to approximately coincide with those suggested by independent investigations (Fairbanks, 1989; Blanchon and Shaw, 1995).

4. In the last part of the manuscript we have focussed our attention on the Mediterranean RSL observations, in an attempt to put bounds to the time–history of the late–Holocene ice sheets using an improved data set for this region extracted from the recent literature. A site–to–site study has shown that the Mediterranean RSL observations demand a CRE3 event of Antarctic origin between 8 and 7 kyrs BP. Allowing for such a pulse, and assuming a moderate viscosity increase across the mantle, our model reproduces both the SE Tunisia highstand at 7 kyrs BP and the generally monotonous sea level rise observed in the bulk of the Mediterranean and along its northern coasts.

5. The results obtained from the study of the Mediterranean record indicate that the CRE3 melt water pulse at $\sim$ 8 kyrs BP may have concluded the whole history of the last deglaciation. This view is in contrast with previous reconstructions of the Antarctic chronology in which the melting of this ice sheet throughout the Holocene (Nakada and Lambeck, 1988). With the preferred viscosity value adopted here (VP1), such a delayed melting would fit the northern Mediterranean observations reasonably well (see Chapter 9) but would be totally unable to reproduce the observations relative to SE Tunisia (Morhange and Pirazzoli, 2005). As we have verified, the misfit would even be larger in the case of model VP2.

6. In the absence of observations from SE Tunisia, the Mediterranean observations would be reasonably reproduced by ice chronology ICE3G[18–3], which

is broadly consistent with the Ant-3a melting history previously introduced by Nakada and Lambeck (1988) to explain postglacial RSL in the Australian region. However, when the datum from SE Tunisia is accounted for and it is assumed to be reliable, the only model that reconciles northern and southern Mediterranean RSL curves is the melt water pulse model CRE3.

Chapter 11

Final remarks

In this work we have investigated the numerical and geophysical aspects of post–glacial isostatic readjustment, with particular emphasis on the Holocene and present–day sea level change in the Mediterranean Sea. Results of our investigations are reported in details at the end of the Chapters 6, 8, 9, and 10, and are summarized as follows:

1. In Part II of dissertation we have discussed the numerical aspects of the post–glacial rebound by introducing at first the theory of the sea level equation and then describing the pseudo–spectral method for its solution. Solving the SLE for a given Maxwell viscoelastic Earth model and a particular ice chronology allows to study a suite of geophysical processes accompanying the mass redistribution associated with the glacial isostatic adjustment, such as relative sea level variations, vertical deformations of the solid surface of the Earth, and variations of the shape of the geoid. We have presented the program `SELEN` for the computation of the sea level variations following the mass exchange between oceans and continental ice reservoirs. `SELEN` is a useful tool for computing different geophysical observables and therefore solving many problems in the GIA context. As described in Part III, we have adopted and tested the program to study the post–glacial rebound in the Mediterranean Sea.

2. We have investigated the GIA–related phenomena ascribed to the melting of the Würm Alpine glacier. By assuming a 120 km thick elastic lithosphere, a lower mantle viscosity of 2×10^{21} Pa $\cdot$ s, and keeping fixed the value of 10^{21} Pa $\cdot$ s for both the upper mantle and the transition zone (REF rheological model), we have solved the SLE for a simplified model of the Würm Alpine glacier based on geological, glaciological and paleo–ecological evidences. When considered alone, the melting of the Alpine ice cap is expected to mainly affect the northern Tyrrhenian and Adriatic coasts with a Holocene sea level drop typical of the peripheral depression zone. However, when the Alpine glacier is included in the global ice models ICE1 and ICE3G it is not possible to resolve the effects of the small ice cap given the large uncertainties of the RSL data which are more sensitive to the remote ice sheets and suggest the inadequacy of the global model ICE3G. The predicted present–day sea level trends show a fall of $0.1 - 0.3$ mm/yr when the Alpine glacier is considered in conjunction with the ICE3G, while, for ICE1 a sea level rise of $0.2 - 0.4$ mm/yr is expected. While the Alpine glaciers alone may account for an uplift rate of the solid surface of about 0.2 mm/yr in the Alpine region, when considered in conjunction to the remote ice sheets an average rate of subsidence of ~ 0.5 mm/yr corresponding to 1/3 of the observed is expected.

3. On the basis of the results obtained from the study of the Würm Alpine deglaciation, which have in particular enlightened the sensitivity of the RSL observations to the remote ice sheets, and the inadequacy of the widely employed ICE3G model, we have investigated the typology of RSL curves expected in the Mediterranean Sea. We have found the existence of two types of curves: *(i)* the first describes a monotonous to cuspidate sea level rise through the Holocene, while *(ii)* the second is characterized by a sea level highstand at 5.0 kyrs BP followed by a sea level fall. The extent of these two Clark's regions depends on the assumptions regarding the ice chronologies of the Pleistocene remote ice sheets. In particular the extent of the highstand region surrounding

the Mediterranean coasts is found to be mainly influenced by the Antarctic ice chronology. Along the South Tunisian coasts the effects of the melting of the major North Hemisphere ice sheets countervail each other making this region highly sensitive to Holocene Antarctic deglaciation. By reducing of one–half the eustatic contribution and assuming a suite of plausible chronologies for the Antarctic ice sheet in the model ICE3G we have enlightened the sensitivity of the observed sea level highstand in Tunisia to the time–history of Antarctica. While the RSL data from the Northern Mediterranean coasts are in agreement with a delayed melting of the Antarctic ice sheet ending at 1.0 kyrs BP, the observations from Tunisia suggest a linear deglaciation between 12.0 and 5.0 kyrs BP. When the latter Antarctic ice chronology is included in ICE1 the agreement between the whole dataset and predictions significantly improves as a consequence of the reduction of the highstand region extent along the Northern Mediterranean coasts. Furthermore, the agreement between data and predictions for the northern coasts improves when a value of 10^{22} Pa $\cdot$ s is assumed for the lower mantle viscosity. A high lower mantle viscosity implies a noticeable reduction of *(i)* the highstand regions extent, and *(ii)* the highstand peak in SE Tunisia. Given the sensitivity of SE Tunisia to the Holocene Antarctic melting, a more accurate and precise RSL evidence is needed to constrain the eustatic contribution and the melting rates of Antarctica.

4. In view of the results obtained from the investigation of the Clark's zones in the Mediterranean Sea we have studied the sensitivity of the North African coast (from Gulf of Gabes to Gulf of Sirte) to Holocene Antarctic melting. In the range of longitudes between 10° and 20° W, a sea level highstand of $1.0-2.0$ m at 5.0 kyrs BP is expected for ICE3G. Along this coast the melting of northern Hemisphere ice sheets produces a stable sea level for the last $5.0-6.0$ kyrs and the predicted highstand is solely driven by the Antarctic melting. We have calibrated recently published ^{14}C RSL data from Djerba (SE Tunisia). The new evidences show an anticipated sea level highstand of ~ 2.0 m between 6

and 7 kyrs BP kyrs BP followed by a sea level drop to the present–day position. By varying the temporal parameters describing the deglaciation of Antarctica and assuming for this remote ice sheet a sensibly reduced equivalent sea level, we have reproduced the observed sea level highstand by means of a sudden Antarctic melting occurring between 8 and 6 kyrs BP. We have verified that for a $\sim 60\%$ ESL reduction of Antarctica the agreement with RSL data from far–field sites improves. By keeping the Antarctic ESL value fixed to 11.2 m we have found that the misfit between RSL prediction and observations from the Pacific Islands, where the hydro–isostatic effects drive the Holocene sea level variations, reduces when a catastrophic melting (CRE3 event) is assumed to occur between 8 and 7 kyrs BP. However, an improved agreement between far–field data and prediction is not univocally attained for this ice chronology and also an Antarctic melting through the entire Holocene is fit to reproduce the observations. Though a linear Antarctic melting through the Holocene is in good agreement with the observations from the North Mediterranean sites, a catastrophic deglaciation at 8 kyrs BP is able to reconcile both the Tyrrhenian RSL data and the sea level highstand in SE Tunisia yielding the best fit value.

Appendix A

Maxwell visco–elasticity

On the basis of the *correspondence principle* (e. g., Fung, 1965), the governing equations for a linear viscoelastic continuum can be retrieved once the viscous ones are known.

By considering for simplicity unidimensional constitutive equations, the elastic and viscous components of the Maxwell rheology are described by

$$\epsilon_l = \frac{\sigma}{2G}, \tag{A.1}$$

and

$$\dot{\epsilon_v} = \frac{\sigma}{2V}, \tag{A.2}$$

respectively, where ϵ_l is the elastic deformation, $\dot{\epsilon_v}$ is the rate of viscous deformation, σ is the applied stress, G is the elastic modulus of rigidity, V is viscosity and the dot denotes time derivative. By deriving Eq. (A.1) with respect to time and combining it in series with the viscous component (Eq. A.2), the rate of the total deformation reads

$$\dot{\epsilon} = \dot{\epsilon_l} + \dot{\epsilon_v}, \tag{A.3}$$

that is

$$\dot{\epsilon} = \frac{\dot{\sigma}}{2G} + \frac{\sigma}{2V}, \tag{A.4}$$

which represents the constitutive equation for a viscoelastic Maxwell continuum, and which incorporates both the effects of elasticity and the behavior of a viscous fluid. In the particular case of a deformation constant with time ($\dot{\epsilon} = 0$), the stress evolves as

$$\sigma = \sigma_0 e^{-t/\tau}, \tag{A.5}$$

where $\tau = \nu/\mu$ is the Maxwell relaxation time. Following the Laplace transformation of the differential equation (A.4) it comes that

$$\epsilon s = \frac{\sigma(s)}{2G(s)}, \tag{A.6}$$

where $\sigma(s)$ and $\epsilon(s)$ are the Laplace transforms of $\sigma(t)$ and $\epsilon(t)$ respectively, and

$$G(s) = \frac{G_s}{s + G/V}, \tag{A.7}$$

is *complex rigidity*. Eq. (A.6) is the constitutive relation for an elastic continuum. The solution of the governing equations for the equilibrium of a viscoelastic medium is obtained by replacing in the elastic case equations the elastic shear modulus with its complex equivalent, and than by interpreting the remaining quantities as Laplace transforms. Once the solution of the problem in the complex plane has been achieved, it is possible to retrieve the time dependence of the viscoelastic solutions by means of an anti–transformation. This represents the essential content of the correspondence principle for the linear viscoelasticity.

The Maxwell viscoelastic continuum shows opposite behaviors on different time scales:

- In the limit $s \to \infty$ (i. e. for $t \to 0$), Eq. (A.6) gives

  $$\sigma(s) = 2\mu\epsilon(s), \tag{A.8}$$

  whereof the Laplace anti–transform is

  $$\sigma = 2\mu\epsilon, \tag{A.9}$$

which represents the constitutive relation for an elastic medium. Thus, for short time scales, the viscoelastic continuum exhibits a purely elastic behavior whose analogue model is the spring (Figure A.1a).

- for $s \to 0$ (i. e. $t \to \infty$), Eq. (A.6) gives

$$\sigma(s) = 2\nu s\epsilon(s), \tag{A.10}$$

whereof the Laplace anti–transform is

$$\sigma = 2\nu\dot{\epsilon}, \tag{A.11}$$

which represents the viscous constitutive relation. The analogue model for a viscous body is the dashpot (Figure A.1b).

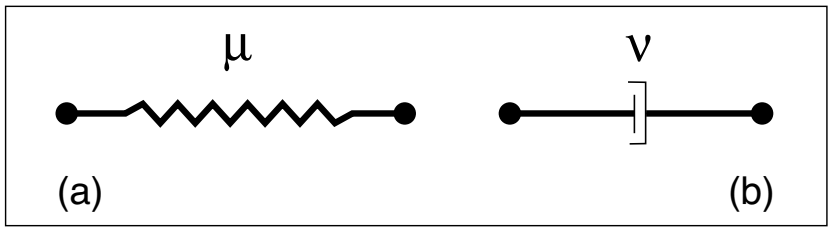

Figure A.1: Analogue rheological models for (a) elastic (Hooke) and (b) linearly viscous (Newton) bodies.

The behavior of a Maxwell viscoelastic body can be represented by combining in series an elastic and a viscous element (Figure A.2). Different viscoelastic rheologies can be represented by various combinations of elastic and viscous elements.

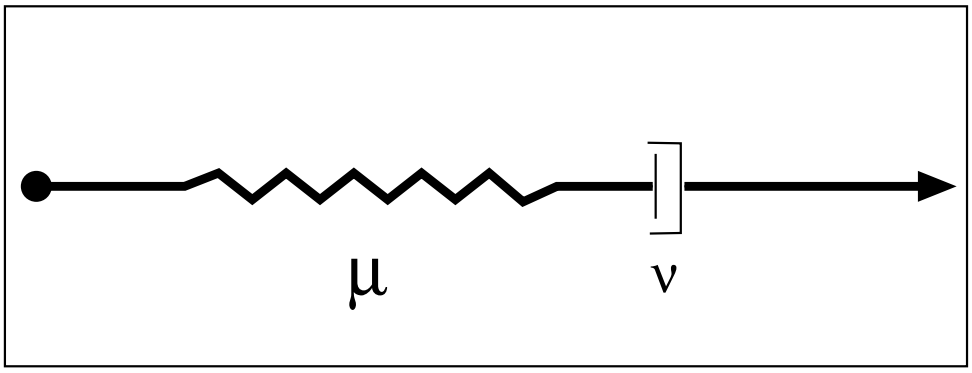

Figure A.2: Maxwell viscoelastic model. The spring (Hooke) and the dashpot (Newton) are combined in series to couple the elastic instantaneous and delayed viscous responses.

Appendix B

Spherical Harmonics

Here we provide the basic definitions and conventions concerning the Legendre polynomials, the associated Legendre functions, and the spherical harmonics.

B.1 Legendre polynomials

The Legendre polynomials are defined by the Rodriguez formula as

$$P_l(x) = \frac{1}{2^l l!}\frac{d^l}{dx^l}(x^2-1)^l, \tag{B.1}$$

where l is the degree, $x = \cos\theta$, and θ is colatitude. Some low–degree polynomials are given in Table B.1.

B.2 Associated Legendre functions

The associated Legendre function of degree l ($l = 0, 1, 2, \ldots$) and order m ($m = 0, 1, 2, \ldots l$) is

$$P_{lm}(x) = (-1)^m(1-x^2)^{m/2}\frac{d^m}{dx^m}P_l(x), \tag{B.2}$$

where $P_l(x)$ is the Legendre polynomial (B.1). A few associated Legendre functions are given in Table B.2.

Table B.1: Legendre polynomials for degrees $0 \leq l \leq 5$.

l	$P_l(x)$
0	1
1	x
2	$(1/2)(3x^2 - 1)$
3	$(1/2)(5x^3 - 3x)$
4	$(1/8)(35x^4 - 30x^2 + 3)$
5	$(1/8)(63x^5 - 70x^3 + 15x)$

Table B.2: Associated Legendre functions for degrees $0 \leq l \leq 3$.

l	m	$P_{lm}(\cos\theta)$
0	0	1
1	0	$\cos\theta$
1	1	$-\sin\theta$
2	0	$(1/2)(3\cos^2\theta - 1)$
2	1	$-3\sin\theta\cos\theta$
2	2	$3\sin^2\theta$
3	0	$(1/2)(5\cos^3\theta - 3\cos\theta)$
3	1	$(-3/2)\sin\theta(5\cos^2\theta - 1)$
3	2	$15\sin^2\theta\cos\theta$
3	3	$-15\sin^3\theta$

B.3 Complex spherical harmonics

The complex spherical harmonics are

$$\mathcal{Y}_{lm}(\theta,\lambda) = \mu_{lm} P_{lm}(\cos\theta)\ e^{im\lambda}, \tag{B.3}$$

where l and m are the degree and the order, θ is colatitude, λ is longitude, $i = \sqrt{-1}$, and

$$\mu_{lm} = \sqrt{(2l+1)\frac{(l-m)!}{(l+m)!}}, \tag{B.4}$$

with

$$\mathcal{Y}_{l-m}(\theta,\lambda) \equiv (-)^m \mathcal{Y}^*_{lm}(\theta,\lambda). \tag{B.5}$$

The $\mathcal{Y}$ harmonics (see Table B.3) are referred as to "4π–normalized harmonics" because of the orthogonality relationship

$$\int_\Omega d\omega \mathcal{Y}^*_{l'm'}(\theta,\lambda)\mathcal{Y}_{lm}(\theta,\lambda) = 4\pi\ \delta_{ll'}\delta_{mm'}, \tag{B.6}$$

where Ω is the unit sphere, and

$$\int_\Omega d\omega(\cdot) \equiv \int_0^{2\pi}\int_0^{\pi} (\cdot)\sin\theta d\theta d\lambda. \tag{B.7}$$

The addition theorem for the spherical harmonics states that

$$P_l(\cos\Theta) = \frac{1}{2l+1}\sum_{m=-l}^{+l} \mathcal{Y}^*_{lm}(\theta',\lambda')\mathcal{Y}_{lm}(\theta,\lambda), \tag{B.8}$$

where (θ,λ) and (θ',λ') are the spherical coordinates of two points, and Θ is the colatitude of the second relative to the first, such that

$$\cos\Theta = \frac{\vec{r}'\cdot\vec{r}}{rr'}, \tag{B.9}$$

with $r' = \|\vec{r}'\|$ and $r = \|\vec{r}\|$.

Table B.3: Complex spherical harmonics for degrees $0 \leq l \leq 3$.

l	m	$\mathcal{Y}_{lm}(\theta, \lambda)$
0	0	1
1	0	$\sqrt{3}\ \cos\theta$
1	1	$-\sqrt{3/2}\ \sin\theta e^{\iota\lambda}$
2	0	$(1/2)\sqrt{5/4}\ (3\cos^2\theta - 1)$
2	1	$-\sqrt{15/2}\ \sin\theta\cos\theta e^{\iota\lambda}$
2	2	$(1/2)\sqrt{15/4}\ \sin^2\theta e^{2\iota\lambda}$
3	0	$(1/2)\sqrt{7}\ (5\cos^3\theta - 3\cos\theta)$
3	1	$-(1/4)\sqrt{21}\ \sin\theta(5\cos^2\theta - 1)e^{\iota\lambda}$
3	2	$(1/2)\sqrt{105/2}\ \sin^2\theta\cos\theta e^{2\iota\lambda}$
3	3	$-(1/4)\sqrt{35/2}\ \sin^3\theta e^{3\iota\lambda}$

Appendix C

Input files and main units of SELEN

Table C.1 gives the names of the input files which are required by the program units summarized in Table C.2.

Table C.1: User–supplied input files of SELEN.

File	Content
selen.sh	Bash shell script that executes SELEN
data.inc	Include file with the SELEN settings, see Section C.1
ice3(1).dat	Ice thickness information for the ICE3G (ICE1) ice aggregate
sea level.dat	RSL data from the Tushingham and Peltier (1993) database
psmsl.dat	Sea level secular trends from the PSMSL database

Table C.2: Main functions of Fortran 90, GMT, and gnuplot programs accessed by script selen.sh.

Fortran 90	Purpose or task
PX.F	Determines the pixels coordinates
SH.F	Computes the SH at pixels centroids
SHTOOLS.F	Include file with ALFPACK SH routines
WNW.F	Performs the SH 'Window' test
SH_OF.F	Computes the ocean function SH coefficients
REC_OF.F	Synthesis of the ocean function
SH3(1)_C.F	ICE3G (ICE1) shape factors
SH3(1).F	ICE3G (ICE1) SH coefficients
REC_ICE.F	Reconstructs the ice sheets thickness
TB.F	Computes LDCs and relaxation spectrum
SLE.F	Solves the SLE
SH_RSL.F	Computes SH at RSL sites
RSL.F	Determines the RSL curves
GMAPS.F	Determines the scalar fields $\dot{S}$, $\dot{U}$, and $\dot{N}$
SH_PSMSL.F	Computes SH at PSMSL sites
PSMSL.F	Computes $\dot{S}$ at PSMSL sites
STOKES.F	Time–derivatives of the Stokes coefficients
COPY.F	Moves output files into the */depot*
GMT	
px.gmt	Separates wet from dry pixels
pxmap.gmt	Plots global, wet and dry pixels
of.gmt	Plots the reconstructed ocean function
ice3(1).gmt	Produces maps of the ICE3G (ICE1) ice sheets
gmaps.gmt	Produces maps of $\dot{S}$, $\dot{U}$, and $\dot{N}$
gnuplot	
spectrum.gnu	Plots the relaxation spectrum
elastic.gnu	Plots the elastic LLNs
fluid.gnu	Plots the fluid LLNs
stokes.gnu	Plots the Stokes coefficients

C.1 Sample *data.inc* input file

Below we provide a sample input file *data.inc*. The configuration shown that can be used as a starting point to obtain all the results presented in this manuscript.

```
!
!   ======================
!   This is file 'data.inc'
!   ======================
!
!   Last modified by GS on 7/20/2006
!
!#------------- 1)  General settings ----------------------------------------------------
 CHARACTER*4, PARAMETER :: RUN='_yyy'                ! Label for the output files
 INTEGER, PARAMETER :: RES=14                        ! Resolution
 INTEGER, PARAMETER :: NP=2*RES*(RES-1)*20+12        ! Number of pixels
 INTEGER, PARAMETER :: LMAX=72                       ! Maximum harmonic degree
 INTEGER, PARAMETER :: JMAX=(LMAX+1)*(LMAX+1)/2      ! Harmonics for l=l_max
 REAL*4,  PARAMETER :: PIG=3.14159265358979323840    ! Pi
 REAL*4,  PARAMETER :: ERADIUS=6.371E6               ! Radius of the earth, m
 REAL*4,  PARAMETER :: RHOE=5511.57                  ! Earth's average density, kg/m^3
 REAL*4,  PARAMETER :: RHOW=1000.0                   ! Water density, kg/m^3
 REAL*4,  PARAMETER :: RHOI=931.0                    ! Ice density, kg/m^3
!
!# ------------ 2) Ice models settings ------------------------------------------------
 INTEGER, PARAMETER :: NE3=808                       ! Elements of ICE3G
 INTEGER, PARAMETER :: NE1=153                       ! Elements of ICE1
 INTEGER, PARAMETER :: NN=18                         ! Number of time steps
 REAL*4,  PARAMETER :: DELTA=1.                      ! Time increment, kyrs
!
!# ------------ 3) TABOO settings -----------------------------------------------------
 INTEGER, PARAMETER :: NV=3, CDE=2        ! Earth model (see TABOO user guide)
 REAL*4   VSC(NV)                         ! Viscosity array data
 DATA VSC/2.0,1.0,1.0/                    ! Viscosities from bottom to top, *1E21 Pa.s
 REAL*4,  PARAMETER :: LTHIC=120.         ! Thickness of the elastic litosphere, km
!
!# ------------ 4) Sea level Equation settings ----------------------------------------
 INTEGER, PARAMETER :: SMAX=3             ! Number of iterations for the SLE
 INTEGER, PARAMETER :: IMODE=1            ! Mode of solution - see below -
!
! IMODE =1 -> Gravitationally Self-Consistent (GSC)
! IMODE =2 -> GSC, but only elastic (ELA)
! IMODE =3 -> Eustatic (EUS)
! IMODE =4 -> Woodward (WDW)
! IMODE =5 -> Ice Load Neglected (ILN)
!
!# ------------ 5) Relative sea level curves settings ---------------------------------
 INTEGER, PARAMETER :: NRSL = 392          ! Number of RSL sites
!
!# ------------ 6) PSMSL predictions settings -----------------------------------------
 INTEGER, PARAMETER :: NPSMSL=1016         ! Number of PSMSL stations
!
!# ------------ 7) Stokes coefficients settings ---------------------------------------
 INTEGER, PARAMETER :: STMIN=0           ! Min. degree for the Stokes coefficients
 INTEGER, PARAMETER :: STMAX=6           ! Max. degree
!
! End of file
!
```

Bibliography

Abdennadher, J., and M. Boukthir, 2006. Numerical simulation of the barotropic tides in the Tunisian Shelf and the Strait of Sicily, *Journal of Marine Systems,* 63, 162–182.

Alessio, M., L. Allegri, F. Antonioli, G. Belluomini, S. Improta, L. Manfra, and M. Preite Martinez, 1994. La curva di risalita del mare Tirreno negli ultimi 43 ka ricavata da datazioni su speleotemi sommersi e dati archeologici, *Mem. Descr. Carta Geol. d'Italia,* LII, 261–276.

Aloisi, J. C., A. Monaco, N. Planchais, J. Thommeret, and Y. Thommeret, 1978. The Holocene transgression in the Golfe du Lion, southwestern France: paleogeographic and paleobotanical evolution, *Geogr. Phys. Quat.,* 32 (2), 145–162.

Antonioli, F. and M. Frezzotti, 1989. I sedimenti tardo–pleistocenici e olocenici compresi nella fascia costiera tra Sabaudia e Sperlonga, *Mem. Soc. Geol. Ital.,* 42, 321–334.

Bassett, S. E., G. A. Milne, J. X. Mitrovica, and P. U. Clark, 2005. Ice sheet and solid Earth influences on far–field sea–level histories, *Science,* 309, 925–928.

Bentley, M. J., 1999. Volume of Antarctic Ice at the Last Glacial Maximum, and its impact on global sea–level change, *Quat. Sci. Rev.,* 18, 1569–1595.

Bintanja, R., R. S. W. van de Wal, and J. Oerlemans, 2002. Global ice volume variations through the last glacial cycle simulated by a 3–D ice–dynamical model, *Quat. Int.,* 95–96, 11–23.

Blanchon, P., and J. Shaw, 1995. Reef drowning during the last deglaciation: evidence for catastrophic sea–level rise and ice sheet collapse, *Geology,* 23, 1, 4–8.

Bond, G., and 13 others, 1992. Evidence for massive discharges of icebergs into the North Atlantic Ocean during the last glacial period, *Nature,* 360, 245–249.

Bond, G., W. Broecker, S. Johnsen, J. McManus, L. Labeyrie, J. Jouzel, and G. Bonani, G., 1993. Correlations between climate and records from North Atlantic sediments and Greenland ice, *Nature,* 365, 143–147.

Carminati, E. and G. Di Donato, 1999. Separating natural and anthropogenic vertical movements in fast subsiding areas: the Po plain (N. Italy) case, *Geophys. Res. Lett.,* 26, 2291–2294.

Carminati, E., C. Doglioni, and D. Scrocca, 2003 Apennines subduction–related subsidence of Venice (Italy), *Geophys. Res. Lett.,* 30, 1717, doi:10.1029/2003GL017001.

Cianetti, S., C. Giunchi, and G. Spada, 2002. Mantle viscosity beneath the Hudson Bay: an inversion based on the Metropolis algorithm, *J. Geophys. Res.,* doi: 10,1029/2001JB000585.

Clapperton, C. M., 1995. Fluctuation of local glaciers at the termination of the Pleistocene: 18–8 ka BP, *Quat. Int.,* 28, 41–50.

Clark, J. A., W. E. Farrell, and W. R. Peltier, W. R., 1978. Global changes in postglacial sea level: A numerical calculation, *Quat. Res.,* 9, 265–287.

Clark, J. A. and C. S. Lingle, 1979. Predicted Relative sea level Changes (18.000 Years B.P. to present) Caused by Late–Glacial Retreat of Antarctic Ice Sheet, *Quat. Res.,* 11, 279–298.

Clark, J. A., 1980. The reconstruction of the Laurentide ice sheet of North America from sea level data: Method and preliminary results, *J. Geophys. Res.,* 104, 29,077–29,093.

Clark, P. U., R. A. Alley, L. D. Keigwin, J. M. Licciardi, S. J. Johnsen, and H. Wang, H., 1996. Origin of the first meltwater pulse following the last glacial maximum, *Palaeoceanography,* 11, 563–577.

Clark, P. U., J. X. Mitrovica, G. A. Milne, and M. E. Tamisiea, 2002. sea–level finger print as a direct test for the source of global meltwater pulse 1a. *Science,* 295, 2438–2441.

Dahlen, F. A., 1976. The passive influence of the oceans upon the rotation of the Earth, *Geophys. J. R. Astron. Soc.,* 46, 363–406.

Daly, R. A., 1920. A recent worldwide sinking of the ocean level, *Geol. Mag.,* 57, 246–261.

Daly, R. A., 1943. *The Changing World of the Ice Age*, Yale Univ. Press, New Haven.

Daly, R. A., 1940. *Strength and Structure of the Earth*, Prentice–Hall, New York.

Daly, J. L., 2002. Testing the Waters; A report on Sea Levels, *Greening Earth Society Science Advisor*, http://www.greeningearthsociety.org/Articles/2000/sea.htm.

Darwin, G. H., 1879. On the bodily tides of viscous and semi–elastic spheroids, and the ocean tides upon a yelding nucleus, *Phil. Trans. Roy. Soc. London,* Ser. A, 170, 1–35.

Denton, G. H. and T. H. Hughes, 1981. *The last greast ice sheets*, John Wiley, New York, 484 pp.

Denton, G. H. and T. H. Hughes, 2002. Reconstructing the Antarctic Ice Sheet at the Last Glacial Maximum, *Quat. Sci. Rev.,* 21, 193–202.

Domack, E., and 9 others, 2005. Stability of the Larsen B ice shelf on the Antarctic Peninsula during the Holocene epoch, *Nature,* 436, 681–685.

Dubar, M., 1987. Donnees nouvelles sur la transgression holocène dans la region de Nice (France), *Bull. Soc. geol. Fr.,* (8), 3, (1), 195–198.

Duplessy, J. C., G. Delibrias, J. L. Turon, C. Pujol, and J. Duprat, 1981. Deglacial warming of the northeastern Atlantic ocean: correlation with the palaeoclimatic evolution of the european continent, *Palaeogeography, Palaeoclimatology, Palaeoecology,* 35, 121–144.

Ehlers, J., 1996. *Quaternary and glacial geology*, John Wiley and Sons, New York, 578 pp.

Emiliani, C., 1955. Pleistocene temperatures, *Jour. Geol.,* 63, 538–578.

Emiliani, C., 1956. Oligocene and Miocene temperatures of the equatorial and Subtropical Atlantic Ocean, *Jour. Geol.,* 64, 281–288.

Emiliani, C., 1957. Temperature and age analysis of deep–sea cores,, *Science,* 125, 383–387.

Emiliani, C., 1958. Paleotemperature analysis of core 280 and Pleistocene conditions, *Jour. Geol.,* 66, 264–275.

Fairbanks, R. G., 1989. A 17,000 year glacio–eustatic sea–level record: influence of glacial melting rates on the Younger Dryas event and deep ocean circulation, *Nature,* 342, 637–642.

Fairbanks, R. G., C. D. Charles, and J. D. Wright, 1982. Origin of global meltwater pulses, In R. E. Traylor, A. Long, & R. S. Kra (Eds.), Radiocarbon after four decades, (pp. 473–500). New York: Springer.

Fairbanks R. G., R. A. Mortlock, RC. Tzu-Chien, C. Li, A. Kaplan, T. P. Guilderson, T. W. Fairbanks, and A. L. Bloom, 2005. Marine Radiocarbon Calibration Curve Spanning 0 to 50,000 Years B.P. Based on Paired 230Th/234U/238U and 14C Dates on Pristine Corals. *Quat. Sci. Rev.,* 24, 1781-1796.

Fairbridge, R. W., 1961. Eustatic changes in sea–level, *Physics and Chemistry of the Earth,* 5, 99–185.

Farrell, W. E., 1973. Earth tides, ocean tides and tidal loading, *Phil. Trans. R. Soc. Lond. A,* 274, 253–259.

Farrell, W. E., and J. A. Clark, 1976. On postglacial sea level, *Geophys. J. R. Astron. Soc.,* 46, 647–667.

Fleming, K., P. Johnston, D. Zwartz, Y. Yokoama, K. Lambeck, and J. Chappell, 1998. Refining the eustatic sea–level curve since the Last Glacial Maximum using far– and intermediate–field sites, *Quat. Res.,* 9, 265–287.

Fleming, N. C., 1972. *Eustatic and tectonic factors in the relative vertical displacement of the Aegean coast, in The mediterranean Sea: A Natural Sedimentation Laboratory,* Ed. Stanley, D. J., Dowden, Hutchinson and Ross, Strodsberg, 189–200.

Fleming, N. C., 1978. Holocene eustatic changes and coastal tectonics in the Northeast Mediterranean: Implications for models of crustal consumption, *Phil. Trans. R. Soc. Lond.,* 289, 405–458.

Florineth, D. and C. Schlüchter, 2000. Alpine evidence for atmospheric circulation patterns in Europe during the Last Glacial Maximum, *Quat. Res.,* 54, 295–308.

Forte, A. M. and J. X. Mitrovica, 1996. New inferences of mantle viscosity from joint inversion of long-wavelenght mantle convection and post-glacial rebound data, *Geophys. Res. Lett.,* 23, 1147–1150.

Fung, Y. C., 1965. *Fundation of solid mechanics,* Chapter 15, Prentice–Hall, Englewood Cliffs, N. J., 525 pp.

Galili, E., M. Weinstein–Evron, and A. Ronen, 1988. Holocene sea–level changes based on submerged archaeological sites of the northern Carmel coast in Israel, *Quat. Res.,* 29, 36–42.

Gasperini P., Dal Forno G. and Boschi E., 2004. Linear or non-linear rheology in the Earth's mantle: the prevalence of power-law creep in the postglacial isostatic readjustment of Laurentia, *Geophys. J. Int.,* 157, 1297-1302, doi: 10.1111/j.1365-246X.2004.02319.x.

Giunchi, C., and G. Spada, 2000. Postglacial rebound in a non–Newtonian spherical Earth, *Geophys. Res. Lett.,* 27, 2065–2068.

Goodwin, I. D., 1996. A mid to late Holocene readvance of the Law Dome ice margin, Budd Coast, East Antarctica, *Antarctic Science,* 8, 395–406.

Goodwin, I. D., 1998. Did changes in Antarctic ice volume influence the late Holocene sea–level lowering ?, *Quat. Sci. Rev.,* 17, 319–332.

Gudmundsson, G. H., 1994. An order–of–magnitude estimate of the current uplift–rates in Switzerland caused by the Würm Alpine deglaciation, *Eclogae geol. Helv.,* 87, 545–557.

Haskell, N. A., 1935. The motion of a viscous fluid under a surface load, I, *Physics,* 6, 265–269.

Haskell, N. A., 1936. The motion of a viscous fluid under a surface load, II, *Physics,* 7, 56–61.

Huybrechts, P., 1992. The Antarctic ice sheet and environmental change: A three–dimensional modelling study, *Reports on Polar Research,* 99, Alfred Wegener Institute, Brehemerhaven, 242 pp.

Huybrechts, P., 2002. Sea–level changes at the LGM from ice–dynamic reconstructions of the Greenland and Antarctic ice sheets during the glacial cicles, *Quat. Sci. Rev.,* 21, 203–231.

Jedoui, Y., N. Kallel, M. Funtugne, H. B. Ismail, A. M'Rabet, and M. Montacer, 1998. A high relative sea–level stand in the middle Holocene in southeastern Tunisia, *Marine Geology,* 147, 123–130.

Johnston, P., 1993. The effect of spatially non–uniform water loads on prediction of sea–level change, *G*eophys. J. Int., 114, 615–634.

Johnston, P. and K. Lambeck, 2000. Automatic inference of ice models from post-glacial sea level observations: Theory and application to the British Isles, *J. Geophys. Res.,* 105, 13,179–13,194.

Kanfoush, S. L., D. A. Hodell, C. D. Charles, T. P. Guilderson, P. G. Martyn, and U. S. Ninnemann, 2000. Millennial–scale instability of the Antarctic ice sheet during the last glaciation, *Science,* 288, 1815–1819.

Kaufman, D. S., G. H. Miller, J. A. Stravers, and J. T. Andrews, 1993. Abrupt early Holocene (9.9–9.6 ka) ice–strean advance at the mouth of the Hudson strait, Arctic Canada, *Geology,* 21, 1063–1066.

Kaufmann, G., 2002. Predictions of secular geoid changes from the late Pleistocene and Holocene Antarctic ice–ocean mass imbalance, *Geophys. J. Int.,* doi:10.1046/j.1365-246X.2002.01596.x.

Keigwin, L. D., G. A. Jones, S. J. Lehman, and E. A. Boyle, 1991. Deglacial meltwater discharge, North Atlantic deep circulation, and abrupt climate change, *J. Geophys. Res.,* 96, 16811–16826.

Kidson, C., 1982. Sea level changes in the Holocene, *Quat. Sci. Rev.,* 1, 121–151.

Krasnov, M., A. Kisselev, and G. Makarenko, 1977. *Equations integrales,* Mir, Moscou, in french.

Laborel, J., M. Aarnold, F. Laborel–Deguen, C. Morhange, and N. Tisnerat–Labard, 1998. Confirmation of a Pleistocene age for the marine notch at Cap Romarin (Port–La–Nouvelle, Languedoc, france), *Geomorfol. Relief. Process. Environ.,* 2, 125–130.

Lakdar, R., M. Soussi, M. H. Ben Ismail, and A. M'Rabet, 2006. A Mediterranean Holocene restricted coastal lagune under arid climate: case of the sedimentary record of Sabkha Boujmel (SE Tunisia), *Palaeogeography, Paleoclimatology, Paleoecology,* 241, 177–191.

Lambeck, K., 1980. *The Earth's variable rotation, Geophysical causes and consequences,* Cambridge University Press, Cambridge, 449 pp.

Lambeck, K., 1988. *Geophysical geodesy: the slow deformations of the Earth,* Oxford University Press, Oxford.

Lambeck, K., 1995. Late Pleistocene and Holocene sea–level change in Greece and south–western Turkey: a separation of eustatic, isostatic, and tectonic contributions, *Geophys. J. Int.,* 122, 1022–1044.

Lambeck, K., and P. Johnston, 1995. Land subsidence and sea level change: contributions from the melting of the last great ice sheets and the isostatic adjustment of the Earth, In: Barends, F.B.J., et al., (Eds.), Land Subsidence. Balkema, Rotterdam, 3 18.

Lambeck, K., C. Smither, and P. Johnston, 1998. Sea–level change, glacial rebound and mantle viscosity for northern Europe, *Geophys. J. Int.,* 134, 102–144.

Lambeck, K., and E. Bard, 2000. Sea level changes along the French Mediterranean coast from the past 30,000 years, *Earth and Plan. Sci. Lett.,* 175, 203–222.

Lambeck, K., F. Antonioli, A. Purcell, and S. Silenzi, 2004. Sea level change along the Italian coast from the past 10,000 yr, *Quat. Sci. Rev.,* 23, 1567–1598.

Lambeck, K., M. Anzidei, F. Antonioli, A. Benini, and A. Esposito, 2004 Sea level in Roman time in the Central Mediterranean and implications for recent change, *Earth and Plan. Sci. Lett.,* 224, 563–575.

Lambeck, K. and A. Purcell, 2005. Sea–level change in the Mediterranean Sea since th LGM: model predictions for tectonically stable areas, *Quat. Sci. Rev.,* 24, 1969–1988.

Licht, K. J., 2004. The Ross Sea's contribution to eustatic sea–level during meltwater pulse 1A, *Sedimentary Geology,* 165, 343–353.

Lisiecki, L. E., and M. E. Raymo, 2005. A Pliocene-Pleistocene stack of 57 globally distributed benthic $\delta^{18}O$ records, *Paleoceanography,* 20, 1003, doi:10.1029/2004PA001071.

Lippitsch, R., E. Kissling, and J. Ansorge, 2003. Upper mantle structure beneath the Alpine orogen from high–resolution teleseismic tomography, *J. Geophys. Res.,* 108, 2376, doi:10.1029/2002JB002016.

Love, A. E. H., 1911. *Some Problems of Geodynamics,* Cambridge University Press, London.

Mahamoud, S., R. Reilinger, S. McClusky, P. Vernant, and A. Tealeb, 2005. GPS evidence for northward motion of the Sinai Block: implications for E. Mediterranean tectonics, *Earth and Plan. Sci. Lett.,* 238, 217–224.

Meghraoui, M., et al., 2004. Coastal uplift and thrust faulting associated with the $M_w = 6.8$ Zemmouri (Algeria) earthquake of 21 May, 2003, *Geophys. Res. Lett.,* doi:10.1029/2004GL020466.

Milankovitch, M., 1930. *Mathematische klimalehre und astronomische Theorie der Klimaschwankungen,* in Handbuch der Klimatologie, vol. 1, ed. W. Koppen and R. Geiger, 1–76, Gebruder Borntrager, Berlino.

Milne, G. A., 1998. Refining models of the glacial isostatic adjustment process, *Ph. D. Thesis,* Toronto, CA, 126 pp.

Milne, G. A., J. X. Mitrovica, 1998. Postglacial sea–level change on a rotating Earth, *Geophys. J. Int.,* 114, doi:10.1046/j.1365-246X.1998.1331455.x.

Milne, G. A., J. X. Mitrovica, and J. L. Davis, 1999. Near–field hydro–isostasy: the implementation of a revised sea–level equation, *Geophys. J. Int.,* 139, 464–482.

Mitrovica, J. X., and W. R. Peltier, 1991. On post–glacial geoid subsidence over the equatorial ocean, *J. Geophys. Res.,* 96, 20,053–20,071.

Mitrovica, J. X., J. L. Davis, and I. I. Shapiro, 1994 A spectral formalism for computing three–dimensional deformations due to surface loads, *J. Geophys. Res.,* 99, 7057–7073.

Mitrovica, J. X. and W. R. Peltier, 1995 Constraints on mantle viscosity based on the inversion of post–glacial uplift data from the Hudson Bay region, *Geophys. J. Int.,* 122, 353–377.

Mitrovica, J. X., 1996. Haskell [1935] revisited, *J. Geophys. Res.,* 101, 555–569.

Mitrovica, J. X. and A. M. Forte, 1997. Radial profile of mantle viscosity: Results from the joint inversion of convection and convection and postglacial rebound observables, *J. Geophys. Res.,* 102, 2751–2769.

Mitrovica, J. X. and G. A: Milne, 2002. On the origin of late Holocene sea–level highstands within equatorial ocean basins, *Quat. Sci. Rev.,* 21, 2179–2190.

Mitrovica, J. X. and G. A. Milne, 2003. On post–glacial sea level: I. General theory, *Geophys. J. Int.,* 154, 253–267.

Morhange, C., J. Laborel, and A. Hesnard, 2001 Changes of relative sea level during the past 5000 years in the ancient harbor of Marseilles, Southern France, *Paleogeogr. Paleoclimatol. Paleoecol.,* 166, 319–329.

Morhange, C. and P. A: Pirazzoli, 2005. Mid–Holocene emergence of southern Tunisian coasts, *Marine Geology*, 220, 1–4.

Morhange, C., P. A. Pirazzoli, N. Marriner, L. F. Montaggioni, and T. Nammour, 2006. Late Holocene relative sea–level changes in Lebanon, Eastern Mediterranean, *Marine Geology* 230, 99–114.

Nakada, M. and K. Lambeck, 1988. The melting history of the late Pleistocene Antarctic ice sheet, *Nature,* 333, 36–40.

Nakada, M. and K. Lambeck, K., 1989. Late Pleistocene and Holocene sea–level change in the Australian region and mantle rheology, *Geohpysical Journal,* 96, 497–517.

Nir, Y. and I. Eldar, 1987. Ancient wells and their geoarchaeological significance in detecting tectonics of the Israel Mediterranean coastline region, *Geology,* 15, 3–6.

Okuno, J. and M. Nakada, 2001. Effects of water load on geophysical signals due to glacial rebound and implications for mantle viscosity, *Earth Planets Space,* 53, 1121–1135.

Paskoff, R. and P. Sanlaville, 1983. Les côtes de la Tunisie. Variations du niveau marin depuis le Tyrrhénien, *Maison de l'Orient Mediterraneen, Lyon*, 192 pp.

Peltier, W. R., 1974. The impulse response of a Maxwell earth, *Rev. Geophys. Space Phys.,* 12, 649–669.

Peltier, W. R., and J. T. Andrews, 1976. Glacial isostatic adjustment, I, the forward problem, *Geophys. J. R. Astron. Soc.,* 46, 605–646.

Peltier, W. R., W. E. Farrell, and J. A. Clark, 1978. Glacial isostasy and relative sea level: a global finite element model, *Tectonophys.,* 50, 81–110.

Peltier, W. R., 1985. The LAGEOS constraint on deep mantle viscosity; results from a new normal mode method for the inversion of the viscoelastic relaxation spectra, *J. Geophys. Res.,* 90, 9421–9421.

Peltier, W. R., 1994. Ice age paleotopography, *Science,* 265, 195–201.

Peltier, W. R., 1996. Mantle viscosity and ice-age ice sheet topography, *Science,* 273, 1359–1364.

Peltier, W. R., 2005. On the hemispheric origins of meltwater pulse 1a, *Quat. Sci. Rev.,* 24, 1655–1671.

Peltier, W. R., and R. G. Fairbanks, 2006. Global glacial ice volume and last Glacial Maximum duration from an extended barbados sea–level record, *Quat. Sci. Rev.,* in press.

Pirazzoli, P. A., 1987. Sea level changes in the Mediterranean, in Tooley, M. J. and Shennan, I., eds., Sea–level changes, *Inst. of Brit. Geogr. Spec. Pub. Series,* 20, 152–181.

Pirazzoli, P. A., 1991. *World atlas of Holocene sea–level changes*, Elsevier, Amsterdam, 300 pp.

Pirazzoli, P. A., 1996. *Sea level changes, the last 20,000 years*, John Wiley and Sons, Chichester, 211 pp.

Pirazzoli, P. A., G. Mastronuzzi, J. F. Saliège, and P. Sansò, 1997. Late Holocene emergence in Calabria, Italy, *Marine Geology,* 141, 61–70.

Pirazzoli, P. A., 2003. Mid– and late–Holocene relative sea–level changes in the Mediterranean area: a review of selected sites with discussion of the possible eustatic, isostatic, and tectonic contributions, in Proceedings of the IGCP 437 Final Conference, Otranto–Taranto (Italy), September 22–28.

Pirazzoli, P. A., 2005. A review of possible eustatic, isostatic, and tectonic contributions in eight late–Holocene relative sea–level histories from the Mediterranean area, *Quat. Sci. Rev.,* 24, 1989–2001.

Piromallo, C. and A. Morelli, 2003. P–wave tomography of the mantle under the Alpine–Mediterranean area, *J. Geophys. Res.,* 108, 2065, doi:10.1029/2002JB001757.

Platzman, G. W., 1971. Ocean tides, in *Lectures in Applied Mathematics,* 14, part 2, 239–292, American Mathematical Society, Providence, RI.

Press, W. H., S. A. Teukolsky, W. T. Vetterling, and B. P. Flannery, 1992. *Numerical recipes in Fortran: the art of scientific computing,* Cambridge University Press, New York, 936 pp.

Raban, A., and E. Galili, 1995. Recent maritime archaeological research in Israel – A preliminary report, *Int. J. Naut. Archaeol. Underw. Explor.,* 14, (4), 321–356.

Rananalli, G., 1987. *Rheology of the Earth,* Allen and Unwin, London, 366 pp.

Ruddiman, W. F., 1987. Synthesis; the ocean ice-sheet record, in *North America and adjacent oceans during the last deglaciation,* Ruddiman W. F. and H. E. Jr. Wright, Eds., K3, 463–478, Geological Society of America, Boulder, CO, United States.

Saarman, G., Eustatische Bewegungen im Lichte der Forschung, 1948. *Petermanns Geogr. Mitt. Gotha.,* 3/4, 158–161.

Sabadini, R., D. A. Yuen, and E. Boschi, 1982. Polar wandering and the forced responses of a rotating, multilayered, viscoelastic planet, *J. Geophys. Res.,* 87, 2885–2903.

Sammari, C., V. G. Koutitonsky, and M. Moussa, M., 2006. Sea level variability and tidal resonance in the Gulf of Gabes, Tunisia, *Cont. Shelf. Res.,* 26, 338–350.

Sivan, D., S. Wdowinski, K. Lambeck, E. Galili, and A. Raban, 2001. Holocene sea–level changes along the Mediterranean coast of Israel based on archaeological observations and numerical model, *Paleogeogr. Paleoclimatol. Paleoecol.,*, 167, 101–117.

Sivan, D., K. Lambeck, R. Toueg, A. Raban, Y. Porath, and B. Shirman, B., 2004. Ancient coastal wells of Caesarea Maritima, Israel, an indicator for relative sea level changes during the last 2000 years, *Earth and Pla. Sci. Lett.,* 222, 315–330.

Schmiedt, G., 1972. *Il livello antico del Mar Tirreno, Testimonianze dei resti archeologici*, Olschki, Florence, 323 pp.

Smiraglia, C., 1992. *Guida ai ghiacciai e alla glaciologia: forme, fluttuazioni, ambienti*, Zanichelli, 240 pp.

Sneh, Y. and M. Klein, M., 1984. Holocene Sea Level Changes at the Coast Dor, Southeast Mediterranean, *Science,* 226, 831–832.

Spada, G., D. A. Yuen, R. Sabadini, and Y. Ricard, 1992. Effects on post–glacial uplift from the hard rheology in the transition zone, *Geophys. J. Int.,* 109, 683–700.

Spada, G., 2001. Mantle viscosity from Monte Carlo inversion of very long baseline interferometry data, *J. Geophys. Res.,* 106, 16,375–16385.

Spada, G., 2003. *The theory behind TABOO,* Samizdat Press, Golden–White River Junction.

Spada, G., and ten others, 2003. *TABOO User Guide,* Samizdat Press, Golden–White River Junction.

Spada, G., A. Antonioli, L. Boschi, S. Cianetti, G. Galvani, C. Giunchi, B. Perniola, N. Piana Agostinetti, A. Piersanti, and P. Stocchi, 2004. Modeling Earth's post glacial rebound, *EOS Trans. Am. Geophys. Un.,* 85, 62–64.

Spada, G., and L. Boschi, 2006. Using the Post–Widder formula to compute the Earth's Love numbers, *Geophys. J. Int.,* submitted.

Spada, G., and P. Stocchi, P., 2006. *The Sea level Equation - Theory and numerical examples*, Aracne Ed., Rome, 81pp.

Spada, G., A. Antonioli, S. Cianetti, and C. Giunchi, 2006. Glacial isostatic adjustment and relative sea–level changes: the role of lithospheric and upper mantle

heterogeneities in a 3-D spherical Earth, *Geophys. J. Int.,* 165 (2), 692-702. doi: 10.1111/j.1365-246X.2006.02969.x.

Spada, G., and P. Stocchi, 2007. `SELEN`: a Fortran 90 program for solving the "sea–level Equation", *Computer and Geosciences, in press,* doi:10.1016/j.cageo.2006.08.006.

Stewart, I. S., J. Sauber, and J. Rose, 2000. Glacio–seismotectonics: ice sheets, crustal deformation and seismicity, *Quat. Sci. Rev.,* 19, 1367–1389.

Stocchi, P., G. Spada, and S. Cianetti, 2005. Isostatic rebound following the Alpine deglaciation: impact on the sea level variations and vertical movements in the Mediterranean region, *Geophys. J. Int.,* doi: 10.1111/j.1365-246X.2005.02653.x..

Stocchi, P., S. Cianetti, L. Girometti, and G. Spada, G., 2005. Holocene sea–level changes in the Mediterranean: the role of remote and near–field ice sheets, Proceedings of the 9$^{\text{th}}$ International Workshop on Numerical Modeling of Mantle Convection and Lithospheric Dynamics, Erice, September 2005 (available at http://www.ingv.it/erice2005/).

Stocchi, P., G. Spada, S. Cianetti, and L. Girometti. Variazioni post-glaciali di livello marino nel Mediterraneo: zone di Clark e ruolo dei ghiacciai remoti, Gruppo Nazionale di Geofisica della Terra Solida, 24 Convegno Nazionale, Consiglio Nazionale delle Ricerche, Presentazione Orale, Roma 15 17 novembre 2005.

Stocchi, P., and G. Spada, 2006. Post–glacial sea–level in the Mediterranean Sea: Clark's zones and role of remote ice sheets, *Quat. Sci. Rev.,* submitted.

Stocchi, P., and G. Spada. Il livello marino antico lungo le coste del nord Africa : una finestra sul budget di massa dellAntartide, Gruppo Nazionale di Geofisica della Terra Solida, 25 Convegno Nazionale, Consiglio Nazionale delle Ricerche, Poster, Roma 28 30 novembre 2006.

Stocchi, P., and G. Spada, 2007. Bounds on the time–history and the mass budget of Antarctica from the Holocene sea–level records in SE Tunisia, *Global and Planetary Change*, submitted, 2007.

Suess, E., 1906. *Face of the Earth,* Clarendon Press, Oxford.

Tegmark, M., 1996. An icosahedron–based method for pixelizing the celestial sphere, *ApJ Lett.,* 470, L81–L84.

Turcotte, D. L., and G. Shubert, 1982. *Geodynamics,* ed. John Wiley and Sons, New York, 456 pp.

Tushingham, A. M., and W. R. Peltier, 1991. Ice-3G: a new global model of late Pleistocene deglaciation based upon geophysical prediction of post–glacial sea level change, *J. Geophys. Res.,* 96, 4497–4523.

Tushingham, A. M., and W. R. Peltier, 1992. Validation of the ICE–3G model of Würm–Winsconsin deglaciation using a global data base of relative sea level histories, *J. Geophys. Res.,* 97, 3285–3304.

Tushingham, A. M., and W. R. Peltier, 1993. Relative Sea Level Database. IGPB PAGES/World Data Center–A for Paleoclimatology Data Contribution Series # 93–106, NOAA/NGDC Paleoclimatology Program, Boulder CO, USA.

Van Husen, D., 1997. LGM and late–glacial fluctuations in the eastern Alps, *Quat. Int.,* 38–39, 109–118.

Veizer, J., and fourteen others, 1999. 87Sr/86Sr, d13C and d18O evolution of Phanerozoic seawater, *Chemical Geology,* 161, 59–88.

Veizer, J., Y. Godderis, and M. Francois, 2000. Evidence for decoupling of atmospheric CO2 and global climate during the Phanerozoic eon, *Nature,* 408, 698–701.

Verleyen, E., D. A. Hodgson, G. A. Milne, K. Sabbe, and W. Vyverman, 2005. Relative sea–level history from the lambert Glacier region, East Antarctica, and its relation to deglaciation and Holocene glacier readvance, *Quat. Res.,* 63, 45–52.

Vermeersen, L. L. A., and R. Sabadini, 1997. A new class of stratified viscoelastic models by analytical techniques, *Geophys. J. Int.,* 129, 531–570.

Vermeersen, L. L. A., R. Sabadini, R. Devoti, V. Luceri, P. Rutigliano, C. Sciarretta, and G. Bianco, 1998. Viscosity inferences from Joint Inversions of Pleistocene Deglaciation–Induced Changes in Geopotential with a New SLR Analysis and Polar Wander, *Geophys. Res. Lett.,* 25, 4261-4264.

Vigny, C., J. Chery, T. Duquesnoy, F. Jouanne, J. Ammann, M. Anzidei, J. P. Avouac, F. Barler, R. Bayer, P. Briole, E. Calais, F. Cotton, F. Duquenne, K. L. Feigl, G. Ferhat, M. Flouzat, J. F. Gamond, A. Geiger, A. Harmel, M. Kasser, M. Laplanche, M. Le pape, J. Martinod, G. Menard, B. Meyer, J. C. Ruegg, J. M. Scheubel, O. Scotti, and G. Vidal, 2002. GPS network monitors the Western Alps' deformation over a five–year period 1933–1998, *J. Geod.,* 76, 63–76.

Vouvet, J., Ph. Malaurent, and J. Brunet, 1996. Caractérisation physique et environmentale d'un sanctuarie préhistorique sous–marin, semi–noyé et orné préalablement a l'élaboration d'une démarche conservatoire. Cas de la grotte Cosquer, France, *Comp. Rend. Acad. Sci. Paris,* 322 (2A), 935–942.

Walcott, R. I., 1972. Past sea levels, eustasy and deformation of the Earth, *Quat. Res.,* 2, 1–14.

Weaver, A. J., O. A. Saenko, P. U. Clark, and J. X. Mitrovica, 2003. Meltwater pulse 1a from Antarctica as a trigger of the Bolling–Allerod warm interval, *Science,* 299, 1709–1713.

Wessel, P. and W. H. F. Smith, 1991. Free software helps map and display data, *EOS Trans. AGU,* 72, 441.

Wessel, P. and W. H. F. Smith, 1998. New, improved version of generic mapping tools released, *EOS* 79, 579.

Woodward, R. S., 1888. On the form and position of mean sea level, *United States Geol. Survey Bull.,* 48, 87–170.

Wu, P., W. R. Peltier, 1982. Viscous gravitational relaxation, *Geophys. J. R. Astron. Soc.,* 70, 435–486.

Wu, P., and W. R. Peltier, 1983. Glacial isostatic adjustment and the free–air gravity anomaly as a constraint on deep mantle viscosity, *Geophys. J. R. Astron. Soc.,* 74, 377–449.

Wu, P., and Z. Ni, 1996. Some analytical solutions for the viscoelastic gravitational relaxation of a two–layer non–self–gravitating incompressible spherical Earth, *Geophys. J. Int.,* 126, 413–426.

Wu, P., and W. Van der Wal, 2003. Postglacial sea–levels on a spherical, self–gravitating viscoelastic earth: effects of lateral viscosity variations in the upper mantle on the inference of viscosity contrasts in the lower mantle, *Earth and Planet. Sci. Lett.,* 21, 57–68.

Wu, P., 2004. Using commerical finite element packages for the study of earth deformations, sea levels and the state of stress, *Geophys. J. Int.,* 158, 401-408.

Wu, P., H. S. Wang, H. S., and H. Schotman, 2004. Postglacial induced surface motion, sea–levels, and geoid rates on a spherical, self–gravitating laterally heterogeneous Earth, *Journal of Geodynamics,* 39 (2), 127–142.

Zachos, J., M. Pagani, L. Sloan, E. Thomas, and K. Billups, 2001. Trends, Rhythms, and Aberrations in Global Climate 65 Ma to Present, *Science,* 292, 686–693.